Integrated analysis of kerogen maturation and microfracture dynamics in organic-rich shales

James Ronald Johnson

Dissertation for the degree of Philosophiae Doctor (PhD)

Department of Geosciences

University of Oslo

December 2022

Series of dissertations submitted to the
Faculty of Mathematics and Natural Sciences, University of Oslo
No. 2580

ISSN 1501-7710

Cover: UiO.
Print production: Graphics Center, University of Oslo.

Preface

This dissertation has been submitted to the Department of Geosciences, Faculty of Mathematics and Natural Sciences at the University of Oslo following the requirements for the degree of Philosophiae Doctor (Ph.D.). The study was conducted under the project "PROMETHEUS" and focused on the impact of maturation on organic-rich shales as it influences both source and seal capabilities. The research was funded by the Research Council of Norway (RCN) and undertaken as a joint project between the University of Oslo, Norway, and the University of Grenoble, France. The project had strong links with the "ReSource" (Quantitative Analysis of Reservoir, Source, and Cap rocks of the Central North Sea), and "OASIS" (Overburden Analysis and Seal Integrity Study for CO_2 sequestration) projects. The principal supervisor of this work was Professor Nazmul Haque Mondol (UiO & NGI), and co-supervisors were Professor François Renard (UiO & UGA) and Dr. Maya Kobchenko (UiO).

The main objective of this study is to evaluate the impact of maturation in organic-rich shales on the material and acoustic properties to better understand the subsurface processes. The focus of the study is the Upper Jurassic Draupne Formation in the North Sea and the Upper Jurassic Hekkingen Formation in the Barents Sea. Moreover, analogue modeling is utilized to understand the processes. The dissertation is divided into three sections.

- **Section-1 (Overview of the Ph.D. dissertation):** This section includes an introduction to the research objectives, geological and theoretical background, experimental approach, database, methodologies, and key findings.

- **Section-2 (Journal papers):** This section includes three publications submitted or published in peer-reviewed journals, where I am the first author.

- **Section-3 (Appendix)**: This section includes six conference extended abstracts relevant to this Ph.D. research where I am the first author of five and coauthor (2nd author) of one of them.

Acknowledgements

‘IF I have seen further, IT IS by standing on the shoulders of giants.’ - Isaac Newton, 1675

Before I begin, I would like to dedicate this Ph.D. to my grandparents, all of whom have passed during my studies - Charles and Jessie McCurdy, as well as Dr. Ronald and Shirley Johnson. You will all be dearly missed.

There are many people to thank, but gratitude first to my advisors that took on the task to mold and shape - Professor Nazmul Haque Mondol and Professor François Renard. To the people that made this possible, I hope this experience has been as fruitful for you as it has been for me. I would be remiss to not also thank Dr. Maya Kobchenko, who committed countless hours in helping me grow as an independent researcher. Then, there were numerous individuals who provided technical and academic support – Thanusha Naidoo, Salahalldin Akhavan, Siri Simonsen, Mufak Said Naoroz, Michel Heeremans, Kjetil Bakke, Catherine Braathen, Anne Cathrine Modahl, Anne Gunhild Innes, Thor Axel Thorsen, Benoît Cordonnier.

All scientific endeavours are also supported by the many that have travelled the path before (i.e. advisors), are travelling the path now (i.e. colleagues), and those destined to do so in the future (i.e. protégés). For me, far too many individuals fall into these categories to thank, but I’d like to mention a couple names amongst them. To those that picked me up when I fell – Tom Davis, Corey Bourque, Brennan Meidinger, Jake Utley. And those that shone a light on the path ahead – Jamilur Rahman, Ole Rabbel, Jørgen Hansen, Marthe Guren, Austin Bailey. And those that reminded me of my passion for science – Bobby Gunning, Ryan Morrow, Thea Faleide, Stephen Michalchuk, Clayton Gouin, Robert Spall. Undoubtedly I have missed people, some that would prefer not to be mentioned and perhaps some that would have. Thank you to all of you for being a part of my life in whatever measure you are, and I hope that I contribute positively to yours.

The fortunate have two families in their life – the ones they are born into and the ones they later choose. Mom and Dad, you built the foundation on which I’m building my life. Andrew, please continue to provide the best council with greatest care. Christeen, buoyant laughs and quiet words of advice are gifts for all those you love. To the family that I chose, and who have graciously also chosen me – due to the shear number of you I cannot mention you all. So, special thanks to Gustave, Kathinka, Nicolas, Agnes, and Thekla – thank you for believing in me when I didn’t yet believe in myself, for welcoming me to a world where I still don’t always find my footing, and for countless hours of council and support.

Finally –

Celine, you are wise beyond your years and have a tranquil disposition that is at times infectious. You provide order in chaotic world – wind when caught in a doldrum, a respite when caught in a storm, direction when the compass misbehaves, and light when all seemed dark. The PhD was not a possibility without you, and I cannot thank you enough for taking this journey with me. Moreover, because you have also blessed us with two beautiful children and one more on the way in these past four years. Nicolas, Lily, and any other future little friends – you are shining beacons capable of immeasurable heights. To enjoy your own journies, first remember this world offers amazing opportunities. Second, be curious, think critically, and savour it all – the good and the bad, for there will be lots of both in your lives. Know that there have been many days in the last years where you provided me the strength to follow this advice, and I will never be able to thank you enough for it.

Summary

The relationship between the organic (i.e., kerogen) and inorganic (i.e., mineralogy) components of shales is presented utilizing a multiscale (i.e., μm–km) approach, with a focus on how kerogen maturation and microfracture dynamics may influence the material properties (e.g., mechanical, acoustic, elastic, and brittleness indices). Microtomography and SEM are used to investigate and understand the microstructure of organic-rich shales, particularly the size, geometry, orientation, and distribution of kerogen lenses within the mineralogical framework. Analogue models utilizing sugar, yeast, and gelatin enabled studies of the microfracturing process that occurs in three phases: (1) microfracture nucleation, (2) microfracture interconnection creating a complex network, and (3) fluid flow throughout the network. Seismic inversion is also utilized in order to understand the relationship between organic matter concentration and maturation at a basin scale. Data were collected predominantly from two source rocks, the Upper Jurassic Draupne Formation in the North Sea and the Upper Jurassic Hekkingen Formation in the Barents Sea along the Norwegian Continental Shelf for the portions of the study that required physical investigations. At the microscale (μm – cm), results demonstrate a relationship between both kerogen lens size and distribution. The shape of Type II/Type III kerogen lenses are classified into four categories according to the aspect ratio and one that relates to a depositional process. The mesoscale (cm – dm) shows that the fabric of shale influences fracture topology (i.e., microfracture network pattern) and that fracture topology impacts fluid flow (e.g., rate, periodicity). At the macroscale (m-km), increasing organic matter concentration is frequently correlated with greater maturation, resulting in poorer mechanical strength and greater brittleness, also expressed in changing acoustic and elastic properties (e.g., P-wave, S-wave, Young's Modulus, Poisson's Ratio). The collaborative study is placed within the current understanding of primary migration and how the physical processes alter organic-rich shales. Conclusions can be utilized to better understand organic-rich shale as both a source/reservoir (e.g., conventional and unconventional resources) and a seal (e.g., CO_2 sequestration, nuclear waste repository).

List of articles, extended abstracts, conference proceedings, and invited presentations

List of peer-reviewed articles (Section-2)

This dissertation includes the following three peer-reviewed journal papers where I am the principal authors.

Johnson, J.R., Hansen, J.A., Rahman, J., Renard, F., and Mondol, N.H., (2022a). Mapping the maturity of organic-rich shale with combined geochemical and geophysical data, Draupne Formation, Norwegian Continental Shelf. *Marine and Petroleum Geology, 138*(2022), 105525.

Johnson, J.R., Kobchenko, M., Mondol, N.H., and Renard, F., (2022b). Multiscale synchrotron microtomography imaging of kerogen lenses in organic-rich shales from the Norwegian Continental Shelf. *International Journal of Coal Geology, 253*(2022), 103954.

Johnson, J.R., Kobchenko, M., Johnson, A.C., Mondol, N.H., and Renard, F., (2022c). Experimental modelling of primary migration in a layered, brittle analogue system. *Tectonophysics, 840(2022), 229575*

List of extended abstracts (Section-3, Appendix-1)

This dissertation includes the following six extended abstracts. I am the principal author of five of them, and co-author of one.

Johnson, J.R., Hansen, J.A., Renard, F., Mondol, N.H., 2019. Geomechanical analysis of maturation for the Draupne Shale, Offshore Norway. In: Sixth EAGE Shale Workshop, European Association of Geoscientists and Engineers.

Hansen, J.A., **Johnson, J.R.,** Mondol, N.H., 2019. Cap rock evaluation of central North Sea shales, through log-derived Poisson's ratio and Young's modulus. In: Sixth EAGE Shale Workshop, European Association of Geoscientists and Engineers.

Johnson, J.R., Hansen, J.A., Renard, F., Mondol, N.H., 2019. Modeling maturation, elastic, and geomechanical properties of the Draupne Formation, offshore Norway. In: SEG Technical Program Expanded Abstracts 2019. Society of Exploration Geophysicists.

Johnson, J.R., Renard, F., Mondol, N.H., 2021. Salt remobilization timing and its impact on two Norwegian Continental Shelf organic-rich shale formations. In: Geoconvention 2021, CSEG CSPG CWLS.

Johnson, J.R., Kobchenko, M., Mondol, N.H., Renard, F., 2022. A potential alternative to Rock-Eval or wireline log calculations of TOC? – A case study from the Norwegian Continental Shelf. In: 83rd EAGE Annual Meeting Technical Program Expanded Abstracts 2022, European Association of Geoscientists and Engineers.

Johnson, J.R., Bailey, A., Mondol, N.H., Renard, F., 2022. Using microscopy image analysis to calculate the Mineral Brittleness Index in organic-rich shale. In: Sixth International Conference on Fault and Top Seals Technical Program Expanded Abstracts 2022, European Association of Geoscientists and Engineers.

List of conference proceedings (not included in the thesis)

Johnson, J.R., Hansen, J.A., Fawad, M., Mondol, N.H., 2019. Relationship between maturation and geomechanical parameters of the Upper Jurassic organic-rich Draupne Shale, Norwegian North Sea. In: 33rd NGF Winter Conference Technical Program Expanded Abstracts 2019, Norwegian Geological Society. 8 January 2019. Bergen, Norway.

Hansen, J.A., **Johnson, J.R.,** Fawad, M., Mondol, N.H., 2019. Quantitative characterization of the central North Sea Jurassic petroleum system. In: 33rd NGF Winter Conference Technical Program Expanded Abstracts 2019, Norwegian Geological Society. 8 January 2019. Bergen, Norway.

Fawad, M., Hansen, J.A., **Johnson, J.R.,** Mondol, N.H., 2019. Seal characterization of the Amundsen Formation for CO2 storage in the northern North Sea. In: 33rd NGF Winter Conference Technical Program Expanded Abstracts 2019, Norwegian Geological Society. 8 January 2019. Bergen, Norway.

Johnson, J.R., Kobchenko, M., Mondol, N.H., Renard, F., 2020. Analogue modeling of an organic-rich shale utilizing a smectite-based gelatin. In: 34th NGF Winter Conference Technical Program Expanded Abstracts 2020, Norwegian Geological Society. 9 January 2020. Oslo, Norway.

Johnson, J.R., Kobchenko, M., Mondol, N.H., Renard, F., 2021. Multiscale synchrotron X-ray microtomography imaging of organic material in shales in the context of primary migration. In: 35th NGF Winter Conference Technical Program Expanded Abstracts 2021, Norwegian Geological Society. 10 January, 2021 Trondheim, Norway

Johnson, J.R., Kobchenko, M., Mondol, N.H., Renard, F., 2021. Analogue modeling of primary migration in shales using organic-rich and organic-poor layered gel. In: 35th NGF Winter Conference Technical Program Expanded Abstracts 2021, Norwegian Geological Society. January 9, 2021. Trondheim, Norway.

List of invited presentations (not included in the thesis)

Johnson, J.R., Johnson, A.C., Ilagan, T., Haid, M., 2018. Laurie Dake Competition Finalist – FIELD Challenge. In: 80th EAGE Annual Meeting. 11 June 2018. Copenhagen, Denmark

Johnson, J.R., Mondol, N.H., Renard, F., 2018. Shale as a source and seal: an overview. Prometheus Workshop (Understanding Organic-Rich Shales) annual meeting, 11 December 2018. Oslo, Norway

Johnson, J.R., Hansen, J.A., Mondol, N.H., Renard, F., 2019. Elastic and mechanical properties of the Draupne Shale, Norwegian Continental Shelf. Prometheus Workshop (Understanding Organic-Rich Shales) annual meeting, 29 November 2019. Oslo, Norway

Johnson, J.R., Mondol, N.H., Renard, F., 2020. 3D microtomographical analysis of organic-rich shale in order to understand the sealing qualities as they relate to CO2 Sequestration in the North and Barents Seas. OASIS (Overburden Analysis and Seal Integrity for CO2 Sequestration in the North Sea) project annual meeting. 11 December 2020. Oslo, Norway

Johnson, J.R., Kobchenko, M., Mondol, N.H., Renard, F., 2021. A study on kerogen lenses and the fabric of organic-rich shale. Institute for Energy and Nuclear Technology Research (IFE). May 6 2021. Oslo, Norway

Johnson, J.R., Renard, F., Mondol, N.H., 2022. Microfracture to fault analysis risk for organic-rich shales as a CO2 sequestration seal: Draupne Formation, Norwegian Continental Shelf. In: 83rd EAGE Annual Meeting Workshop, Mapping and Quantifying CO2 in the Subsurface – data, models, and uncertainty. 5 June 2022. Madrid, Spain

Johnson, J.R., Kobchenko, M., Mondol, N.H., Renard, F., 2022. Analogue modeling of fluid-rock interactions related to source and seal analysis of organic-rich shales. Institute for Energy and Nuclear Technology Research (IFE). 15 June 2022. Oslo, Norway

Table of Contents

Section 1
Overview of the Ph.D. Dissertation

1.0 Introduction

1.1 ***Organic-rich shales, maturation and microfracturing***

Shales contribute 50-70 % of sedimentary rocks in sedimentary basins wordlwide, and ~80% of all boreholes drilled for hydrocarbon exploration and production. The definition of 'shale' is wide-ranging. However, it is agreed that it is a clastic sedimentary rock of fine-grained material composed at least in part of clay minerals (Vandenbroucke and Largeau, 2007; EIA, 2013; Ougier-Simonin et al., 2016). Furthermore, the nature of clay minerals results in an indurated, laminated rock with transversely isotropic (i.e., anisotropic) behavior (Alfred and Vernik, 2013; Zhao et al., 2016; Ougier-Simonin et al., 2016; Holt and Kolstø, 2017).

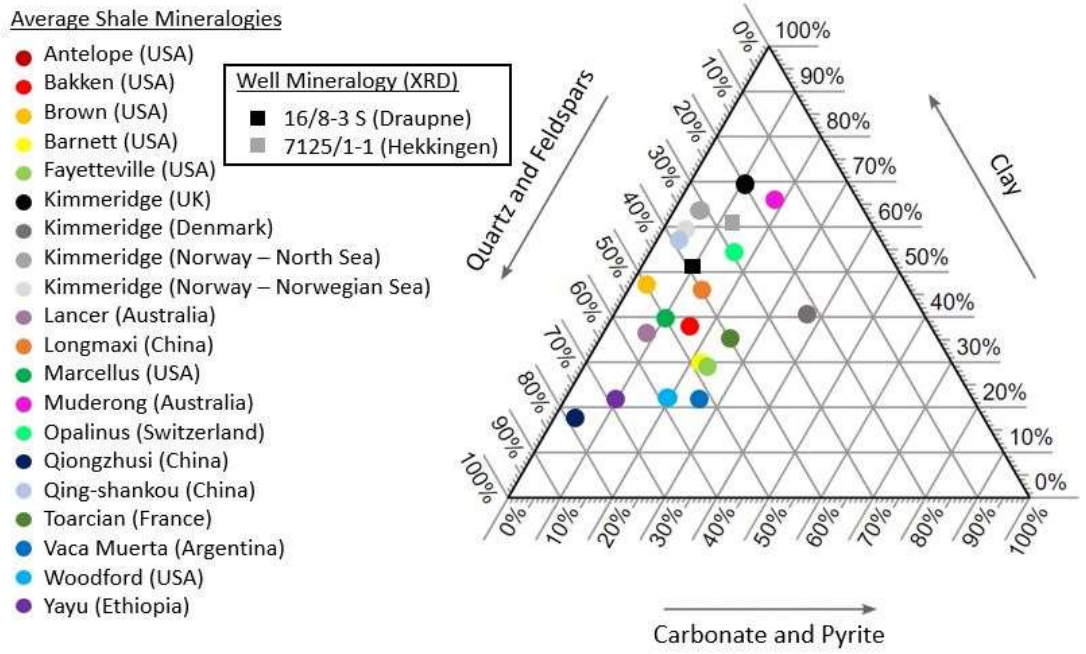

Figure 1.1: Ternary diagram showing the average composition of twenty shales worldwide (based on Ougier-Simonin et al., 2016) compared to the mineralogical compositions of the Draupne and Hekkingen Formation from wells representative of the area studied in this thesis (based on Zadeh et al., 2017).

Variability in the 'shale' definition stems from the wide-ranging definition of mineralogy for shale (Figure 1.1 resulting in part from a variety of depositional systems for shale (e.g., deep marine, lacustrine, tidal estuary, transitional, etc.) (James and Dalrymple, 2004). Shale is considered organic-rich when the organic matter exceeds 2 wt. % of the total mass (Kuuskraa et al., 2013; Cooke, 2014). Microfracture growth within organic-rich shales during maturation controls the mechanical and elastic properties of shale. Other factors, including rock fabric and composition, fluid types, and pressure-temperature (PT) regime, influence microfracture network development. Shale has a broad range of

mineralogical composition (James and Dalrymple, 2004; Mondol et al., 2008; Ougier-Simonin et al., 2016), resulting in an equally wide range of fabrics in both bedding parallel and perpendiculardirections (James and Dalrymple, 2004; Ougier-Simonin et al., 2016; Fjær et al., 2021; Johnson et al., 2022b). Fluid types and their presence are controlled by kerogen types and network connectivity. Basin modeling has shown that different basin types (e.g., foreland, depression, craton) associated with divergent PT-regimes will result in oil and gas development from kerogen maturation (Tissot and Welte, 1984; Johnson, D., 1995; Vandenbroucke and Largeau, 2007; Fjær et al., 2021). In all cases, the resulting microfracture network enables primary migration through material changes in the mechanical and elastic properties (Ougier-Simonin et al., 2016; Teixeira et al., 2017; Johnson et al., 2022b; Johnson et al., 2022c). These factors, including the shift in kerogen state, affect the macroscale detection and signatures of shale's rock and fluid properties (Alfred and Vernik, 2013; Zhao et al., 2016; Johnson et al., 2022a).

Microfracture creation has been proposed to be driven by the conversion of kerogen lenses (Anders et al., 2014; Teixeira et al., 2017). As such, the geometry, orientation, and distribution of kerogen lenses within the fabric of organic-rich shales will define the nature of microfracture nucleation and, ultimately, the connectivity of the networks. Modeling has shown that variations in kerogen lens size, shape, and orientation are important to the microfracturing process (Fan et al., 2010; Jin et al., 2010; Chauve et al., 2020; Rabbel et al., 2020). Furthermore, the success of microfracture propagation and interconnection will depend upon the surrounding inorganic constituents (i.e., minerals). Therefore, mineralogy will influence the ability of fractures to heal (Hernandez et al., 2004; Brun-Lie, 2017; Voltolini and Franklin, 2020) after kerogen extrusion (Pepper et al., 2017; Zhao et al., 2016).

Shale rocks may include a diverse range of both inorganic contents (i.e., mineralogy) and organic content (e.g., kerogen, macerals). The result of this is a rock that can vary greatly in terms of material properties, including layer thickness, anisotropy, and rigidity. Depositional systems set layer thickness that are subsequently influenced by diagenesis (Johnson, 1974; James and Dalrymple, 2004). Anisotropy can vary both in terms of layering (Hernandez et al., 2004; Ougier-Simonin et al., 2016), and stress regime (Rabbel et al., 2020; He et al., 2021). The rigidity can be particularly complex, as it is influenced not only by the rock's material properties but also by fluid amount, content, and viscosity (He et al., 2021).

The impact of kerogen maturation, observed at the microscale, has an effect on the mechanical and elastic properties of shales at the macroscale (Ougier-Simonin et al., 2016; Zhao et al., 2016). Increasing maturation will result in a shale that behaves in a more brittle manner mechanically, while the elastic response is more complex. The elastic properties of organic-rich shales depend on various factors, including alterations in mineralogy, the introduction of porosity, and increased anisotropy as the result of fracturing (Prasad et al., 2009; Alfred and Vernik, 2013; Zhao et al., 2016). The rate of

transformation from mechanically ductile to brittle shale is influenced by the total organic carbon (TOC) content (wt. %) (Avseth et al., 2015; Badics et al., 2015).

1.2 Motivation and objectives

The present Ph.D. research integrates a three-pronged approach utilizing 3D microtomography and scanning electron microscopy (SEM) in concert with image analysis, laboratory analysis of analogue experiments, and seismic inversion in order to answer the following questions:

- What is the relationship between the size of kerogen lenses and their spatial distribution?
- What are the geometrical properties of 'typical' Type II and III kerogen lenses (i.e., size, shape, aspect ratio)?
- How does the fabric of shale influence microfracture creation and interconnection?
- How do the fracture topology and the rigidity of the host solid influence fluid flow?
- How does the total organic content influence shale properties?
- How does maturation influence shale mechanical properties?

The thesis seeks to answer these questions by first addressing observations at the microscale, then by utilizing analogue experiments to understand the processes that occur at the mesoscale, and finally by reviewing the impacts of these on the mechanical/elastic behaviors at the macroscale. The effects of microfracturing during the conversion of kerogen due to maturation have an impact on understanding shale as potential source rock and how the rock properties of a seal have been or may be altered due to a change in either temperature or pressure. As a result, the research has an extensive impact relevant to a wide variety of sectors (e.g., nuclear repositories, CO_2 sequestration, unconventional and conventional hydrocarbon exploration/exploitation and development, and geotechnical investigations).

1.3 Study area

The study area focus for this Ph.D. research is on the Norwegian Continental Shelf, more specifically, the central North Sea and the Barents Sea (Figure 1.2). While some elements of my research extend to all organic-rich shales, it is helpful to place portions of it in a geological context. My work has a strong focus on Kimmeridge equivalent Jurassic-Cretaceous source rocks within the Norwegian Continental Shelf, particularly the upper units of the organic-rich shales in the North Sea (Draupne Formation) and the Barents Sea (Hekkingen Formation) (Figure 1.2).

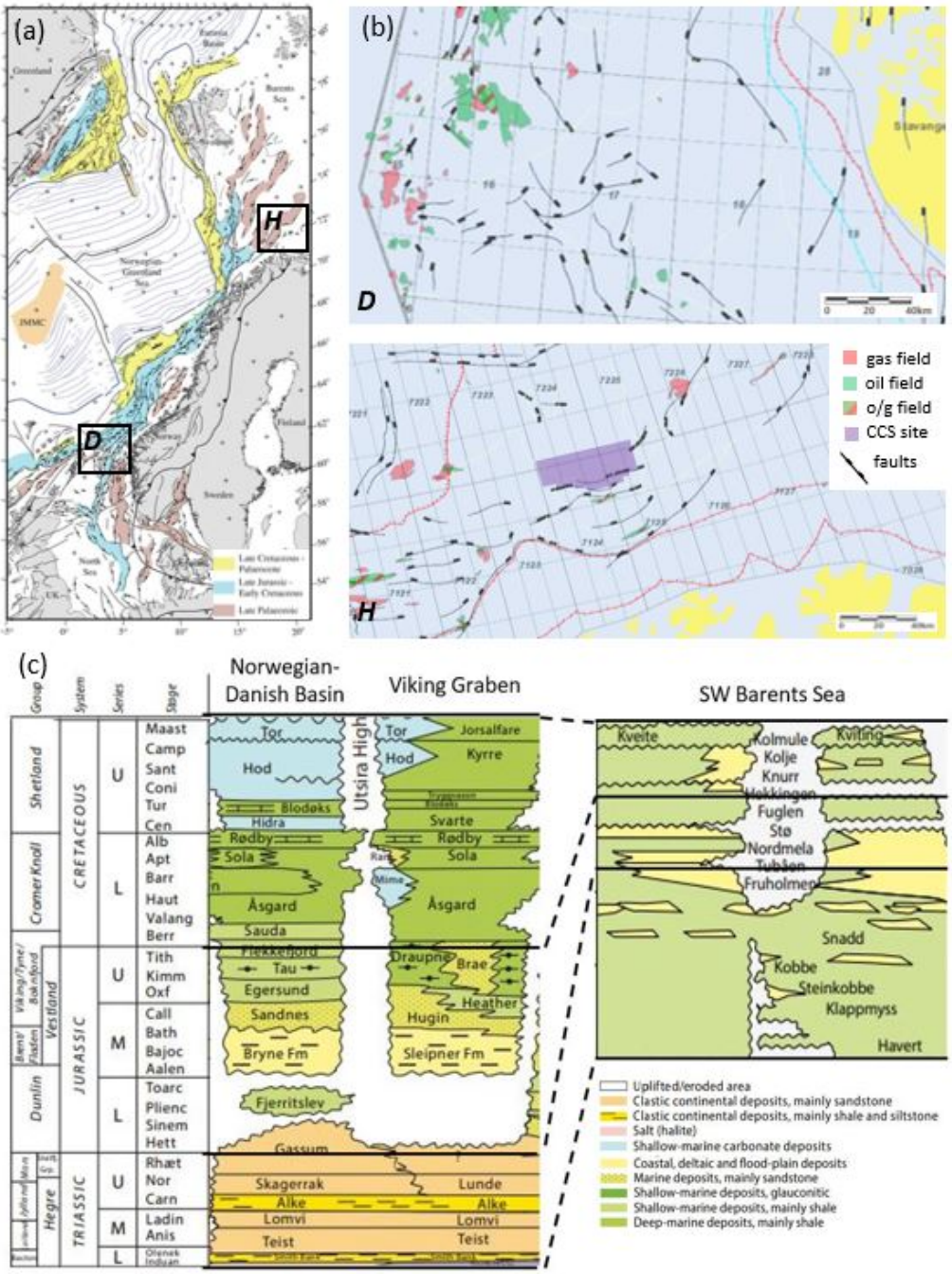

Figure 1.2: (a) Structural elements and associated timing of rift phases of the Norwegian Continental Shelf (modified from Faleide et al., 2015) with main study areas highlighted by two black boxes in the Barents (H) and North Sea (D). (b) Local structural maps including oil and gas fields and present and future potential carbon capture and sequestration (CCS) sites within the local study areas for the Barents (H) and North Sea (D). (c) Geological timeline (modified from NPD, 2022) providing context for the Upper Jurassic source rocks (e.g., Draupne, Hekkingen formations) that are a primary focus for this Ph.D.

The Draupne Formation was deposited in a quiescent, anoxic marine environment (Hansen et al., 2020; Rahman et al., 2021; NPD, 2022), occasionally perturbed by turbidite flows (Jackson et al., 2011; Johnson et al., 2022a; NPD, 2022). This quiescent environment was ideal for the deposition of comparatively fine low-density clay minerals, while the anoxic environment was suited to the preservation of organic matter resulting in a wide range of 2-15% TOC (total organic carbon), tied to biotic crises (Badics et al., 2015; Hansen et al., 2020; NPD, 2022). The deposition of the Draupne formation was influenced by two major rifting events that occurred in the Triassic and the Late Jurassic-Early Cretaceous periods (Ziegler, 1992; Faleide et al., 2008) (Figure 1.2b). The first set of rifting events helped establish the geometry of the basin (Faleide et al., 2008; Faleide et al., 2015). Coupled with the eustatic sea-level rise, the second rifting event was directly responsible for the ideal 'organic-rich shale' depositional environment of the Draupne Formation (Whipp et al., 2014; Hansen et al., 2020; NPD, 2022).

Similarly, the Hekkingen Formation was deposited in a restricted deep marine environment ideal for the deposition of organic-rich shale (Dore et al., 1985; Ohm et al., 2008; Hansen et al., 2020; NPD, 2022). The formation is also defined by the same two rifting events that encompass the Norwegian Continental Shelf (Faleide et al., 2015; Hansen et al., 2020; Johnson et al., 2022b; NPD, 2022). However, the Hekkingen Formation underwent multiple uplift and erosional events resulting in a diminished total thickness in the range of ~ 0-100m (Henriksen et al., 2011; Baig et al., 2016; NPD, 2022). These uplift events are related to exhumation that varies from 0.4-3.0 km (Ohm et al., 2008; Henriksen et al., 2011; Zadeh et al., 2017; Baig et al., 2019) in the Barents Sea.

Four key differences between the Draupne and Hekkingen Formations, and the impact that they have in the context of primary migration, are described below:

- Evidence suggests the Hekkingen Formation deposited in a deeper, more restricted marine environment than the Draupne Formation (Johnson et al., 2021; Johnson et al., 2022b). This resulted in greater organic matter or total organic carbon (TOC) content on average for the Hekkingen Formation than for the Draupne Formation (Johnson et al., 2022b). It may have also impacted the ratio of Type II:Type III kerogen, and by extension the degree of microfracturing that will occur during diagenesis (Johnson et al., 2022c).
- Turbidites can be found in both formations. However, the more distal environment of the Hekkingen Formation results in fewer, more fine-grained turbidites (Jackson et al., 2011; Marin et al., 2020; NPD, 2022). A reduction in the amount of hard (i.e. stiff) minerals (e.g., quartz, feldspar) will reduce microfracturing and enhance the ability for said shale to heal (Bourg, 2015; Voltolini and Franklin, 2020).
- Multiple uplift events occurred post-deposition in the Hekkingen Formation resulting in significant erosion (Baig et al., 2016; Zadeh et al., 2017; Marin et al., 2020) as reflected in the

difference in formation thickness (Johnson et al., 2022b). The variable timing in uplift is the result of salt tectonism (Johnson et al., 2021).

- Later salt remobilization of the Draupne Formation resulted in less erosion (Baig et al., 2016; Zadeh et al., 2017; Marin et al., 2020). It also had an impact on kerogen maturation within the two formations (Johnson et al., 2021) wherein the Hekkingen Formation on average is slightly more mature (Johnson et al., 2022b).

Upper Jurassic/Late Cretaceous organic-rich shales (e.g., Draupne, Hekkingen formations) of the Norwegian Continental Shelf share a common depositional history, although there are subtle differences dependent on the region. Other organic-rich shales in the Norwegian Continental Shelf that are roughly time equivalent include the Tau, Farsund, and Spekk Formations. However, the subsequent diagenetic history of these shales differentiates substantially by region. The subtle differences in deposition and significant differences in diagenesis result in variations of mechanical properties.

1.4 Database

The database utilized was very broad in nature including several seismic datasets, well logs, vertical seismic profiles (VSP) surveys, a geochemical database, core data, powder X-ray diffraction (XRD) data, thin sections, scanning electron microscopy (SEM) images, and microtomography images. In addition to this, an analogue laboratory dataset was created to reproduce fluid expulsion during primary migration and that is discussed more in section *3.3 Analogue Experiment Methodology*. Table 3.1a explores the relationship between all of the data available for the North Sea, while Table 3.1b explores the data available for the Barents Sea.

Table 3.1a: The North Sea data associated with each well log, including whether it is located within a utilized 3D seismic survey, the well logs available (B = basic inclusive of gamma ray, density, P-wave, and resistivity, S = S-wave, and P = neutron porosity, NPHI), whether a VSP dataset was available, geochemical data available (V = vitrinite reflectance, T = TOC calculations, and O = other, possibly inclusive of hydrogen index, oxygen index, T_{max}, and S_2), core data available, XRD data acquired or used from a project within the study area, thin sections produced, SEM images acquired, and microtomography (MT) images acquired.

North Sea Dataset									
Well Log (#)	Within 3D Seismic Survey	Well Logs (B, S, P)	VSP Survey	Geochemical Dataset (V, T, O)	Core Data Available	XRD Data Available	Thin Sections Produced	SEM Images Acquired	MT Images Acquired
15/3-1	-	BP	-	VT	-	-	-	-	-
15/3-3	-	BP	-	TO	X	-	X	X	-
15/3-5	-	BSP	-	VTO	-	-	-	-	-
15/3-8	-	BSP	-	TO	X	X	X	X	-
15/5-2	-	B	-	TO	-	-	-	-	-
15/5-3	-	B	-	-	-	-	-	-	-

15/6-4	-	B	-	-	-	-	-	-	-
15/6-6	ST14M06	BP		VT	-	-	-	-	-
15/6-10	-	BSP	-	TO	-	-	-	-	-
15/8-2	-	BSP	-	-	-	-	-	-	-
15/9-1	ST14M06	BP	-	-	-	-	-	-	-
15/9-2	ST14M06	BP	-	VTO	-	-	-	-	-
15/9-4	ST14M06	BP	-	-	X	-	X	X	-
15/9-6	ST14M06	BP	-	-	-	-	-	-	-
15/9-11	ST14M06	BSP	X	VTO	-	-	-	-	-
15/9-18	ST14M06	BP	-	-	-	-	-	-	-
15/9-21	ST14M06	BP	-	-	-	-	-	-	-
15/9-22	ST14M06	BP	-	VTO	-	-	-	-	-
15/9-23	ST14M06	BSP	X	-	-	-	-	-	-
15/12-1	-	BP	-	TO	X	X	X	X	-
16/1-7	-	BP	-	VTO	X	-	-	-	-
16/4-2	-	BP	-	TO	-	-	-	-	-
16/6-1	-	B	-	TO	-	-	-	-	-
16/7-2	-	P	-	VTO	X	-	-	-	-
16/8-3S	ST0611	BSP	X	TO	X	X	X	X	3
16/9-11	ST0611	BP	-	-	-	-	-	-	-
16/10-3	ST0611	BP	-	TO	-	-	-	-	-
16/11-2	ST0611	BP	-	VTO	-	-	-	-	-
17/4-1	-	BP	-	VTO	X	X	X	X	-
34/4-3	-	BP	-	TO	X	-	X	X	-

Table 3.1b: The Barents Sea data associated with each well log, including whether it is located within a utilized 3D seismic survey, the well logs available (B = basic inclusive of gamma ray, density, P-wave, and resistivity, S = S-wave, and P = neutron porosity, NPHI), whether a VSP dataset was available, geochemical data available (V = vitrinite reflectance, T = TOC calculations, and O = other, possibly inclusive of hydrogen index, oxygen index, T_{max}, and S_2), core data available, XRD data acquired or used from a project within the study area, thin sections produced, SEM images and microtomography (MT) images acquired.

Barents Sea Dataset									
Well Log (#)	Within 3D Seismic Survey	Well Logs (B, S, P)	VSP Survey	Geochemical Dataset (V, T, O)	Core Data Available	XRD Data Available	Thin Sections Produced	SEM Images Acquired	MT Images Acquired
7124/3-1	-	BP	-	VTO	-	-	-	-	-
7125/1-1	-	BP	-	VTO	X	X	X	X	3
7125/4-1	-	BSP	X	VTO	-	-	-	-	-
7224/7-1	-	BP	X	VTO	-	-	-	-	-
7226/11-1	-	BP	-	TO	X	X	-	-	-

More complete listings of the available datasets as they were utilized for the individual studies can be referred to in both the publications and extended conference papers. The dataset in the North Sea focusing on the Kimmeridge equivalent (e.g., Draupne Formation, Tau Formation) was significantly more robust than that for the Barents Sea Kimmeridge equivalent (i.e., Hekkingen Formation) as there were significantly more data available within that sector of the Norwegian Continental Shelf.

1.5 Thesis Organization

The thesis is submitted to get a Ph.D. degree from the University of Oslo. The thesis contains three sections. The first section is an overview of the entire topic and focus of the Ph.D., including an introduction to the research objectives, geological and theoretical background, experimental approach, database, methodologies, and the key findings, including summaries for each publication. The second section contains the three peer-reviewed journal papers in Marine and Petroleum Geology (Johnson et al., 2022a), International Journal of Coal Geology (Johnson et al., 2022b), and is under revision in Tectonophysics (Johnson et al., 2022c). Finally, section three contains six conference publications.

The first part of this thesis contains five chapters, including the introduction and geological background (***Chapter 1***). ***Chapter 2*** summarizes the theoretical background and the scientific questions that motivated my research. Outlining the complexity of organic-rich shale, it aims to present the current understanding of how kerogen maturation influences the creation of microfractures. It characterizes the influence microfractures have on shale both as a potential source rock for hydrocarbon exploration but also as a seal for a variety of systems/uses (e.g., CO_2 sequestration, nuclear waste storage, geotechnical analysis, conventional and unconventional hydrocarbon resources). ***Chapter 3*** summarizes the diverse experimental approaches used in this Ph.D., including 3D tomography, SEM, XRD, analogue experiments, geochemical techniques (e.g., Rock-Eval), and seismic inversion. The 3D microtomography data was acquired on beamline ID19 at the European Synchrotron Radiation Facility (ESRF), while the SEM images were acquired at the University of Oslo, Department of Geosciences. The analogue experiments were designed in order to understand microfracture creation in organic-rich shales in the context of primary migration. Special attention was paid to designing the experiments in such a way as to address complex problems specific to shale, including anisotropy and rigidity. Seismic inversion was utilized in order to characterize maturation and TOC content over a broad area. Geochemical characterization was used in combination with elastic parameters (Vp, Vs, rho, E, v) in order to create a novel facies classification that is called the Organic Maturation Product (OMP). ***Chapter 4*** contains a summary of the major findings of the three publications that make up this body of research and how they relate to the key overarching scientific questions. Finally, ***Chapter 5*** provides an outlay of the major conclusions of this Ph.D. research alongside an outlook for potential future work.

2.0 Theoretical Background

Microfracture nucleation, growth, and interaction are controlled by a number of processes, each of which can be influenced by different factors. Within organic-rich shale, the common causes of microfracturing can be divided into internal causes and external causes. Internal causes include the conversion of kerogen to hydrocarbons and the transformation of hydrous into anhydrous minerals (e.g., smectite/illite transition) (Figure 2.1) (Mondol et al., 2008; Vidal and Dubacq, 2009; Anders et al., 2014; Teixeira et al., 2017; Johnson et al., 2022b). External causes include significant alterations in pressure-temperature (PT) regimes (e.g., uplift, tectonic activity) over relatively short geological periods (Baig et al., 2019; Rabbel et al., 2020; Rummel et al., 2020). However, in the case of organic-rich shale, increasing PT regime will result in the aforementioned conversion of kerogen, as well as hydrous minerals (Anders et al., 2014; Teixeira et al., 2017).

Kerogen lenses convert into hydrocarbons first, followed by potentially catalyzing the conversion of smectite to illite (Figure 2.1). Fracturing is initiated by kerogen lenses, due to volume expansion, and assisted by clay mineral conversion/alteration. However, the composition of the organic-rich shale will also play a role in terms of the degree of fracture propagation and the likelihood of fracture healing (Bourg, 2015; Voltolini and Franklin, 2020). In order to understand the three phases that characterize microfracturing within organic-rich shales, overall compaction trends for pure clay and clean sand endmembers for both mechanical and chemical effects first need to be explored (Figure 2.1a). Mechanical compaction within the subsurface results from increasing overburden and is governed by effective stress. Vertical stress (i.e., overburden stress) can be calculated as follows:

$$\sigma_v = \rho_b g h \tag{2.1}$$

where σ_v is vertical stress, ρ_b is bulk density of the overburden rock and fluids, g is due to the acceleration of gravity, and h is depth. Effective stress (σ_e) can be calculated from vertical stress (σ_v) and pore pressure (P_p).

$$\sigma_e = \sigma_v - P_p \tag{2.2}$$

Horizontal effective stress can be either measured in boreholes or calculated by the k_0 method, which is the ratio between minimum horizontal stress and effective vertical stress (Engelder and Fischer, 1994) as follows:

$$k_0 = \frac{\sigma_h - P_p}{\sigma_v - P_p} \tag{2.3}$$

where , σ_h is effective horizontal stress. The equation can be rearranged to calculate effective horizontal stress, σ_h, where:

$$\sigma_h = k_0 \sigma_v + (1 - k_0) P_p \tag{2.4}$$

The relationship between effective and vertical stresses has been shown to impact large-scale failure processes (i.e., faulting) as a result of principal stress directions (Eisbacher, 1996; Chauve et al., 2020),

that define Anderson faulting resulting in regimes for normal faulting, reverse faulting, and strike-slip faulting. These relationships have also been shown to impact hydrofracture propagation (i.e., artificial fracturing) (Teixeira et al., 2017), as well as natural microfracture processes (Chauve et al., 2020).

Chemical compaction is dependent on temperature and time. Initial high porosity within shales decreases rapidly with compaction (Mondol et al., 2008; Bjørlykke et al., 2017) due to the rearranging of platy clay minerals. Smectite becomes thermodynamically unstable around ~70°C, marking the transition zone between mechanical and chemical compaction (Figure 2.1a), resulting in conversion to illite. The conversion requires the presence of potassium, most often found in potassium feldspar grains within the matrix (Figure 2.2). The conversion is described as follows:

$$2KAlSi_3O_8 + 3Al_2Si_4O_{10}(OH)_2 = 2KAl_3Si_3O_{10}(OH)_2 + 12SiO_2 + 2H_2O \quad (2.5)$$

The formation of H_2O resulting in microfractures that create pore-space and mechanically weaken the organic-rich shale. However, the creation of microquartz (Equation 2.5) opposes this acting to mechanically strengthen the host rock (Mondol et al., 2008; Bjørlykke et al., 2017). At ~120°C kaolinite may also convert to illite given a significant enough concentration of potassium (Mondol et al., 2008; Bjørlykke et al., 2017). This is described as:

$$2KAlSi_3O_8 + Al_2Si_2O_5(OH)_4 = 2KAl_2Si_2O_{10}(OH)_2 + 4SiO_2 + 2H_2O \quad (2.6)$$

The chemical conversion from kaolinite to illite also results in the creation of both microquartz and water, which will enact processes for the organic-rich shale that will mechanically oppose one another (Mondol et al., 2008; Bjørlykke et al., 2017). However, this conversion will likely occur after kerogen conversion (Tissot and Welte, 1984). The types of clay minerals present in shales are strongly dependent on a number of factors, including provenance, tectonic settings, and erosion processes, including the particle transportation rate (Mondol et al., 2008; Bjørlykke et al., 2017).

Now, the three phases of microfracturing (Johnson et al., 2022c) can be discussed. Phase I is characterized by an immature organic-rich source rock dominated by the typical clay minerals (i.e., kaolinite, smectite, chlorite). In Phase II, kerogen lenses will begin to expel hydrocarbons resulting in the creation of porosity and microfractures. Additionally, if smectite is present then a certain percentage of it will begin converting to illite. Based on Draupne and Hekkingen Formations clay mineralogy comparison (Kalani et al., 2015; Zadeh et al., 2017; Johnson et al., 2021), rock can be considered immature from a geochemical perspective (e.g., Rock-Eval analyses) while in Phase II. Phase III is dominated by kerogen lenses that have largely expanded, resulting in significant porosity creation, including a complex network of microfractures. Additionally, at this point, smectite will be largely converted to illite (Figure 2.1). Note that both of these processes are chemically irreversible (Tissot and Welte, 1984; Koo et al., 2014), making them good markers of the PT-regimes an organic-rich shale has undergone even if they should later be uplifted (e.g., Hekkingen Formation).

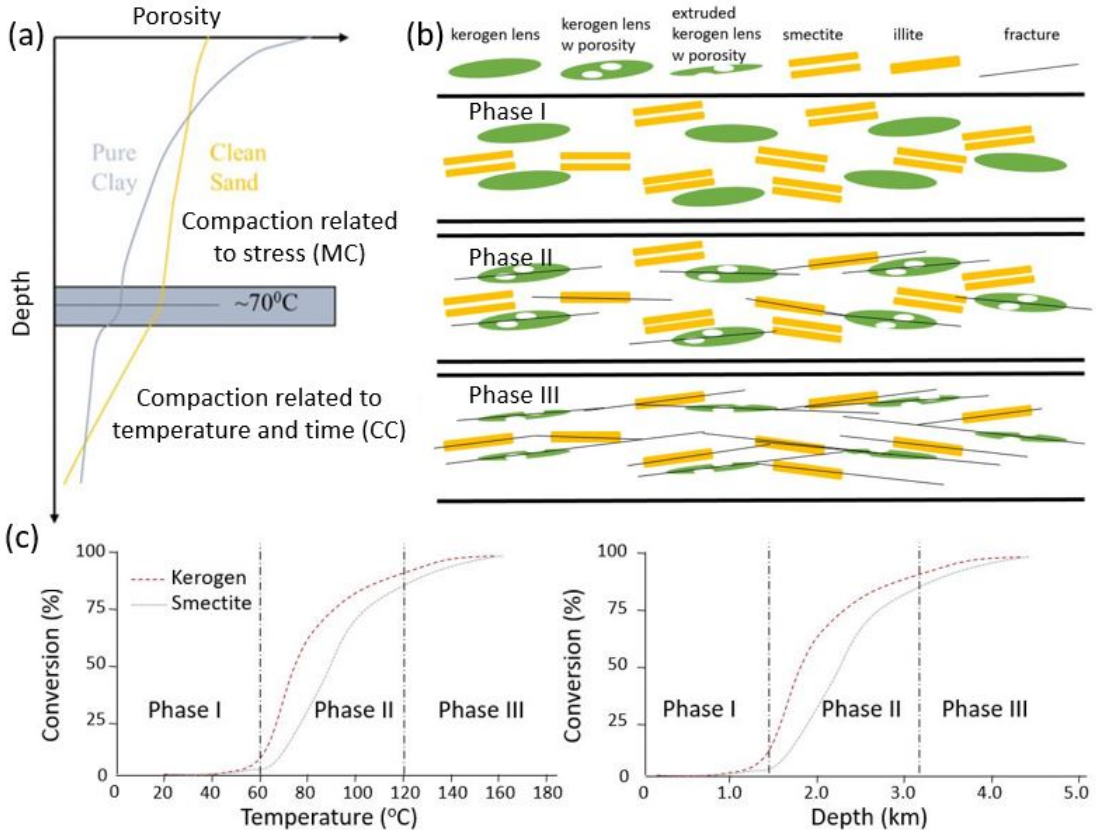

Figure 2.1: (a) Compaction trends for pure clay and clean sand highlighting the mechanical compaction (MC) zone, a transition zone around 70°C, and chemical compaction (CC) thereafter (Avseth et al., 2010), wherein (b) the microfracturing process can be divided into three phases. (c) The conversion of kerogen and smectite compared to one another in terms of temperature and depth as a percentage of conversion, in the three phases of microfracturing. The comparison here is based on Tissot and Welte (1984) for kerogen lenses and Carcione and Avseth (2015) for the smectite-illite transition.

2.1 Microscale controls and microfracturing in organic-rich shales

Absent fluid, shales are a complex assemblage of the inorganic (i.e., mineralogy) and the organic (i.e., kerogen) components. The inorganic component can be separated into hard (i.e., stiff) and soft minerals. The ratio of these two categories has implications for how shale behaves mechanically (Jarvie et al., 2007; Jin et al., 2014) and calculated as follows:

$$MBI = \frac{\text{Qtz+Carb+Fsp+P}}{Qtz+Carb+Fsp+Py+Cly} \tag{2.7}$$

where, MBI is the mineralogy-based brittleness index, Qtz is quartz, Carb is carbonate, Fsp is feldspar, Py is pyrite, and Cly is clay. Several studies recognized that in organic-rich shales, the organic component would influence the mechanical properties (Alzahabi et al., 2015; Rahman et al., 2020; Johnson et al., 2022a). However, it is important to note that the impact that this has is dependent on the

degree of maturation (Johnson et al., 2022a; Johnson et al., 2022b). The proxy (i.e. MBI) for mechanical behavior, including the organic materials, uses the equation here:

$$MBI = \frac{\text{Qtz+Carb+Fsp}}{Qtz+Carb+Fsp+Py+Cly+TO} \tag{2.8}$$

Prior to primary migration, resulting from increasing PT (pressure-temperature) regimes, the ratio of soft minerals and kerogen lenses to hard (i.e., stiff minerals) determines mechanical behavior. These changes during maturation, as the kerogen lenses, resulting in the creation of a microfracture network that facilitates migration (Fan et al., 2010; Anders et al., 2014; Teixeira et al., 2017). Note that the alteration of clay minerals can also play a role in the creation of microfractures. Pore pressure determines the amount of organic material extruded (Pepper and Corvi, 1995). After complete conversion of kerogen, PT regime, in combination with the mineralogy, once again determines mechanical and elastic behaviors, including the degree of microfracture healing that occurs (Hernandez et al., 2004; Voltolini and Franklin, 2020).

2.1.1 Impact of composition, inorganic elements (i.e., mineralogy) on organic-rich shales

While the ratio of hard to soft minerals is important to the mechanical strength of shale, the hard minerals themselves vary somewhat in terms of mechanical properties (Table 2.1). The range of grain sizes most commonly associated with shale (i.e., silt, 4-63 μm) appears to determine the thickness and diameter ranges for most hard minerals. This supposition is supported by studies, particularly those investigating quartz (Blatt and Schultz, 2006) and feldspar (Skobe et al., 2013). Pyrite, however, has a smaller range that is determined by its paleoredox environment, wherein grains larger than 5 μm is unlikely to occur in shales with organic matter content larger than 1 wt. % (Raiswell and Berner, 1985; Bond and Wignall, 2010; Liu et al., 2021). Note that framboidal pyrite growth alters depending on when it forms during diagenesis. The salient changes are overall diameter (D) and the diameter of the associated microcrystals (d) of the framboidal pyrite (Bond and Wignall, 2010; Liu et al., 2021). Based on the two diameters, both the Hekkingen and Draupne Formation shales have dominantly syngenetic pyrites, a potential marker for high gas content within an appropriate oil and gas window (Bond and Wignall, 2010; Liu et al., 2021). This is consistent with Type II and III kerogen types that are oil and gas prone and gas prone, respectively (Tissot and Welte, 1984).

While not observed in either the SEM or microtomography images, microquartz growth is known to occur within organic-rich shales of the Norwegian Continental Shelf (Jahren et al., 2007; Thyberg et al., 2010; Hansen et al., 2020). Carbonate (e.g., calcite, dolomite, siderite) dissolution into surrounding microfractures is not common in organic-rich shales of the Norwegian Continental Shelf (Ogata et al., 2014); however, they are abundant in the UK sector in equivalent Jurassic/Cretaceous shales (Meng et al., 2017). Bedding-parallel veins of fibrous calcite (BEEF) are associated with overpressure that occurs during rapid burial (Duhailen et al., 2015; Chenrai et al., 2022). The presence of BEEF increases anisotropy (Duhailen et al., 2015) and the act of carbonate dissolution from the shale physically weakens

the material strength of the host rock (Duhailen et al., 2015; Chenrai et al., 2022). It has been suggested that at a local scale microquartz impacts the material strength by introducing a plain of weakness (Thyberg et al., 2010; Hansen et al., 2020) by encouraging microfracturing (Hernandez et al., 2004; Ougier-Simonin et al., 2016; Johnson et al., 2022b). The creation of microquartz results from the smectite-illite transition (Jahren et al., 2007; Thyberg et al., 2010).

Table 2.1: Hard (i.e., stiff) minerals and their attributes displaying the degree of geometrical and material (i.e., moduli) anisotropy (Blatt and Schultz, 2006; Guo et al., 2013; Skobe et al., 2013; Zhao et al., 2016; Liu et al., 2019). *Microquartz dimensions resulting from the illite-smectite transition (Jahren et al., 2007; Thyberg et al., 2010).

Clay Group	Thickness (μm)	Diameter (μm)	Density (g/cm^3)	Bulk Modulus (GPa)	Shear Modulus (GPa)
Quartz	4-63 (1-3)*	4-63 (1-3)*	2.65	37	44
Feldspar	4-63	4-63	2.71	38	15
Carbonate	4-63	4-63	2.75	76	26
Pyrite	0.5 – 5	0.5 - 5	4.81	147	133

Similar to hard (i.e., stiff) minerals, soft minerals (i.e., clays) have a variety of attributes that impact the material properties of shales (Table 2.2). Major clay mineral groups include kaolinite, smectite, illite, and chlorite. All clay groups are present in the Norwegian Continental Shelf. However, chlorite is exceedingly rare (<5 wt.%) in most samples (Kalani et al., 2015; Nooraiepour et al., 2017; Zadeh et al., 2017; Skurtveit et al., 2018; Hansen et al., 2020; Johnson et al., 2022a). Clay minerals are often associated with organic matter (Vandenbroucke and Largeau, 2007), which may explain why the rugosity (i.e., surface roughness) of organic matter starkly contrasts with hard (i.e., stiff) minerals (Johnson et al., 2022b). While most clay minerals have a similar average density, smectite is ~0.6 g/cm^3 lower (Table 2.2), influencing the material properties of shale. Hernandez et al. (2004) noted that smectite, a swelling clay, easily heals fractures in hydration-dehydration cycles while illite, a non-swelling clay, does not. This is likely related in part to bulk and shear modulus values for smectite (Table 2.2). The conversion between illite and smectite also mechanically results in a more anisotropic rock (Table 2.2).

Table 2.2: Clay mineral groups with attributes displaying the degree of geometrical and material (i.e. moduli) anisotropy (Mondol et al., 2008; Ougier-Simonine et al., 2016; Zhao et al., 2016; Sayers and Boer, 2018). '*' indicates a swelling clay, while '**' indicates a non-swelling clay.

Clay Group	Thickness (Å)	Diameter (μm)	Density (g/cm3)	Bulk Modulus (GPa)	Shear Modulus (GPa)
Kaolinite**	7.1	0.1 – 1.0	2.65	44.0	21.0
Smectite*	9.6 – 14.8	~2.0	2.15	9.3	6.9
Illite**	10.0	~2.0	2.75	60.1	25.3
Chlorite**	14.1	0.3 – 2.0	2.80	81.0	27.0

While diagenesis is known to impact the ratio of clay minerals (i.e., smectite-illite transition), it has also been demonstrated that clay mineral content is indicative of depositional environments (Nielsen et al., 2015; Jung et al., 2019). The low chlorite is likely indicative of limited metamorphic rocks constituting the source material (Nielsen et al., 2015). Both density and aspect ratio likely contribute to kaolinite being transported shorter distances (Table 2.2), a supposition supported by the literature (Nielsen et al., Jung et al., 2019). The known clay mineralogy composition (Johnson et al., 2022b) complements the proposed subtle differences in depositional history between the Draupne and Hekkingen Formations.

Utilizing SEM, it is possible to separate the soft and hard (i.e., stiff) minerals from one another (Figure 2.2c and d). The organic component can also be separated (Figure 2.2b), which will be discussed in more detail in *Section 2.12* below.

Johnson et al. (2022b) explores how the overall composition and distribution of minerals (e.g., Figure 2.2) affect the quality of the rock as both a source and seal. Special attention is given to how primary migration influences major changes within organic-rich shales. The distribution of hard and soft minerals is just as important as understanding their material properties, as location and orientation will dictate how they influence the rock properties of shale as a whole. The distribution of stiff minerals will influence the microfracture pathway as it has been shown that the presence of said minerals facilitates fracture growth (Hernandez et al., 2004; Ougier-Simonin et al., 2016; Zhao et al., 2016), as seen in Figure 2.3a. In contrast, the distribution of soft minerals will influence the ease with which microfractures can heal (Bourg, 2015; Voltolini and Franklin, 2020). Particularly kaolinite and illite can assist in the resealing (Bourg and Franklin, 2017). Shales that are matrix-supported by the clay minerals (e.g., Hekkingen, Draupne) are more likely to be able to heal microfractures subsequent to maturation.

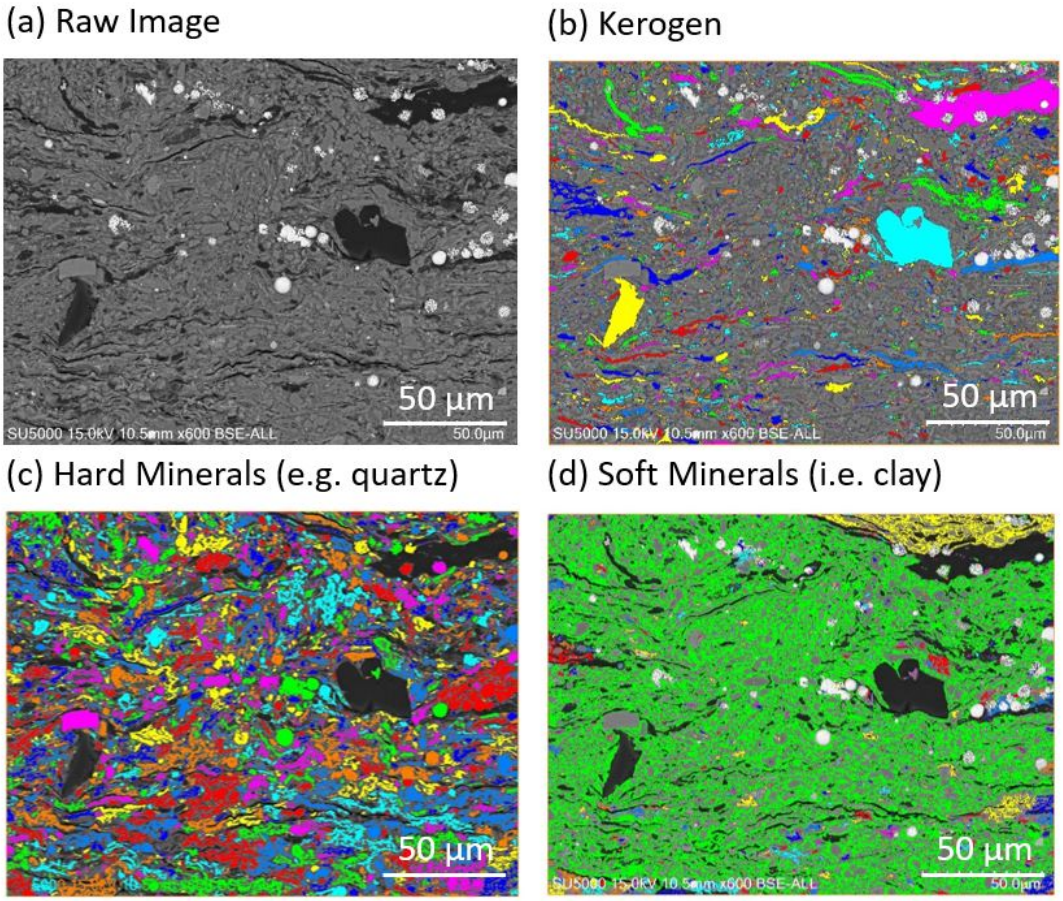

Figure 2.2: SEM image from the Hekkingen Formation (7125/1-1), segmented into (a) raw image, (b) kerogen lenses, (c) hard (e.g., quartz, feldspar, pyrite) minerals, and (d) soft (i.e., clay) minerals. A given color shows how well given components are connected (e.g., clay minerals are dominantly connected, indicated by green).

2.1.2 Impact of organic content (i.e., kerogen) on organic-rich shales

While the presence of organics always plays a role in the strength of the shale, the kerogen lenses become particularly important during maturation leading to primary migration. The increase in PT regime results in the transformation of the kerogen lenses (Figure 2.2) from being a rigid, matrix supporting structure into a ductile pore-filling mass (Prasad et al., 2009; Zargari et al., 2013). The kerogen state transformation results in an increase in pore porosity from the creation of tensile microfractures and the primary migration of hydrocarbons (Figures 2.1 and 2.3). Figure 2.3a shows the transition of kerogen into microfractures and other pores space as the result of heating a sample in the laboratory (Zhao et al., 2016). Figure 2.3b are SEM images captured of the Draupne Formation at two different locations and maturity levels. At a bottom-hole temperature (BHT) of 98°C the kerogen lenses are clearly visible and have not yet begun extruding, while at a BHT of 140°C a microfracture network

starts to become visible. Some of the microfractures follow the long-axis of the kerogen lenses, while others are the result of mineral conversion (i.e., smectite to illite). Figure 2.3c highlights the growth of microfractures within a larger kerogen lens that has begun the extrusion process.

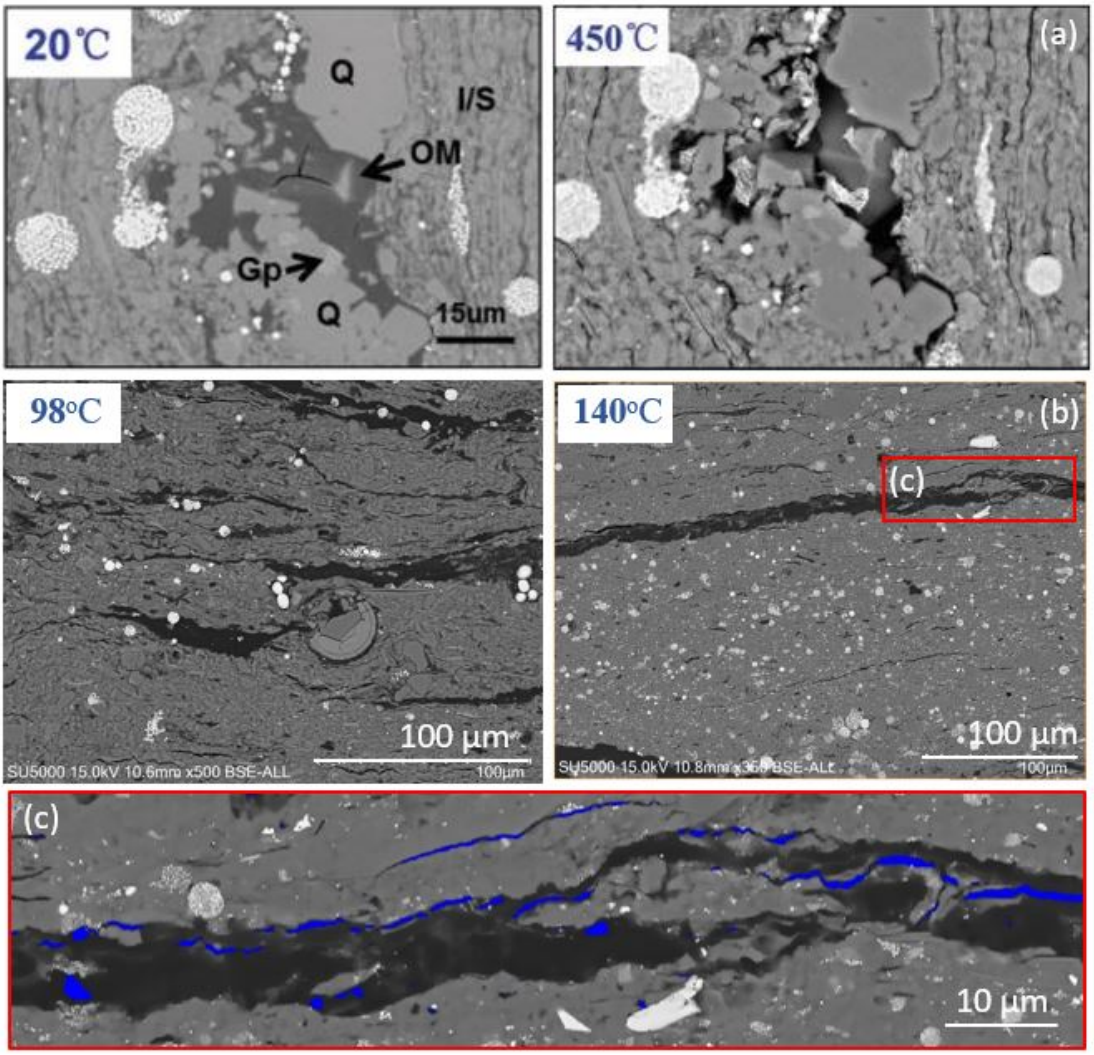

Figure 2.3: SEM images of an organic-rich shale sample (a) from the Bakken Formation before and after artificial pyrolysis (from Zhao et al., 2016), compared to (b) SEM images of the Draupne Formation from the variable depth and maturation states. (c) Zoom highlighting fractures in blue, with some propagating through and following the fabric direction of a kerogen lens.

The conversion of both kerogen to hydrocarbons and smectite to illite results in the creation of pore space (i.e., porosity) that will impact the material properties (Alfred and Vernik, 2013; Zhao et al., 2016), as seen in Figure 2.3. Significant porosity, even if fluid is present, will have an impact on the average density of the host rock. Further to this, microfractures themselves reduce material strength setting up planes of weakness. The degree of kerogen extrusion is dependent on pore pressure (Pepper

and Corvi, 1995; Carcione and Avseth, 2015; Burnham, 2017), which is directly controlled by lithostatic load. By extension lithostatic load has an important influence on the degree of microfracturing and porosity creation (Pepper and Corvi, 1995; Carcione and Avseth, 2015; Burnham, 2017).

Johnson et al., (2022b) explores the average size, shape, distribution, and orientation of kerogen lenses within the Draupne and Hekkingen Formation. Key learnings explore how microfracturing during primary migration influences organic-rich shale as a source and seal. Understanding the size and shape of kerogen lenses is important to understanding how the microfracture network will initially propagate (Johnson et al., 2022b). Utilizing Equation 2.9, it can be inferred that the size of the kerogen lens has first-order implication:

$$P_p = \frac{K_c}{\sqrt{\pi l}} \tag{2.9}$$

where P_p is the overpressure required to propagate a fracture and is inversely proportional to l, the size of the initial crack (kerogen lens or smectite mineral). K_c is fracture toughness. The shape has a second order control on both directions size of the initial crack.

The distribution and orientation of kerogen lenses will control microfracture interconnectivity (Johnson et al., 2022b). The proximity of kerogen lenses and smectite minerals to one another will influence the connectivity of the microfracture network in the context of primary migration (Figure 2.1). Orientation of both kerogen lenses and smectite minerals to bedding planes will influence the likelihood that microfractures will have the ability to interconnect (Johnson et al., 2022b; Johnson et al., 2022c). Collinear, subhorizontal cracks are connecting kerogen lenses within a local area influence the pace at which kerogen lenses are converted (Jin et al., 2010). As the crack length grows, oil pressure decreases, resulting in cracking to cease propagation (Jin et al., 2010; Liu et al., 2021). Understanding how material properties (e.g., anisotropy, rigidity) impact fracture topology and fluid expulsion rate is enhanced through understanding the microscale, organic and inorganic components.

2.2 Mesoscale influences on microfracture nucleation and growth

Both the organic and inorganic components impact the behavior of organic-rich shale in the context of primary migration at the microscale (Vandenbroucke and Largeau, 2007; Ougier-Simonin et al., 2016; Johnson et al., 2022b). However, the system behaves and interacts at a larger scale that includes the degree of structural and compressional anisotropy (i.e., effective stress, vertical and horizontal), as well as material rigidity shown to be directly influenced by material composition. Microfracture network creation and internal interaction (i.e., fracture topology) depend on these same variables. The resulting fracture topology will profoundly influence the strength of shale, in addition to the rate of fluid expulsion (Sanderson and Nixon, 2015; Alvarez et al., 2021; Silva et al., 2021). The

degree of rigidity, partially controlled by mineralogy, also influences rate of fluid expulsion during primary migration.

Analogue experiments were carried out as a part of this Ph.D. in order to bridge the gap between the microscale (μm to cm) characterization of subsurface samples and the macroscale observations made utilizing seismic inversion (m to km). A particular focus was paid to the subsurface process of microfracture nucleation, internetwork connection, and fluid flow migration as described within the literature (Anders et al., 2014; Kobchenko et al., 2014; Teixeira et al., 2017; Chauve et al., 2020; Rabbel et al., 2020). The analogue experiments within the Ph.D. were designed to test three parameters – anisotropy through layering, material rigidity through sealing, and impact of variable TOC content by varying sugar:yeast concentration. Fracture topology and fluid expulsion are influenced by altering these parameters. Figure 2.4 shows an example of the final fracture pattern for each experiment type tested.

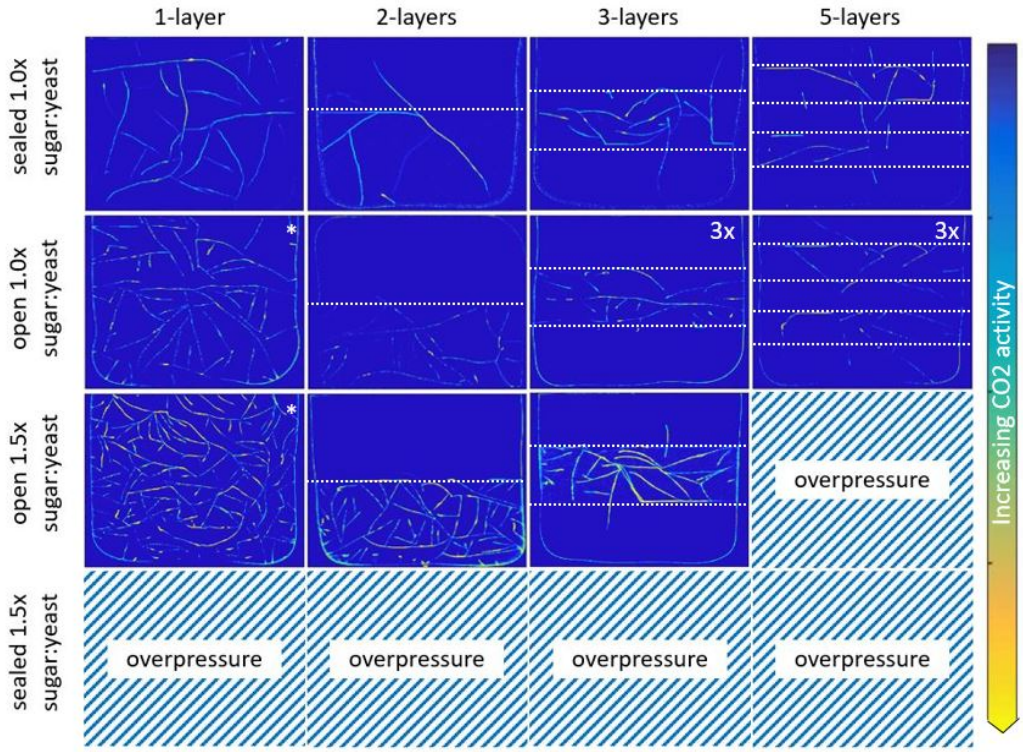

Figure 2.4: In yellow, gelatin experiments final fracture patterns highlighting network connectivity and increasing CO2 activity. 3-layers and 5-layers experiments were run three times each showing repeatability. Experiments based on those run by Kobchenko et al. (2014) are denoted by a '*'. In the case of all sealed 1.5x sugar:yeast concentration experiments and the 5-layers open 1.5x sugar:yeast concentration experiments overpressure separated the glass Hele-Shaw cell from the gelatin making, precluding the ability to quantify results.

Figure 2.4 indicates that higher sugar:yeast concentration (i.e., greater organic matter content) results in a larger number of fractures with greater connectivity and more fluid flow. This extends to the ability for microfractures to propagate further into an inactive gelatin layer (i.e., no sugar and yeast) without the presence of sealing (Figure 2.4). Pathways created early that allow for fluid escape are the most traveled (Figure 2.4). The results of the Ph.D. characterize how increased fracturing results in greater fracture topology complexity that then influences fluid flow (Johnson et al., 2022c).

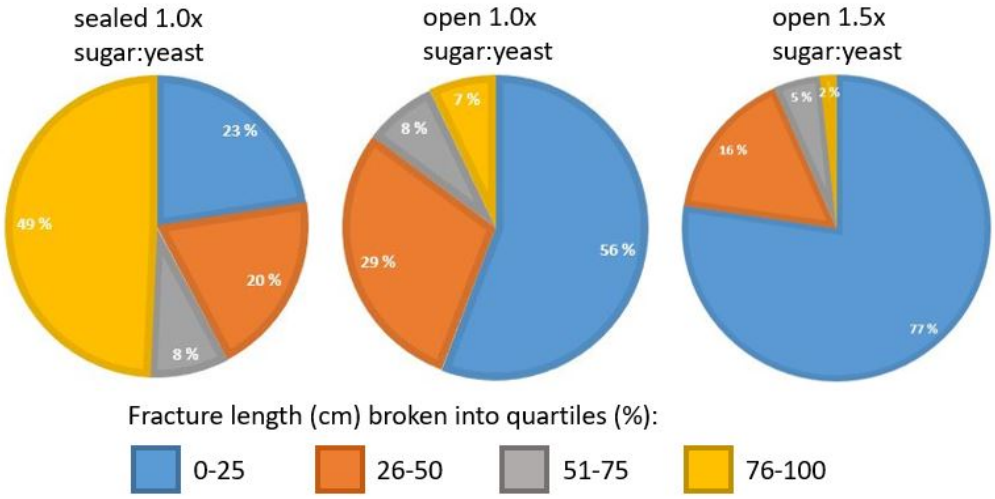

Figure 2.5: Total fracture length, cm, in quartiles (%) for the average of all experiments within a given class type, not taking layering into account.

A greater percentage of fractures is a part of the smallest quartile for higher concentrations of sugar and yeast (i.e., TOC) than for other experiments (Figure 2.5). It has been observed that fracture propagation is higher for organic-rich shales with a greater amount of TOC (Vandenbroucke and Largeau, 2007; Fan et al., 2010; Kobchenko et al., 2011; Ougier-Simonin et al., 2016; Johnson et al., 2022b). Furthermore, fracture propagation as a means to release pressure is limited by other areas where pressure has already been released (Jin et al., 2010; Kobchenko et al., 2014; Liu et al., 2021).

The distance between any two fractures is usually greater for the sealed experiments than for the open experiments, given the same number of layers (Figure 2.6). Increasing the concentration of sugar and yeast results in less space between fractures. Regardless of the number of layers, the penetration depth into the inactive layer is also greater for higher concentrations of sugar and yeast (Figure 2.6). The greatest distance between two fractures for the sealed, 1-layer experiment is ~6 cm (Figure 2.6). Comparatively, the greatest distance between any two fractures for the open experiments is ~4 cm for the 1.0x sugar and yeast concentration and <2 cm for the 1.5x sugar and yeast concentration (Figure 2.6). Within active yeast, these values remain accurate regardless of the number of layers; however, the distances are greater within inactive layers (Figure 2.6).

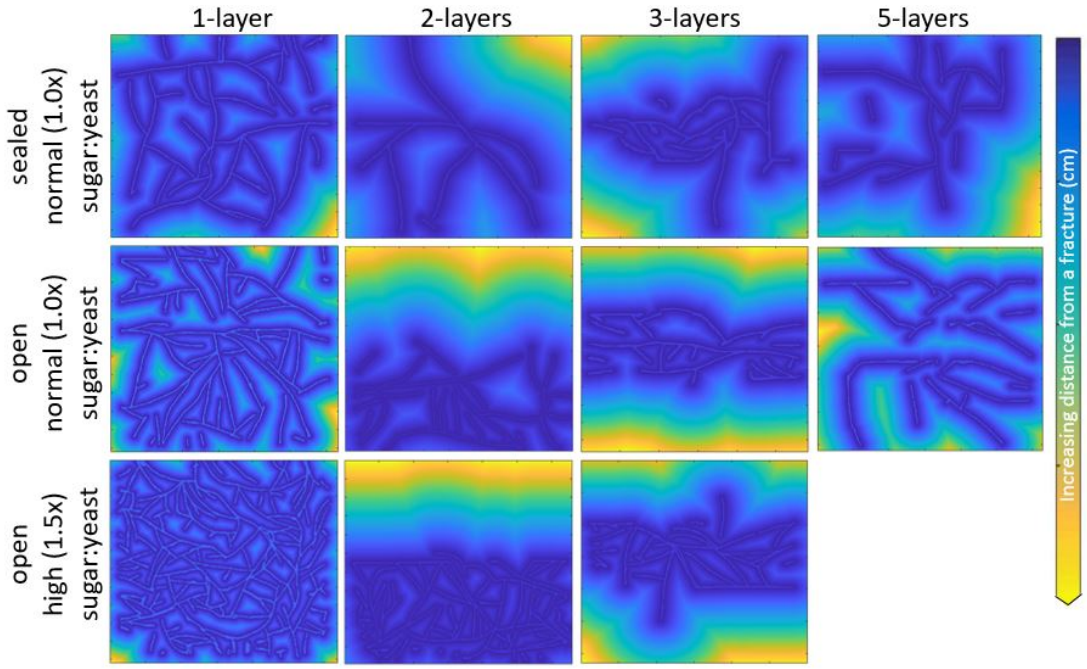

Figure 2.6: Fracture patterns for each experiment type showing the total distance from all fractures (cm), where dark blue is close to a given fracture and yellow is distant from the nearest possible fracture. Note – while XY scales are the same with the negligible error between them, color scales are relative to each experimental setup (i.e., not consistent between experiments).

Two methods, the XYI-method (i.e., Sanderson-Nixon method) and the ω-method (i.e., Kobchenko method), were used to describe fracture topology (Kobchenko et al., 2013; Sanderson and Nixon, 2015). The Kobchenko method for describing fracture topology is best suited to the understanding likelihood of fracture propagation in variable material properties. In contrast, the Sanderson-Nixon method is ideal for characterizing potential fluid flow (Johnson et al., 2022c).

For the Sanderson-Nixon method, there is a good crossover between the analogue models (e.g., Figure 2.7a) and the actual shale images (e.g., Figure 2.7c). While the digital (i.e., numeral) modeling has the right proportion of Y- and I-nodes models consistently fail to consider the possibility of X-nodes. This may be an attempt to account for fracture growth, avoiding areas where pressure has been released. However, X-nodes do occur in natural systems (Sanderson and Nixon, 2015; Lovell et al., 2018; Johnson et al., 2022c). The presence of X-nodes is crucial as they shift flow properties from consistently below ε=2 into a range that straddles ε=2 and even approaches ε=3 (Figure 2.7).

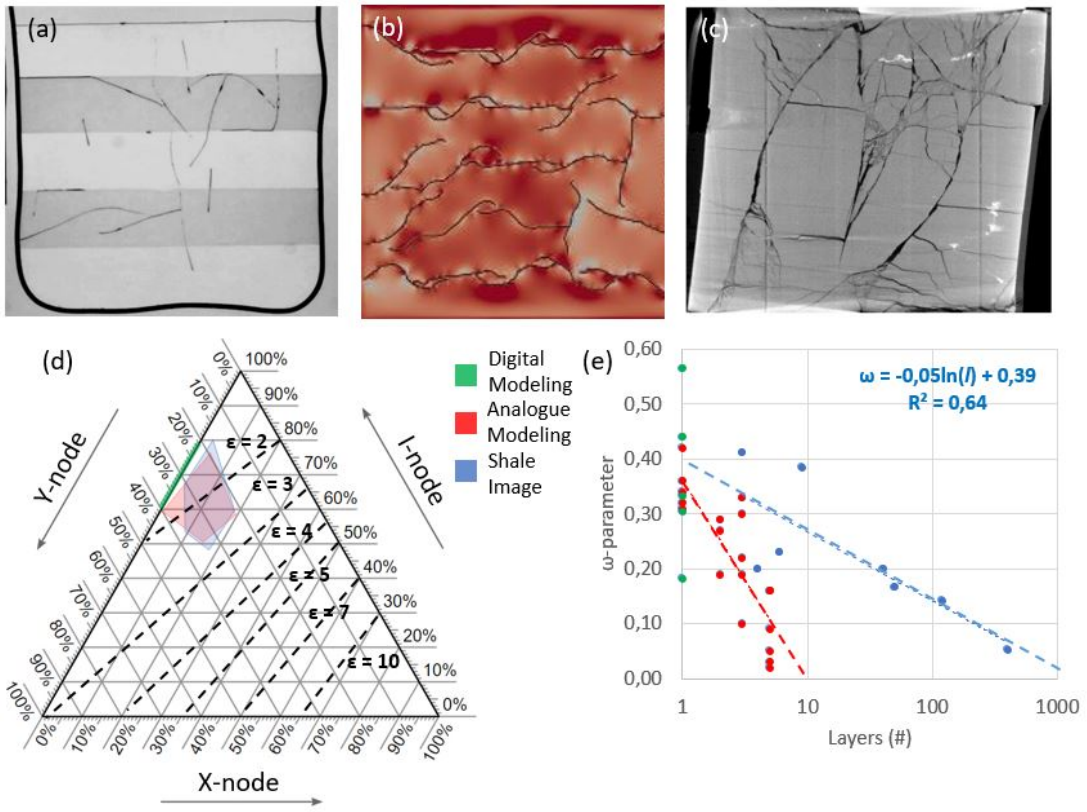

Figure 2.7: Fracture topology for (a) analogue models (Kobchenko et al., 2014; Johnson et al., 2022c), (b) digital numerical models (Rabbel et al., 2020; Vega et al., 2020), and (c) shale images (Kobchenko et al., 2011; Ougier-Simonin et al., 2016; Zhao et al., 2016; Zhang et al., 2016; Li et al., 2019; Johnson et al., 2022b). Two fracture topology methods are shown, the (d) XYI-method (i.e. Sanderson-Nixon method) and the (e) ω-method (i.e. Kobchenko method) being utilized to draw a relationship between itself and the number of layers. For the Sanderson-Nixon method, higher values of ε correlate to higher values of porosity and permeability and have a positive relationship with faster flow-rate.

2.2.1 Impact of anisotropy on organic-rich shales

Fracture propagation is known to be influenced by anisotropy (Chauve et al., 2020; Rabbel et al., 2020). It is such a major consideration that it is considered for artificial fracturing of shales, often requiring mapping of PT regimes (Zoback, 2007; Heinemann and Mittermeir, 2012; Li et al., 2020). A large percentage of natural microfractures propagate in line with anisotropy (Rabbel et al., 2020; Rummel et al., 2020), impacting microfracture topology. Variable layer thicknesses are inherent to transversely isotropic mediums (e.g., shale), where the thickness of a given layer can control the propagation of microfractures (Rijken and Cooke, 2001), confirmed by the Ph.D. (Johnson et al., 2022c).

Thicker layers present in the 2-layers and 3-layers experiments result in less microfracture propagation into and through them than in the thinner 5-layers experiments (Figure 2.4). While

anisotropy has no influence on nucleation density, it has been shown that increases result in fractures propagating roughly parallel to the transverse isotropy (Johnson et al., 2022c). This agrees with observations of shale on the surface and subsurface (Kobchenko et al., 2011; Ougier-Simonin et al., 2016). Furthermore, the angle of approach controls the likelihood a fracture will break through the layer above or be deflected along the interface (Johnson et al., 2022c). Finally, increased anisotropy results in a network with less connectivity than would be present for similar isotropic material (Johnson et al., 2022c). Utilizing the Kobchenko method (i.e., ω-method), it becomes clear that increasing anisotropy results in a network with a greater number of microfracture dead-ends. This relationship can be quantified; based on the analogue models alone Johnson et al. (2022c) suggested the relationship between ω and the number of layers is:

$$\omega = -0.07l + 0.43 \tag{2.10}$$

where ω is calculated from the ratio of the number of dead-ends to junction nodes (Kobchenko et al., 2013; Johnson et al., 2022c) and l is the number of layers that fracture penetrates (Figure 2.7). Utilizing a limited number of shale images from research pertaining dominantly to fracture topology with shales during the maturation process and an estimation of average laminae thickness of ~0.5 mm (O'Brien, 1996), another relationship is established:

$$\omega = -0.05 \ln(l) + 0.39 \tag{2.11}$$

While further testing and image analysis are required to refine these relationships (Equations 2.10 and 2.11) and the degree to which they resemble one another, it is clear that increasing anisotropy results in more dead-ends. Consequently, increased anisotropy will have poorer fluid interconnectivity (Johnson et al., 2022c).

Poorer fluid with increased anisotropy, is confirmed by the Sanderson-Nixon method (i.e., XYI method) for both natural and analogue systems (Figure 2.7d). While it cannot be seen here, Johnson et al. (2022c) explore how increasing the number of layers results in a drop in value for ε. Given that transverse isotropy has been shown to correlate to lower levels of porosity and permeability, this portion of the results confirms what is already seen in the literature (Meng et al., 2019; Zhang, 2019).

2.2.2 Impact of rigidity (i.e., sealing) on organic-rich shales

Sealing or confinement are commonly introduced during lab experiments (e.g., triaxial testing, Rock-Eval analysis) on shale. Sealing, in our analogue experiments, were shown to alter the rigidity of the system, providing a good analogue for alteration of stiffness. A number of factors (e.g., mineralogy) influence stiffness in shales. It has been documented that increasing stiffness results in greater pressure required for internal fracture creation (Pineau and Pardon, 2007; Zhang, 2019; Johnson et al., 2022c),

contrasted by high fluid expulsion once it has begun (Bense et al., 2013; Fjær et al., 2021; Johnson et al., 2022c).

Lateral sealing is also common in the subsurface, wherein a zone of higher porosity and permeability is next to a zone of comparatively higher porosity and permeability (Bense et al., 2013; Feldman and Demko, 2015; Zecchin and Catuneanu, 2015). These can occur as the result of facies changes, as well as structural changes (e.g., fracturing, faulting). Critically, the percentage of organic matter present significantly influences porosity regardless of the state of diageneses (Alfred and Vernik, 2013; Guo et al., 2013; Zhao et al., 2016; Wang et al., 2019). Maturation increases both porosity and permeability as a part of the process (Alfred and Vernik, 2013; Anders et al., 2014; Teixeira et al., 2017; Johnson et al., 2022b; Johnson et al., 2022c). Therefore, even subtle shifts in the degree of biological life deposited can significantly impact the presence of lateral sealing.

Fracture length is affected by rigidity (i.e., sealing), wherein there is a greater number of the largest quartile (i.e., 75-100%) of fractures (Figure 2.5). This coincides with a greater number of vertical fractures with connectivity across layers (Figures 2.4 and 2.6). As a result of this, the total distance between fractures in the inactive layers is lower for sealed experiments, in contrast to the distance between fractures within the active layers (Figure 2.7). Johnson et al. (2022c) established that increased rigidity (i.e. sealing) impacts fluid flow. Particularly, rigidity (i.e., sealing) results in a higher ε value, suggesting better fluid flow (Figure 2.7). However, Johnson et al. (2022c) contrast these results with a greater and less consistent periodicity for sealed experiments. This suggests that while connected, there are times that different portions of the system behave independently.

2.3 Macroscale detection of maturation and organic materials

At the macroscale (m – km), it becomes difficult to directly approximate the mechanical parameters of shale. The tools utilized (e.g., seismic) are unable to properly quantify fracture networks, although attempts have been made (Neves et al., 2004; Gray, 2008; Pan et al., 2021). As a result, petrophysical and geophysical tools are most commonly utilized to approximate mechanical strength utilizing elastic (i.e., dynamic) moduli (Rickman et al., 2008; Perez and Marfurt, 2014; Johnson et al., 2022a). This includes the calculation of parameters, including Young's modulus (E) and Poisson's ratio (ν).

$$E = \frac{\sigma}{\varepsilon} = 2G(1+\nu) = 3K(1-2\nu) = \rho V_p^2 \frac{3V_p^2 - 4V_s^2}{V_p^2 - V_s^2} \tag{2.12}$$

where σ is stress (i.e., force applied), ε is a strain (i.e., deformation), G is shear modulus, K is the bulk modulus, Vp is P-wave, Vs is S-wave, and ρ is density. The first derivation of Equation 2.12 is the definition of Young's modulus that is attained by applying a physical force and measuring the deformation that occurs (i.e., static modulus), while the last derivation can be attained by utilizing waves

(i.e., dynamic moduli). It is important to empirically define the relationship between static and dynamic moduli whenever these are calculated independently for a given material (e.g., organic-rich shale). The two middle derivations are useful in defining the force applied in the shear and normal direction, assuming an isotropic material (Zoback, 2007). Given the absence of anisotropic derivations for shale, the isotropic estimations are a reasonable place to start (references).

$$\nu = \frac{\Delta\varepsilon_{trans}}{\Delta\varepsilon_{axial}} = 0.5 - \frac{E}{6K} = \frac{V_p^2 - 2V_s^2}{2V_p^2 - 2V_s^2} \tag{2.13}$$

where $\Delta\varepsilon_{trans}$ is the change in transverse strain, $\Delta\varepsilon_{axial}$ is the change in axial strain. Again, the first equation describes static moduli, while the last equation describes dynamic. The middle equation is Lame's relation, based on isotropic estimations, and is a reasonable place to start (Zoback, 2007). Some proponents state that the isotropic estimations are more accurate if the inputs cannot be separated into their anisotropic components (Vernik and Nur, 1992; Sayers, 1999; Zoback, 2007).

Perez and Marfurt (2014) relate calculated values of Young's modulus and Poisson's ratio to material property descriptors (i.e., brittle, ductile) through a rock-physics template (RPT) commonly used in the Ph.D. Brittleness indices estimate mechanical properties (Grieser and Bray, 2007; Rickman et al., 2008; Johnson, 2017; Wilson et al., 2017; Mondol, 2018; Mews et al., 2019; Johnson et al., 2022a). In order to relate these mechanical property descriptors back to what organic-rich shale is composed of, all obtained values from seismic inversion are compared to established end member values (Table 2.3).

Table 2.3: Comparison of values for Young's modulus and Poisson's ratio for organic-rich shales of the Norwegian Continental Shelf

Endmember	Young's modulus* (E)	Poisson's ratio* (ν)	Young's modulus** (E)	Poisson's ratio** (ν)	Density*** (g/cm3)
Kerogen	10	0.25	10	0.20	1.25
Quartz	95	0.08	85	0.10	2.65
Calcite	75	0.30	-	-	2.71
Clay	25	0.30	30	0.25	2.73

*Values are based on Kolmule Formation, Barents Sea (Mondol, 2018)

**Values are based on Draupne Formation, North Sea (present study)

***Values for kerogen based on Okiongbo et al., (2005), Draupne Formation, North Sea; quartz and calcite values (Zhao et al., 2016); clay density based on a clay mineralogy average for the Draupne Formation (Johnson et al., 2021)

Elastic brittleness indices (EBI) can be calculated using the following equation from Grieser and Bray (2007):

$$EBI = \frac{1}{2}\left[\frac{E - E_{min}}{E_{max} - E_{min}} + \frac{\nu - \nu_{max}}{\nu_{min} - \nu_{max}}\right] \tag{2.14}$$

where E_{min} is the minimum value of Young's modulus, while E_{max} is the maximum value. Similarly, ν_{min} is the minimum value of Poisson's ratio, and ν_{max} is the maximum value of Poisson's ratio. Fawad and

Mondol (2021) suggest an EBI equation better suited for organic-rich shales of the Norwegian Continental Shelf :

$$EBI^3 = \frac{0.00044AI - 1.3 - \sqrt{0.62\frac{R_W}{R_D}}(0.00019AI + .25)}{1.35 + 0.00028AI} \quad (2.15)$$

EBI (Equation 2.15) and MBI (Equation 2.8) can be correlated to one another (Mo et al., 2018; Mews et al., 2019). This suggests that mineralogy remains a critical factor influencing the mechanical and elastic properties of shale. Further to this, a correlation between EBI and MBI is possible and a future avenue of research.

2.3.1 Impact of maturation on organic-rich shales

Maturation of kerogen (Figure 2.1) within organic-rich shale, can be exist in three different states: immature, mature, and overmature (Vernik and Landis, 1996). Mature kerogen can be further delineated into early oil generation, late oil generation, and gas generation (Vernik and Landis, 1996). Geochemical tools that investigate how organics vary under different PT regimes are adept at separating out varying levels of maturation. Cutoffs for transitions for various geochemical indicators, as utilized for this Ph.D., are defined in Table 2.4.

Table 2.4: Geochemical cutoffs separating out immature, mature, and overmature kerogen of organic-rich shale (Espitalie et al., 1985; Vernik and Landis, 1996; Isaksen and Ledje, 2001; Johnson et al., 2022a)

Maturation state	Vitrinite Reflectance (R_o)	T_{max} (°C)	Hydrogen Index* (mg HC/g TOC)	Depth range** (m)
Immature	<0.7	<430	>500	<2200
Mature – Early Oil	~0.7-0.9	~430-460	~350-500	~2200-3200
Mature – Late Oil	~0.9-1.1	~460-480	~210-350	~2600-3500
Mature – Gas	~1.1-1.7	~480-530	~60-210	~3400-4050
Overmature	>1.7	>530	<60	>4000

*Only applicable above 5 wt.% TOC

**Dependent on kerogen type (Type II/Type III). Furthermore, it will vary significantly based on basin type and proximity of heat source (e.g., salt tectonism)

Hydrogen index cutoffs only apply above 5.00 wt. % (Table 2.4), between 0.00 – 4.99 wt. % TOC utilizes Equations 2.16a-d for cutoffs between immature, mature – early oil, mature – late oil, and mature – gas, and overmature, respectively (modified from Vernik and Landis, 1996):

$$HI = 118.7\ln(TOC) + 264.5 \quad (2.16a)$$

$$HI = 86.7\ln(TOC) + 195.1 \quad (2.16b)$$

$$HI = 77.7\ln(TOC) + 70.6 \quad (2.16c)$$

$$HI = 14.7\ln(TOC) + 28.4 \quad (2.16d)$$

where HI is hydrogen index (mg HC/g TOC) and total organic carbon is TOC (wt. %). Maturation facies in Johnson et al., (2022a) are based on Equations 2.16a-d.

Maturation within the Norwegian Continental Shelf is highly variable and dependent on the geological context, particularly diagenesis to catagenesis (Badics et al., 2015; Baig et al., 2016; Baig et al., 2019; Johnson et al., 2022a). Within the study area of this Ph.D., it varies from immature to mature, early gas generation phase (Johnson et al., 2022a; Johnson et al., 2022b). Figure 2.9 characterizes maturation and kerogen type utilizing a variety of geochemical templates (Espitalie et al., 1985; Vernik and Landis, 1996; Isaksen and Ledje, 2001; Johnson et al., 2022a). Note that similar maturation ranges exist for the Hekkingen and Draupne components of the study area (Johnson et al., 2022a; Johnson et al., 2022b) despite significant uplift (Baig et al., 2016; Baig et al., 2019).

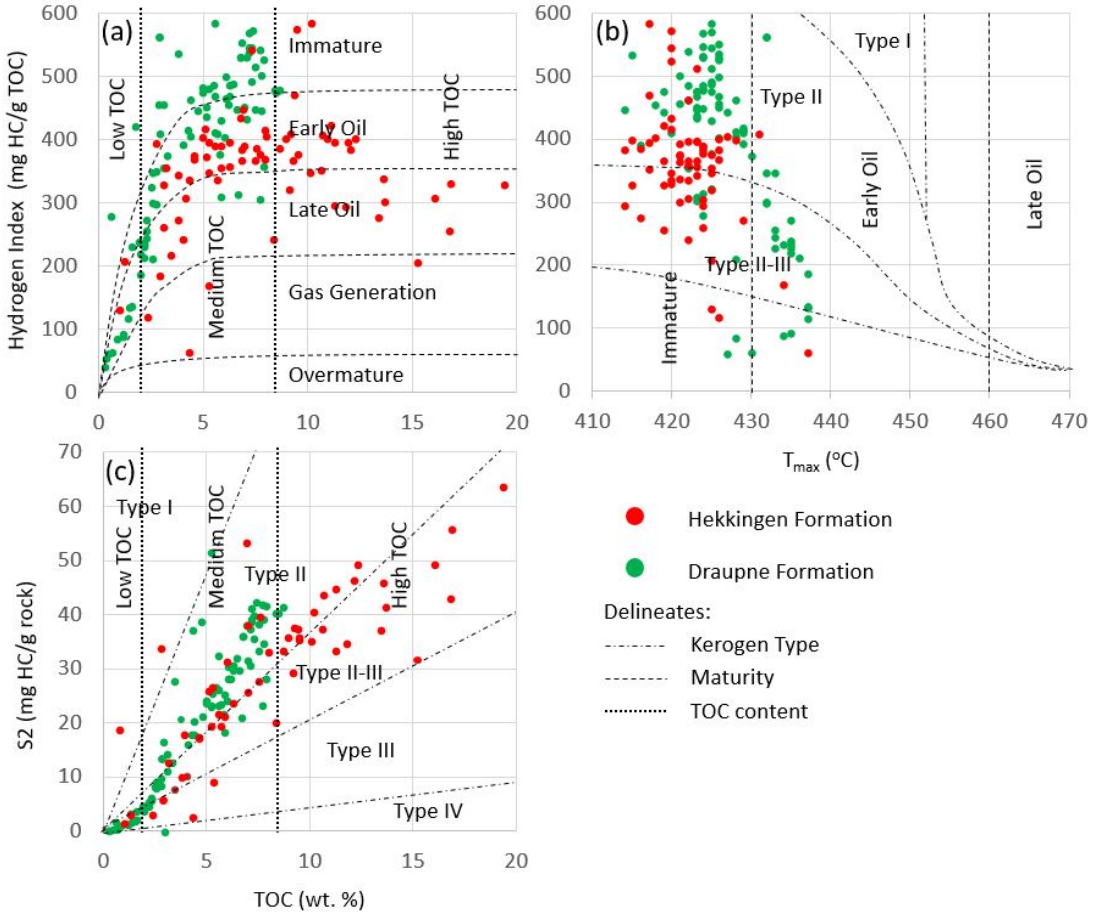

Figure 2.8: Geochemical analyses representative of the Draupne and Hekkingen Formations within the study area (see Figure 1.2). (a) Hydrogen Index vs. TOC is used to identify TOC content and maturity. (b) Hydrogen Index vs. Tmax is used o investigate maturity and kerogen type. (c) S2 vs. TOC is used to investigate TOC content and kerogen type.

Figure 2.8 can be used to separate out the subtle differences between the Draupne Formation and the Hekkingen Formation in terms of kerogen type, TOC content, and maturation state. Kerogen type (Figure 2.8b and c) for both formations consists of Type II and III kerogen. However, the Hekkingen Formation has a greater percentage of Type III kerogen kerogen (Figure 2.8b and c). This may result in more complex and, therefore, more communicative for fluid-flow, fracture formation during maturation (Johnson et al., 2022c). TOC content is separated out into low (<2 wt. %), medium (2-8 wt. %) based on a fundamental change in kerogen properties (i.e., size, geometry) (Johnson et al., 2022b), and high (>8 wt. %). High kerogen content is dominantly present in the Hekkingen, although there are instances of high kerogen content in the Draupne (Figure 2.8a and c). Otherwise, kerogen content is predominantly medium (2-8 wt. %). Maturation is the hardest to assess (Figure 2.8a and b) as Figure 2.8a indicates that the Hekkingen is more mature, while Figure 2.8b indicates that the Draupne Formation is slightly more mature. However, vitrinite reflectance data and a rock-physics analysis of the two formations within the study area conclude that the Hekkingen is the more mature (Johnson et al., 2021; Johnson et al., 2022a; Johnson et al., 2022b).

Regionally applied models for maturation for the Norwegian Continental Shelf that is not wholly dependent on depth as a proxy are limited (Badics et al., 2015; Baig et al., 2016; Baig et al., 2019; Rahman et al., 2020), in part because a limited amount of clear, consistent vitrinite reflectance data and that all other proxies are significantly more complicated to employ (Johnson et al., 2022a). This PhD shows that employing seismic inversion in combination with a variety of maturation proxies provides a credible way to map the maturation of organic-rich shales in the Norwegian Continental Shelf (Johnson et al., 2022a). This is important since the microscale changes in organic-rich shale due to maturation (Figure 2.1) affect elastic properties (i.e. P-wave, S-wave, density, Vp/Vs).

For example, pore porosity created (Figure 2.3) have a measurable impact on the elastic properties of shale at both the local (Prasad et al., 2009; Prasad et al., 2011; Zargari et al., 2013) and regional scales (Alfred and Vernik, 2013; Guo et al., 2013; Zhao et al., 2016). Further, the anisotropic nature of a complex microfracture network will also impact the elastic properties (Pan et al., 2021; Zhao et al., 2016; Johnson et al., 2022b; Johnson et al., 2022c). Many studies have modeled the impact that maturation should have (Alfred and Vernik, 2013; Guo et al., 2013; Zhao et al., 2016). Johnson et al., (2022a) correlate the impact maturation has and then investigate how variable levels of TOC affect the material properties of organic-rich shale.

2.3.2 Impact of TOC content on organic-rich shales

Establishing the difference between organic matter and total organic carbon (TOC) content is important. There is an incongruity in the way these terms are used in the literature; however, further review shows they are often used to identify the same thing (i.e., organic content). The incongruity stems

from an important difference when analyzing soil that recognizes that organic matter is made up of more than just carbon and even proposes a relationship between the two (Nelson and Sommers, 1996). However, investigations of the subsurface (i.e., post diagenesis) rarely make this distinction identifying kerogen as organic matter when investigating the microscale and utilizing TOC when investigating the macroscale, without utilizing any relationship to equate the two (Vandenbroucke and Largeau, 2007). Further to this, TOC is used as an indicator of hydrocarbon (i.e., not just carbon) potential (AAPG, 2022). Therefore, while other literature may discern a difference between organic matter and TOC, this Ph.D. utilizes organic matter at the microscale and TOC at the macroscale, with the understanding the two are fundamentally interchangeable.

Schmoker and Hester (1983) established that there is a strong correlation between density and TOC, utilizing Equation 2.17a:

$$TOC = \frac{154.5}{\rho} - 57.3 \tag{2.17a}$$

where ρ is density, and total organic carbon is TOC (wt. %). While other methods have been shown to estimate TOC (Table 2.5) utilizing different well logs, density-based TOC remains one of the most accurate (Passey et al., 1990; Mallick and Raju, 1995; Vernik and Landis, 1996; Johnson, 2017; Huang et al., 2015) as is this case here (Johnson et al., 2022a).

Table 2.5: Selection of methods utilized to calculate TOC from dominantly well log information tested as a part of the Ph.D.'s investigation into TOC (Passey et al., 1990; Vernik and Landis, 1996; Heslop, 2010; Charsky and Herron, 2013; Huang et al., 2015)

Method (Year Proposed)	Logs Utilized	Equations (2.17b – 2.17f)	R^2*	R^2**	R^2***
Passey (1990)	neutron porosity, resistivity	$TOC = \Delta \log(R)\, 10^{(2.297-0.1688LOM)}$	0.65	0.56	0.57
Modified Passey (1995)	neutron porosity, resistivity, sonic, density	$TOC = (\Delta \log(R) + m)10^{(2.297-0.1688LOM)}$ $m = K * s - a * \rho + b$	0.72	0.67	0.64
Vernik and Landis (1996)	Density	$TOC = 67\frac{\rho_k\,(\rho_s - \rho)}{\rho(\rho_s - \rho_k)}$	0.75	0.86	0.74
Heslop (2010)	gamma ray, resistivity	$TOC = \frac{\Delta GR + \Delta R}{GR_{TOC} + \log(R_{TOC})}$	0.78	-	-
Charsky and Herron (2013)	spectral gamma ray	$TOC = a * \omega(U) + b$	0.85	0.91	-

*Based on original research from the author.

**Based on research from Huang et al. (2015).

***Based on research from the Ph.D. – data not available to test either Heslop (2010) or Charsky and Heron (2013).

Further to this, significant quantities of TOC (i.e., <2 wt. %) with its lower density has been established to impact seismic signature (Løseth et al., 2011; Alfred and Vernik, 2013; Avseth and Veggeland, 2015; Badics et al., 2015). Figure 2.9 shows the degree to which higher levels of TOC will separate themselves from the background seismic signature.

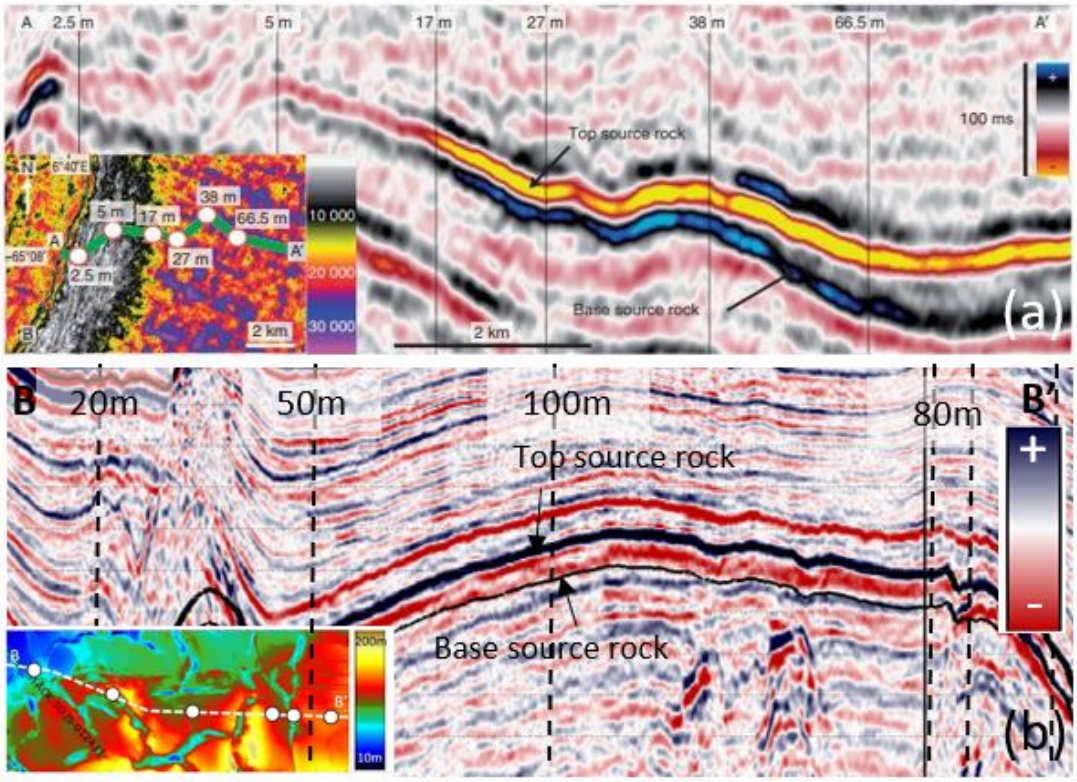

Figure 2.9: Seismic amplitude highlighting the presence and impact of TOC, with the top and bottom of the source rock clearly identified. (a) The thickness of the Spekk Formation (i.e., equivalent to the Draupne and Hekkingen Formations), the Norwegian Sea is seen in a cross-section with an overlaid isopach map (Løseth et al., 2011). (b) The thickness of the Draupne Formation, the North Sea in cross-section with an overlaid isopach map. In both cases, lower amplitude (i.e., hot colours) correlates to greater TOC content.

Seismic amplitude can even indicate the amount of TOC (Figure 2.9), as is fully explored in Figure 2.9a in Løseth et al. (2011) and Figure 2.9b in Johnson et al. (2022a). Furthermore, TOC (wt. %) can be delineated up to a single percentage point showing the profound impact of impact lower kerogen density has on the elastic-based tools utilized here. Figure 2.9b confirms the Upper Draupne is typically more TOC-rich, grading into lower levels of TOC through the Lower Draupne into the Heather Formation.

3.0 Experimental approach

A diverse set of experimental approaches were employed for the research, with the major components being image analysis (e.g., 3D X-Ray tomography, scanning electron microscopy),

analogue laboratory experiments, and seismic inversion. Therefore, a large range of scales within the subsurface was analyzed (Figure 3.1).

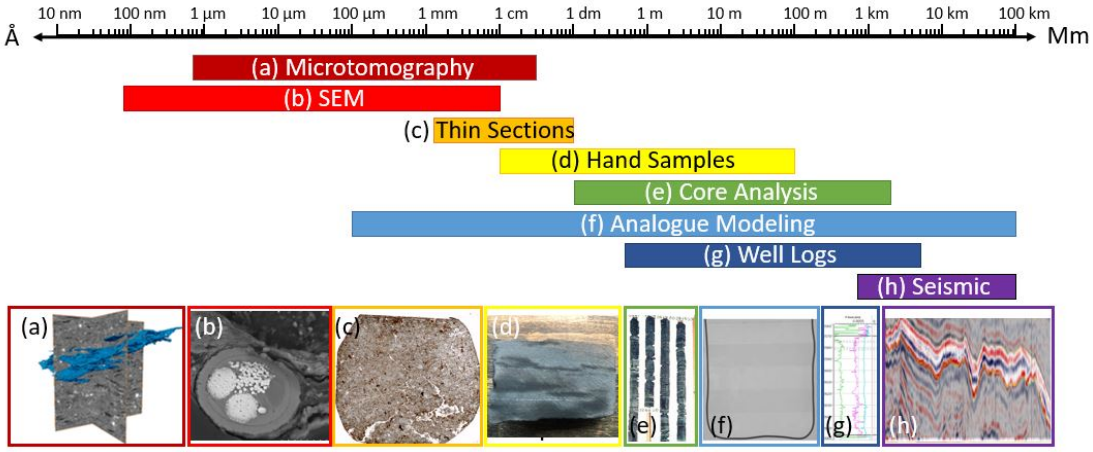

Figure 3.1: Scale (i.e., resolution) range for a variety of methods utilized in the pursuit of understanding organic-rich shales as a part of this Ph.D.: (a) microtomography (b) SEM (c) thin section (d) hand sample (e) core analysis (f) analogue modeling (g) well logs and (h) seismic.

Image analysis focused on the 3D microtomography and 2D SEM images while utilizing thin sections and core samples. Seismic inversion utilized hand samples and core analyses while focusing on combining information from well logs and seismic. Analogue modeling could be applied to a wide range of scales (Figure 3.1) in the subsurface; however, the focus was on the mesoscale in order to bridge the gap between the microscale analysis (e.g., microtomography, SEM) and the macroscale (e.g., well logs, seismic).

3.1 Image Analysis Techniques

Imaging techniques can be used to isolate and understand specific components of shale, including but not limited to the kerogen lenses, mineralogical composition (best used in conjunction with XRD), and any microfracturing that has occurred. Different imaging techniques and scales (Figure 3.1) will highlight different characteristics of the shales (Alfred and Vernik, 2013; Ougier-Simonin et al., 2016; Zhao et al., 2016). For the purpose of this Ph.D., image analysis was also used for the analogue models in order to track the creation of microfractures and the expulsion of fluid.

3.1.1 3D X-Ray Microtomography

X-ray microtomography is a non-destructive imaging technique that allows 3D visualization of material from the outside surfaces through to the inside. The technique depends on the interaction of X-rays, electromagnetic radiation with a wavelength of 0.01-10 nm, with matter (Cierniak, 2011; Kandula,

2021). Energies in the range of 10^2 – 10^5 eV (Cierniak, 2011) are responsible for the loss of photons from incident flux, a process called attenuation or adsorption (Ketcham, 2005; Kyle and Ketcham, 2015; Kandula, 2021). The relationship between X-ray intensity (I_0) and attenuated intensity (I) after X-rays have passed through a multi-phase material is:

$$I = I_0 \exp(-\sum_i \mu_i X_i) \tag{3.1}$$

where μ_i is the attenuation coefficient for the ith phase, X_i is the path length for each phase.

Beamline ID19 at the European Synchrotron Radiation Facility (ESRF) was used for the collection of six samples. The radiographs acquired were reconstructed in three-dimensions at a higher resolution (i.e., 0.7 μm/voxel) and a lower resolution (i.e., 6.63 μm/voxel) using plain filtered back-projection (Mirone et al., 2014). The image reconstruction process is based on Paganin et al., (2004).

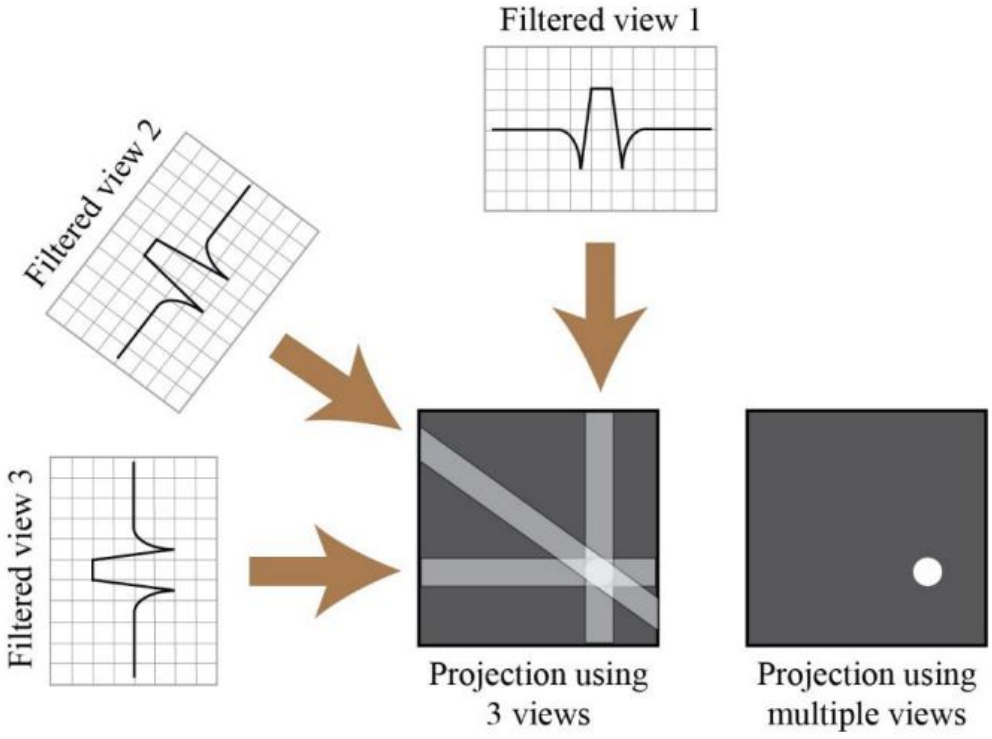

Figure 3.2: Sketch of the image reconstruction process with a back-projection algorithm from multiple filtered rotations. Filtering ensures a clear image. The figure is from Kandula (2021).

Beam hardening is the most common artifact seen in tomography systems using conventional X-ray sources, although it is considerably less common utilizing synchrotron X-rays with a monochromatic source (Colijn et al., 2004; Davis and Elliott, 2006), as is the case here. As the X-ray beam attenuates, the energy spectrum shifts higher, usually becoming greatest at the center of the specimen resulting in a characteristic dishing effect (Davis and Elliott, 2006), seen in Figure 3.3a. The

microtomographical image of the figure is seen as being less dense than it actually is. In this case, the decrease in density was enough to allow the center of the organic-rich shale image to resemble the density of kerogen (Figure 3.3d). The beam hardening effect was removed utilizing a combination of a background trend correction algorithm, masking, and spectra filters (e.g., non-local means filter). While the removal of the beam hardening artifact is not directly discussed, more details on the image cleaning process are discussed in Johnson et al. (2022b).

This results in the centroid of the high resolution having a significantly different background trend than the rest (Figure 3.3c) and is apparent when you look at the image in plain view and section view (Figure3.3a and b). A background trend is also present (Figure 3.3y), possibly resulting from the image reconstruction process.

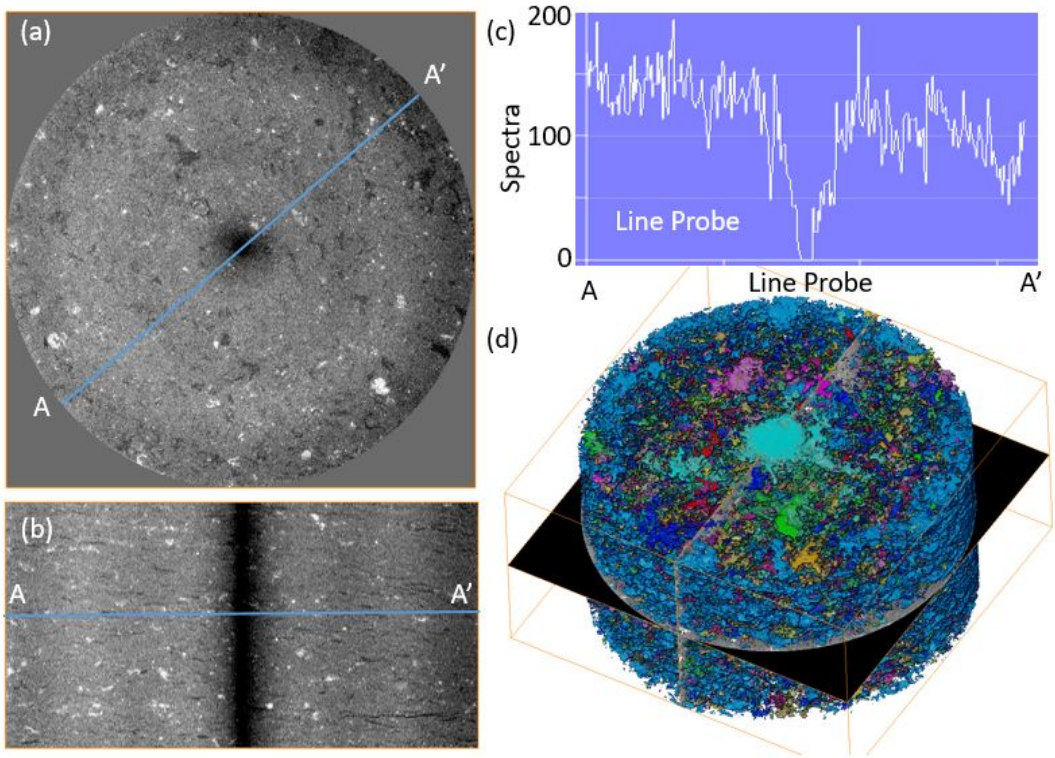

Figure 3.3: Shows a raw, high resolution 3D micotographical scan of a Draupne Formation core, organic-rich shale sample with both a beam hardening artifact and a background trend. (a) Plane-view of the sample with the line probe location. (b) Cross-section view of the sample with the line-probe location. (c) Line probe showing the variation in grayscale spectra, including a clear drop in the center (i.e., beam hardening) and a general background trend. (d) 3D capture of low-value grayscale spectra (i.e., low density) intended to capture kerogen lenses.

A strong-motion artifact was also present for one of the scanned samples which was discarded as a result. The likelihood of motion artifacts increases with resolution (Davis and Elliott, 2006). At

higher resolutions, as in these samples, even small disturbances can result in motion artefacts being introduced. After the 3D tomography images were captured, the hand samples were recovered and then made into thin sections to analyze them in two dimensions utilizing scanning electron microscopy (SEM).

3.1.2 Scanning Electron Microscopy

A Hitachi SU5000 FE-SEM (Schottky FEG), including low vacuum mode and inlens secondary detector (SE) was utilized to capture SEM images. An energy-dispersive X-ray spectroscopy (EDS) attachment utilizing X-rays gives a quantitative chemical composition analysis in the shape of a point, line, or area (Figure 3.4).

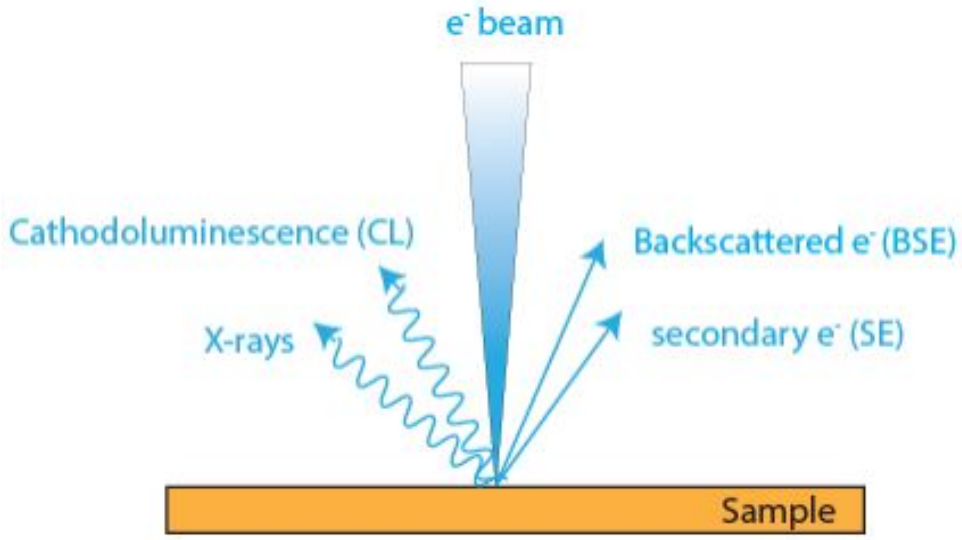

Figure 3.4: Sketch of SEM image capturing process. The figure is from the SEM Guide, University of Oslo (2022).

SEM produces images of a sample by scanning the surface with a focused beam of electrons. From the interaction between the electrons and the atoms of the sample, a variety of signals that contain information about the surface topography and composition are returned (Figure 3.4). While the cathodoluminescence (CL) was not necessary to the work carried out, the secondary detector (SE) and backscattered electron detector (BSE) were both critical. The SE has the best resolution and is used to see the surface, as well as get a sense of what may be behind it (e.g., pyrite embedded in kerogen). The BSE is used for elemental contrast since the minerals with the highest average atom will appear brightest (UiO SEM Guide, 2022). The X-rays are used for the energy dispersive spectroscopy (EDS), the use of which is shown in Figure 3.5 to separate kerogen from epoxy utilizing chemical composition.

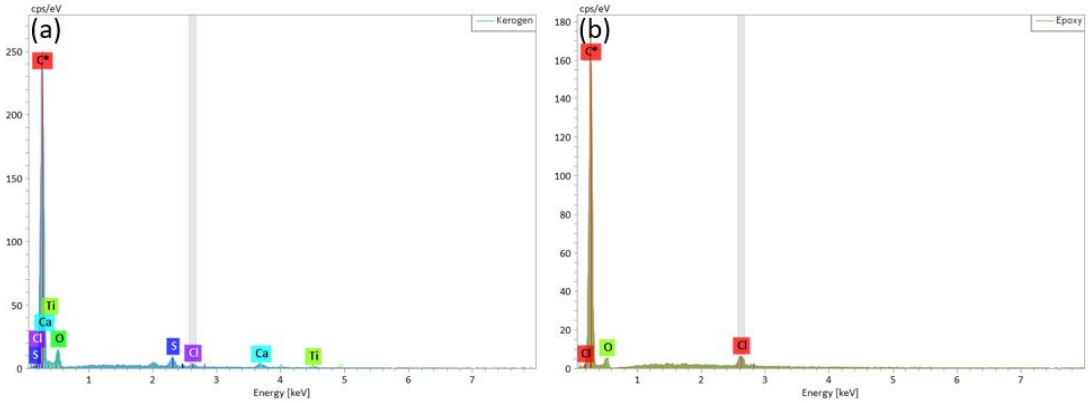

Figure 3.5: Chemical element profiles of kerogen (a) and epoxy (b) highlighting key compositional differences. While both contain significant amounts of C and O, kerogen will often have other trace elements (e.g., S, Ca, Ti), while epoxy will have a stronger Cl peak.

The epoxy utilized contains more than a trace amount of chlorite (Greenlee, 1946) and a significant amount of oxygen and hydrogen (Figure 3.5). While sulphur and nitrogen are commonly encountered constituents of kerogen (Vandenbroucke and Largeau, 2007; Selley et al., 2005; Keleman et al., 2006), heavy metal (e.g., Ti) and radioactive trace elements (e.g., U, Th) are known to be commonly associated (Selley et al., 2005; Yang et al., 2016). Regions of epoxy we re removed from the SEM during image analysis (Johnson et al., 2022b).

3.2 Analogue Experiment Methodology

Analogue experiments are comprised of simple physical models with predetermined scales of time and length in order to model geological scenarios that cannot be observed in real-time (Ranalli, 2001; Schellart and Strak, 2016). In this case, the goal was to model the process of primary migration in organic-rich shales. This was done by introducing a mixture of sugar and yeast into a low permeability elastic substance that would break in a brittle manner when the rate of CO_2 creation outstripped the total possible rate of diffusion. The elastic substances tested were laponite and gelatin (Figure 3.6). While laponite provided a greater number of nucleation points and fractures, superior for potential statistics, it was difficult to maintain two phases (i.e., solid and gas). Furthermore, the fractures created did not behave elastically, making it a non-ideal candidate (Figure 3.6). Gelatin had previously been established as ideal for representing low permeability elastic-brittle systems such as shale (Kobchenko et al., 2013; Kobchenko et al., 2014; Vega and Kovscek, 2019; Li et al., 2020). Therefore, it was decided to use gelatin (Figure 3.6b).

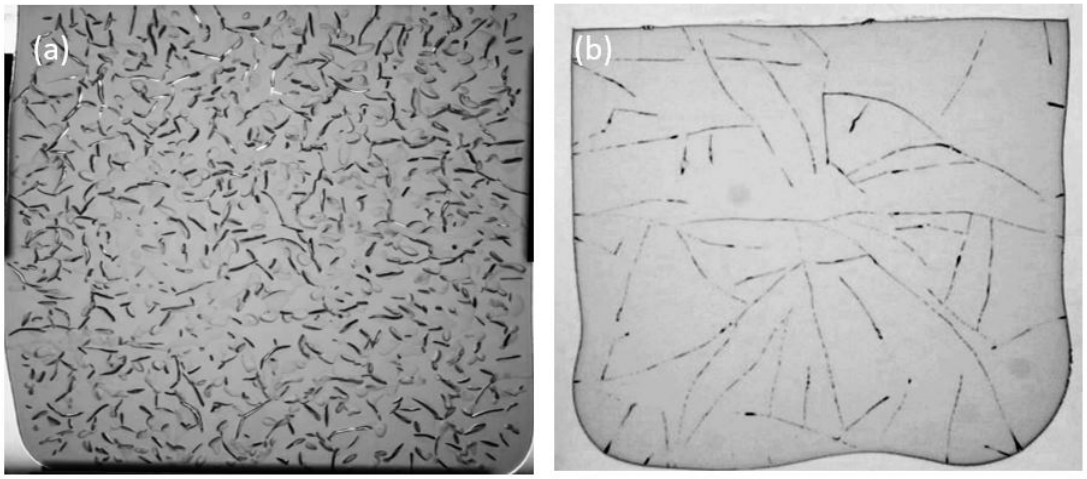

Figure 3.6: Comparison of a 1-layer (a) laponite experiment setup showing greater fracture density with three phases (i.e., solid, liquid, gas) and the (b) gelatin experiment setup showing fewer fractures in two phases

Gelita gelatin plates (2 gm/per) are first placed in cold Type II distilled water in order to enable later dissolving in hot water. A ratio of 24gm (i.e., 12 plates) of gelatin to 300 mL of hot water is the standard utilized for all layers in each experiment (Johnson et al., 2022c). Sugar and yeast, with 3gms sugar and 1gm yeast for a ratio of 3:1 for the baseline 1.0x experiments was placed in active layers. Inactive layers had only the gelatin and water mixture. 1.5x experiments keep the same ratio as 1.0x sugar and yeast experiments; however, the total amount of sugar is 4.5gms, and yeast is 1.5gms. Leftover gelatin from active layers is placed in a sealed bottle and then into a cooling apparatus set to 4^{o}C to track CO_2 production during the experiment.

The Hele-Shaw cell is constructed of two 40x40x1cm glass plates separated by a 0.5cm diameter rubber line. The rubber line is placed in a U-shape mirroring three sides of the glass plates, and the Hele-Shaw cell is clamped firmly shut. For a 1-layer experiment, 300 mL is placed in the Hele-Shaw cell and then placed upright in a cooling apparatus set to 4^{o}C. After 60 minutes, the Hele-Shaw cell is set on the face of one of the glass plates in order to ensure proper sealing between the gelatin and the Hele-Shaw cell for the remaining 1440 minutes. For experiments of 2-layers or more, the next layer(s) is placed on top of the presiding after each 60-minute interval. Table 3.2 outlines the amount of gelatin emplaced for all other experiments. The highest standard deviation for pixels, based on image analysis, for the experiments run, was 6%.

Table 3.3: Outlines the amount of gelatin emplaced (mL) for every layer, active (i.e., sugar and yeast) or inactive, and the corresponding thickness (cm) of each layer within the Hele-Shaw cell. Additionally,

the total pixel (#) for each layer was identified using image analysis, and the standard deviation for a number of pixels (#) between all experiments conducted with the same number of layers.

Experiment (# layers)	Gelatin emplaced (mL)	Hele-Shaw Thickness (cm)	Pixel Avg. (#)	Pixel Std. Dev. (#)
1	300	~30	319672	4128
2	150	~15	206173	4232
3	100	~10	106488	4639
5	60	~6	68175	4053

For open experiments, the 0.5cm rubber line is removed prior to placing the experiment within the image analysis apparatus set to 16ºC +/- 2ºC (Johnson et al., 2022c). For sealed experiments, the rubber line is left in place and can be seen outlining the gelatin in pictures (Figure 2.7a). The image analysis apparatus and the CO_2 production analysis apparatus are described in great detail in Johnson et al., (2022c).

The experiment is based on previously designed analogue models of primary migration (Kobchenko et al., 2013; Kobchenko et al., 2014; Vega and Kovscek, 2019) and complement similar experiments analyzing artificial fracturing methods (i.e., hydraulic fracturing) (Li et al., 2020). , The key to understanding these processes is implementing fracture topology description. Although the study of fracture topology is a comparatively new field (Kobchenko et al., 2014), a number of different approaches have been proposed. This Ph.D. research utilizes two methodologies, the Kobchenko method (i.e., ω-method) after Kobchenko et al. (2013); and the Sanderson-Nixon method (i.e., XYI method) after Sanderson and Nixon (2015). For more details on how these methodologies are employed, the reader can refer to Johnson et al. (2022c).

3.3 Organic-rich shale Characterization Methodology

The organic-rich shale characterization study utilized petrophysical analysis, rock physics templates, and seismic inversion workflows in conjunction with one another. Whenever possible, comparisons were made between the observations derived from these methods and those pulled from the image analysis utilizing both SEM and microtomography.

3.3.1 Petrophysical Analysis

The use of wireline logs are essential to geological and geophysical subsurface characterization. Table 3.4 explores some of the more common wireline logging tools, their resolutions, and use cases. Furthermore, logs can be used in combination with one another to calculate TOC (Equations 2.17a-f), lithology not studied here as the focus was on shale (Passey et al.,1990; Vernik and Landis, 1996), and geomechanical strength (Equations 2.12 – 2.13). Bottom hole temperature (BHT) can be used in

combination with total vertical depth (TVD) to define where in the mechanical or chemical compaction the shale is today. An understanding of regional uplift is required to provide historical context.

Table 3.4: A selection of commonly used wireline logging tools, the scientific principles they operate on, resolutions, and potential use cases (collected from Passey et al., 1990; Petrowiki, 2022).

Wireline Tool Name	Principles	Resolution	Use Case(s)
Gamma Ray	Responds to naturally occurring gamma radiation (K, Th, U/Ra)	~15 – 30 cm	- Identify lithology (shale vs. sands) - Identify salts - Spectral gamma ray can also be useful to help identify TOC content
Neutron Porosity	Measures the falloff of neutrons, particularly targeting hydrogen atoms (e.g., H_2O, CH_4, etc.)	~30 cm	- Help identify total porosity - Can be helpful in identifying TOC content - Identify fluid effects - Lithology indicator (shales)
Density	Measures the falloff of electrons from a Ce137 source; density of the rock controls the degree of falloff at the detectors	~15 – 30 cm	- Measures density of the rock - Can be helpful in identifying TOC content - Indirect lithology indicator - Indirect fluid indicator - Can be helpful in determining mechanical properties
Sonic (P-wave)	Measures travel time of P-wave in μs/ft	~30 cm	- Measures acoustic properties of the rock - Indirect lithology indicator - Indirect fluid indicator - Can be helpful in determining mechanical properties
Sonic (S-wave)	Measures travel time of S-wave in μs/ft	~30 cm	- Measures acoustic properties of the rock - Indirect lithology indicator - Indirect fluid indicator - Can be helpful in determining mechanical properties
Resistivity	Measures electrical resistivity	~60 cm	- Lithology indicator - Fluid indicator - Can be helpful in identifying TOC content
Spontaneous Potential (SP)	Measures small electric potentials in mV between two given depths	~1 m	- Lithology indicator - Fluid indicator
Caliper	Measures size and shape of the borehole	~15 – 30 cm	- Mechanical property indicator

3.3.2 Rock Physics Templates

Rock physics templates (RPTs) are a valuable way to characterize organic-rich shale. Several RPTs were utilized in the geological and geophysical characterization of the shales within this study. The important RPTs to this study are as follows:

- Perez and Marfurt (2014) classification of ductile to brittle zones utilizing Young's Modulus (Equation 2.12) and Poisson's ratio (Equation 2.13) values
- Mondol (2018) classification of compositional endmembers (i.e., kerogen, quartz, calcite, and clay) utilizing values of Young's modulus (Equation 2.12) and Poisson's ratio (Equation 2.13)
- Lithological separation using Gardner et al., (1974) and Castagna et al. (1985) for P-wave vs. Density plots and P-wave vs. S-wave plots, respectively.

The first two RPTs (Perez and Marfurt, 2014; Mondol, 2018) were instrumental in comparing EBI with MBI. The lithological RPTs (Gardner et al., 1974; Castagna et al., 1985) were critical to separating organic-rich shale from interbedded turbiditic members discussed in great detail in Johnson et al., 2022a.

3.3.3 Seismic Inversion Workflows

Seismic inversion is a good first step in bridging the fields of geology, engineering, and geophysics (Yilmaz, 2001). It does this by integrating data from all of these sources and extracting properties critical to understanding each of these fields, including lithology (i.e., shale, sandstone, etc.), rock properties (e.g., mechanical, porosity), and fluid properties (Russell, 1988; Goodway et al., 2010). The process is the opposite of the seismic acquisition, wherein the inversion algorithm effectively reverses the modeling algorithm (i.e., seismic processing) to take the seismic response and represent the earth model (Yilmaz, 2001). Seismic inversion workflow (Figure 3.7) outlines the inputs, processes, and basic outputs.

It has been established that any petrophysical property can be mapped through the transitive properties of base elastic parameters (i.e., P-wave, S-wave, and density) present in both seismic and well logs (Mukerji et al., 2001). These properties are called 'output' facies (Figure 3.7). This can be extended to any properties represented in well log (i.e., LAS) format. Our research utilizes this to integrate geochemical characterization (e.g., Rock-Eval analyses) in order to create a maturation and TOC facies (Figure 3.7) (Johnson et al., 2022a).

Two different facies, one characterizing maturation and the other TOC, were then combined in order to create the Organic Maturation Product (OMP). OMP is a unique way to classify shale that can assist in understanding the mechanical and elastic properties of shale in terms of both source and seal. The equation indicates that there is a positive relationship between the amount of TOC and the rate of maturation, as established within the literature (Fan et al., 2010; Fan et al., 2012; Voltolini and Franklin, 2020). Rock physics templates were utilized to place the equation within the framework of both mechanical and elastic behavior as to understand the impact these two parameters had (Perez and Marfurt, 2014; Mondol, 2018).

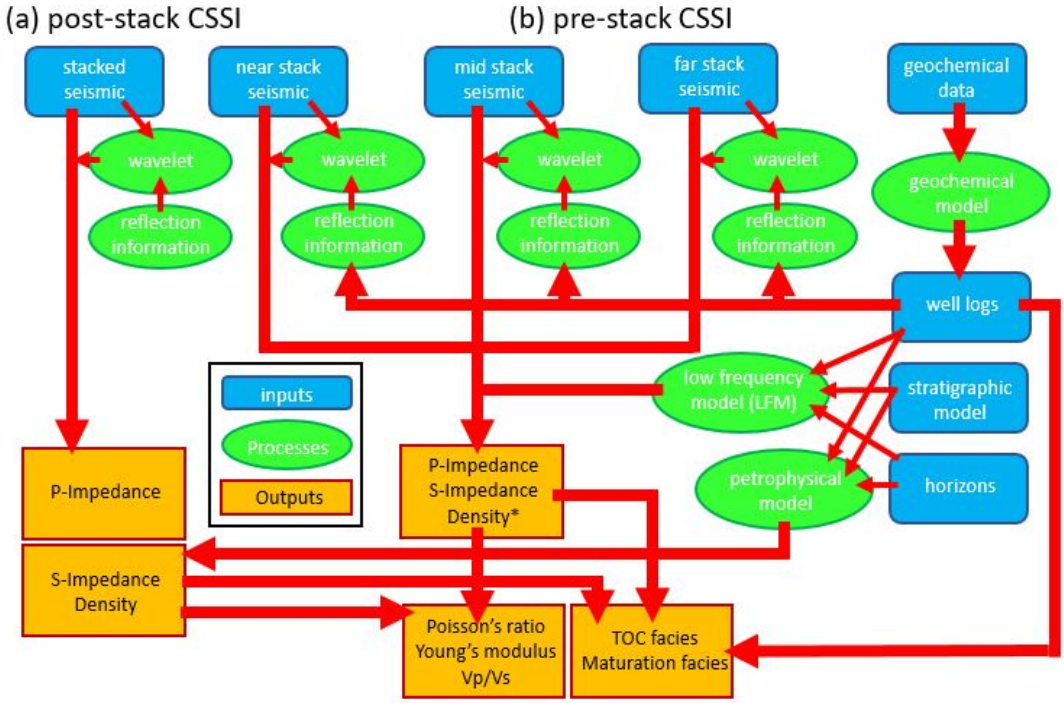

Figure 3.7: Seismic inversion workflows for (a) post-stack constrained sparse-spike inversion (CSSI) and (b) pre-stack CSSI. Base inputs are in blue, processes are in green, and final outputs are in orange.

4.0 Summary of the published papers

4.1 Multiscale synchrotron microtomography imaging of kerogen lenses in organic-rich shales from the Norwegian Continental Shelf (International Journal of Coal Geology, 2022)

Contribution: I have performed some of the experiments, processed and analyzed the data, and written the manuscript.

Summary: Failure mechanisms in organic-rich shale have microstructural origins (i.e. microfracturing), driven by kerogen lenses. The size, geometry, orientation, and distribution of kerogen lenses control how the microfracture will develop. The development of these microfractures and the potential for forming a larger, communicative (i.e., capable of fluid flow) microfracture network is influenced by the inorganic constituents (i.e., minerals). Of particular importance is the distribution of hard (i.e., stiff) minerals (e.g., quartz, feldspar, pyrite) to soft minerals (i.e., clays), as well as the distribution of the clays (i.e., smectite, illite, kaolinite, chlorite). We have imaged the microstructure of six samples from the Draupne and Hekkingen Formations, respectively, utilizing 3D X-ray tomography at two resolutions. These images have been compared to 2D SEM scans in order to elucidate both processes.

Detailed mapping of the tomographical images reveals that the largest ~20% of kerogen lenses, the ones that control the microfracturing process, can be separated into three groups: (i) large, $<10^{-11}$ m^3, that has no relationship with the number of kerogen lenses (ii) medium, 10^{-13}-$10^{-11}m^3$, that has a described relationship, and (iii) small, $>10^{-13}m^3$, that has a separate described relationship. Kerogen lenses are transversely isotropic as expected; however, they demonstrate a wide range of shapes. Four shapes (i.e., fill in here) have been proposed based on aspect ratio. Orientation ranges from +/- 30° of bedding, which is essential, as it makes fracture growth that cross-cuts laminae a likelihood without the need for a strictly vertical fracture. Finally, the distribution of lenses and the material properties of kerogen lenses themselves is significantly altered above 8 wt. % organic matter. Kerogen lenses begin to combine with one another at a substantially greater rate, resulting in fewer, larger lenses distributed in the organic-rich shale fabric. The larger lenses are often best characterized by a patchwork shape.

4.2 Experimental modeling of primary migration in a layered, brittle analogue system (Tectonophysics, 2022)

Contribution: I have performed the experiments, analyzed the data, and written the manuscript.

Summary: Analogue modeling of mesoscale processes and interactions in the context of primary migration in a layered, brittle system has been carried out in order to investigate how three parameters influence microfracture growth, final microfracture network topology, and the influences this has on fluid flow. The experiments were conducted by utilizing an elastic substance, gelatin, which breaks in a brittle fashion at certain temperatures. Sugar and yeast, mixed into active layers, react with one another, creating CO2, and ultimately exceed pore pressure limits of the gelatin resulting in failure (i.e. microfractures). The combination of gelatin, sugar, and yeast is placed inside a quasi-2D Hele-Shaw cell in order to track the creation and interaction of the microfractures. Finally, fluid flow was mapped by tracking the opening and closing of the microfracture network.

We studied the impact of anisotropy through the introduction of layers, both active (i.e., gelation, sugar, and yeast) and inactive (i.e., gelatin). Experiments were divided into 1-layer, 2-layers, 3-layers, and 5-layers. Anisotropy had no impact on nucleation density; however, increasing anisotropy results in microfractures having a greater alignment with anisotropy. It has been shown that this decreases the likelihood of microfractures breaking into layers above, resulting in a decrease in fluid flow rate. We studied the impact of sealing, which consequently altered the rigidity of the experiments, by placing a thin rubber line on 3-sides of the Hele-Shaw cell. This profoundly influenced the density of microfracture nucleations, fracture topology, and fluid flow. Increasing rigidity results in fewer microfracture nucleations; however, the microfracture network connectivity is actually increased. Further to this, fluid flow rate, while less periodic, increased. Finally, we altered the concentration of sugar and yeast within the experiments to 0.5x, 1.0x, and 1.5x in order to analyze the impact of varying levels of organic matter. The 0.5x experiment showed that given significantly low enough levels of

organic matter, the kerogen will simply diffuse given appropriate porosity and permeability. In contrast, the 1.5x experiments demonstrated that comparatively small increases in organic matter result in larger increases in microfracture nucleation density and the network itself. As a result, the fluid flow rate is enhanced.

4.3 Mapping the maturity of organic-rich shale with combined geochemical and geophysical data, Draupne Formation, Norwegian Continental Shelf (Marine and Petroleum Geology, 2022)

Contribution: I have performed the experiments, processed, analyzed and interpreted the data, and written the manuscript.

Summary: The relationship between maturation and total organic carbon (TOC) content is investigated. Two seismic surveys, twenty-nine (29) wells, and geochemical data from eighteen (18) wells representing a range of organic-rich shale maturity levels and TOC content for the Draupne Formation are compared and contrasted in order to quantify the relationship between these two parameters. Seismic inversion was used to correlate the geochemical data with well logs and seismic data. Using the transitive properties of the shared elastic response (i.e., P-wave, S-Wave, density), the relationship between TOC and maturation is mapped out.

Seismic facies were created for both TOC and maturation. TOC was identified first utilizing Rock-Eval, and then estimating it for the well log using a density-based method (e.g., Schmoker, Vernik and Landis). Maturation was initially estimated with vitrinite reflectance. However, given the limited amount of data, geochemical relationships (e.g., hydrogen index vs. TOC, hydrogen index vs. T_{max}) were utilized to identify maturation levels. The relationship between maturation and TOC was mapped out utilizing Rock Physics Templates (RPTs) that quantified brittleness indices according to material strength and RPTs that quantified mineralogical composition. From this, we propose a new RPT that quantifies the relationship between TOC content and maturation (i.e. Organic Maturation Product). Specifically, higher TOC concentrations are correlated to greater maturation and a quicker transition from ductile to brittle behavior. The results are placed within the framework of depositional and diagenetic influences for the Draupne Formation. Depositional systems of interest include turbidites, hyperpycnal flows, submarine channels, and fans, while diagenetic systems contrast normal PT-gradients with those associated with salt-tectonism.

5.0 Conclusions

Shales represents between 50-70% of all sedimentary rocks in the Earth's shallow crust and ~80% of all sections drilled for hydrocarbon exploration. Kerogen, although percentage-wise a small component of even the most organic-rich shales, is responsible for the most significant changes in physical properties that occur in organic-rich shales. This is the direct result of microfracturing within

the context of primary migration. The inorganic constituents (i.e., mineralogy) and the overall fabric influence the complexity of microfracturing, and by extension, possible properties of fluid flow (e.g., rate, periodicity). As such, understanding the influence this has on organic-rich shales before, during, and after the alteration of kerogen lenses into hydrocarbons is critical to understanding shales as both a potential source rock (i.e., unconventional and conventional hydrocarbon systems) and a potential seal (e.g., CO_2 sequestration, nuclear repository, conventional hydrocarbon systems).

The influence of microfracture dynamics during kerogen maturation and the impact this has on the rock properties of organic-rich shale is investigated here across a broad range of scales (i.e., μm-km). The investigation utilized microtomography and SEM in order to quantify the microscale (μm-cm) fabric, both organic (i.e., kerogen) and inorganic (i.e., minerals) for Type II/Type III organic-rich shale. Seismic inversion allowed investigation of the rock properties at the macroscale (m-km), particularly the influence of the relationship between total organic carbon (TOC) content and degree of maturation. Analogue modeling was utilized to bridge the gap between these scales, providing a mesoscale sense of the microfracture process of shale within the context of primary migration. Efforts were made to investigate how parameters that influence shale properties (e.g., anisotropy, rigidity, organic matter content) affect the microfracturing process. The impact of these processes was then placed within the framework of rock and fluid properties.

At all scales, there is a clear relationship between the amount of organic matter as a percentage of the whole with the rate and degree of microfracturing. Higher organic matter content results in faster, greater, and more complex microfracturing during maturation, having a direct influence on the rock properties and by extension, fluid-flow properties. At the microscale, it is observed that kerogen can be separated into three groups, (i) low (0-2 wt.%), (ii) medium (2-8 wt. %), and (iii) high (<8 wt. %). Kerogen properties shift above 8 wt. % resulting in fewer, larger lenses that will expedite the microfracturing process and influence rock properties at all scales. At the mesoscale, the microfracture network is observed to also be impacted by anisotropy (i.e., layering) and rigidity (i.e., sealing). The microscale shows that the fabric of shale is affected by mineralogy content. Shale fabric, at the mesoscale, is shown to influence fracture topology wherein more significant anisotropy correlates to a more disconnected network. However, microfracture breakthroughs across layering occur with relatively few nucleation points. As the microscale shows that the number of nucleation points is potentially vast, the formation of a complex fracture network in shales during maturation that allows fluid communication across layers is probable. Note that increased rigidity will decrease the number of nucleation points but assist in faster fluid flow. At the macroscale, kerogen content and type (i.e., Type II vs. Type III) have been shown to be influenced by the microfracture process inherent to maturation.

By using a multifaceted approach, it was shown that the fabric of shale has a clear impact on rock properties before, during, and after the maturation process. Microfractures will decrease the

coherent strength of shale while providing pathways for the created hydrocarbons during maturation. Prior to maturation, kerogen content within organic-rich shales will act as brittle-constituent that diminishes strength. After maturation, the ability for the created microfractures to heal is dependent on the mineralogy, wherein a greater percentage of clay minerals will assist in providing sealing capabilities. Understanding the impact organic element (i.e., kerogen) has on microfracturing, and in return, understanding the impact the inorganic element (i.e., mineralogy) has on effect on material strength of organic-rich shales at all portions before, during, and after maturation.

5.1 Outlook

Organic-rich shale makes for fascinating subject matter that is important to understand for a large variety of fields, including but not limited to CO_2 and H_2 sequestration, geothermal energy, conventional and unconventional petroleum exploration and production, geotechnical risk analysis, and nuclear waste site storage. It acts as a seal, source, and occasionally a reservoir as well. New ideas and avenues of research were often encountered during this Ph.D., far more than could actually be pursued. Despite a deep interest in the subject matter, I do not have time to investigate organic-rich shale further. However, a couple of key directions related to this study, in my opinion, deserve further research.

5.1.1 Microscale Considerations

The limits of resolution for microtomography are constantly being extended. Johnson et al. (2022b) compared and contrasted the results from 3D microtomography with 2D SEM images. Later, Johnson et al. (2022d) and Johnson et al. (2022e) established that you could separate out kerogen, soft minerals, and hard minerals on SEM images. These same processes can be applied utilizing microtomography. As resolutions become better, it will be possible to separate out clay mineralogy and map the interaction that kerogen lenses and the conversion of certain clay minerals (i.e., smectite-illite, kaolinite-illite) have. Specifically, it will be possible to make suppositions about the microfracturing process and whether mineralogy or kerogen lenses play a greater role in the change of material properties of shale.

5.1.2 Mesoscale Considerations

Analogue modeling is a very fun and insightful way to investigate earth system processes, so much so that every Ph.D. should benefit from pursuing this particular avenue of research. While the use of laponite was ultimately unsuccessful, it has the possibility to allow for much better statistical analysis. Given the further time it would be interesting to perfect the workflow with laponite. Further to this, there are a number of other ways that the parameters could have been altered to allow further insight:

- Alteration of mechanical strength of layers, both active and inactive

- Surrounding the active sugar:yeast layer with an inactive sugar:yeast layer in order to test confinement
- Tracking of the initial diffusion process utilizing pH indicators in the gelatin
- Introduction of glass beads or mica in order to create a different form of heterogeneity

The scope and range of experiments are limited only by imagination, time, and money, with geological processes as the unlimited inspiration.

5.1.3 Macroscale Considerations

The diverse dataset available and their integration made the macroscale research motivating. Not enough studies utilize multiple 3D seismic datasets across a broad range of a given basin or shelf region (e.g., Norwegian Continental Shelf) to understand basin or regional dynamics. Further to this, while the use of both geochemical and geophysical tools to characterize rock properties is common – the integration of them is less common. This work provided a way to map geochemical properties across an entire basin to better understand the impact of maturation. However, mapping maturation states and extents are still yet to become best practice, both along the Norwegian Continental Shelf and globally.

References

American Association of Petroleum Geologists (AAPG) Wikipedia, 2022; AAPG: *Accessed* 2022 https://wiki.aapg.org/Kerogen

Alfred, D., and Vernik, L., (2013). A new petrophysical model for organic shales. *Petrophysics, 54*(3), 240-247.

Alvarez, L.L., Guimares, L.J.N., Gomes, I.F., Beserra, L., Pereira, L.C., Miranda, T.S., Maciel, B., and Barbosa, J.A., (2021). Impact of fracture topology on the fluid flow behavior of naturally fractured reservoirs. *Energies, 14*(5488).

Alzahabi, A., AlQahtani, G., Soliman, M.Y., Bateman, R.M., Asquith, G., Vadapalli, R., (2015). Fracturability index is a mineralogical index: a new approach for fracturing decision. In *SPE Saudi Arabia Section Annual Technical Symposium and Exhibition, SPE.*

Anders, M.H., Laubach, S.E., and Scholz, C.H., (2014). Microfractures: a review. *Journal of Structural Geology, 69,* 377-394.

Avseth, P., and Caricione, J.M., (2015). Rock-physics analysis of clay-rich source rocks on the Norwegian Shelf. *Leading Edge, 34,* 1340-1348.

Avseth, P., Mukrji, T., Mavko, G., Dvorkin, J., (2010). Rock-physics diagnostics of depositional texture, diagenetic alterations, and reservoir heterogeneity in high-porosity siliciclastic sediments and rocks – A review of selected models and suggested work flows. *Geophysics, 75*(5), 31-47.

Avseth, P., and Veggeland, T., (2015). Seismic screening of rock stiffness and fluid softening using rock-physics attributes. *Interpretation, 3*(4), 85-93.

Badics, B., Avu, A., and Mackie, S., (2015). Assessing source rock distribution in Heather and Draupne Formations of the Norwegian North Sea: a workflow using organic geochemical, petrophysical, and seismic character. *Interpretation, 3*(3), 45-68.

Baig, I., Faleide, J.I., Jahren, J., and Mondol, N.H., (2016). Cenozoic exhumation on the southwestern Barents Shelf: estimates and uncertainties constrained from compaction and thermal maturity analyses. *Marine and Petroleum Geology, 73,* 105-130.

Baig, I., Faleide, J.I., Mondol, N.H., Jahren, J., (2019). Burial and exhumation history control on shale compaction and thermal maturity along the Norwegian North Sea basin margin areas. *Marine and Petroleum Geology, 104*, 61-85.

Bense, V.F., Gleeson, T., Loveless, S.E., Bour, O., and Scibek, J., (2013). Fault zone hydrogeology. *Earth-Science Reviews, 127*, 171-192.

Blatt, H., and Schultz, D.J., (2006). Size distribution of quartz in mudrocks. *Sedimentology, 23*(6), 857-866.

Bond, D.P.G., and Wignall, P.B., (2010). Pyrite framboid study of marine Permian-Triassic boundary sections: a complex anoxic event and its relationship to contemporaneous mass extinction, *GSA Bulletin, 122*(7-8), 1265-1279.

Bourg, I.C., (2015). Sealing shales versus brittle shales: a sharp threshold in the material properties and energy technology uses of fine-grained sedimentary rocks. *Environmental Science Technology Letters, 2,* 255-259.

Bourg, I.C., and Franklin, J.B.A., (2017). Clay, water, and salt: controls on the permeability of fine-grained sedimentary rocks. *Accounts of Chemical Research, 50,* 2067-2064.

Brun-Lie, C.M.K., (2017). Oedometer tests for assessing possible impact of fluid-shale interactions on a shale barrier formation. *M.Sc. Thesis. Norwegian University of Science and Technology.*

Burnham, A.K., (2017). Porosity and permeability of Green River oil shale and their changes during retorting. *Fuel, 203,* 208-213.

Carcione, J.M., and Avseth, P., (2015). Rock-physics templates for clay-rich source rocks. *Geophysics, 80*(5), 481-500.

Castagna, J.P., Batzle, M.L., and Eastwood, R.L. (1985). Relationship between compressional-wave and shear-wave velocities in clastic silicate rocks. *Geophysics, 50*, 571-581.

Charsky, A., and Herron, S., (2013). Accurate, direct total organic carbon (TOC) log from a new advanced geochemical spectroscopy tool: comparison with conventional approaches for TOC estimation. *AAPG Search and Discovery, 41162*(2013).

Chauve, T., Scholtes, L., Donze, F., Mondol., N.H., Renard, F., (2020). Layering in shales controls microfracturing at the onset of primary migration in source rocks. *Journal of Geophysical Research: Solid Earth, 125*(5), e2020JB019444.

Chenrai, P., Assawincharoenkij, T., Warren, J., Sa-nguankaew, S., Meepring, S., Laitrakull, K., and Cartwright, I., (2022). The occurrence of bedding-parallel fibrous calcite veins in Permian siliciclastic and carbonate rocks in central Thailand. *Frontiers in Earth Science, 9*, 781782.

Cierniak, R. (2011). *X-ray computed tomography in biomedical engineering*. Springer Science and Business Media.

Colijn, A.P., Zbijewski, W., Sasov, A., and Beekman, F.J., (2004). Experimental validation of a rapid Monte Carlo based micro-CT simulator. *Physics in Medicine and Biology, 49*(2004), 4321-4333.

Cooke, I.L., (2014). User guide total organic carbon (TOC) dataset: *British Geological Survey (BGS) Internal Report*

Davis, G.R., and Elliott, J.C., (2006). Artefacts in X-ray microtomography of materials. *Materials Science and Technology, 22*(9), 1-8

Dore, A.G., Vollset, J., Hamar, G.P., (1985). Correlation of the offshore sequences referred to the Kimmeridge Clay Formation – relevance to the Norwegian sector. *Petroleum Geochemistry in Exploration of the Norwegian Shelf, 1*, 27-37

Duhailen, M.A.A., Sonnenberg, S.A., Longman, M., (2015). Analyzing beef fractures: genesis and relationship with organic-rich shale facies. In *SPE/AAPG/SEG URTEC Conference, San Antonio, Texas, July 2015.*

Kuuskraa, V.A., Stevens, S.H., and Moodhe, K., (2013). Technically recoverable shale oil and shale gas resources: an assessment of 137 shale formations in 41 countries outside of the United States. *US EIA.*

Engelder and Fischer, 1994

Espitalie, J., Deroo, G., and Marquis, F., (1985). La pyrolysis Rock-Eval etses applications. *Oil and Gas Science and Technology, 40*, 755-784.

Faleide, J.I., Tsikalas, F., Breivik, A.J., Mjelde, R., Ritzmann, O., Engen, O., Wilson, J., and Eldhom, O., (2008). Structure and evolution of the continental margin off Norway and the Barents Sea. *Episodes, 31*, 82-91.

Faleide, J.I., Bjørlykke, K., and Gabrielsen, R.H., (2015). Geology of the Norwegian Continetal Shelf. *Petroleum Geoscience*, 603-637.

Fan, Z.Q., Jin, Z.H., and Johnson, S.E., (2010). Subcritical propagation of an oil-filled penny-shaped crack during kerogen-oil conversion. *Geophysical Journal International, 182,* 1141-1147

Fan, Z.Q., Jin, Z.H., and Johnson, S.E., (2012). Gas-driven subcritical crack propagation during conversion of oil to gas. *Petroleum Geoscience, 18*, 191-199.

Fawad, M., and Mondol, N.H., (2021). Monitoring geological storage of CO2: a new approach. *Nature: Scientific Reports, 2021*(11), 5942.

Feldman, H., and Demko, T., (2015). Recognition and prediction of petroleum reservoirs in the fluvial/tidal transition. *Developments in Sedimentology, 68*, 483-528.

Fjær, E., Holt, R.M., Horsrud, P., Raaen, A.M., Risnes, R., (2021). Geological aspects of petroleum related rock mechanics. *Developments in Petroleum Science, 72,* 157-200.

Gardner, G.H., Gardner, L.W., and Gregory, A.R., (1974). Formation velocity and density – the diagnostic basis for stratigraphic traps. *Geophysics, 39*, 770-780.

Goodway, B., Perez, M., Varsek, J., Abaco, C., (2010). Seismic petrophysics and isotropic-anisotropic AVO methods for unconventional gas exploration. *Leading Edge, 29*(12), 1500-1508.

Gray, D., (2008). Fracture detection using 3D seismic azimuthal AVO. *CSEG Recorder, 3*, 38-49.

Grieser, B., and Bray, J., (2007). Identification of production potential in unconventional reservoirs. In *SPE Production and Operations Symposium, 2007.*

Greenlee, O.S., (1946). Synthetic drying compositions (US Patent No. 2456408A). *US Patent and Trademark Office.*

Guo, Z., Li, X.Y., Liu, C., Feng, X., and Shen, Y., (2013). A shale rock physics model for analysis of brittleness index, mineralogy, and porosity in the Barnett Shale. *Journal of Geophysics and Engineering, 10*(2013), 025006.

Hansen, J.A., Mondol, N.H., Tsikalas, F., Faleide, J.I., (2020). Caprock characterization of Upper Jurassic organic-rich shales using acoustic properties: Norwegian Continental Shelf. *Marine and Petroleum Geology, 121,* 104603.

He, Q., He., B., Li, F., Shi, A., Chen, J., Xie, L., and Ning, W., (2021). Fractal characterization of complex hydraulic fractures in oil shales via topology. *Energies, 14,* 1123.

Heinemann, Z.E., and Mittermeir, G.M., (2012). Derivation of Kazemi-Gilman-Elsharkawy generalized dual porosity shape factor. *Transport in Porous Media, 91*, 123-132.

Heslop, K.A., (2010). Generalized method for the estimation of TOC from GR and Rt. *AAPG Search and Discovery, 80117*(2010).

Henriksen, E., Bjornseth, H.M., Hals, T.K., Heide, T., Kiryukhina, T., Klovjan, O.S., Larssen, G.B., Ryseth, A.E., Ronning, K., Sollid, K., Stoupakova, A., (2011). Uplift and erosion of the greater Barents Sea: impact on prospectivity and petroleum systems. *Geological Society Memoirs, 35,* 1-271.

Hernandez, M.G., Duplay, J., Martinez, L., Escoffier, S., Rousset, D., (2004). Structural modifications of Callovo-Oxfordian argillite under hydration/dehydration conditions. *Applied Clay Science, 25*(3-4), 187-194.

Huang, R., Yan, W., Sijie, C., Shuai, L., Li, C., (2015). Selection of logging-based TOC calculation methods for shale reservoirs: a case study of the Jiaoshiba shale gas field in the Sichuan Basin. *Natural Gas Industry, 2*(2015), 155-161.

Holt, R.M., and Kolstø, M.I., (2017). How does water near clay mineral surfaces influence the rock physics of shales?. *Geophysical Prospecting, 65*(6), 1615-1629.

Isaksen, G.H., and Ledje, H.I., (2001). Source rock quality and hydrocarbon migration pathways within the greater Utsira High area, Viking Graben, Norwegian North Sea. *AAPG Bulletin, 85,* 861-883.

Jackson, C.A.L., Larsen, E., Hanslien, S., Tjemsland, A.E., (2011). Controls on synrift turbidite deposition on the hanging wall of the South Viking Graben, North Sea rift system, offshore Norway. *AAPG Bulletin, 95*(9), 1557-1587.

Jahren, J., Thyberg, B., Marcussen, Ø., Winje, T., Bjørlykke, K., and Faleide, J.I., (2007). From mud to shale: the role of microquartz cementation. *AAPG Search and Discovery, 50206*(2009).

James, N.P., and Dalrymple, R.W., (2004). Facies Models 4. *Canadian Society of Petroleum Geologists.*

Jarvie, D.M., Hill, R.J., Ruble, T.E., Pollastro, R.M., (2007). Unconventional shale-gas systems: the Mississippian Barnett Shale of north-central Texas as one model for thermogenic shale-gas assessment. *AAPG Bulletin, 91*, 475-499.

Jin, Z.H., Johnson, S.E., and Fan, Z.Q., (2010). Subcritical propagation and coalescence of oil-filled cracks: getting the oil out of low-permeability source rocks. *Geophysical Research Letters, 37*, L01305.

Jin, X., Shah, S.N., Roegiers, J.C., Zhang, B., (2014). Fracability evaluation in shale reservoirs-an integrated petrophysics and geomechanics approach. In *SPE Hydraulic Fracturing Technology Conference, SPE*.

Johnson, D.D. (1995). Modelling tectonic, climatic, and eustatic effects on orogen/foreland basin systems. *Ph.D. Thesis. Dalhousie University.*

Johnson, J.R. (2017). Applications of geostatistical seismic inversion to the Vaca Muerta Neuquen Basin, Argentina. *M.S. Thesis. Colorado School of Mines.*

Johnson, J.R., Renard, F., and Mondol, N., (2021). Salt remobilization timing and its impact on two Norwegian Continental Shelf organic-rich shale formations. In *Geoconvention 2021.*

Johnson, J.R., Hansen, J.A., Rahman, J., Renard, F., and Mondol, N.H., (2022a). Mapping the maturity of organic-rich shale with combined geochemical and geophysical data, Draupne Formation, Norwegian Continental Shelf. *Marine and Petroleum Geology, 138*(2022), 105525.

Johnson, J.R., Kobchenko, M., Mondol, N.H., and Renard, F., (2022b). Multiscale synchrotron microtomography imaging of kerogen lenses in organic-rich shales from the Norwegian Continental Shelf. *International Journal of Coal Geology, 253*(2022), 103954.

Johnson, J.R., Kobchenko, M., Johnson, A.C., Mondol, N.H., and Renard, F., (2022c). Experimental modeling of primary migration in a layered, brittle analogue system. *Tectonophysics (submitted).*

Johnson, R.D. (1974). Dispersal of recent sediments and mine tailing in a shallow-silled fjord, Rupert Inlet, British Columbia. *Ph.D. Thesis, University of British Columbia.*

Jung, J., Yoo, K., Lee, K., Park, Y.K., Lee, J.I., and Kim, J., (2019). Clay mineralogical characteristics of sediments deposited during the late quaternary in the Larsen ice shelf b embayment, Antarctica. *Minerals, 9,* 153, 1-12.

Kalani, M., Jahren, J., Mondol., N.H., and Faleide, J.I., (2015). Petrophysical implications of source rock microfracturing. *International Journal of Coal Geology, 143*, 43-67.

Kandula, N. (2021). Dynamic synchrotron imaging of brittle failure in crustal rocks. *PhD Thesis. University of Oslo.*

Keleman, S.R., Walters, C.C., Ertas, D., Kwiatek, L.M., Curry, D.J., (2006). Petroleum expulsion part 2. Organic matter type and maturity effects on kerogen swelling by solvents and thermodynamic parameters for kerogen from regular solution theory. *Energy Fuel, 20*, 301-308.

Ketcham, R.A., (2005). Three-dimensional grain fabric measurements using high-resolution X-ray computed tomography. *Journal of Structural Geology, 27*, 1217-1228.

Kobchenko, M., Panahi, H., Renard, F., Dysthe, D.K., Malthe-Sørenssen, A., Mazzini, A., Scheibert, J., Jamtveit, B., and Meakin, P., (2011). 4D imaging of fracturing in organic-rich shale during heating. *Journal of Geophysical Research, 116*, B12201.

Kobchenko, M., Hafver, A., Jettestuen, E., Galland, O., Renard, F., Meakin, P., Jamtveit, B., Dysthe, D.K., (2013). Drainage fracture networks in elastic solids with internal fluid generation. *Europhysics Letters. 102,* 66002.

Kobchenko, M., Hafver, A., Jettestuen, E., Renard, F., Galland, O., Jamtveit, B., Meakin, P., Dysthe, D.K., (2014). Evolution of a fracture network in an elastic medium with internal fluid generation and expulsion. *Physical Review, 50*, 052801.

Koo, T., Jang, Y., Kogure, T., Kim J.H., Park, B.C., Sunwoo, D., and Kim, J., (2014). Structural and chemical modification of nontronite associated with microbial Fe(III) reduction: indicators of "illitization". *Chemical Geology, 377*(2014), 87-95.

Kuuskra, V.A., Steven, S.H., and Moodhe, K., (2013). Technically recoverable shale oil and shale gas resources: an assessment of 137 shale formations in 41 countries outside the United States: *US Energy Information Admistration (EIA)*

Kyle, J.R., and Ketchum, R.A., (2015). Application of high resolution X-ray computed tomography to mineral deposit origin, evaluation, and processing. *Ore Geology Reviews, 65*, 821-839.

Li, S., Liu, L., Chai, P., Li, X., He, J., Zhang, Z., and Wei, L., (2019). Imaging hydraulic fractures of shale cores using combined positron emission tomography and computed tomography (PET-CT) imaging technique. *Journal of Petroleum Science and Engineering, 182*(2019), 106283.

Li, Z., Wang, J., Gates, I.D., (2020). Fracturing gels as analogs to understand fracture behavior in shale gas reservoirs. *Rock Mechanics and Rock Engineering, 53*, 4345-4355.

Liu, Z., Chen, D., Zhang, J., Lu, X., Wang, Z., Liao, W., Shi, X., Tang, J., and Xie, G., (2019). Pyrite morphology as an indicator of paleoredox conditions and shale gas content of the Longmaxi and Wufeng shales in the middle Yangtze area, South China. *Minerals, 9*(428), 1-18.

Liu, G., Chen, Y., Du, X., Xiao, P., Liao, S., and Azzam, R., (2021). Investigation of microcrack propagation and energy evolution in brittle rocks based on the voronoi model. *Materials, 14*, 1-24.

Lovell, A.E., Srinivasan, S., Karra, S., O'Malley, D., Makedonska, N., Viswanathan, H.S., Srinivasan, G., Carey, J.W., and Frash, L.P., (2018). Extracting hydrocarbon from shale: an investigation of

the factors that influence the decline and the tail of the production curve. *AGU: Water Resources Research, 54*, 3748-3757.

Løseth, H., Wensaas, L., Gading, M., Duffaut, K., Springer, M., (2011). Can hydrocarbon source rocks be identified on seismic data? *Geology, 39*, 1167-1170.

Mallick, R.K., and Raju, S.V., (1995). Application of wireline logs in characterization and evaluation of generation potential of Palaeocene-lower Eocene source rocks in parts of Upper Assam Basin, India. *The Log Analyst, 36*, 3.

Marin, D., Helleren, S., Escalona, A., Olaussen, S., Cedeno, A., Nøhr-Hansen, H., Ohm, S., (2020). The middle Jurassic to lowermost Cretaceous in the SW Barents Sea: interplay between tectonics, coarse-grained sediment supply and organic matter preservation. *Basin Research, 33*, 1033-1055.

Meng, Q., Hooker, J., and Cartwright, J., (2017). Early overpressuring in organic-rich shales during burial: evidence from fibrous calcite veins in the Lower Jurassic Shales-with-Beef member in the Wessex Basin, UK. *Journal of Geological Society, 174* (2017), 869-882.

Meng, T., Liu, R., Meng, X., Zhang, D., and Hu, Y., (2019). Evolution of the permeability and pore structure of transversely isotropic calcareous sediments subjected to triaxial pressure and high temperature. *Engineering Geology, 253*(2019), 27-35.

Mews, K.S., Alhubail, M.M., and Barati, R.G., (2019). A review of brittleness index correlations for unconventional tight and ultra-tight reservoirs. *Geosciences, 9*(319), 1-21.

Mirone, A., Brun, E., Gouillart, E., Tafforeau, P., & Kieffer, J. (2014). The PyHST2 hybrid distributed code for high speed tomographic reconstruction with iterative reconstruction and a priori knowledge capabilities. *Nuclear Instruments and Methods in Physics Research Section B: Beam Interactions with Materials and Atoms, 324*, 41-48.

Mo, C.H., Lee, G.H., Jeoung, T.J., Ko, K.N., Kim, K.S., Park, K., and Shin, C.H., (2018). Prediction of shale prospectivity from seismically-derived reservoir and completion qualities: application to a shale-gas field, Horn River Basin, Canada. *Journal of Applied Geophysics, 151*(2018), 11-22.

Mondol, N.H., Bjørlykke, K., and Jahren, J., (2008). Experimental compaction of clays: relationship between permeability and petrophysical properties in mudstones. *Petroleum Geoscience, 14*(4), 319-337.

Mondol, N.H. (2018). Seal quality prediction using E-Poisson's ratio rock physics template – a case study from the Norwegian Barents Sea. In *Geoconvention, 2018*.

Mukerji, T., Jørstad, A., Avseth, P., Mavko, G., and Granli, J.R., (2001). Mapping lithofacies and pore-fluid probabilities in a North Sea reservoir: seismic inversions and statistical rock physics. *Geophysics, 66*(4), 988-1001.

Nelson, D.W., and Sommers, L.E., (1996). Methods of Soil Analysis: Part 3 Chemical Methods, Chapter 34, Total carbon, organic carbon, and organic matter.

Neves, F.A., Zahrani, M.S., and Bremkamp, S.W., (2004). Detection of potential fractures and small faults using seismic attributes. *The Leading Edge, 9*, 903-906.

Nielsen, O.B., Rasmussen, E.S., and Thyberg, B.I., (2015). Distribution of clay minerals in the Northern North Sea basin during the Paleogene and Neogene: A result of source-area geology and sorting processes. *Journal of Sedimentary Research, 85*, 562-581.

Nooraiepour, M., Mondol, N.H., Hellevang, H., and Bjørlykke, K., (2017). Experimental mechanical compaction of reconstituted shale and mudstone aggregates: Investigation of petrophysical and acoustic properties of SW Barents Sea cap rock sequences. *Marine and Petroleum Geology, 80*, 265-292.

NPD, 2022 NPD FactPages, https://npdfactpages.npd.no/factpages/Default.aspx?culture=en

O'Brien, N., (1996). Shale lamination and sedimentary processes, Paleoclimatology and Paleooceanography from Laminated Sediments. *Geological Society Special Publication, 116*, 23-26.

Ogata, K., Senger, K., Braathen, A., Tveranger, J., and Olaussen, S., (2014). Fracture systems and mesoscale structural patterns in the siliciclastic Mesozoic reservoir-caprock succession of the Longyearbyen CO2 Lab project: Implication for geological CO2 sequestration in Central Spitsbergen, Svalbard. *Norwegian Journal of Geology, 12*, 121-154.

Ohm, S.E., Karlsen, D.A., and Austin, T.J.F., (2008). Geochemically driven exploration models in uplifted area: examples from the Norwegian Barents Sea. *AAPG Bulletin, 92*, 1191-1223.

Okiongbo, K., Aplin, A., and Larter, S., (2005). Changes in type II kerogen density as a function of maturity: evidence from the Kimmeridge clay formation. *Energy Fuel, 19,* 2495-2499.

Ouiger-Simonin, A., Renard, F., Boehm, C., and Vidal-Gilbert, S., (2016). Microfracturing and microporosity in shales. *Earth-Science Reviews, 162*(2016), 198-226.

Paganin, D., Gureyev, T.E., Pavlov, K.M., Lewis, R.A., and Kitchen, M. (2004). Phase retrieval using coherent imaging systems with linear transfer functions. *Optic Communications, 234*(1-6), 87-105.

Pan, X., Zhang, D., and Zhang, P., (2021). Fracture detection from Azimuth-dependent seismic inversion in joint-time frequency domain. *Nature, Scientific Reports, 11*(2021), 1269-1284.

Passey, Q.R., Creaney, S., Kulla, J.B., Moretti, F.J., and Stroud, J.D., (1990). A practical model for organic richness from porosity and resistivity logs. *AAPG Bulletin, 74*(12), 1777-1794.

Pepper, A.S., and Corvi, P.J., (1995). Simple kinetic models of petroleum formation. Part III: modeling an open system. *Marine and Petroleum Geology, 12*(4), 417-452.

Pepper, A. (2017). Definition, modes of occurrence and pitfalls in understanding the term 'bitumen' in conventional and unconventional petroleum systems. In *2017 AAPG Convention & Exhibition*

PetroWiki, *Accessed* 2022, https://petrowiki.spe.org/PetroWiki

Prasad, M., Pal-Bathija, A., Johnston, M., Rydzy, M., and Batzle, M., (2009). Rock physics of the unconventional. *Leading Edge*, 28, 34-38.

Prasad, M., Kenechukwu, C., McEvoy, T.E., and Batzle, M., (2011). Maturity and impedance analysis of organic-rich shales. *SPE Reservoir Evaluation Engineering, 14*, 533-543.

Perez, R., and Marfurt, K., (2014). Mineralogy based brittleness prediction from surface seismic data: application to the Barnett Shale. *Interpretation, 2*, 1-17.

Pineau, A., and Pardoen, T., (2007). Failure of Metals. *Comprehensive Structural Integrity, 2*(2007), 684-797.

Rabbel, O., Mair, K., Galland, O., Gruhser, C., and Meier, T., (2020). Numerical modeling of fracture network evolution in organic-rich shale with rapid internal fluid generation. *Journal of Geohysical Research: Solid Earth, 125*(2020), 1-19.

Rahman, M.J., Fawad, M., and Mondol, N.H., (2020). Organic-rich shale caprock properties of potential CO2 storage sites in the northern North Sea, offshore Norway. *Marine and Petroleum Geology, 122*, 104665.

Rahman, M.J., Lebedev, M., and Mondol, N.H., (2021). Nanoscale mechanical properties of organic-rich Draupne shale caprock, offshore Norway. In *2021 SEG Annual Meeting*

Raiswell, R., and Berner, R.A., (1985). Pyrite formation in euxinic and semi-euxinic sediments. *American Journal of Science, 285*(8), 710-724.

Ranalli, G., (2001). Experimental tectonics: from Sir James Hall to the present. *Journal of Geodynamics, 32*(2001), 65-76.

Rickman, R., Mullen, M., Petre, E., Grieser, B., and Kundert, D., (2008). A practical use of shale petrophysics for stimulation design optimization: all shale plays are not clones of the Barnett Shale. *SPE*.

Rijken, P., and Cooke, M.L., (2001). Role of shale thickness on vertical connectivity of fractures: application of crack-bridging theory to the Austin Chalk, Texas. *Tectonophysics, 337*, 117-133.

Rummel, L., Kaus, B.J.P., Baumann, T.S., White, R.W., and Riel, N., (2020). Insights into the compositional evolution of crustal magmatic systems from the coupled petrological-geodynamical models. *Journal of Petrology, 61*(2), egaa029.

Russell, B.H., (1988). Introduction to seismic inversion methods: *SEG*.

Sanderson, D.J., and Nixon, C.W., (2015). The use of topology in fracture network characterization. *Journal of Structural Geology, 72*(2015), 55-66.

Sayers, C., (1999). Stress-dependent seismic anisotropy of shales. *Geophysics, 64*(1), 93-98.

Sayers, C., and Boer, L.D., (2018). The elastic properties of clay in shales. *Journal of Geophysical Research: Solid Earth, 123*, 5965-5974.

Schellart, W.P., and Strak, V., (2016). A review of analogue modeling of geodynamic processes: Approaches, scaling, materials, and quantification, with an application to subduction experiments, *Journal of Geodynamics, 100*(2016), 7-32.

Schmoker, J.W., and Hester, T.C., (1983), Organic carbon in Bakken Formation, United States portion of Williston basin. *AAPG Bulletin, 67*, 2165-2174.

Selley, R.C., Cocks, R.M., and Plimer, I.R., (2005). Encyclopedia of Geology.

Silva, J.P., Gomes, I.F., Santos, R.F.V.C., Mirand, T.S., Gueses, R.P., Barbosa, J.A., Guimaraes, E.X., Beserra, L.B., and Guimaraes, L.J.N., (2021). Topological analysis of fracture networks integrated with flow simulation models for equivalent fracture permeability estimation. *Journal of Structural Geology, 147*, 104338.

Skobe, S., Gorican, S., Skaberne, D., Verbic, T., Misic, M., and Zupancic, N., (2013). K-feldspar rich shales from Jurassic bedded cherts in southeastern Slovenia. *Swiss Journal of Geoscience, 106*(2013), 491-504.

Skurtveit, E., Miri, R., and Hellevang, H., (2018). Geological carbon storage: subsurface seals and caprock integrity. *American Geophysical Union*.

Teixeira, M.G., Donze, F., Renard, F., Panahi, H., Papachristos, E., and Scholtes, L., (2017). Microfracturing during primary migration in shales. *Tectonophysics, 694*, 268-279.

Thyberg, B., Jahren, J., Winje, T., Bjørlykke, K., Faleide, J.I., and Marcussen, O., (2010). Quartz cementation in Late Cretaceous mudstones, northern North Sea: Changes in rock properties due to dissolution of smectite and precipitation of micro-quartz crystals. *Marine and Petroleum Geology, 27*, 1752-1764.

Tissot, B.P., and Welte, D.H., (1984). Petroleum formation and occurrence. *Springer-Verlag Berlin Heidelberg GmbH.*

University of Oslo, Scanning Electron Microscope Manual, *accessed* 2022.

Vandenbroucke, M., and Largeau, C., (2007). Kerogen origin, evolution, and structure. *Organic Geochemistry, 38*, 719-833.

Vega, B., and Kovscek, A.R., (2019). A systematic study of internal gas generation in shale source rocks using analogy experiments. *Journal of Petroleum Science and Engineering, 173*, 209-221.

Vega, B., Yang, J., Tchelepi, H., and Kovscek, A.R., (2020). Investigation of stress field and fracture development during shale maturation using analog rock systems. *Transport in Porous Media, 131*(2020), 503-535.

Vernik, L., and Landis, C., (1996). Elastic anisotropy of source rocks – implications for hydrocarbon generation and primary migration. *AAPG Bulletin, 80*, 531-544.

Vernik, L., and Nur, A., (1992). Ultrasonic velocity and anisotropy of hydrocarbon source rocks. *Geophysics, 57*, 727-735.

Vidal O., and Dubacq, B., (2009). Thermodynamic modeling of clay dehydration, stability and compositional evolution with temperature, pressure, and H20 activity. *Geochemica et Cosmochimica Acta, 73*, 6544-6564.

Voltolini, M., and Franklin, J.G.A., (2020). The sealing mechanisms of a fracture in Opalinus clay as revealed by in situ synchrotron X-Ray Micro-tomography. *Frontiers in Earth Sciences, 8*, 1-13.

Wang, Q., Wang, T., Liu, W., Zhang, J., Feng, Q., and Lu, H., (2019). Relationships among composition, porosity, and permeability of Longmaxi Shale reservoir in the Weiyuan block, Sichuan basin, China. *Marine and Petroleum Geology, 102*(2019), 33-47.

Whipp, P.S., Jackson, C.A.L., Gawthorpe, R.L., Dreyer, T., and Quinn, D., (2014). Normal fault array evolution above a reactivated rift fabric; a subsurface example from the northern Horda Platform, Norwegian North Sea. *Basin Research, 26*, 523-549.

Wilson, M.P., Worrall, F., Davies, R.J., and Hart, A., (2017). Shallow aquifer vulnerability from subsurface fluid injection at a proposed shale gas hydraulic fracturing site. *Water Resources Research, 53,* 9922-9940.

Yang, A., Firdaus, G., and Heidari, Z., (2016). Electrical resistivity and chemical properties of kerogen isolated from organic-rich mudrocks. *Geophysics, 81*(6), 643-655.

Yilmaz, O, (2001). Seismic data analysis: processing, inversion, and interpretation of seismic data: *SEG.*

Zadeh, M.K., Mondol, N.H., and Jahren, J., (2017). Velocity anisotropy of Upper Jurassic organic-rich shales, Norwegian Continental Shelf. *Geophysics, 82*, 61-75.

Zargari, S., Prasad, M., Kenechukwu, C., and Mattson, E.D., (2013). Organic maturity, elastic properties, and textural characteristics of self resourcing reservoirs. *Geophysics, 78*, 223-235.

Zecchin, M., and Catuneanu, O., (2015). High-resolution sequence stratigraphy of clastic shelves III: Applications to reservoir geology, *Marine and Petroleum Geology, 62*(2015), 161-175.

Zhao, L., Qin, X., Han, D.H., Geng, J., Yang, Z., and Cao, H., (2016). Rock-physics modeling for the elastic properties of organic shale at different maturity stages. *Geophysics, 81*(5), 527-541.

Zhang, X., Lu, Y., Tang, J., Zhou, Z., and Liao, Y., (2016). Experimental study on fracture initiation and propagation in shale using supercritical carbon dioxide fracturing. *Fuel, 190*(2017), 370-378.

Zhang, Q., Choo, J., and Borja, R.I., (2019). On the preferential flow patterns induced by transverse isotropy and non-Darcy flow in double porosity media. *Computer Methods in Applied Mechanics and Engineering, 353*, 570-592.

Ziegler, P.A., (1992). North Sea rift system. *Tectonophysics, 208*, 55-75.

Zoback, M., (2007). Reservoir Geomechanics. *Cambridge University Press.*

Section-2
(Articles)

Paper 1

I

Mapping the maturity of organic-rich shale with combined geochemical and geophysical data, Draupne Formation, Norwegian Continental Shelf

James R. Johnson
Jørgen A. Hansen
MD Jamilur Rahman
François Renard
Nazmul H. Mondol

Marine and Petroleum Geology, 2022

Marine and Petroleum Geology 138 (2022) 105525

Contents lists available at ScienceDirect

Marine and Petroleum Geology

journal homepage: www.elsevier.com/locate/marpetgeo

Mapping the maturity of organic-rich shale with combined geochemical and geophysical data, Draupne Formation, Norwegian Continental Shelf

James Ronald Johnson [a,*], Jørgen André Hansen [a], MD Jamilur Rahman [a], François Renard [a,b], Nazmul Haque Mondol [a,c]

[a] Department of Geosciences, The Njord Centre, University of Oslo, P.O. Box 1047, Blindern, NO-0316, Oslo, Norway
[b] ISTerre, Univ. Grenoble Alpes, Grenoble INP, Univ. Savoie Mont Blanc, CNRS, IRD, Univ. Gustave Eiffel, 38000, Grenoble, France
[c] Norwegian Geotechnical Institute (NGI), P.O. Box 3930, Ullevaal Stadion, NO-0806, Oslo, Norway

ARTICLE INFO

Keywords:
Norwegian Continental Shelf
Source rock shale
Upper Jurassic shale
TOC
Maturation
Kerogen
Brittleness
Rock physics
Seismic inversion

ABSTRACT

The evaluation of the interplay between kerogen maturation and total organic carbon (TOC) content within an organic-rich shale is critical to characterizing source rock shale's elastic behavior. We analysed a comprehensive database of twenty-nine well logs, two 3D seismic surveys, and geochemical data of eighteen wells within the Draupne Formation in the Norwegian North Sea. The Upper Jurassic (Kimmeridgian) Draupne Formation Shale is found throughout the Norwegian Continental Shelf and is the primary source, carrier, and seal rock in several oil and gas fields. The dataset explores a broad range of depths (2–5 km), total organic contents (0–20 wt%), and various maturation states ranging from immature to overmature. We study the relationship between rock brittleness and organic content as shale matures. We use calculated values of Young's modulus and Poisson's ratio. Academic and industry-standard cutoffs are applied to both the TOC content and maturation level. We introduce here the Organic Maturation Product (OMP) rock physics template, which incorporates a relationship between organic content and any subsequent maturation. The degree of brittleness or ductility is impacted directly by the kerogen maturation process, with lower TOC content having a dampening effect on the transition towards increasing brittleness. This template allows one to classify rock maturation in nine categories, from low to high maturation, and link these categories to rock geomechanical properties. Seismic inversion of the 3D surveys and mapping utilizing the OMP classification reveal how large-scale depositional environment and subsequent diagenetic events influence both placement and quality of source rock broadly within the basin context of the North Sea.

1. Introduction

The exploitation of unconventional shale reservoirs has driven continued interest in the characterization and understanding of their microstructure and their mechanical and hydraulic properties (e.g., Vernik and Landis, 1996; Sonnenberg, 2011; Ewy, 2019; Ougier-Simonin et al., 2016; Kennedy and Mayer, 2019). A benefit of these efforts has been a greater understanding of shales and the importance they have within conventional and unconventional hydrocarbon plays as both source and seal/cap rocks. The maturation of organic-rich shales results in fundamental variations of their geophysical, geochemical, and petrophysical properties (Prasad et al., 2009; Anders et al., 2014). Further to this, the interaction between the amount of total organic carbon (TOC) content and kerogen maturation will directly impact the organic-rich shale's quality as a source and cap rock (Hansen et al., 2020; Rahman et al., 2020).

The Upper Jurassic (Kimmeridgian) Draupne Formation (Fig. 1b) is a world-class source rock and an effective seal in the Central and Northern North Sea. This formation stretches over a broad range of depths (500–6500 m), thicknesses (0–550 m), TOC, and maturity (NPD, 2021). It provides an ideal candidate to study the interplay between kerogen maturation and TOC content. In the Southern North Sea, the equivalents to the Draupne Formation are the Mandal and Tau Formations, which vary in thickness ranges 1–170 m for the Mandal Formation) and 2–118 m for the Tau Formation. In the Norwegian Sea and the Barents Sea, the equivalents to the Draupne Formation are the Spekk and Hekkingen Formations, which vary in thickness range 1–150 m for the Spekk Formation and 2–190 m for the Hekkingen Formation (NPD, 2021).

* Corresponding author.
E-mail address: j.r.johnson@geo.uio.no (J.R. Johnson).

https://doi.org/10.1016/j.marpetgeo.2022.105525
Received 21 September 2021; Received in revised form 17 December 2021; Accepted 3 January 2022
Available online 6 January 2022

Mapping how the Draupne Formation varies across the Norwegian North Sea is an important task that is made difficult by the size of the basin compared to the number of wells, consistency of the quality of data, and the relative dimension of seismic surveys to the size of the basin. A relationship between maturation and geomechanical properties represented by alterations in brittleness of organic-rich shale has been proven (Prasad et al., 2011; Zargari et al., 2016). Besides, a relationship between TOC content and geomechanical properties has been the topic of many studies, with sometimes contrary conclusions (Grieser and Bray, 2007; Wilson et al., 2017, Mondol, 2018). One group concludes that an increase in TOC correlates to an increase in brittleness (Grieser and Bray, 2007; Wilson et al., 2017), while another group shows that increased TOC correlates to increased ductility (Mondol, 2018). Here, we study the interaction between TOC and kerogen maturation in relationship to seismic velocity and elastic parameters. While the use of correlations between elastic properties and brittleness parameters is debated (Thomsen, 1990, 1996; Holt et al., 2015), it remains a useful tool to approximate geomechanical properties.

Here, we seek to understand how TOC and maturation can vary both in terms of depositional and diagenetic characteristics in the Draupne Formation. To reach this goal, we use mapping of two specific sections of the basin and utilize 3D seismic surveys at different depths and locations. Knowledge of TOC and maturation differences are initially built upon rock physics templates to compare a broad range of well log data in terms of both depth and shale thickness. The dataset is further supported by geochemical data, primarily based upon cuttings analysis of geochemical reports produced by the Norwegian Petroleum Directorate ((NPD, 2021). We introduce a rock physics template called the Organic Maturation Product (OMP) and demonstrate its utility in clarifying the relationship between the net amount of organic content and any subsequent maturation. OMP is also used to characterize the impact of salt diapirism upon maturation.

2. Geological setting

The study area contains structural elements of the Ling Depression, Utsira High, Patch Bank Ridge, and Gudrun Terrace that constitute the main geological structures in the Central North Sea Basin (Fig. 1). Exploration and development in the region have been variable, with more data coming from areas that have had greater economic success. The study area includes the Sleipner Vest and Sleipner Øst fields, providing significantly more data where the study area overlaps with these fields.

Two major rifting events occurred in the Norwegian North Sea (Ziegler, 1992; Faleide et al., 2008). The first rifting event occurred in the Triassic, followed by post-rifting tectonic quiescence. The second rifting event that occurred in the Late Jurassic – Early Cretaceous in the North Sea formed significant structural relief (Whipp et al., 2014). This rifting event, coupled with eustatic sea-level rise, resulted in anoxic, restricted environments. Subsequent uplift and erosion regionally have resulted in lateral variations of sediment thickness across the region, perhaps most significant during the Barremian (Bugge et al., 2001; Isaksen and Ledje, 2001; Faleide et al., 2008; Hansen et al., 2017). Uplift of the Mid-North Sea Dome during the Early Jurassic resulted in subsequent nondeposition in certain areas (Ziegler, 1992; Mannie et al., 2014). Further complicating the geological history, major salt deposition occurred during the Permian in the Norwegian Continental Shelf (Jackson et al., 2010; Rossland et al., 2013). Subsequent passive salt diapirism was shown to impact the structure of the overlying Jurassic-Cretaceous age deposits, including the Draupne Formation around the Utsira High and the Ling Depression (Jackson et al., 2010; Johnson et al., 2021). The salt's thermal properties can significantly alter thermal gradient (Daniilidis and Herber, 2017), which in turn can have an impact on kerogen maturation and the rate of maturation of organic-rich shale (Johnson et al., 2021).

The Draupne Formation within the Viking Group, part of the Upper Jurassic, is an organic-rich shale formation equivalent to the Kimmeridgian Shale in the UK sector. The formation consists of dark grey-brown to black, usually non-calcareous claystone, that is occasionally fissile in nature (NPD, 2021). The mineralogy for the Draupne Formation is dominated by clays and organic matter. The average clay content for the Draupne Formation from these studies, within our study area, is 66 ±

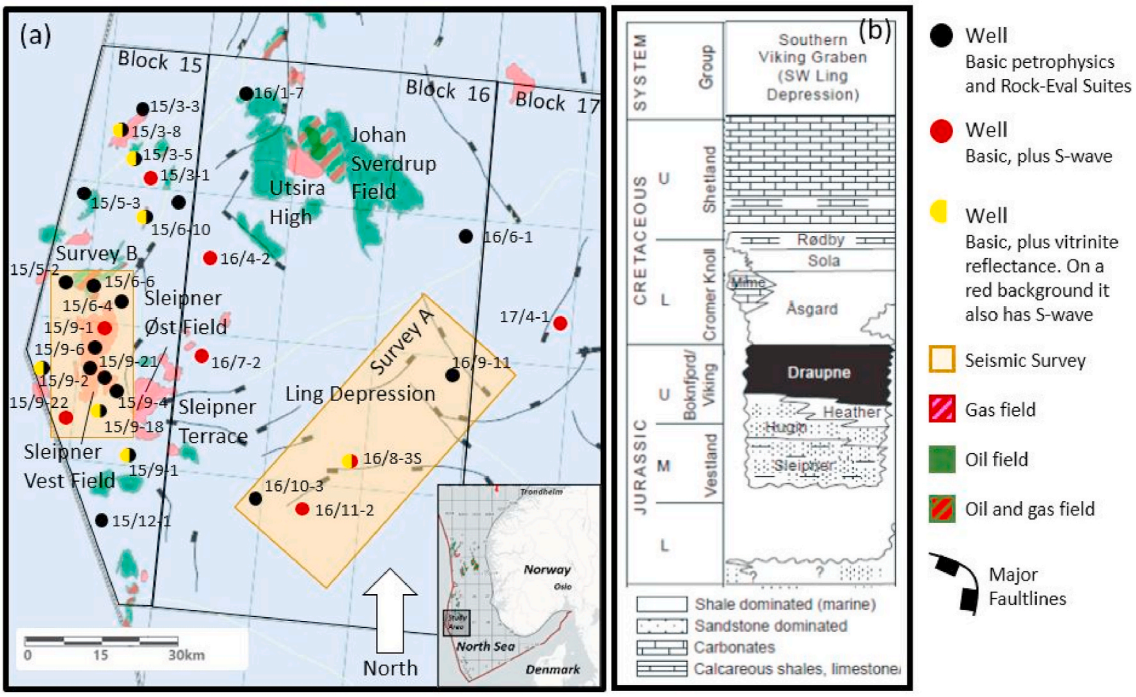

Fig. 1. (a) Map of the study area, including all 29 wells with varying amounts of information, both petrophysical and Rock-Eval suites as defined in the legend, and the locations and relative sizes of the two 3D seismic surveys utilized (Surveys A and B) (b) Stratigraphy of the Draupne Formation and the underlying and overlying formations deposited during the Early Jurassic to Late Cretaceous (modified from NPD, 2021).

4%, the average quartz and feldspar content is 21 ± 5%, and the average carbonate and pyrite content is 13 ± 1% (Kalani et al., 2015; Skurtveit et al., 2018; Nooraiepour et al., 2017; Zadeh et al., 2017; Hansen et al., 2020; Johnson et al., 2021). The total depth range for the Draupne Formation from penetrated well in the Norwegian North Sea is from ~500 to 6500 m depth, while thickness ranges from ~0 to 550 m (NPD, 2021). While TOC can reach upwards of 20 wt% in the Draupne Formation (Løseth et al., 2011), a more typical range is from 2 to 15 wt%. Due to a broad range in depth, TOC richness, and maturity, the hydrogen index (HI) can vary significantly (present study, Hansen et al., 2019). Another characteristic of the Draupne Formation in some regions of the North Sea is intermittent quartz-rich sandstone sections resulting from sporadic debris flows or turbidites that broke up the deposition of the clay-rich sections (Bugge et al., 2001; Isaksen and Ledje, 2001). While the formations Tau, Sauda, Egersund, and Heather also have source rock potential (Fig. 1b), the quality is poorer and significantly more variable (Hansen et al., 2019); as such, they were not included in the present study.

3. Database and methods

Two three-dimensional (3D) seismic datasets, named A and B, have been used alongside a selected database of twenty-nine exploration wells based on the location, depth, and thickness of the Draupne Formation (Fig. 1). The Draupne Formation depth in our study area is ~2.0–5.0 km, while the thickness is 20–800 m (Table 1). Seismic survey A covers a large swathe of the Ling Depression and a portion of the Sele High, while survey B covers a part of the Sleipner Terrace and then extends west towards the Norway-UK maritime border. Survey A is roughly four times the size of Survey B (Fig. 1). Despite the difference in sizes, both datasets provide insight into the Draupne Formation showing regions with large thickness, depth, and maturity variations. Mapping out both surveys also allows for broader depositional and diagenetic trends influencing the Draupne Formation to be inferred.

Well data consisted of both petrophysical well log measurements in addition to geochemical data acquired in the laboratory on rock samples along with the wells (Table 1). All well data contained petrophysical

Table 1
Overview of the twenty nine (29) exploration wells included in the database, the depth and thickness of the Draupne Formation. Well logs and Rock-Eval data available for each well are indicated. Logging data are Kelly Bushing (KB), Gamma Ray (GR), P-sonic (Vp), S-sonic (Vs), Hydrogen Index (HI), Oxygen Index (OI), Temperature Max (Tmax), Vitrinite Reflectance (VR), Production Index (PI), and Total Organic Carbon (TOC).

Well (prospect/ field)	Content	Draupne Top KB (km)	Draupne Thickness (m)	GR	Vp	Vs	Density	Resistivity	Neutron Porosity	HI	OI	Tmax	VR	S2	TOC (measured)
15/3–1 (Gudrun)	Gas/ Cond	3.84	807	X	X	–	X	–	X	–	–	X	X	–	X
15/3-3 (Gudrun)	Gas/ Cond	3.91	208	X	X	–	X	X	X	X	X	X	–	–	X
15/3–5(Sigrun)	Oil	3.70	73	X	X	X	X	–	X	X	X	X	X	X	X
15/3–8 (Gudrun)	Oil/Gas	3.82	222	X	X	X	X	X	X	–	–	–	–	–	–
15/5–2 (Eirin)	Gas	3.64	72	X	X	–	–	X	–	X	X	X	–	–	X
15/5-3	Oil Shows	3.56	135	X	X	–	–	X	–	X	X	X	–	–	X
15/6-4	Dry	3.05	30	X	X	–	–	X	–	X	X	X	–	X	X
15/6-6 (Sleipner Vest)	Gas/ Cond	3.28	20	X	X	–	X	X	X	X	X	X	–	–	X
15/6–10 (Freke)	Gas/ Cond	3.35	36	X	X	X	X	X	X	–	–	–	–	–	–
15/8-2	Dry	3.65	76	X	X	X	X	X	X	–	–	–	–	–	–
15/9–1 (Sleipner Vest)	Oil/Gas	3.27	108	X	X	–	X	X	X	–	–	–	X	–	X
15/9–2 (Sleipner Vest)	Gas/ Cond	3.29	82	X	X	–	X	X	X	X	X	X	–	–	X
15/9–4 (Sleipner Vest)	Gas/ Cond	3.17	147	X	X	–	X	X	X	–	–	–	–	–	–
15/9–6 (Sleipner Vest)	Dry	3.36	230	X	X	–	X	X	X	–	–	–	–	–	–
15/9–11 (Sleipner Øst)	Gas/ Cond	2.66	14	X	X	X	X	X	X	X	X	X	X	X	X
15/9-18	Dry	3.01	105	X	X	–	X	X	X	–	–	–	–	–	–
15/9–21 (Sleipner Vest)	Dry	4.32	269	X	X	–	X	X	X	–	–	–	–	–	–
15/9-22	Dry	3.30	148	X	–	–	–	X	–	X	X	X	X	X	X
15/9-23	Dry	2.86	100	X	X	X	X	X	X	–	–	–	–	–	–
15/12-1	Oil Shows	2.91	23	X	X	–	X	X	X	X	X	X	–	X	X
16/1–7 (Ivar Aasen)	Oil	2.64	171	X	X	–	X	X	X	X	X	X	X	X	X
16/4-2	Dry	2.87	152	X	X	–	X	X	X	X	X	X	–	X	X
16/6-1	Dry	1.90	32	X	X	–	X	X	–	X	X	X	–	–	X
16/7-2	Gas	2.50	89	–	X	–	X	X	X	X	X	X	X	X	X
16/8-3S (Lupin)	Dry	2.50	86	X	X	X	X	X	X	X	X	X	–	X	X
16/9-1	Dry	2.21	169	X	X	–	X	X	–	–	–	–	–	–	–
16/10-3	Dry	2.43	20	X	X	–	X	X	–	X	X	X	–	X	X
16/11-2	Dry	2.06	75	X	X	–	X	X	–	X	–	–	X	X	X
17/4–1 (Vette)	Dry	2.02	95	X	X	–	X	X	X	X	X	X	X	–	X

measurements that include the typical suite of wireline logs such as gamma ray (GR), bulk density (ρ), neutron porosity, resistivity (R), and P-wave velocity (Vp). Among the twenty-nine wells, only seven of them contained S-wave velocity (Vs) data. There was a wide range in the vintages of well logs, ranging from 1967 to 2013, with ~80% of the wells from the 1960s–1990s (NPD, 2021). Sonic logs were de-spiked and filtered to remove and correct for anomalous data points. Additionally, all well logs were checked for artifacts from washouts, casing points, and mud filtrate invasion. Corrections were made where they were required. Finally, all well logs were normalized to determine appropriate ranges and cutoffs. Note, most corrections that were applied occurred outside of the Draupne Formation and therefore had no material impact on the study. Geochemical data were also available through Rock-Eval and optical reflectance measurements for eighteen out of the twenty-nine wells. The amount of data and data type available varied greatly between wells, possibly including Hydrogen Index (HI), Oxygen Index (OI), TOC, S2, T_{max}, and vitrinite reflectance (R_o). Here, S2 represents the amount of hydrocarbons generated through the thermal cracking of nonvolatile organic matter.

Efforts were made to fully utilize the available dataset; however, there were several inherent limitations presented by both the type and quality of data. The seismic datasets allow for the estimation of P-Impedance and S-Impedance; however, angle limitations (~40°) for both datasets prevent the use of density. Further to this, anisotropy information is not available for either seismic cube, which limits the geomechanical interpretations possible for shale with the seismic data (Sayers and Dasgupta, 2019). If well log data available were plentiful, the study would have benefitted from nuclear spectroscopy logs, which could have been used to directly estimate the TOC and mineralogy (Craddock et al., 2019).

The mineralogical composition has an impact on brittleness. In shales, the content of soft components (clay minerals, TOC) and stiff components (quartz, feldspar, carbonate, pyrite) control brittleness (Jarvie et al., 2007; Jin et al., 2014; Alzahabi et al., 2015; Bourg, 2015). The acccumulations of microquartz, which precipitates at around 80 °C, may increase brittleness (Thyberg et al., 2009). Avseth and Carcione (2015) highlight that the presence of calcitic beds interbedded with the Draupne Formation near the Horda Platform would also increase brittleness. On the other side, Bourg (2015) argues that shale behavior will be inherently ductile above a threshold of 34% clay content. With a clay content of ~66%, the Draupne Formation exceeds this threshold, and in Bourg (2015) the Draupne Formation had one of the highest clay contents investigated. While clay mineralogy is of secondary importance to overall mineralogy in terms of brittleness (Rahman et al., 2020), it has been shown that clay mineralogy can have an impact on brittleness and even the behavior of faults (Haines et al., 2009; Soto et al., 2021).

In addition to mineralogy, pore pressure and fluid effects are also known to have an impact on the brittleness of organic-rich shales (Cook, 1999; Nygård et al., 2006). Increases in pore pressure will cause an increase in brittleness (Nygård et al., 2006), which can have an impact on the integrity of a shale formation (Rahman et al., 2020). Maturation transforms brittle kerogen lenses into hydrocarbons (Chauve et al., 2020). The expulsion of fluids will have an impact on the pore fluid pressure in the shale, which is controlled by the rate of expulsion, compared to the ability of the shale to either absorb or expulse the fluid to surrounding formations (Wu et al., 2016). The expulsion of fluids to surrounding formations will be directly impacted by the degree of microfracture creation linked to hydrocarbon expulsion (Chauve et al., 2020).

3.1. Reference rock physics analysis

Rock physics analysis presented here is based on well log data and separated into two basic templates. We selected these templates to investigate the relationship between elastic properties and TOC, as well as influences on maturation. The first template is a crossplot of P-wave velocity with bulk density utilized for both simplicity and consistency. Additionally, the results and the conclusions drawn from these data are the same for this dataset when compared to a P-wave velocity with S-wave velocity crossplot. As a result, we will focus on P-wave velocity with bulk density crossplots. The second template utilized is a cross plot between Young's modulus and Poisson's ratio. Poisson's ratio contains information of P- and S-wave velocities, while Young's modulus contains information on bulk density in addition to the other two. Young's modulus and Poisson's ratio were calculated using Equations (1) and (2) (Zoback, 2007):

$$\upsilon = \frac{V_p^2 - 2V_s^2}{2V_p^2 - 2V_s^2} \tag{1}$$

$$E = \rho V_s^2 \frac{3V_p^2 - 4V_s^2}{V_p^2 - V_s^2} \tag{2}$$

where υ, E, Vp, Vs, and ρ are Poisson's ratio, Young's modulus, P-wave velocity, S-wave velocity, and density, respectively. The two rock physics templates utilize three independent properties: P-wave velocity, S-wave velocity, and bulk density. However, by combining and displaying these three parameters in different ways, one can highlight different rock properties. For example, the cross-plot between P-wave velocity and either density or S-wave velocity is used to differentiate broadly between lithologies (Gardner et al., 1974; Castagna et al., 1985). Poisson's ratio and Young's modulus can be crossplotted in order to investigate the ductility or brittleness of rock (e.g., Perez and Marfurt, 2014). Young's modulus is a proxy for a rock's brittleness, with a built-in assumption that a higher value will correspond to a greater required applied stress to induce a given strain (Fox et al., 2013), while Poisson's ratio describes lateral expansion to axial contraction (e.g., Fjaer et al., 2008). When calculating Young's modulus and Poisson's ratio, one must remember that they are calculated utilizing both P- and S-wave velocities (Equations (1) and (2)). As such, they are not perfect representations of their laboratory counterparts (Thomsen, 1990, 1996).

Further to this, brittleness in itself is a broadly defined term (Holt et al., 2015). Jarvie et al. (2007), among others (Glorioso and Rattia, 2011; Jin et al., 2014; Alzahabi et al., 2015) relate brittleness to mineralogy directly (MBI), utilizing variations on the equation:

$$\mathrm{MBI} = \frac{\mathrm{Qtz} + \mathrm{Carb} + \mathrm{Fsp} + \mathrm{Py}}{\mathrm{Qtz} + \mathrm{Carb} + \mathrm{Fsp} + \mathrm{Py} + \mathrm{Cly} + \mathrm{TOC}} \tag{3}$$

where Qtz is quartz (wt%), Carb is carbonate (wt%), Fsp is feldspar (wt %), Py is pyrite (wt%), Cly is total clay (wt%), and TOC is total organic carbon (wt.%). MBI ranges between 0 (ductile) to 1 (brittle) and increases with increasing brittleness. As previously stated, mineralogy data are not available for many wells in our study area. However, the MBI range given by bulk mineralogy analysis from other studies within the area (Kalani et al., 2015; Skurtveit et al., 2018; Nooraiepour et al., 2017; Zadeh et al., 2017; Hansen et al., 2020; Johnson et al., 2021) is confined to 0.18–0.28 based on Equation (3). This confirms that the Draupne Formation would be considered ductile utilizing this method, and that it would plot within a narrow window for the study area.

An alternative definition for brittleness is based on elastic properties (EBI), utilizing calculated values of Young's modulus and Poisson's ratio. Grieser and Bray (2007) provide an empirical equation for this approach:

$$\mathrm{EBI} = \frac{1}{2}\left[\frac{E - E_{min}}{E_{max} - E_{min}} + \frac{\nu - \nu_{max}}{\nu_{min} - \nu_{max}}\right] \tag{4}$$

where E is the static Young's modulus, E_{max} is 69 GPa, E_{min} is 0 GPa, ν is the static Poisson's ratio, ν_{max} is 0.5, and ν_{min} is 0. Also, the higher the EBI value is, the more brittle the caprock is. Given data availability, and the nature of the dataset, the present study focuses on the elastic approach to brittleness. Therefore, we use the template provided by

Perez and Marfurt (2014). This template has been widely utilized in geomechanical studies (e.g., Gray et al., 2012; Johnson, 2017; Hansen et al., 2020) and applied to shale reservoirs, caprocks, and seals alike.

This template was calculated for the eighteen wells where Vs data were not available. A comparison was made between Castagna et al. (1985) empirical method and an empirical relationship between Vp and Vs. While both methods are imperfect, based on a blind well test, the empirical relationship estimated purely from Vp was more accurate and therefore used for the present study. However, it was only utilized as a point of comparison to the seven wells with available Vs data and as an independent verification against the two seismic inversion's results. Thereby, the Z-axis is used on both of the rock physics templates to investigate how the rock properties vary with depth, temperature, porosity, and TOC content, respectively. Porosity and depth were taken directly from the well logs. Temperature (°C) was taken from recorded bottom-hole temperatures (BHTs) and then extrapolated for all of the data points based on a depth-temperature curve established from all of the wells (Equation (5)) with a high R^2 value of 0.9.

$$T = 0.031d + 20.8 \tag{5}$$

where T is temperature measured in degrees Celcius and d is depth measured in meters. Temperature is not Horner (1951) corrected, as the data required to do so are rarely available. However, it appeared to confirm the trend established where data were available. TOC was calculated in various ways and compared for the results that best match the laboratory values of TOC. The ΔlogR method utilizes sonic and resistivity logs (Passey et al., 1990, 2012), while both Schmoker and Hester (1983), as well as Vernik and Landis (1996), proposed density-based methods. Further to these, Heslop (2010) proposed a method that utilizes gamma ray and deep resistivity logs. While all methods matched the data well, we found that the density-based approach by Schmoker suited the results best. A high R^2 value of 0.95 was found between the calculated and measured data.

3.2. Seismic inversion workflow

The seismic datasets were all processed prior to receiving them, and we inspected them to ensure they matched the criteria for successful seismic inversion (Yilmaz, 2001). Both Hampson-Russell and Jason Geoscience Workbench softwares were used for the inversions. Survey A is post-stack data, while Survey B is pre-stack data. For both seismic surveys, velocity models were created or improved upon utilizing sonic curves and Vertical Seismic Profiles (VSPs). Improving the velocity models was assisted in part by confirming horizons with an extensive 2D seismic line network. The velocity models were later improved through the horizon picks and the well-ties as part of the seismic inversion process. The 3D seismic datasets show a variation in depth and thickness. Both datasets had sufficient seismic coverage (i.e. frequency range, fold) for the Draupne Formation. The processing for both seismic cubes was completed to preserve amplitudes and was consistent with what is required for post- and pre-stack inversion and amplitude versus offset/angle (AVO/AVA) analysis (Yilmaz, 2001). Analysis of frequency content for both cubes revealed similar qualities, with frequency ranges from 4 to 70 Hz. Seismic artifacts, which can be due to either acquisition or processing, correspond to coherent anomalies (Galbraith and Hall, 1997; Marfurt and Alves, 2014). They were identified and removed where possible. Cross-equalization of the surveys was carried out to compare the two surveys (Rickett and Lumley, 1999; Baytok and Pranter, 2013). Wavelet equalization was not critical as a comparison between wavelets in the two datasets revealed no major deviation in the reflective character of the Draupne Formation.

After a rock physics review of the well logs, a critical step for successful inversion, one can proceed with the inversion itself. A three term, Aki-Richards, constrained sparse-spike inversion (CSSI) was utilized for this study as it sets the correct absolute impedance range but does not depend directly on the impedance log information (Russell, 1988; Duenas, 2014). The objective function (Equation (6)) for CSSI outlines the core constraints that the user attempts to minimize. For the most accurate representation of the subsurface model, it is best if the inversion relies on the fewest number of free parameters as possible because of the non-uniqueness inherent to the problem (MacFarlane, 2014).

$$\mathrm{F}(V_p, V_s, \rho) = \sum \left(F_{seismic} + F_{contrast} + F_{trend} + F_{spatial} + F_{SVD} + F_{Gardner} + F_{mudrock}\right) \tag{6}$$

where each term represents a misfit function that has been calculated for each seismic trace as a function (F) of the three basic parameters that result from seismic inversion: P-wave velocity (V_p), S-wave velocity (V_s), and bulk density (ρ). Specifically, $F_{seismic}$ controls the seismic residuals, $F_{contrast}$ ensures the solution is sparse by controlling the parameter variance, F_{trend} stabilizes the frequencies related to the trend, $F_{spatial}$ controls the smoothness of the output, F_{SVD} (singular value decomposition) stabilizes the inversion, $F_{Gardner}$ constrains the density, and $F_{Mudrock}$ constrains the S-wave velocity component. Note, accurate Gardner and mudrock trends (Gardner et al., 1974; Castagna et al., 1985) are critical inputs and part of why the rock physics templates used here were chosen. Joint facies-impedance inversion which uses local, facies dependent depth trends (Kemper and Gunning, 2014; Somoza et al., 2015) and supervised machine learning derived depth trends (Yenwongfai et al., 2019) were not investigated here. Joint-facies-impedance inversion updates the low-frequency model through an iterative approach resulting in optimized facies models and elastic properties (Kemper and Gunning, 2014). Supervised machine learning, while relatively new is an approach being further investigated in the literature (Yenwongfai et al., 2019).

A low-frequency model accomplishes two critical goals (1) it accurately represents the well data, and (2) it accounts for the missing low-frequency information not present in the seismic data (Kumar and Negi, 2012). A simple low-frequency model was used with five different methods tested within the software Jason Geoscience Workbench: inverse distance weighted, locally weighted, triangulation, natural neighbor, and global kriging. Global kriging uses a linear combination of weights applied to known data based on a model of spatial correlation, in which the global mean frequency is based on all of the control points (Sheriff, 2002). Well tie and wavelet estimation were carried out for all wells within both surveys. An inverse wavelet, typical for the North Sea (Cox et al., 2020), with a phase of 180° was found for all wells. The time-depth relationships for each well-tie showed little variation suggesting no major alterations due to the stretch-squeeze process. A comparison of seismic data with synthetic traces reveals a strong correlation suggesting reliable seismic inversions for both surveys. Signal-to-Noise Ratio (S/N) was shown to be high for all stacks suggesting good seismic quality. Key parameters for the inversion (Equation (6)) and the rock physics review are shown in Table 2. After initial data

Table 2
Overview of inversion parameters for both 3D seismic surveys. SVD is singular value decomposition.

Parameter	Survey A (value)	Survey B (value)
Window	Draupne FM	Draupne FM
Gardner Slope	0.30	0.30
Mudrock Slope	0.86	0.86
Contrast misfit P-Impedance uncertainty (%)	1	1
Contrast misfit S-Impedance uncertainty (%)	5	5
Contrast misfit Density uncertainty (%)	10	10
Seismic misfit S/N ratio average	18	12
Relative SVD threshold (%)	1	1
Wavelet scale factor	1	1
Merge cutoff frequency (Hz)	4	4

quality control, the workflow for the seismic inversion is shown in Fig. 2.

Finally, the most critical external review is a blind well test, which compares how well the inversion predicts the seismic wave velocities and elastic properties of a well that has not been included in the inversion process. To do this test, we extracted a pseudo-well at the same location as the blind well from the inversion results. In turn, the pseudo-well results were crossplotted with the actual elastic properties from the blind well. An improvement upon this method included pseudo-wells at the same location as the wells involved in the inversion process, in addition to the blind well (Fig. 3). A comparison of all of these results, with a good correlation, was indicative that the petrophysical and seismic inversion results mirror one another. A significant improvement resulted for the S-Impedance, while P-Impedance slightly degraded.

3.3. Quantity of organic material and maturation thereof (organic maturation product)

We have obtained maturation trends by utilizing geochemical data. These data also provided baseline knowledge of the source rock shales and the hydrocarbon therein, including kerogen type and organic content variations. Note that while there is usually an abundance of points taken for the whole well from cuttings, focusing solely on the Draupne Formation severely cuts the number of potential data points per well. Vitrinite reflectance (R_0) data provides the best proxy for maturation (Tissot and Welte, 1984) where available. However, there were fewer initial datapoints for vitrinite reflectance (R_o) available within our study than there were for other data types, including but not limited to Hydrogen Index, TOC, and T_{max}. This is not an uncommon problem with Rock-Eval datasets, especially for the North Sea (NPD, 2021; Sadeghtabaghi et al., 2020). Subsequently, the limited numbers of vitrinite reflectance data were further reduced due to the high uncertainty values present in some of our samples. Also, geochemical data were quality controlled with the specific intention of culling maturity data with low TOC (<2 wt %) or low S2 values (<5 mg HC/g rock) for the calculations with T_{max}, HI, and OI as they are not representative of the Draupne Formation as a whole. Here, S2 represents the amount of hydrocarbons generated through thermal cracking of nonvolatile organic matter. Despite these uncertainties, crossplotting of depth and vitrinite reflectance provided insight into the maturation level. Vitrinite reflectance can be quantified, where there are fewer data points, with the interpretation of hydrogen index (HI) versus TOC. While crossplotting hydrogen index (HI) and T_{max} can provide insight into maturation, one can also confirm kerogen type with this plot (Banerjee et al., 1998). Finally, kerogen type can also be investigated using cross-plots of S2 versus TOC (Espitalie et al., 1985).

A linear relationship can be identified between maturation and depth, with an R^2 value of 0.73 (Fig. 4). The empirical relationship that correlates depth (d) in meters with vitrinite reflectance (R_o) for this region is given by:

$$R_0 = \frac{d}{6181.2} + 0.04 \tag{7}$$

where vitrinite reflectance is represented as a mean R_0 value based on all vitrinite particles measured for a given sample, and depth is represented in meters. However, recognizing that the slope of the trendline within a linear system was different depending on the depth provided the opportunity to view it as potentially exponential. The analysis indicates that an exponential relationship, representative of the chemical kinetics of thermal maturation, may better fit the empirical data. The value of R^2 for the empirical exponential law relationship is 0.82, while the empirical relationship is as follows:

$$R_0 = e^{\left(\frac{d}{3921.4} - 1.41\right)} \tag{8}$$

While the relationship between vitrinite reflectance and depth (Fig. 4) shows that our estimate is close to the regional trend (Baig et al., 2019), it is also true that both for the study area and within the Norwegian North Sea vitrinite reflectance data can be limited. So while a clear trend exists, due to the limited number of vitrinite reflectance datapoints and the quality thereof, the estimation of vitrinite reflectance utilizing a crossplot of hydrogen index (HI) with measured TOC from Vernik and Landis (1996) is used for this study. The trendlines are best representative of type II and III kerogen (Vernik and Landis, 1996), which this dataset predominantly contains, discounting some data from well 15/9–11 and limited data from well 15/3–1. First, the results were

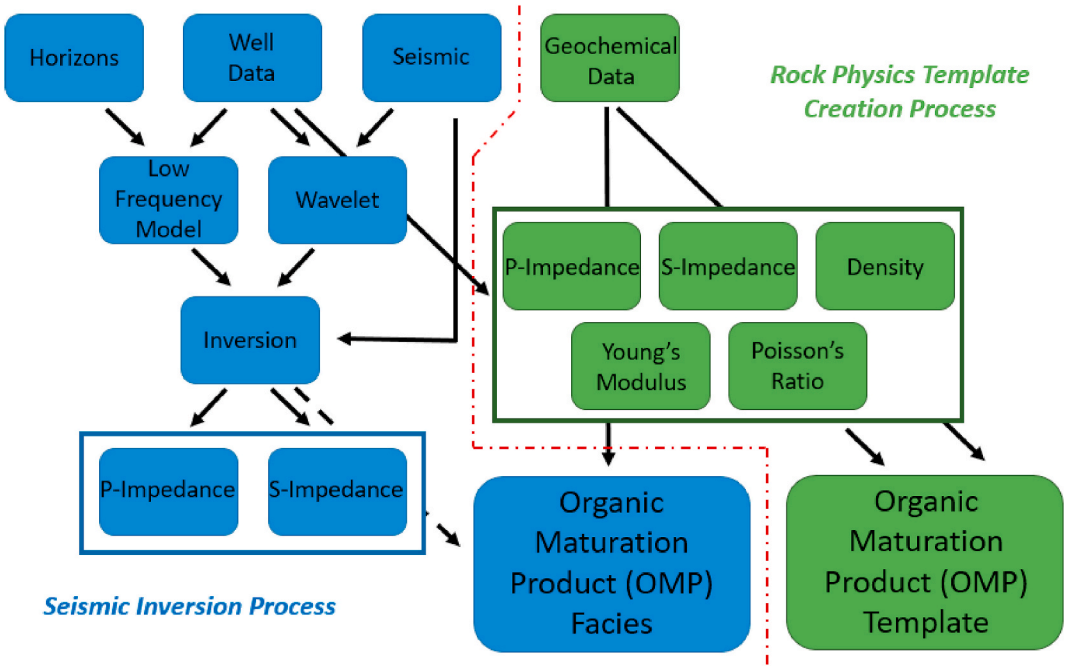

Fig. 2. Workflows implemented for the seismic inversion (blue) and for the creation of the Organic Maturation Product (OMP) rock physics template (green) that describes the relationship between seismic velocities and elastic parameters that accounts for geochemical data.

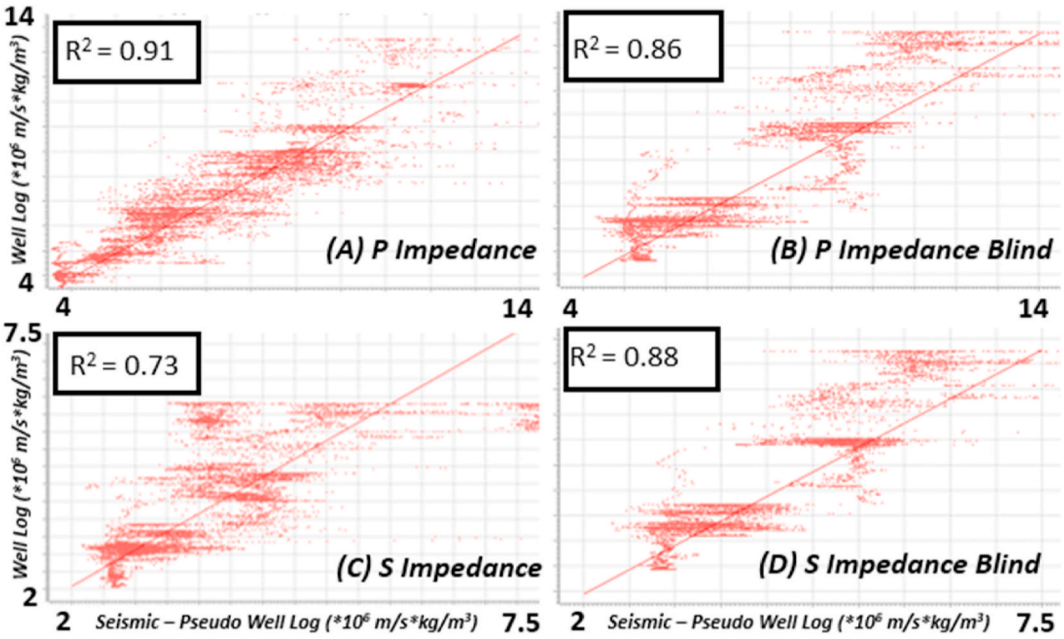

Fig. 3. Seismic and well log comparison with and without blind wells. A comparison of impedance calculated from well logs (y-axis) and pseudo-logs (x-axis) extracted from Survey B shows strong correlations between them for both P-Impedance (a) and S-Impedance (c). A comparison with a blind well is calculated as an additional quality check, revealing a comparably good correlation for P-Impedance (b) and S-Impedance (d).

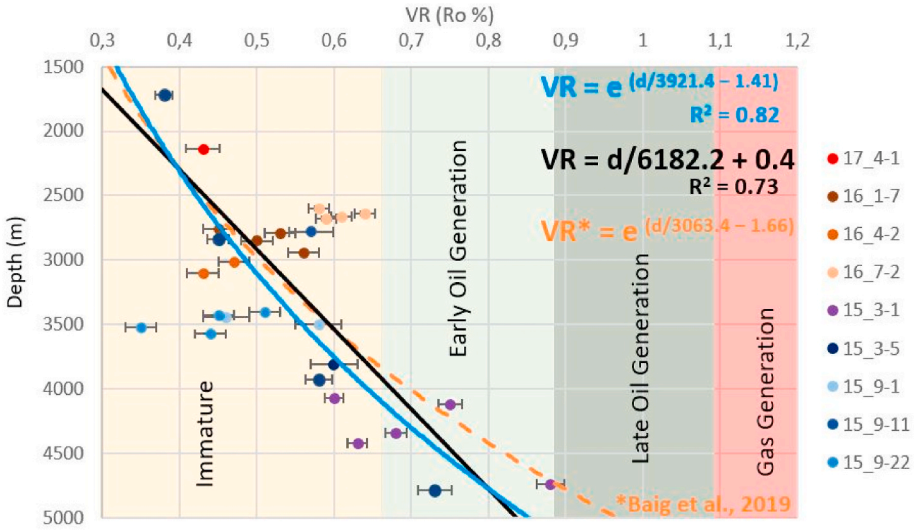

Fig. 4. Crossplot of depth (m) versus vitrinite reflectance (Ro %) showing a relationship between maturation and depth for the study area with three different trendlines applied. The blue trendline shows the relationship as an exponential function, while the black trendline shows it as a linear trend. The green dashed trendline shows the relationship from Baig et al. (2019) which was based on an extensive study on the Norwegian North Sea. (For interpretation of the references to color in this figure legend, the reader is referred to the Web version of this article.)

divided into three categories with regards to TOC, low (<2 wt %), medium (2–5 wt %), and high (>5 wt %). Utilizing the vitrinite reflectance trendlines, the data were further classified into immature, early mature oil generation, late mature oil generation, and gas generation. Table 3 summarizes the combinations of these categories.

The TOC (wt %), to a large degree, determines the potential quantity of expelled hydrocarbon. Low TOC, or low potential hydrocarbon, was determined to be 2 wt% based on accepted industry and academic standards (Kuuskraa et al., 2013; Cooke, 2014; Steiner et al., 2016). Where there is a deviation from this number, it remains ±0.5 wt%. Regionally, Hansen et al. (2019) established that a significant amount of the source rock for the Draupne Formation and surrounding source rocks have a TOC ranging from 5 to 12 wt%. TOC above 5 wt % is considered to be top tier by Beaumont and Foster (1999). Here, it was considered that 5 wt% defines the cutoff between medium TOC and high TOC. While rocks with higher TOC have greater hydrocarbon potential, this parameter does not alone guarantee hydrocarbon expulsion. Maturation, as defined through its proxy vitrinite reflectance, is another control parameter of expulsion. The trends established by Vernik and Landis (1996) were used to estimate vitrinite reflectance values, which were in turn, used to define if hydrocarbon expulsion occurred.

Seismic facies were produced based on the Organic Maturation Product (OMP) facies. To do this, two distinct, discrete background models were created utilizing Bayesian theory to generate probability volumes from the inversion results (Pendrel et al., 2006). The first discrete model separated TOC into the three distinct classes discussed above. The second discrete model separated maturation, as vitrinite reflectance was estimated from the crossplot of hydrogen index and TOC, into the four classes discussed above. In order to combine them, we took the product of TOC as a discrete model and its maturation as a discrete model, i.e., the Organic Maturation Product (OMP), as shown in Table 3 and represented in Equation (9).

Table 3
The Organic Maturation Product (OMP) facies contains nine classes defined based on two components, TOC and maturation, as estimated using vitrinite reflectance (VR).

Organic Maturation Product Facies	Total Organic Carbon (TOC wt.%)	Vitrinite Reflectance (VR % Ro)
Low TOC	<2	–
Medium TOC, Immature	2–5	<0.5
Medium TOC, Early Oil Generation		0.5–0.75
Medium TOC, Late Oil Generation		0.75–1.3
Medium TOC, Gas Generation		>1.3
High TOC, Immature	>5	<0.5
High TOC, Early Oil Generation		0.5–0.75
High TOC, Late Oil Generation		0.75–1.3
High TOC, Gas Generation		>1.3

$$OMP = TOC_{discrete\ model} * Maturation_{discrete\ model} \quad (9)$$

Discrete models create a relationship between calculated elastic properties, in this case, P-Impedance and S-Impedance, and other calculated rock properties. The other calculated rock properties here are TOC and maturation, which have cut-off values assigned based on industry and academic standards as previously discussed. Prior probabilities were then calculated for each discrete model's different components for both seismic Surveys A and B based on the well logs. Finally, probability distribution functions (PDFs) were used to separate the components of each discrete model in a crossplot of P-Impedance and S-Impedance. Fig. 5 displays an example of the product of this workflow, where data in well 15/9–18 have been classified into its discrete components TOC and maturation. The result, the Organic Maturation Product, for well 15/9–18 can be seen overlaid onto the Organic Maturation Product of seismic traces from Survey B around that well. The result is a classification of rock maturation property into nine different classes and provides a way to characterize better the interaction between TOC and maturation in organic-rich shales. Additionally, the mapping of the OMP allows one to investigate depositional and diagenetic impacts simultaneously.

4. Results

The results of our investigation are based on geochemical analyses, rock physics relationships, seismic inversion signatures, and the derived seismic facies. For both simplicity and consistency, our study focuses on two rock physics models. P-wave velocity and density data have approximate ranges of ~2.2–3.6 km/s and ~2.3–3.0 g/cm^3. Poisson's ratio and Young's modulus, calculated from these two basic parameters and S-wave velocity, have a range of ~0.2–0.4 and ~10–80 GPa. In an X–Y plot, Gardner and mudrock slopes (Gardner et al., 1974; Castagna et al., 1985), key inputs to the seismic inversion, are calculated utilizing rock physics modeling and are 0.3 and 0.86, respectively, for the organic-rich shale portion of the Draupne Formation. For Gardner slope estimation, the X–Y plot is density-Vp, and for mudrock estimation, the plot is Vs-Vp. Comparisons of the organic maturation product, as seismic facies, with the seismic inversion results is instructive because there is an effect of both TOC content and maturation on seismic inversion parameters, i.e., P-Impedance, S-Impedance, and Poisson's ratio.

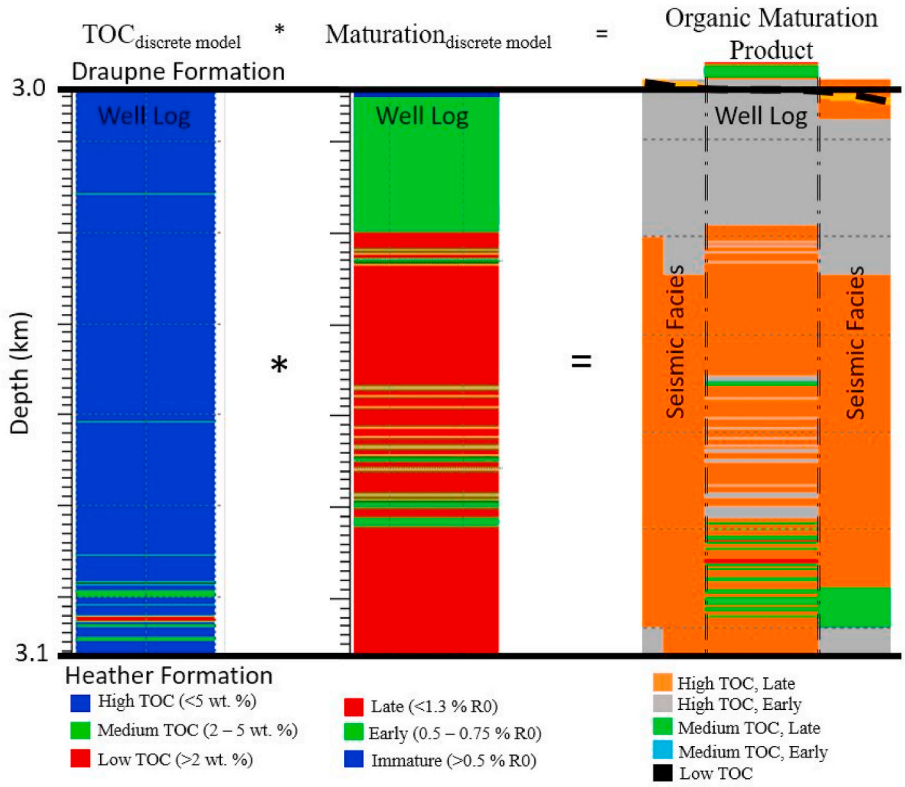

Fig. 5. TOC discrete model (left column) and maturation discrete model (middle column) for well 15/9–18, with the resulting Organic Maturation Product, OMP (right column). The corresponding seismic facies (3D seismic Survey B) is indicated for the well sitting on the background in the right column. TOC is separated out into low, medium, and high values. Maturation is separated out into immature, early oil generation, and late oil generation. A higher spatial resolution is present for the well log data than for the seismic data, and therefore more details are represented in the well log data. Considering the difference in spatial resolution, the background trend is consistent between the well log and the seismic data.

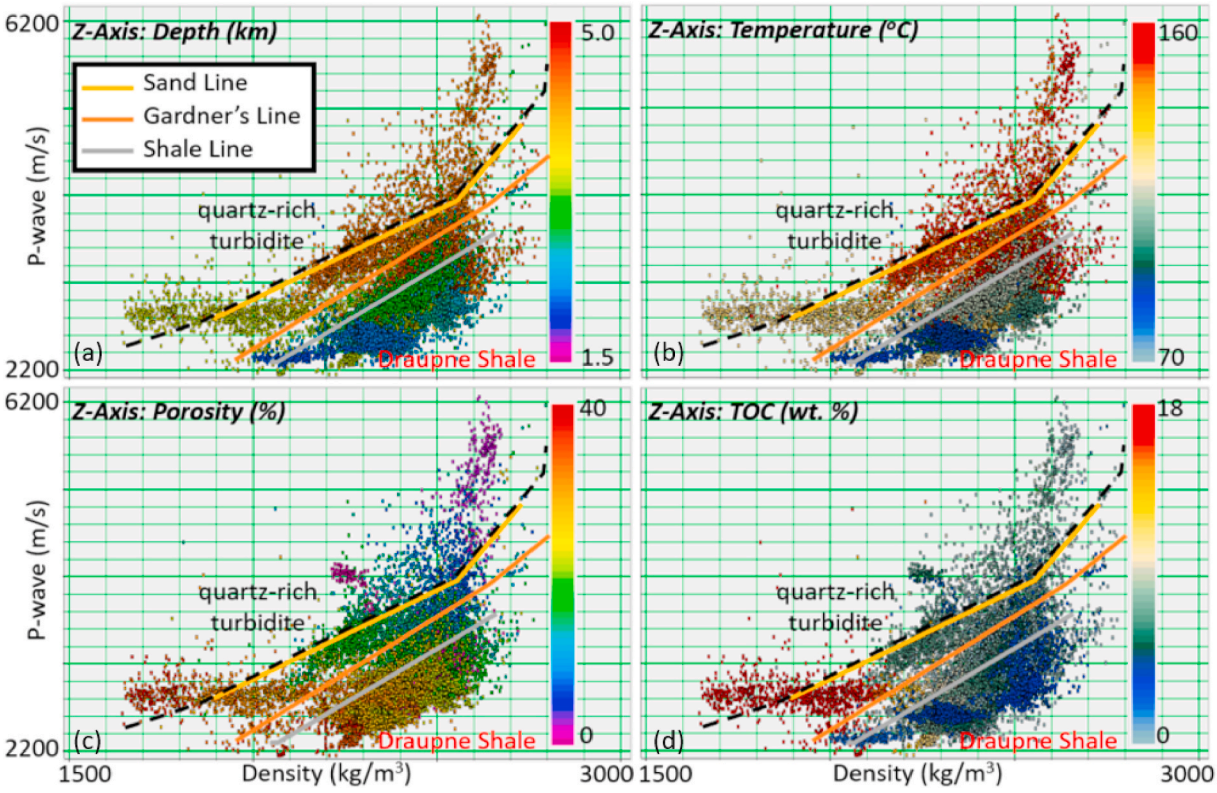

Fig. 6. Four parameters on a P-wave velocity versus density rock physics template. P-wave velocity and density in Draupne shale rocks are crossplotted with depth (a), temperature (b), porosity (c), and TOC (d). Averages for sand and shale facies are shown in yellow and grey, respectively, with Gardner's relationship in orange (Gardner et al., 1974). Data above the sand line (yellow) show quartz-rich intra-Draupne turbidites, while data below the shale line (grey) correspond to extremely clay-rich Draupne shale. Between these two lines, data contain shales with varying amounts of quartz content. In this study, data points located above the black dashed line are related to quartz-rich intra-Draupne turbidites, for which the TOC content values are meaningless in plot (d). (For interpretation of the references to color in this figure legend, the reader is referred to the Web version of this article.)

4.1. Rock physics analysis

A clear link exists between depth and elastic properties, wave velocities, and density (Fig. 6a). The increase in bulk density and V_p is likely due to compaction with depth. An inspection of the data utilizing the rock physics template proposed by Perez and Marfurt (2014) for geomechanical studies shows a relationship between depth and mechanical properties where shallower rocks are more ductile in nature than deeper rocks (Fig. 7a). However, data confirm that depth alone does not explain the mechanical properties of the rock (Fig. 7a). The Gardner relationship shows a separation between the organic-rich shale from the turbiditic quartz-rich sequences (Fig. 6). Averages for quartz-rich rocks and clay-rich rocks are located above and below the Gardner relationship, respectively. Any values for TOC above the sand line (Fig. 6d) must be strictly ignored as TOC is not present in the quartz-rich sequences. It can be seen that the average depths of the quartz-rich turbiditic sequences are typically deeper than that of the organic-rich shales. However, there are some shallow quartz-rich sections as well (Fig. 6a). Organic-rich shales make up a larger portion of this dataset, with more variable depths than the turbiditic sequences.

Similar to the increase in depth, a general rise in temperature relates to the increase in P-wave velocity and density (Fig. 6b). The clay-rich rocks in the data set cover a substantial range of temperatures from ~70 to 160 °C. These significant ranges of temperatures were seen for all the seismic wave velocities with high clay content (Fig. 6b). Overall temperatures tended to be higher for the turbidites than the organic-rich shale. While this effect may be partly attributed to quartz-rich rocks transmitting heat better than clay-rich rocks, as demonstrated experimentally by Robertson (1988), the dominant influence is likely the typical thermal trends with depth.

An inverse relationship exists between porosity and P-wave velocity (Fig. 6c), where shallower rocks tended to have higher porosity values. Porosity also tends to have an inverse correlation with both temperature and depth due to overriding compaction trends (Fig. 6c). However, the data show a smaller range of porosity for the clay-rich shale despite a larger range for both depth and temperature (Fig. 6c). Nonetheless, a deviation from this effect is clearly shown for the Draupne Formation over an extensive range of depths within a dataset (Fig. 7c). Both the highest and lowest porosity rocks are ductile, while a range between these can be classified as being increasingly brittle. A closer inspection of the dataset shows that the orientation of the porosity crosscuts the rock physics template describing the mechanical nature of the rock.

The relationship between TOC and seismic wave velocity properties is more complex, although trends are still present (Fig. 6d). Clear local variations are present within TOC compositions. This varied from all of the other trends, which are readily seen utilizing the Vp-density rock physics template (Fig. 6a–c). However, a comparison between depth and TOC for the Vp-density plots does reveal that higher values of TOC tend to be present for shallower portions of the Draupne Formation. This can also be seen on Young's modulus-Poisson's ratio crossplot (Fig. 7d). Isaksen and Ledje (2001) separated the Draupne formation into Upper and Lower sections, showing that the Upper section had a tendency to be more TOC-rich. This means that both regionally and locally, rocks tend to be more TOC-rich when shallower. The key to the more precise separation of TOC within the elastic parameters is the S-wave component present in both Poisson's ratio and Young's modulus (Fig. 7d), as shown by a comparison of the two rock physics templates.

The rock physics template used for geomechanical studies shows a porosity-dependent relationship between TOC and the mechanical behavior of the material. Specifically, there is a general trend wherein

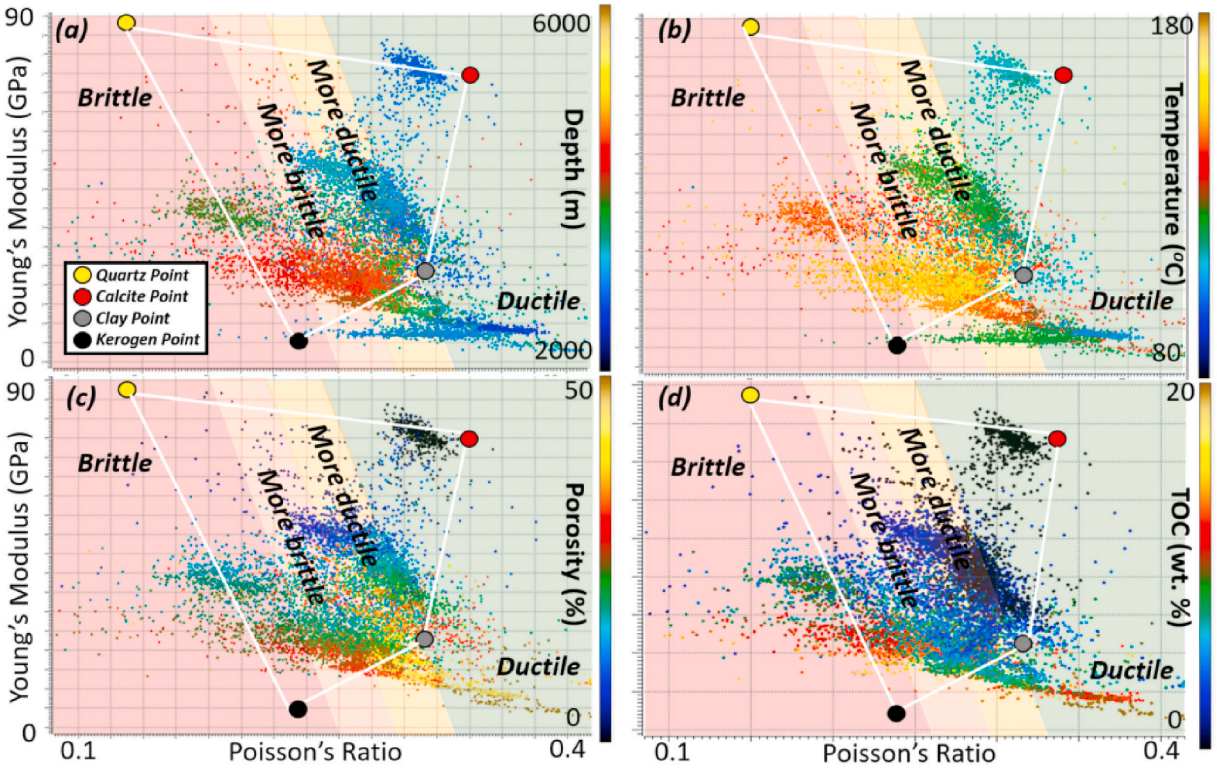

Fig. 7. Four parameters on Young's modulus versus Poisson's ratio rock physics template. Young's modulus and Poisson's ratio in Draupne shale rocks with depth (a), temperature (b), porosity (c), and TOC (d). The separation of the rock into regimes ranging from ductile to brittle (Perez and Marfurt, 2014) is overlain. Points representative of different materials (quartz, calcite, clay, kerogen) have also been overlaid (Mondol, 2018).

higher TOC correlates to more brittle behavior (Fig. 7d). However, TOC-rich shale can behave more ductile if it also has higher porosity (high values of ν, low values of E; Fig. 7c and d). Therefore, the relationship between TOC and its mechanical behavior is best considered with knowledge of porosity values.

Fig. 7b shows a generally positive trend between increasing

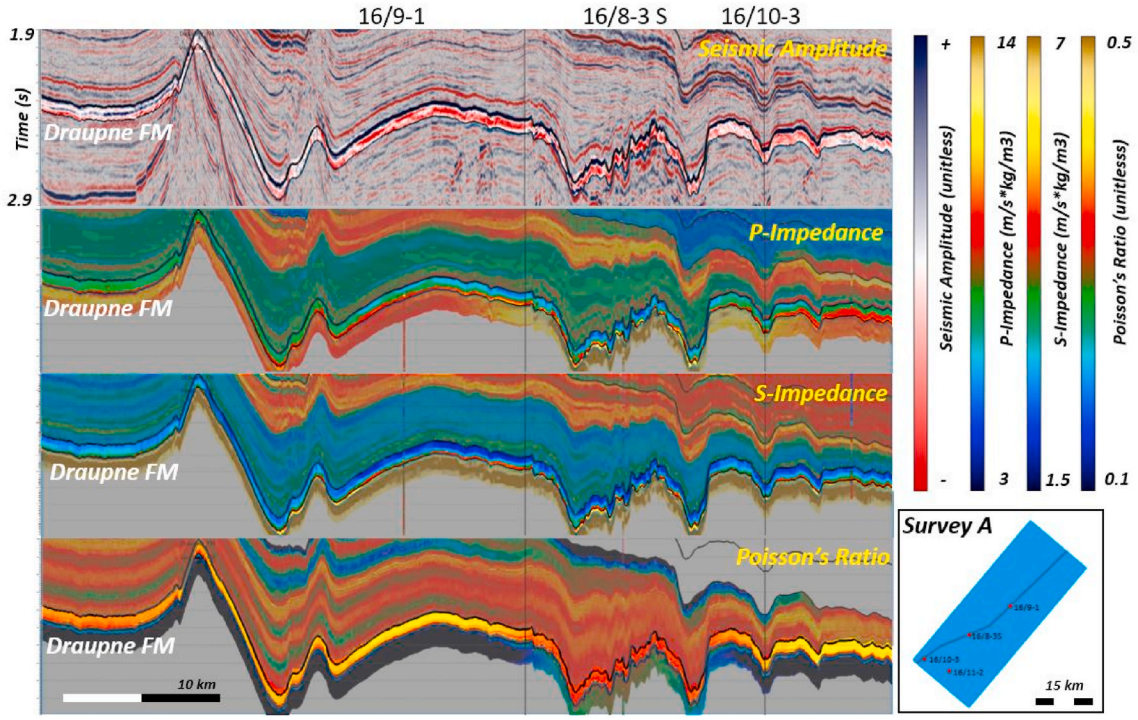

Fig. 8. Comparisons of seismic data with P-Impedance, S-Impedance, and Poisson's ratio with a focus on the Draupne Formation (layer with brighter colors), along a cross-section extracted from an arbitrary profile in Survey A shown in the bottom right inset. (For interpretation of the references to color in this figure legend, the reader is referred to the Web version of this article.)

temperature and brittleness, as expected, however here too, exceptions exist. Specifically, it can be noted that both depth and temperature trends show TOC-rich shale that is increasingly more brittle than their TOC-poor counterparts at similar depths and temperatures (Fig. 7a, b, and d). Finally, it should also be noted that salt intrusions have been shown to significantly alter the thermal gradient (Daniilidis and Herber, 2017) where present and that salt intrusions are clearly visible around Survey A (Fig. 8).

4.2. Mapping rock properties utilizing seismic inversion

Since our dataset includes two 3D seismic volumes, it is possible to map two distinct sections of the basin in terms of depth, temperature, and maturation. While a time-depth conversion of the seismic dataset is beyond the scope of this study, well logs place the Draupne Formation for Survey A at a range of depths of ~2000–2600m. Based on well log data, the depths of the Draupne Formation for Survey B have a range of ~3200–3800m. Rock physics templates show a positive correlation between depth and temperature suggesting ranges of ~82–101 °C and ~119–138 °C for Survey A and B, respectively. However, the temperature range can have a deviation as large as 25 °C higher due to salt intrusions from the background trend (Daniilidis and Herber, 2017). Seismic inversion results included the original amplitude volumes and the seismic inversion derivative volumes of P-Impedance, S-Impedance, and Poisson's ratio. While 3D volumes of Young's modulus can also be created, they were not included here as they rely upon having well-interpreted density results in addition to P-wave and S-wave velocity seismic data sets.

Within Survey A, the Draupne Formation generally appears to have one interface within the formation, as seen on the seismic data. Salt diapirs are present around the formation in two areas towards the shallower section of the arbitrary cross-section, as marked by the dashed outlines (Fig. 8). The P-Impedance and S-Impedance seismic datasets revealed that the Draupne Formation could be classified into upper and lower layers, where the lower layer has significantly higher impedance values. While the Draupne Formation has lower impedance values than both the overlying Åsgard Formation and the underlying Vestland Group, the transition is sharper with the latter. The difference between impedance values is consistent with lithological variations, confirmed by both core and well log analysis. However, the variation in impedance values internal to the Draupne Formation cannot be lithological or mineralogical, as Hansen et al. (2020) showed that disparate data geographically within our study area share the same portion of a mineralogical ternary diagram. Poisson's ratio could not separate the two layers; however, it shows where the Draupne Formation stands mechanically different from the surrounding layers.

For Survey B, the 3D seismic dataset indicates two clear interfaces for the Draupne Formation. Both P-Impedance and S-Impedance results reveal a more complex picture than for Survey A (Fig. 9). The impedance volumes extracted show that the Draupne Formation separates into three layers instead of the expected two layers in this part of the basin. The bottom and top layers typically have lower values of impedance than the central layer, whose values best mimic the overlying Åsgard Formation or underlying Heather or Hugin Formations. While it is known that the impedance differences between formations are lithological, the extreme contrast between values could be indicative of a lithological difference due to the intra-Draupne turbiditic sands. Both well log analysis and core photos available support the interpretation that the central layer is a quartz-rich turbiditic sequence for some of those wells in Survey B. Interestingly, within the Draupne Formation, the impedance trends for Survey B are opposite of those for Survey A. The higher impedance values are in the upper Draupne Formation, as opposed to the lower Draupne Formation. It was difficult to separate the Poisson's ratio into different sub-layers of the Draupne Formation, likely due to similarly low values for both the P-Impedance and S-Impedance data. A comparison of the two 3D seismic datasets revealed that while impedance data have similar values, there is a marked change in the Poisson's ratio with a decrease from Survey A to Survey B (Figs. 8 and 9). Based on established rock physics trends, this would indicate that the deeper Survey B is generally more brittle.

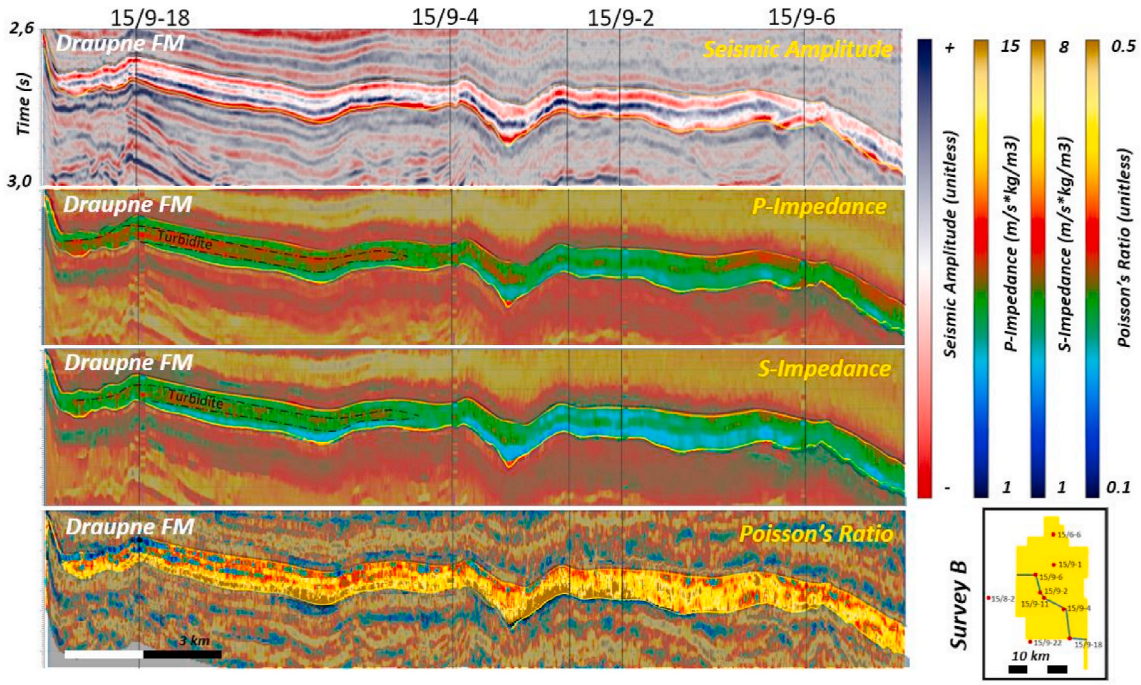

Fig. 9. Comparisons of seismic with P-Impedance, S-Impedance, and Poisson's ratio with a focus on the Draupne Formation (layer with brighter colors), along a cross-section extracted from an arbitrary line in Survey B. Interlayered turbidite highlighted by significantly different impedance values are outlined with a black dashed line in the P-Impedance and S-Impedance panels. (For interpretation of the references to color in this figure legend, the reader is referred to the Web version of this article.)

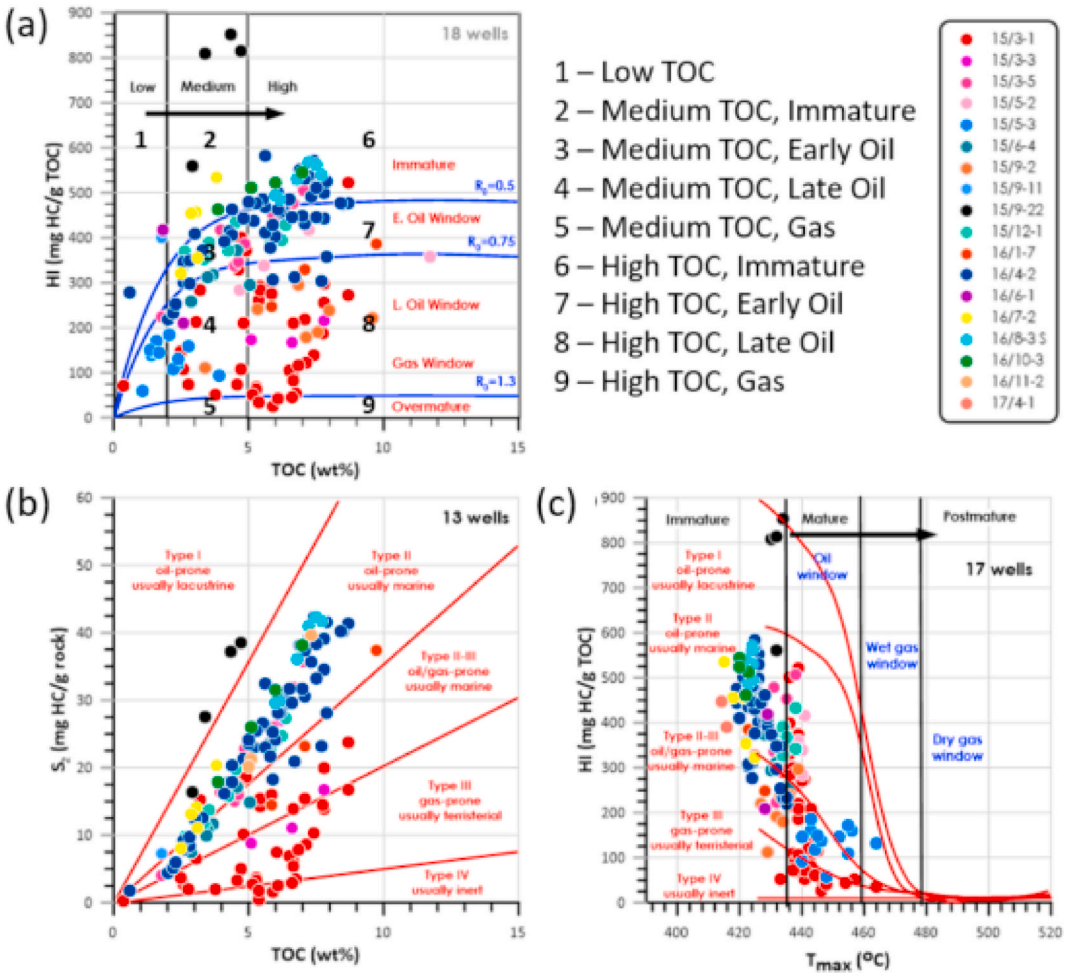

Fig. 10. (a) Hydrogen Index (HI) versus TOC (wt. %) plot from the wells in our dataset allows estimating vitrinite reflectance values (modified from Vernik and Landis, 1996). (b) S2 vs. TOC (wt. %) shows kerogen type and its likely origin, and (c) Hydrogen Index versus T_{max} shows both kerogen type and a general maturation trend (modified from Isaksen and Ledje, 2001).

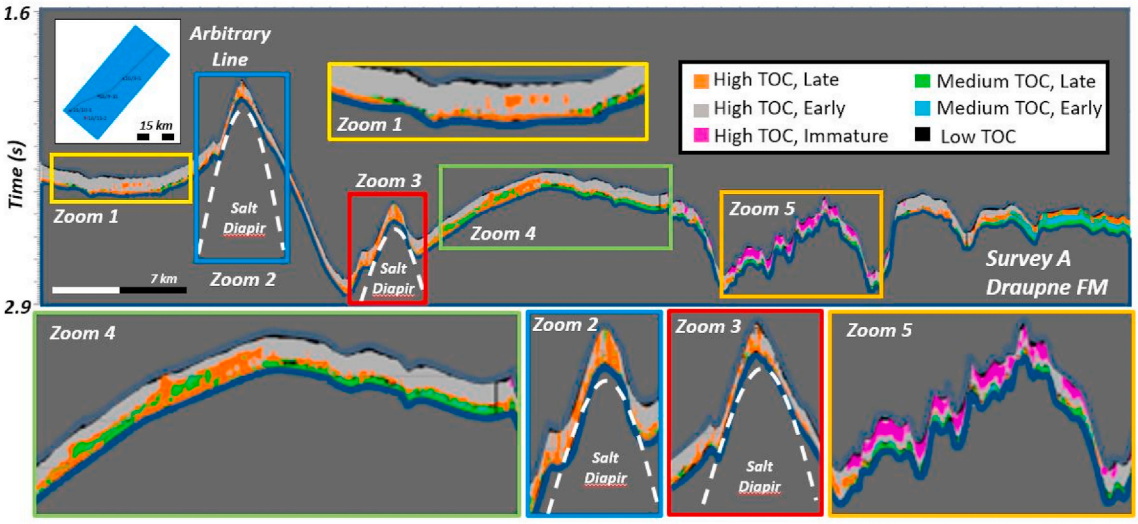

Fig. 11. Values of the organic maturation product (OMP) for the Draupne Formation in a cross-section extracted in Survey A along an arbitrary profile (black line in the upper left inset). Zoomed in sections show details. The impact of maturation on shale due to a salt diapir's proximity is observed (zooms 2 and 3), while zooms 4 and 5 better show stratigraphical separations of maturation.

4.3. Interplay between organic content and maturation

Maturation, TOC content, and kerogen type are the main results from the laboratory geochemical analyses. Kerogen type is predominantly Type II, Type II-III, and Type III with some Type I and Type IV (Fig. 10b). TOC content within the study area is known to vary from 0 to 20 wt % (Thyberg et al., 2010; Zadeh et al., 2017). However, the geochemical data show a more constricted range from 0 to 12 wt % (Fig. 10a and b), with data below ~2 wt % not always being included in the geochemical reports. Rock physics templates show that well log data have a similar TOC range with the highest values around 15 wt% (Figs. 6d and 7d). Understanding maturation, utilizing vitrinite reflectance or an estimate thereof as a proxy, is the main outcome from the geochemical analysis. The dataset is shown to range from immature to late oil generation and possibly into the gas generation window (Fig. 10a and c). However, the majority of data points are located within the immature to oil generation window. Geochemical data indicate that wells around Survey A are predominantly drilled in the immature to early oil generation window, with some in the late oil generation window. In contrast, wells around Survey B are primarily drilled in the early oil generation to late oil generation windows, with some in the early gas window (Fig. 10a and c). Fig. 10a displays how the Organic Maturation Product (OMP) maps can be compared with Vernik and Landis (1996) HI versus TOC cross-plot. Based on the geochemical data, TOC ranges are similar for Surveys A and B.

4.4. Mapping of the organic maturation product (OMP)

Distribution of the seismic facies and of the proposed Organic Maturation Product (OMP), both for the wells and the seismic datasets, confirm that higher TOC is more predominant in the upper Draupne Formation, while medium and low TOC values can more often be found in the lower Draupne Formation (Figs. 11 and 12). In terms of estimated vitrinite reflectance, Survey A is primarily immature or within the early oil generation window, with a few areas showing late oil generation. The areas that show late oil generation are located nearby salt intrusions. The organic maturation product (OMP), which depends on both TOC and vitrinite reflectance along an arbitrary cross-section into the 3D seismic dataset generally increasing in-depth, shows that TOC progresses typically from high to medium, with occasional patches of lower TOC (Fig. 11, zooms 4 and 5). Likewise, maturation progresses with depth unless special conditions, like salt diapirs that alter the temperature trend locally (zooms 2 and 3, Fig. 11). Note that the arbitrary profiles were chosen to best represent data while coinciding with the well logs. Since organic-rich shale is the focus of the present study, these profiles were chosen to illustrate key aspects of our study (Figs. 11 and 12).

However, in contrast to Survey A, the patches of medium TOC in Survey B are more localized, with higher TOC regions being more pervasive (zoom 2, Fig. 12). Since Survey B is also the deepest dataset within a relatively simplistic depositional basin, this deeper location explains why more shale is situated within the late oil generation window. However, some of the shales of Survey B remained within the early oil generation window (zoom 3, Fig. 12). There was little to no presence of immature organic-rich shale in this dataset. Along an arbitrary profile generally increasing with depth, a pattern common to this dataset is visible: organic-rich shale of a given maturity has a window of another maturity encompassing it (e.g., zoom 2, Fig. 12). However, in some sections maturation breaks through vertically, possibly identifying zones of greater thermal maturity (zoom 3, Fig. 12). Note, zones shown to be turbidite in Fig. 9, can be discounted in Fig. 12 (zoom 1) as they represent the quartz-rich turbidite section.

Fig. 13 displays stratigraphic slices of the Organic Maturation Product at two different depths for each Survey. Fig. 13a shows lateral variations in TOC content. Fig. 13b mainly shows the contrast in maturation, while the TOC content remained largely the same throughout. The exception to this is a section of medium TOC with variable maturation in the southwest corner of Survey A (Fig. 13b). A comparison of Figs. 11 and 13a revealed some similarities between the structure of the Draupne Formation and the distribution of maturation. Notably, the comparison of figures showed a generally positive spatial correlation between maturation and depth, with some notable exceptions due to the effect of salt intrusions, as discussed later. Deeper within Survey A, a contrast in TOC content is present (Fig. 13b). While there was no clear relationship between structure and the contrast in TOC content, the organic maturation product (OMP) based on seismic reflectivity may indicate a pattern similar to that found in alluvial depositional systems. In alluvial systems, some channel-like structures of high TOC are surrounded by bank-like structures of medium TOC (Fig. 13a). An investigation of Survey B (Fig. 13c and d) indicates that the shallower stratal slice (Fig. 13c) and the deeper stratal slice (Fig. 13d) show a less distinguishable geomorphological shape when comparing TOC content that could be related to fan structures. The comparison between structure and maturation for Survey B shows a

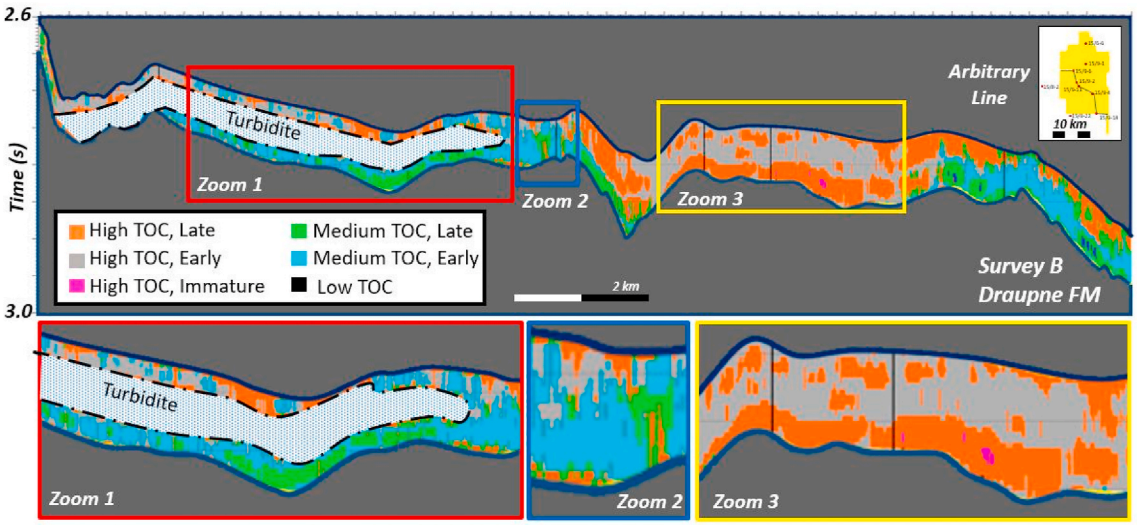

Fig. 12. Values for the organic maturation product (OMP) for the Draupne Formation in a cross-section extracted in Survey B along an arbitrary profile (black line in the upper right inset). The turbidite section, observed from the seismic inversion results and the P-Impedance and S-Impedance, is outlined in dashed black and marked. As such, the OMP results in the turbidite do not represent anything real since no TOC can exist for a quartz-rich turbidite.

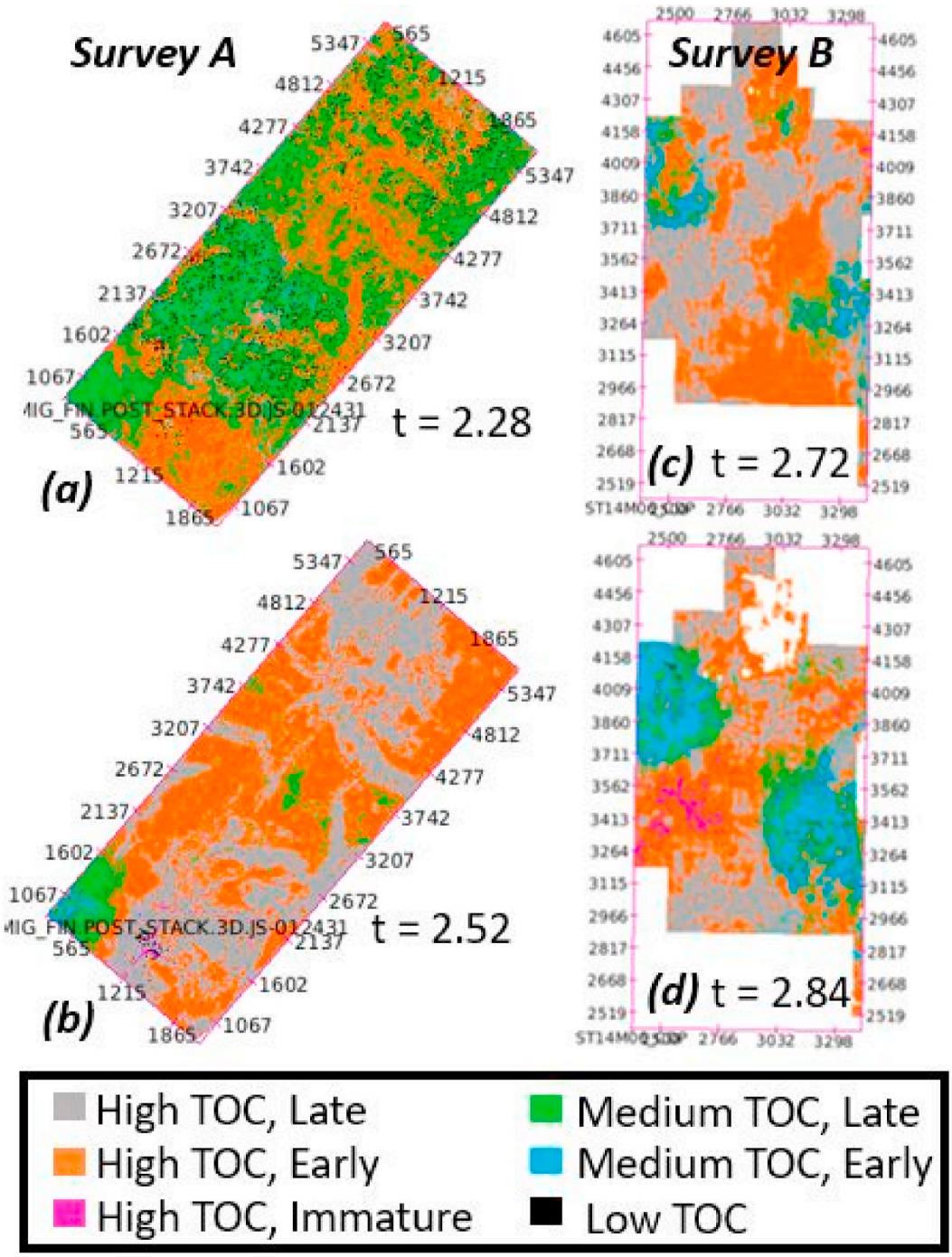

Fig. 13. Map view of stratal slices of the organic maturation product at two different depths for Survey A (a, b) and Survey B (c, d).

positive correlation between depth and maturation. An internal pattern for maturation is present, showing fan-like structures that are particularly apparent for the medium TOC data in Fig. 13d.

The presence of salt diapirism within the study area may modify the relationship between TOC, maturation, and brittleness. We performed a comparison between the frequency of different organic maturation products (OMPs) for the entire Survey A (Fig. 14b), and for a small subset volume focused around a single salt diaper (Fig. 14a). The salt diapir can be seen on both cross-section and map view due to its direct effect on the structure within the area (Figs. 8, 14c and 14d). For the diapir dataset, the two highest groups are Late Oil Generation, either Medium or High TOC. The next largest groups in terms of frequency is Early Oil Generation, either Medium or High TOC. Immature products for both Medium and High TOC have the lowest frequency alongside Low TOC (Fig. 14a). The results for Survey A differed from those seen for the salt diapir dataset, wherein the two categories with the highest frequencies are Medium TOC, with either Late Oil Generation or Early Oil Generation. This is followed by an almost equally high frequency of High TOC, Late Oil Generation. After that, significantly lower levels can be seen for High TOC and Early Oil Generation. While the results for immature shale were roughly the same for the salt diapir and Survey A, there is a marked difference for Low TOC. Significantly higher values for Low TOC are present in Survey A as a whole (Fig. 14b) than for the salt diapir sub-volume (Fig. 14a).

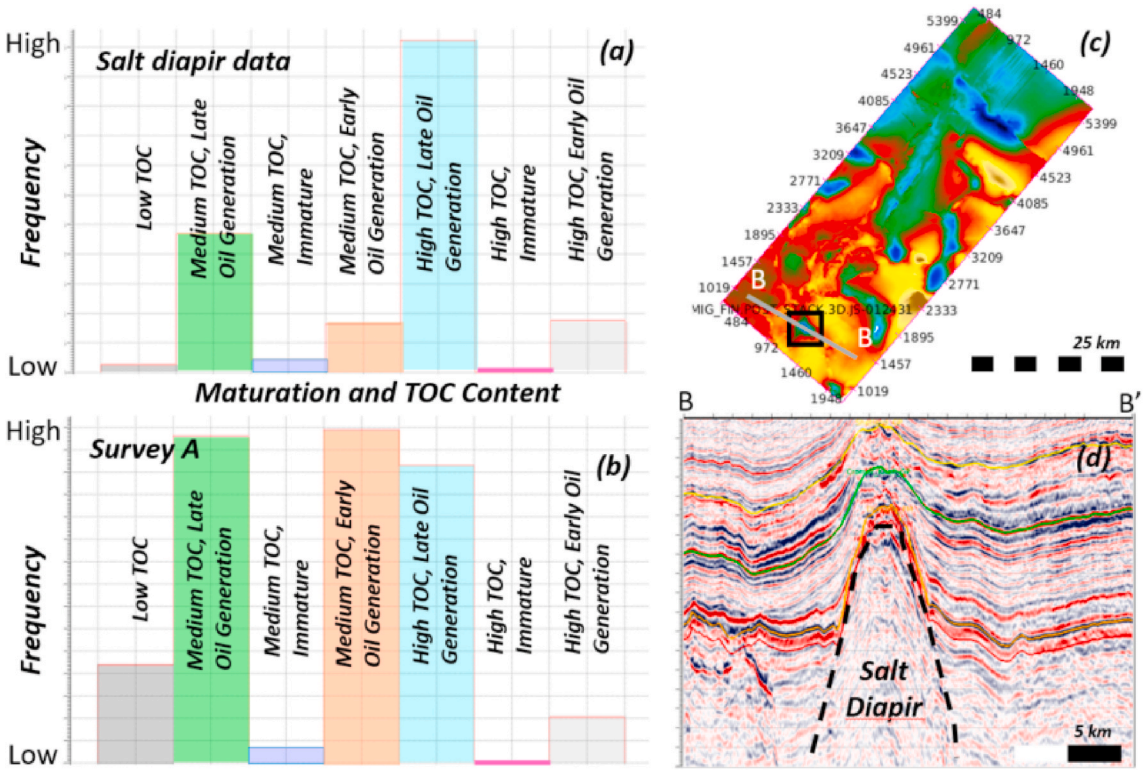

Fig. 14. Distribution of maturation and TOC content, with the frequency of those around a salt diapir (a) and for the entire Survey A (b). The line B–B′ in panel (c) shows the salt diapir displayed in (d).

5. Discussion

The distribution of organic matter, both in terms of the percentage of the rock it constitutes and its geographical location, is critical to understanding the quality of source rocks (Sonnenberg and Meckel, 2017). As a result, understanding the relationship between TOC and organic matter maturation directly impacts drilling success for both conventional and unconventional hydrocarbon resources. High TOC alone does not control the quality of source rock. The degree of maturation the kerogen has undergone dictates the total amount of hydrocarbon produced (Tissot and Welte, 1984; Welte et al., 1997; Ward, 2010). Maturation also has a significant impact on the caprock shales' mechanical properties during and after the conversion of kerogen into hydrocarbon (Prasad et al., 2011; Anders et al., 2014; Zargari et al., 2016; Craddock et al., 2018). The interplay between TOC and maturation as it applies to an organic-rich shale's brittleness allows one to better understand both parameters as they interact with one another and organic-rich shale as a whole. Mapping the organic maturation product (OMP), utilizing seismic inversion and derived seismic facies provides an opportunity to understand what role deposition played in the distribution of kerogen and how diagenetic trends impacted the maturation of kerogen.

5.1. Mapping of TOC and maturation (OMP) - depositional trends

The sediments of the Draupne Formation can be classified into two categories, (1) deep marine anoxic deposits, separated by (2) turbidites or debris-flows (Bugge et al., 2001; Isaksen and Ledje, 2001; Olsen et al., 2017). Even if a depositional system is deep, marine, and anoxic in nature, water bottom currents may occur(Arthur and Sageman, 1994). Literature in comparable portions of the Norwegian North Sea shows that the kerogen type is predominantly Type II and Type III in the North Sea (Isaksen and Ledje, 2001; Hansen et al., 2019). Deep marine anoxic deposition of the organic-rich shale is characterized by relatively low P-Impedance and S-Impedance. P-impedance is high for the intra-Draupne turbiditic flows, while the V_p/V_s is comparably lower (data points above the sand line in Figs. 6 and 9). This is a lithogic indicator as shales usually have higher V_p/V_s values with lower P-Impedance than sand-rich turbiditic deposits (Pendrel et al., 1999; Avseth et al., 2001; Inichinbia et al., 2014), and falls in line with literature on turbidites in the study area (Olsen et al., 2017). Well logs and core data further confirm the presence of turbidites in this area.

Not only can the Draupne Formation be separated into two key lithologies, where the focus of this study is on the organic-rich shale, but it can also be separated into the Upper and Lower Draupne Formation, as proposed by Isaksen and Ledje (2001). This separation is defined by a contrast in the amount of TOC regionally (Isaksen and Ledje, 2001), as well as within our study area (Løseth et al., 2011; Hansen et al., 2020; present study). This increase in TOC towards the Upper Draupne Formation becomes very clear when one looks at the rock physics data and comparing depth with TOC (Fig. 6a, d,7a, 7d). Survey A shows higher impedance values associated with the Lower Draupne Formation (Fig. 8). Since the Upper and Lower Draupne Formations are similar in terms of both lithology and mineralogy (Hansen et al., 2020), excluding the presence of turbidites, one can conclude that this difference is likely the result of TOC. Løseth et al. (2011) noted that it is both possible to separate hydrocarbon source rocks on seismic data, and, as confirmed by other studies, all other things being equal, an increase in impedance results in a decrease in TOC (Broadhead, 2016; Hansen et al., 2019).

Further to this, Hansen et al. (2020) proposed to model the impact of TOC on the Draupne Formation on our study area. Utilizing the approach of Vernik (2016), these authors noted that an increase in TOC from 1.5 wt% to 6.5 wt% would result in a decrease of P-wave velocity by 0.6 km/s and a decrease of 0.15 g/cm^3 for density. Note that the similarity in mineralogy is also partially confirmed by the material points (circles in Fig. 7), based on Mondol (2018). The organic-rich shale portion of the Draupne Formation is shown to plot entirely between the clay and kerogen material points, with a slight skew towards quartz (Fig. 7). It is only in the very low TOC data that it skews towards the

calcite point; however, this is likely due to other factors, as calcareous cement is not common in the Draupne Formation (NPD, 2021).

At the macro-scale, the nature of depositional features varies between Survey A and Survey B. Specifically, submarine channels consisting entirely of fine-grain sediment (i.e., shale, either organic-rich or not) are present within Survey A (Fig. 13a and b). In contrast, submarine fan features are visible on the pre-stack volume of Survey B (Fig. 13c and d). These features fall in-line with their historical proximity to the shoreline and the depositional nature of debris flows (Reading and Richards, 1994; Stow and Mayall, 2000; Olsen et al., 2017). Note the features we see here are composed of the organic-rich shale as indicated by the impedance values and the well log and core data. Depending on the stratal slice, these different depositional features are clearly present (Fig. 13). Medium TOC floodbank-like deposits (Fig. 13a) surround high TOC channel-like structures. Since kerogen is a major constituent of the Draupne Formation, i.e., up to 20 wt% (Løseth et al., 2011), it is conceivable that TOC would interact with deposition as indicated by the stratal slices. Additionally, if TOC data were to interact with deposition, the lower density range of kerogen compared to the other constituents of shales would indicate that TOC would ultimately be higher in rocks formed from the lowest velocity settings deposition.

The shape of fans (Reading and Richards, 1994; Stow and Mayall, 2000) and the shape of wind transported sediment deposits (Blakey and Middleton, 1983) can bear a resemblance to one another. All shapes are seen in Fig. 13b, c, and 13d represent either the front of a fan or pelagic deposition. Kerogen density may assist in higher TOC sediments moving farther than medium TOC sediments, allowing high TOC sediments to sit outside the rim or on the 'over banks' of the medium TOC sediments. In contrast to this, wind-blown deposition is near structureless, allowing an intermixed set of medium and high TOC layers without clear patterns. Fig. 13d better represents an alluvial fan terminus with this additional data, while Fig. 13b and c could better represent wind-blown deposition. Regardless, the data indicates that TOC content impacts depositional features that can be separated in seismic facies within fine-grain sediments (i.e., shale, organic-rich, or not).

5.2. Mapping of TOC and maturation (OMP) – diagenetic trends

Diagenesis of shale directly impacts its capacity to be a seal (Katsube and Williamson, 1994) and controls the hydrocarbon potential of source rocks (Tissot and Welte, 1984). Another impact of increasing temperature and pressure, alongside with depth, is the creation of salt intrusions from previously salt-rich layers (Antoine and Bryant, 1969). Comparing the two 3D seismic datasets shows another impact of variable levels of diagenesis, specifically on the seismic wave parameters and their elastic derivatives. A reduction in Poisson's ratio from Survey A to B, utilizing the rock physics model from Perez and Marfurt (2014), would indicate a movement towards increased brittleness. This is consistent with what one should expect for seismic surveys taken from different depths.

While TOC distribution can be linked to depositional patterns, maturation occurs as a part of diagenesis (Anders et al., 2014). As part of this study, we confirmed that a correlation exists between depth and maturation in this part of the North Sea. This correlation is primarily due to the relatively simple diagenetic history, wherein rifting in the Late Jurassic resulted in the deposition of the Draupne Formation that was subsequently buried relatively continuously without significant uplift afterward (Bugge et al., 2001; Hansen et al., 2020). Furthermore, a comparison of the maturity results from Fig. 4 with the estimations of vitrinite reflectance as a proxy for maturity in Fig. 10, due to the limited amount of vitrinite reflectance data, confirms that the work from Vernik and Landis (1996) also applies to our data set. Additionally, a general comparison of maturation windows with the data from wells around Surveys A and B show that the different approaches produce comparable results.

However, the amount of shale compaction decreases with depth in our data, which is consistent with the literature (Magara, 1980; Dutta et al., 2009), while the compaction for the quartz-rich rock remains relatively constant with depth (Fig. 6a and c). It has long been established that shale's compaction trends are more complicated than they are for sandstone (Magara, 1980; Baldwin and Butler, 1985; Mondol et al., 2007). A possible explanation for the inconsistency with the literature is that the maturation of organic matter can increase porosity (Yenugu and Han, 2013). It has been established that shale will undergo greater compaction, and therefore greater porosity changes than quartz-rich rocks will (Magara, 1980; Baldwin and Butler, 1985). However, deviations from this trend can be seen (Fig. 6) and can be partially explained by the diagenetic process. Prasad et al. (2009) noted that immature shales with a higher organic content will show an increase in P-wave velocity with burial depth, while shales that have undergone greater maturation will show the opposite effect. This is explained by the dual nature of kerogen, in that it will act as load-bearing until maturation occurs and then will become a part of the matrix leaving the clays as load-bearing (Prasad et al., 2009). One can also characterize how diagenesis affected the distribution of variably matured organic-rich shales (Figs. 11–13).

Salt diapirs have been shown to affect maturation, as the thermal conductivity in halite is significantly higher than in other lithologies (Jensen, 1983, 1990; Magri et al., 2008). As such, greater maturation should be present adjacent to the salt diapirs, as shown in both map view (Fig. 13a) and cross-sections (Figs. 8 and 11b) in the data of Survey A (Fig. 14b). Additionally, data show that the increased maturation's effect extends up to 150% of the salt intrusion radius size. This can then be compared to a more quantitative approach. The average distributions of maturation around the salt intrusions are compared to the background maturation in the 3D seismic dataset (Fig. 14). Results show an increase in maturation around the salt intrusions that deviates from the general trend between maturation and depth. This result indicates that salt diapirism influences the maturation of the Draupne Shale within the North Sea and confirms other studies (Jensen, 1983, 1990; Magri et al., 2008).

Since no salt intrusion could be detected in Survey B, this dataset cannot be used to further confirm the effect of diapirism on maturation. However, the lack of diapirism provided an opportunity to characterize factors that might control a deviation from the general trend between depth and maturation. A qualitative comparison of maturation with depth was carried out. Results show that maturation generally follows the geological structures in both map views (Fig. 11c and d) and cross-sections (Figs. 9 and 12).

Given the consistent difference in the amount of TOC for the Upper Draupne Formation compared to the Lower Draupne Formation, one can assume there was a significant dropoff in biological material being fed to the system during sedimentation. In our study, this difference can be used to show how differences in TOC and maturation interplay with one another to influence elastic parameters. Hansen et al. (2020) establish that lower TOC should increase both density and seismic wave velocity based on the work by Vernik (2016). As noted earlier, this is precisely what one sees for the impedance values for the shallower Survey A (Fig. 8), where the majority of shale exists in the immature to early oil generation window (Fig. 11). However, it is also established that increased maturity will have a dampening effect on both velocity and elastic parameters (Prasad et al., 2011; Zargari et al., 2016). Significantly deeper in the basin, at Survey B, the difference between the Upper and Lower Draupne Formations for impedance values is much closer, with the Lower Draupne Formation being slightly lower on average (Fig. 9). At this point, the Lower Draupne Formation is mostly in the late oil generation window (Fig. 12), while the Upper Draupne Formation is still in the early oil generation window (Fig. 12). These results are consistent with the study of Prasad et al. (2009), who suggested that kerogen's transformative effect on elastic properties has taken place, closing the difference between impedance values for Survey B.

5.3. Interplay between TOC and maturation (OMP) within a rock physics model

Many factors influence brittleness (i.e. mineralogy, pore pressure, fluid effects, etc.). Jarvie et al. (2007), Jin et al. (2014), and Alzahabi et al. (2015), highlight the importance of mineralogy, while other studies illustrate how stiff minerals can emplace themselves post-deposition (Thyberg et al., 2009; Avseth and Carcione, 2015). The process of maturation converts kerogen lenses into hydrocarbons, resulting in fluid expulsion and the creation of microfractures (Chauve et al., 2020). The impact that the fluids have on pore pressure is regulated by the interaction between the fluids and formation, particularly controlled by rate of absorption or fluid migration into surrounding formations (Rickman et al., 2008; Wu et al., 2016). While many studies have addressed the impacts of mineralogy, pore pressure, and fluid effects on brittleness (Table 4), fewer studies focus on the impact of TOC and maturation. The present study attempts to fill this gap by addressing the potential effects of TOC, and how maturation alters this impact.

Two interpretations have been proposed in the literature concerning the effect of TOC on the mechanical properties of organic-rich shales (Grieser and Bray, 2007; Wilson et al., 2017; Mondol, 2018), and is summarized in Table 4. The first interpretation correlates an increase in kerogen with an increase in brittleness, citing the presence of kerogen as a brittle constituent (Mondol, 2018). However, it is noted that pure clay content within organic-rich shale is more ductile in nature. These two interpretations provide two opposing trends within clays, one pulling it towards brittleness with the other pulling it towards a more ductile regime (Mondol, 2018). The second interpretation, proposed in a series of studies concerning shales in North and South America, has shown that higher values of TOC correlate to more ductile behavior (Grieser and Bray, 2007; Wilson et al., 2017). These studies had a particular interest in the content of kerogen as organic-rich shales provide an ideal reservoir when hydraulically fractured. However, a medium that is too ductile in nature will dampen the effect of artificial fracturing, and relatively quick healing of the fractures will occur, reducing permeability. Our study shows that an increase in TOC results in greater brittleness in our dataset (Fig. 15). The maturation of the kerogen within organic-rich shale could explain this disparity in the literature. By modeling vitrinite reflectance as a proxy for maturation, our data demonstrate the relationship between maturity and shale's mechanical properties is more complicated than shown by previous studies (Fig. 15).

Table 4
Studies on brittleness highlighting method used (elastic or mineralogy), study focus (brittleness), and any comments the study makes on TOC content and maturation.

Study	Brittleness Method Utilized	Paper Focus (Brittleness)	Comments from study on influence of TOC and maturation
Jarvie et al. (2007)	Mineralogy	Mineralogy dominates, TOC is not considered	Not considered
Jin et al. (2014)	Mineralogy	Mineralogy dominates, TOC is not considered	Not considered
Glorioso and Rattia (2011)	Mineralogy	Mineralogy dominates, TOC is a minor consideration	TOC should be considered in mineralogy brittleness method. Maturation is not considered.
Alzahabi et al. (2015)	Mineralogy	Mineralogy dominates, TOC is not considered	Not considered
Grieser and Bray (2007)	Elastic	Mineralogy dominates, TOC is considered	Higher TOC correlates to more **ductile** behavior. Maturation is not considered.
Rickman et al. (2008)	Elastic	Pore Pressure and Fluid Effects dominates, mineralogy is considered, TOC is not considered	Not considered
Wilson et al. (2017)	Elastic	Mineralogy dominates, TOC is considered	Higher TOC correlates to more **ductile** behavior. Maturation is not considered.
Mondol (2018)	Elastic	Mineralogy dominates, TOC is considered	Higher TOC correlates to more **brittle** behavior. Maturation is not considered.
Present study	Elastic	TOC and Maturation, mineralogy, pore pressure, and fluid effects considered	Higher TOC correlates to more **brittle** behavior. Lower values of TOC will prolong **ductile** behavior during maturation.

Data from the two 3D seismic volumes (Fig. 15) clearly show a gradation from the brittle regime into the ductile through a comparison of TOC content alone. Low TOC rocks tend to populate the ductile regime in both datasets. Further to this observation, both medium and high TOC rocks grade into more brittle regimes based on maturation. Disparities exist in the number of data points available in the different 3D seismic datasets since they represent different depths and represent different levels of potential maturation. The frequency of higher elastic properties due to an increase in depth, especially with a higher level of TOC, is consistent with the literature (Zargari et al., 2013). Survey B contains more data points within the late oil generation window. From a comparison with Survey A, some trends emerge for the maturation as well.

Nonetheless, maturation increases as the organic-rich shale transition its mechanical state from ductile towards brittle. This process occurs at a faster rate for high TOC shale than for the same rock with medium TOC. High TOC, immature shale exists in the ductile regime, with early oil generation data dominantly plotting in a more ductile regime and with late oil generation data dominantly plotting in the more brittle regimes (Fig. 15). However, the relationship of the trend towards maturation depends on TOC. Note that for organic-rich shale with medium TOC, the trend is entirely different. Shales that are both immature and in early oil generation plot dominantly in the ductile regime (Fig. 15). However, medium TOC shale that has entered late oil generation plots predominantly in the more ductile regime and into the more brittle regime showing a marked increase in brittleness. Zargari et al. (2016) also studied this interaction, showing that Young's modulus of kerogen decreases when the kerogen is matured artificially in laboratory experiments. They account for this change as an impact of both increased porosity in remaining kerogen and the presence of fluids or gas with kerogen. This result could help account for why Young's modulus increases at a slower rate with higher TOC levels (Fig. 15). Another critical factor to consider is the changing nature of kerogen within the matrix as maturation occurs. Within immature organic-rich shales, kerogen is load-bearing, while it tends to become a part of the matrix leaving the grains as load-bearing in more mature shale (Prasad et al., 2009). This effect will correlate with the lower value of Poisson's ratio since higher P-wave velocity values relate to increased maturity (Fig. 15).

While no data points are available in our dataset within the gas generation window, one may extrapolate where these data would plot by extending the data available from both medium and high TOC. However, the influence of gas may have a notably stronger impact (Zargari et al., 2016). Note that while low TOC rock was not divided into possible maturation levels due to low kerogen content, the spread of data points, especially in Fig. 15a, indicates that maturation directly influences the shale's geomechanical properties even below a threshold of 2 wt% TOC.

Utilizing our dataset, we developed a rock physics template that classifies qualitatively the broad geomechanical trends for organic-rich shale at variable levels of TOC and maturation in the Draupne Formation (Fig. 16). Young's modulus more aptly separates variations in total TOC content than Poisson's ratio. As highlighted by Fig. 8, TOC better

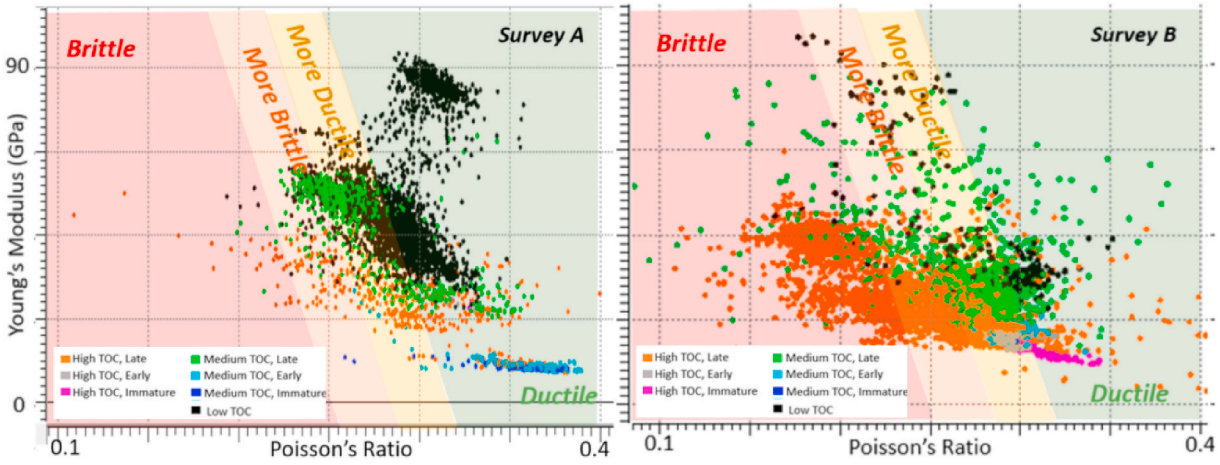

Fig. 15. Results of the Organic Maturation Product (OMP) with a geomechanical template, Young's modulus and Poisson's ratio for both Surveys A and B (from well data), with the organic maturation product (OMP) template that captures both the TOC range and the maturation stage, distributed across the background brittleness index from Perez and Marfurt (2014). Data clearly show a difference in the maturation levels for Survey A and Survey B.

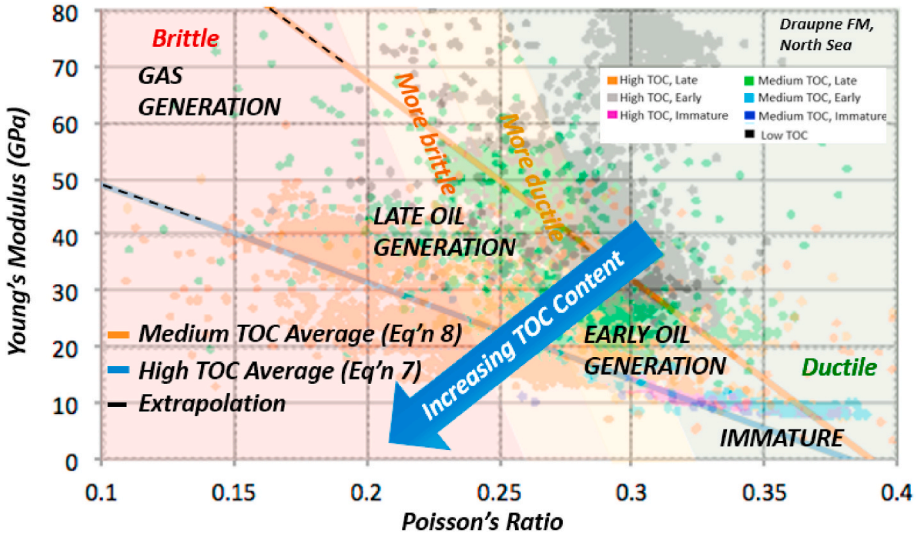

Fig. 16. Organic maturation product (OMP) rock physics template: This template explores how maturation and TOC impact shale brittleness and ductility in the Draupne Formation, the central North Sea. Both TOC and maturation play a significant role, with high TOC shale quickly becoming brittle as it moves from immature towards gas generation. Medium TOC shale, in contrast, moves more slowly from ductile to more brittle between immature and late oil generation. Finally, low TOC rocks have little to no maturation and tend to plot in the ductile region. The blue arrow indicates increasing TOC content. The blue and orange lines indicate trendlines for the average high and medium TOC shales (Equations (10) and (11)). Black dashed lines indicate the domain where these lines have been extrapolated into the gas generation window. (For interpretation of the references to color in this figure legend, the reader is referred to the Web version of this article.)

correlates to Poisson's ratio once porosity has been accounted for. The relationship between TOC and geomechanical properties is further modified by what stage of maturation the shale is currently at. Organic-rich shale with high TOC will quickly grade from ductile into brittle behavior as it matures. In our data, it is defined by the following relationship (Equation (10)):

$$E = -172.2\upsilon + 66.3 \tag{10}$$

where E is Young's modulus (in GPa), and υ is Poisson's ratio (unitless). Contrasting this, an organic-rich shale with medium TOC will progress much more slowly from ductile into brittle behavior. It is defined by the following relationship (Equation (11)):

$$E = -356.3\upsilon + 139.5 \tag{11}$$

These equations are based on the average geomechanical values for high and medium TOC rocks given by the relationships shown in Fig. 16 from both Survey A and B. Since seismic datasets have significantly more data points than well log datasets, the seismic facies dataset was decimated while preserving the trend. It has already been shown that what is true for the petrophysical results is also shown for the inversion results (Fig. 3). Relatively immature rocks plot in the same region despite very different TOC concentrations. This stands in stark contrast to organic-rich shales that have undergone significant maturation, which show a larger difference in geomechanical values depending on the TOC levels. Where gas generation would occur was extrapolated for both curves (black dashed lines in Fig. 16). Increases in TOC also result in a greater uncertainty based on the scatter from the dataset of our study. While there is a possible range for low TOC rocks as well, they were not taken into account for this study.

The proposed OMP template (Fig. 16) represents a novel way to quantify how shale's organic content, in combination with how it matures, impacts its geomechanical parameters. It can be seen that low TOC shales will typically plot within a ductile range, only reaching a more brittle nature under comparatively higher temperature and pressure. In stark contrast to this, a TOC-rich shale will progress relatively rapidly from ductile into brittle, even prior to reaching temperatures and pressures concurrent with gas generation. Shales with neither high nor low TOC are bounded by these two extremes. Therefore, it is expected that shales with greater TOC will result in better mobilization of hydrocarbons because their brittle behavior may allow fractures to propagate and remain open. Note that the results also highlight areas where vastly different rock in terms of TOC and maturation could behave mechanically the same, i.e., a late oil generation rock of medium TOC should behave mechanically similar to an early oil generation rock with high

TOC.

Furthermore, depending on various factors, including possible TOC variation, maturation, and mineralogy, rocks along the medium TOC average curve and the high TOC average curve could have similar mechanical behavior to rocks with low TOC. Utilization of the OMP rock physics template provides a relationship for the impact of variable levels of both TOC and maturation for forward modeling of organic-rich shale. When used for a potential source rock, it may inform as to the quality thereof; however, it could also be used for caprock to help guide interpretation as to its suitability for the play. Furthermore, the results act as verification of laboratory measurements showing the relationship between the maturation of kerogen (Prasad et al., 2009, 2011; Zargari et al., 2013, 2016) and their geomechanical behavior.

6. Conclusions

We introduce a rock physics template, the Organic Maturation Product that classifies semi-quantitatively how the nature of the shale's geomechanical properties evolve with variations in both TOC content and kerogen maturation. This template is built from a comprehensive dataset (3D seismic data, well-logs, geochemical analyses) acquired in the Draupne Formation, a major source rock in the North Sea. Specifically, higher TOC encourages a faster transition from ductile to brittle behavior during the maturation process. This template helps explain how different interpretations of this relationship could exist within the literature. Use of the rock physics template is ideal for better understanding shale as a source rock within an exploration play.

Multiple end-member depositional models exist to explain TOC. We used a combination of arbitrary cross-sections and stratal slices to demonstrate how TOC distribution in the Draupne Formation source rock shale may have been impacted by deposition, with a focus on known depositional environments for the study area in the North Sea. Two depositional models fit the patterns found in the 3D seismic data – submarine debris flows and pelagic deposits. The study confirms a relationship between depth, maturation, and compaction, wherein increased depth correlates positively with maturation and compaction. Deviations from this are explained by the fact that relatively immature organic-rich shale will contain kerogen that is load-bearing. Deviations from the background trend also occurred proximal to salt diapirs, resulting in greater maturation. The typical Draupne Formation distribution for TOC is present and is confirmed by the inversion results.

Declaration of competing interest

The authors declare that they have no known competing financial interests or personal relationships that could have appeared to influence the work reported in this paper.

Acknowledgements

We thank the Norwegian Research Council for providing funding (RCN no. 267775). Further, thanks for helpful conversations are extended to Maya Kobchenko, Austin Bailey, Andrew Johnson, Manzar Fawad and Celine Brun-Lie. Data is made available through the public databases DISKOS (https://portal.diskos.cgg.com/whereoil-data/) and NPD (https://factpages.npd.no/en/wellbore). Academic software licenses have been provided by Lloyd's Register for Interactive Petrophysics, CGG for both Jason and Hampson-Russell, and Schlumberger for Petrel.

References

Alzahabi, A., AlQahtani, G., Soliman, M.Y., Bateman, R.M., Asquith, G., Vadapalli, R., 2015. Fracturability index is a mineralogical index: a new approach for fracturing decision. In: SPE Saudi Arabia Section Annual Technical Symposium and Exhibition. Society of Petroleum Engineers.

Anders, M.H., Laubach, S.E., Scholz, C.H., 2014. Microfractures: a review. J. Struct. Geol. 69, 377–394. https://doi.org/10.1016/j.jsg.2014.05.011. Part B.

Antoine, J.W., Bryant, W.R., 1969. Distribution of salt and salt structures in Gulf of Mexico. AAPG (Am. Assoc. Pet. Geol.) Bull. 53, 2543–2550. https://doi.org/10.1306/5D25C973-16C1-11D7-8645000102C1865D.

Arthur, M.A., Sageman, B.B., 1994. Marine black shales: depositional mechanisms and environments of ancient deposits. Annu. Rev. Earth Planet Sci. 22, 499–511. https://doi.org/10.1146/annurev.ea.22.050194.002435.

Avseth, P., Carcione, J.M., 2015. Rock-physics analysis of clay-rich source rocks on the Norwegian Shelf. Lead. Edge 34, 1340–1348. https://doi.org/10.1190/tle34111340.1.

Avseth, P., Mavko, G., Dvorkin, J., Mukerji, T., 2001. Rock Physics of Seismic Properties of Sands and Shales as a Function of Burial Depth: 2001 SEG Annual Meeting. SEG. https://doi.org/10.1190/1.1816471.

Baig, I., Faleide, J.I., Mondol, N.H., Jahren, J., 2019. Burial and exhumation history controls on shale compaction and thermal maturity along the Norwegian North Sea basin margin areas. Mar. Petrol. Geol. 104, 61–85. https://doi.org/10.1016/j.marpetgeo.2019.03.010.

Baldwin, B., Butler, C.O., 1985. Compaction curves 1. AAPG (Am. Assoc. Pet. Geol.) Bull. 69, 622–626.

Banerjee, A., Sinha, A.K., Jain, A.K., Thomas, N.J., Misra, K.N., Cahndra, K., 1998. A mathematical representation of Rock-Eval hydrogen index vs. Tmax profiles. Organic Geochem. 28, 43–55. https://doi.org/10.1016/S0146-6380(97)00119-8.

Baytok, S., Pranter, M.J., 2013. Fault and fracture distribution within a tight-gas sandstone reservoir: mesaverde group, mamm creek field. Piceance Basin, Colorado, USA: Petrol. Geosci. 19, 203–222. https://doi.org/10.1144/petgeo2011-093.

Beaumont, E.A., Foster, N.H., 1999. Exploring for Oil and Gas Traps: AAPG Treatise Handbook.

Blakey, R.C., Middleton, L.T., 1983. Permian shoreline eolian complex in central Arizona: dune changes in response to cyclic sea level changes: developments in. Sedimentology 38, 551–581.

Bourg, I.C., 2015. Sealing shales versus brittle shales: a sharp threshold in the material properties and energy technology uses of fine-grained sedimentary rocks. Environ. Sci. Technol. Lett. 2, 255–259. https://doi.org/10.1021/acs.estlett.5b00233.

Broadhead, M., 2016. The effect of TOC on acoustic impedance for a Middle Eastern source rock. Lead. Edge 35, 258–264. https://doi.org/10.1190/tle35030258.1.

Bugge, T., Tveiten, B., Backstrom, S., 2001. The Depositional History of the Cretaceous in the Northeastern North Sea, vol. 10. Norwegian Petroleum Society Special Publications, pp. 279–291. https://doi.org/10.1016/S0928-8937(01)80018-7.

Castagna, J.P., Batzle, M.L., Eastwood, R.L., 1985. Relationship between compressional-wave and shear-wave velocities in clastic silicate rocks. Geophysics 50, 571–581. https://doi.org/10.1190/1.1441933.

Chauve, T., Scholtès, L., Donzé, F., Mondol, N.H., Renard, F., 2020. Layering in shales controls microfracturing at the onset of primary migration in source rocks. J. Geophys. Res. 125, e2020JB019444 https://doi.org/10.1029/2020JB019444.

Cook, J., 1999. The effects of pore pressure on the mechanical and physical properties of shales. Oil Gas Sci. Technol. 54, 695–701. https://ogst.ifpenergiesnouvelles.fr/articles/ogst/pdf/1999/06/cook_v54n6.pdf.

Cox, D.R., Newton, A.M.W., Huuse, M., 2020. An introduction to seismic reflection data: acquisition, processing, and interpretation. In: Cox, D.R., Newton, A.M.W., Huuse, M. (Eds.), Regional Geology and Tectonics, pp. 571–603. https://doi.org/10.1016/B978-0-444-64134-2.00020-1.

Cooke, I.L, 2014. User guide total organic carbon (TOC) dataset: British Geological Survey (BGS) Internal Report. http://nora.nerc.ac.uk/id/eprint/509720/1/OR14056.pdf.

Craddock, P.R., Bake, K.D., Pomerantz, A.E., 2018. Chemical, molecular, and microstructural evolution of kerogen during thermal maturation: case study from the Woodford Shale of Oklahoma. Energy Fuel. 32, 4859–4872. https://doi.org/10.1021/acs.energyfuels.8b00189.

Craddock, P.R., Mosse, L., Bernhardt, C., Ortiz, A.C., Tomassini, F.G., Saldungaray, P., Pomerantz, A.E., 2019. Characterization and range of kerogen properties in the Vaca Muerta formation Neuquen basin, Argentina. Org. Geochem. 129, 42–44. https://doi.org/10.1016/j.orggeochem.2019.01.016.

Daniilidis, A., Herber, R., 2017. Salt intrusions providing a new geothermal exploration target for higher energy recovery at shallower depths. Energy 118, 658–670. https://doi.org/10.1016/j.energy.2016.10.094.

Duenas, C., 2014. Understanding Rock Quality Heterogeneity of Montney Shale Reservoir, Pouce Coupe Field. M.S. Thesis, Colorado School of Mines, Alberta, Canada. https://mountainscholar.org/bitstream/handle/11124/441/Duenas_mines_0052N_10446.pdf?sequence=1.

Dutta, T., Mavko, G., Mukerji, T., 2009. Compaction trends for shale and clean sandstone in shallow sediments. Gulf of Mexico: Lead. Edge 28, 590–596. https://doi.org/10.1190/1.3124935.

Espitalie, J., Deroo, G., Marquis, F., 1985. La pyrolysis Rock-Eval etses applications. Oil Gas Sci. Technol. 40, 755–784. https://doi.org/10.2516/ogst:1985045.

Ewy, R., 2019. Claystone Porosity and Mechanical Behavior vs. Geologic Burial Stress: 6th EAGE Shale Workshop. EAGE. https://doi.org/10.3997/2214-4609.201900283.

Faleide, J.L., Tsikalas, F., Breivik, A.J., Mjelde, R., Ritzmann, O., Engen, O., Wilson, J., Eldhom, O., 2008. Structure and evolution of the continental margin off Norway and the Barents Sea. Episodes 31, 82–91. https://doi.org/10.18814/epiiugs/2008/v31i1/012.

Fjaer, E., Holt, R., Raaen, A., Risnes, R., Horsrud, P., 2008. Petroleum Related Rock Mechanics, vol. 53. Elsevier Science.

Fox, A., Snelling, P., McKenna, J., Neale, C., Neuhaus, C., Miskimmins, J., 2013. Geomechanical Principles for Unconventional Reservoirs. Microseismic. http://

www.microseismic.com/wpcontent/uploads/2017/07/2013_Geomechanical_Principles_For_Unconventional_Resources.pdf.
Galbraith, M., Hall, M., 1997. Some causes of artefacts in 3-D seismic surveys and strategies to minimize them. Explor. Geophys. 28, 63–65. https://doi.org/10.1071/EG997063.
Gardner, G.H., Gardner, L.W., Gregory, A.R., 1974. Formation velocity and density – the diagnostic basis for stratigraphic traps. Geophysics 39, 770–780. https://doi.org/10.1190/1.1440465.
Glorioso, J.C., Rattia, A., 2011. Unconventional reservoirs: basic petrophysical concepts for shale gas. In: Proceedings of the SPE/EAGE European Unconventional Resources Conference and Exhibition from Potential to Production. Vienna, Austria, 20–22 March 2012.
Gray, D., Anderson, P., Logel, J., Schmidt, D., Schmid, R., 2012. Estimation of stress and geomechanical properties using 3D seismic data. First Break 30, 59–68. https://doi.org/10.3997/1365-2397.2011042.
Grieser, B., Bray, J., 2007. Identifcation of production potential in unconventional reservoirs: 2007. SPE Production and Operations Symposium. https://doi.org/10.2118/106623-MS. SPE.
Haines, S.H., Plujim, B.A., Ikari, M.J., Saffer, D.M., Marone, C., 2009. Clay fabric intensity in natural and artificial fault gouges: implications for brittle fault zone processes and sedimentary basin clay fabric evolution. J. Geophys. Res. 114, B05406. https://doi.org/10.1029/2008JB005866.
Hansen, J.A., Yenwongfai, H.D., Fawad, M., Mondol, N.H., 2017. Estimating exhumation using experimental compaction trends and rock physics relations, with continuation into analysis of source and reservoir rocks: central North Sea, offshore Norway. In: 88th Annual International Meeting. Expanded abstracts, pp. 3971–3975.
Hansen, J.A., Mondol, N.H., Fawad, M., 2019. Organic content and maturation effects on elastic properties of source rock shales in the Central North Sea: Interpretation. https://doi.org/10.1190/INT-2018-0105.1, 7, 477-497.
Hansen, J.A., Mondol, N.H., Tsikalas, F., Faleide, J.I., 2020. Caprock characterization of Upper Jurassic organic-rich shales using acoustic properties. Norwegian Continental Shelf: Mar. Petrol. Geol. 121, 104603. https://doi.org/10.1016/j.marpetgeo.2020.104603.
Heslop, K.A., 2010. Generalized Method for the Estimation of TOC from GR and Rt: Search and Discovery Article. AAPG Technical Program Expanded Abstracts. No. 80117.
Holt, R.M., Fjaer, E., Stenebraten, J.F., Nes, O.M., 2015. Brittleness of shales: relevance to borehole collapse and hydraulic fracturing. J. Petrol. Sci. Eng. 131, 200–209. https://doi.org/10.1016/j.petrol.2015.04.006.
Horner, D.R., 1951. Pressure build-up in wells: third world petroleum congress. The Hague. https://www.zetaware.com/utilities/bht/horner.html, 34, 316.
Inichinbia, S., Sule, P.O., Ahmed, A.L., Hamza, H., Lawal, K.M., 2014. Petrophysical analysis of among hydrocarbon field fluid and lithofacies using well log data. J. Appl. Geol. Geophys. 2, 86–96. https://doi.org/10.9790/0990-02218696.
Isaksen, G.H., Ledje, H.I., 2001. Source rock quality and hydrocarbon migration pathways within the greater Utsira High area, Viking Graben, Norwegian North Sea. AAPG (Am. Assoc. Pet. Geol.) Bull. 85, 861–883. https://doi.org/10.1306/8626CA23-173B-11D7-8645000102C1865D.
Jackson, C.A.L., Kane, K.E., Larsen, E., 2010. Structural evolution of minibasins on the Utsira High, northern North Sea; implications for Jurassic sediment dispersal and reservoir distribution. Petrol. Geosci. 16, 105–120. https://doi.org/10.1144/1354-079309-011.
Jarvie, D.M., Hill, R.J., Ruble, T.E., Pollastro, R.M., 2007. Unconventional shale-gas systems: the Mississippian Barnett Shale of north-central Texas as one model for thermogenic shale-gas assessment. AAPG (Am. Assoc. Pet. Geol.) Bull. 91, 475–499. https://doi.org/10.1306/12190606068.
Jensen, P.K., 1983. Calculations on the thermal conditions around a salt diapir. Geophys. Prospect. 31, 481–489. https://doi.org/10.1111/j.1365-2478.1983.tb01064.x.
Jensen, P.K., 1990. Analysis of the temperature field around salt diapirs. Geothermics 19, 273–283. https://doi.org/10.1016/0375-6505(90)90047-F.
Jin, X., Shah, S.N., Roegiers, J.-C., Zhang, B., 2014. Fracability evaluation in shale reservoirs-an integrated petrophysics and geomechanics approach. In: SPE Hydraulic Fracturing Technology Conference. Society of Petroleum Engineers. https://doi.org/10.2118/168689-MS.
Johnson, J.R., 2017. Applications of Geostatistical Seismic Inversion to the Vaca Muerta, Neuquen Basin. Colorado School of Mines, Argentina. M.S. thesis. https://mountainscholar.org/bitstream/handle/11124/170976/Johnson_mines_0052N_11230.pdf?sequence=1.
Johnson, J.R., Renard, F., Mondol, N., 2021. Salt Remobilization Timing and its Impact on Two Norwegian Contentinental Shelf Organic-Rich Shale Formations. Geoconvention 2021. https://geoconvention.com/wp-content/uploads/abstracts/2021/67503-salt-removilization-timing-and-its-impact-on-two.n.pdf.
Kalani, M., Jahren, J., Mondol, N.H., Faleide, J.I., 2015. Petrophysical implications of source rock microfracturing. Int. J. Coal Geol. 143, 43–67. https://doi.org/10.1016/j.coal.2015.03.009.
Katsube, T.J., Williamson, M.A., 1994. Effects of diagenesis on shale nano-pore structure and implications for sealing capacity. Clay Miner. 29, 451–461. https://doi.org/10.1180/claymin.1994.029.4.05.
Kemper, M., Gunning, J., 2014. Joint impedance and facies inversion-seismic inversion redefined. First Break 32, 89–95. https://doi.org/10.3997/1365-2397.32.9.77968.
Kennedy, M., Mayer, L., 2019. Dominance of Wind Blown Minerals in Black Shales, Connecting Continentatl Climate, Fe Fertilization and Mineral Ballasting: 6th EAGE Shale Workshop. EAGE. https://doi.org/10.3997/2214-4609.201900282.
Kumar, N., Negi, S.S., 2012. Low frequency modeling and its impact on seismic inversion data. In: 9th Biennial International Conference and Exposition on Petroleum Geophysics. https://doi.org/10.3997/2214-4609.201702511.
Kuuskraa, V.A., Stevens, S.H., Moodhe, K., 2013. Technically Recoverable Shale Oil and Shale Gas Resources: an Assessment of 137 Shale Formations in 41 Countries outside the United States: U.S. Energy Information Administration. https://www.eia.gov/analysis/studies/worldshalegas/pdf/overview.pdf?zscb=79906188.
Løseth, H., Wensaas, L., Gading, M., Duffaut, K., Springer, M., 2011. Can hydrocarbon source rocks be identified on seismic data? Geology 39, 1167–1170. https://doi.org/10.1130/G32328.1.
MacFarlane, T.L., 2014. Amplitude Inversion of Fast and Slow Converted Waves for Fracture Characterization of the Montney Formation in the Pouce Coupe Field. Colorado School of Mines, Alberta, Canada. M.S. Thesis. https://mountainscholar.org/bitstream/handle/11124/10645/MacFarlane_mines_0052N_10560.pdf?sequence=1.
Magara, K., 1980. Comparison of porosity-depth relationships of shale and sandstone. J. Petrol. Geol. 3, 175–185. https://doi.org/10.1111/j.1747-5457.1980.tb00981.x.
Magri, F., Littke, R., Rodon, S., Bayer, U., Urai, J.L., 2008. Temperature fields, petroleum maturation and fluid flow in the vicinity of salt domes. In: Littke, R., Bayer, U., Gajewski, D., Nelskamp, S. (Eds.), Dynamics of Complex Intracontinental Basins: the Central European Basin System. Springer, pp. 323–344.
Mannie, A.S., Jackson, C.A.L., Hampson, G.J., 2014. Structural controls on the stratigraphic architecture of net-transgressive shallow-marine strata in a salt-influenced rift basin: middle-to-Upper Jurassic Egersund Basin. Norwegian North Sea: Basin Res. 26, 675–700. https://doi.org/10.1111/bre.12058.
Marfurt, K.J., Alves, T.M., 2014. Pitfalls and limitations in seismic attribute interpretation of tectonic features. Interpretation 3, 5–15. https://doi.org/10.1190/INT-2014-0122.1.
Mondol, N.H., 2018. Seal Quality Prediction Using E-Poisson's Ratio Rock Physics Template – A Case Study from the Norwegian Barents Sea: Geoconvention 2018. https://geoconvention.com/uploads/2018abstracts/241_GC2018_Seal_quality_prediction_using_E-v_rock_physics_templet.pdf.
Mondol, N.H., Bjørlykke, K., Jahren, J., Høeg, K., 2007. Experimental mechanical compaction of clay mineral aggregates—Changes in physical properties of mudstones during burial. Mar. Petrol. Geol. 24 (5), 289–311. https://doi.org/10.1016/j.marpetgeo.2007.03.006.
NPD, 2021. Norwegian Petroleum Directorate FactPages. http://factpages.npd.no/. (Accessed 6 November 2021).
Nooraiepour, M., Mondol, N.H., Hellevang, H., Bjorlykke, K., 2017. Experimental mechanical compaction of reconstituted shale and mudstone aggregates: investigation of petrophysical and acoustic properties of SW Barents Sea cap rock sequences. Mar. Petrol. Geol. 80, 265–292. https://doi.org/10.1016/j.marpetgeo.2016.12.003.
Nygård, R., Gutierrez, M., Bratli, R.K., Høeg, K., 2006. Brittle–ductile transition, shear failure and leakage in shales and mudrocks. Marine Petrol. Geol. 23, 201–212. https://doi.org/10.1016/marpetgeo.2005.10.001.
Olsen, H., Briedis, N.A., Renshaw, D., 2017. Sedimentological analysis and reservoir characterization of a multi-Darcy, billion barrel oil field – the Upper Jurassic shallow marine sandstones of the Johan Sverdrup field, North Sea, Norway. Mar. Petrol. Geol. 84, 102–134. https://doi.org/10.1016/j.marpetgeo.2017.03.029.
Ougier-Simonin, A., Renard, F., Boehm, C., Vidal-Gilbert, S., 2016. Microfracturing and microporosity in shales. Earth Sci. Rev. 162, 198–226. https://doi.org/10.1016/j.earscirev.2016.09.006.
Passey, Q.R., Creaney, S., Kulla, J.B., Moretti, F.J., Stroud, J.D., 1990. A practical model for organic richness from porosity and resistivity logs. AAPG (Am. Assoc. Pet. Geol.) Bull. 74, 1777–1794. https://doi.org/10.1306/0C9B25C9-1710-11D7-8645000102C1865D.
Passey, Q.R., Bohacs, K.M., Esch, W.L., Klimentidis, R., Sinha, S., 2012. My Source Rock Is Now My Reservoir – Geologic and Petrophysical Characterization of Shale-Gas Reservoirs: Search and Discovery Article. AAPG Technical Program Expanded Abstracts, No. 80231. http://www.searchanddiscovery.com/pdfz/documents/2012/80231passey/ndx_passey.pdf.html.
Pendrel, J., Debeye, H., Pedersen-Tatlovic, R., Goodway, B., Dufour, J., Bogaards, M., Stewart, R., 1999. Estimation and Interpretation of P and S-Impedance Volumes from Simultaneous Inversion of P-Wave Offset Seismic Data. SEG Technical Program Expanded Abstracts 2000. https://pdfs.semanticscholar.org/04a6/9f9803ce0f98a80d2d75a1a9a65998d4d2a3.pdf.
Pendrel, J., Mangat, C., Feroci, M., 2006. Using Bayesian inference to compute facies-fluid probabilities: CSPG-CSEG-CLWS 2006. https://cseg.ca/assets/files/resources/abstracts/2006/238S0131.pdf.
Perez, R., Marfurt, K., 2014. Mineralogy-based brittleness prediction from surface seismic data: application to the Barnett Shale. Interpretation 2, 1–17. https://doi.org/10.1190/INT-2013-0161.1.
Prasad, M., Pal-Bathija, A., Johnston, M., Rydzy, M., Batzle, M., 2009. Rock physics of the unconventional. Lead. Edge 28, 34–38. https://doi.org/10.1190/1.3064144.
Prasad, M., Kenechukwu, C., McEvoy, T.E., Batzle, M., 2011. Maturity and impedance analysis of organic-rich shales. SPE Reservoir Eval. Eng. 14, 533–543. https://doi.org/10.2118/123531-PA.
Rahman, M.D.J., Fawad, M., Mondol, N.H., 2020. Organic-rich shale caprock properties of potential CO2 storage sites in the northern North Sea, offshore Norway. Mar. Petrol. Geol. 122, 104665. https://doi.org/10.1016/j.marpetgeo.2020.104665.
Reading, H.G., Richards, M., 1994. Turbidite system in deep-water basin margins classified by grain size and feeder system. AAPG (Am. Assoc. Pet. Geol.) Bull. 78, 792–822. https://doi.org/10.1306/A25FE3BF-171B-11D7-8645000102C1865D.
Rickett, J.E., Lumley, D.E., 1999. Cross-equalization data processing for time-lapse seismic reservoir monitoring: a case study from the Gulf of Mexico. Geophysics 66, 1015–1025. https://doi.org/10.1190/1.1487049.

Rickman, R., Mullen, M., Petre, E., Grieser, B., Kundert, D., 2008. A Practical Use of Shale Petrophysics for Stimulation Design Optimization: All Shale Plays Are Not Clones of the Barnett Shale. Society of Petroleum Engineers, Richardson, TX, USA.

Robertson, E.C., 1988. Thermal Properties of Rocks. US Department of the Interiror Geological Survey. https://doi.org/10.3133/ofr88441. Open-File Report 88-441.

Rossland, A., Escalona, A., Rolfsen, R., 2013. Permian-Holocene Tectonostratigraphic Evolution of the Mandal High, Central Graben, North Sea: AAPG Bulletin, 97, 923 – 957.

Russell, B.H., 1988. Introduction to Seismic Inversion Methods: SEG. https://doi.org/10.1190/1.9781560802303.

Sadeghtabaghi, Z., Talebkeikhah, M., Rabbani, A.R., 2020. Prediction of vitrinite reflectance values using machine learning techniques: a new approach. J. Petrol. Explor. Prod. Technol. 11, 651–671. https://doi.org/10.1007/s13202-020-01043-8.

Sayers, C.M., Dasgupta, S., 2019. A predictive anisotropic rock-physics model for estimating elastic rock properties of unconventional shale reservoirs. Lead. Edge 38, 358–365. https://doi.org/10.1190/tle38050358.1.

Schmoker, J.W., Hester, T.C., 1983. Organic carbon in Bakken formation, United States portion of Williston basin. AAPG (Am. Assoc. Pet. Geol.) Bull. 67, 2165–2174. https://doi.org/10.1306/AD460931-16F7-11D7-8645000102C1865D.

Sheriff, R., 2002. Encyclopedic dictionary of applied geophysics: SEG. https://doi.org/10.1190/1.9781560802969.

Skurtveit, E., Miri, R., Hellevang, H., 2018. Geological Carbon Storage: Subsurface Seals and Caprock Integrity. American Geophysical Union. https://doi.org/10.1002/9781119118657.

Somoza, A.V., Waters, K., Kemper, M., 2015. Improved Seismic Inversion and Facies Using Regional Rock Physics Trends: Case Study from the Central North Sea: EAGE. 3rd workshop on Rock Physics, pp. 1–5. https://doi.org/10.3997/2214-4609.201414389.

Sonnenberg, S.A., 2011. TOC and pyrolysis data for the Bakken shales, Williston basin, north Dakota and Montana. In: Robinson, J.W., LeFever, J.A., Gaswirth, S.B. (Eds.), Bakken-Three Forks Petroleum System in the Williston Basin. Rocky Mountain Association of Geologists, pp. 308–331.

Sonnenberg, S.A., Meckel, L., 2017. Our Current Working Model for Unconventional Tight Petroleum Systems: Oil and Gas: Search and Discovery. AAPG. http://www.searchanddiscovery.com/documents/2017/80589sonnenberg/ndx_sonnenberg.pdf. (Accessed 17 March 2021).

Soto, J.I., Hudec, M.R., Mondol, N.H., Heidari, M., 2021. Shale transformations and physical properties – implcations for seismic expression of mobile shales. Earth Sci. Rev. 220, 103746. https://doi.org/10.1016/j.earscirev.2021.103746.

Steiner, S., Ahsan, S.A., Raina, I., Dasgupta, S., Lis, G.P., 2016. Interpreting total organic carbon TOC in source rock oil plays. In: SPE International Petroleum Exhibition and Conference. https://doi.org/10.2118/183050-MS.

Stow, D.A., Mayall, M., 2000. Deep-water sedimentary system: new models for the 21st century. Mar. Petrol. Geol. 17, 125–135. https://doi.org/10.1016/S0264-8172(99)00064-1.

Thomsen, L., 1990. Poisson was not a geophysicist. Lead. Edge 9, 27–29. https://doi.org/10.1190/1.1439706.

Thomsen, L., 1996. Poisson was not a rock physicist, either. Lead. Edge 15, 793–880. https://doi.org/10.1190/1.1437382.

Thyberg, B., Jahren, J., Winje, T., Bjørlykke, K., Faleide, J., 2009. From mud to shale: rock stiffening by microquartz cementation. First Break 27, 2. https://doi.org/10.3997/1365-2397.2009003.

Thyberg, B., Jahren, J., Winje, T., Bjorlykke, K., Faleide, J.I., Marcussen, O., 2010. Quartz cementation in Late Cretaceous mudstones, northern North Sea: Changes in rock properties due to dissolution of smectite and precipitation of miro-quartz crystals. Mar. Petrol. Geol. 27, 1752–1764. https://doi.org/10.1016/j.marpetgeo.2009.07.005.

Tissot, B.P., Welte, D.H., 1984. Petroleum Formation and Occurrence. Springer-Verlag Berlin Heidelberg GmbH.

Vernik, L., 2016. Seismic Petrophysics in Quantitative Interpretation: Investigation in Geophysics, vol. 18. SEG, Tulsa, Oklahoma.

Vernik, L., Landis, C., 1996. Elastic anisotropy of source rocks – implications for hydrocarbon generation and primary migration. AAPG (Am. Assoc. Pet. Geol.) Bull. 80, 531–544. https://doi.org/10.1306/64ED8836-1724-11D7-8645000102C1865D.

Ward, J., 2010. Kerogen density in the marcellus shale, SPE unconventional gas conference. https://doi.org/10.2118/131767-MS.

Welte, D.H., Horsfield, B., Baker, D.R., 1997. Petroleum and Basin Evolution, Insights from Petroleum Geochemisty, Geology, and Basin Modeling. Springer.

Whipp, P.S., Jackson, C.A.-L., Gawthorpe, R.L., Dreyer, T., Quinn, D., 2014. Normal fault array evolution above a reactivated rift fabric; a subsurface example from the northern Horda Platform. Norwegian North Sea: Basin Res. 26, 523–549. https://doi.org/10.1111/bre.12050.

Wilson, M.P., Worrall, F., Davies, R.J., Hart, A., 2017. Shallow aquifer vulnerability from subsurface fluid injection at a proposed shale gas hydraulic fracturing site. Water Resour. Res. 53, 9922–9940. https://doi.org/10.1002/2017WR021234.

Wu, Y., Ji, L., He, C., Zhang, Z., Zhang, M., Sun, L., Su, L., Xia, Y., 2016. The effects of pressure and hydrocarbon expulsion on hydrocarbon generation during hydrorous pyrolysis of type-I kerogen in source rock. J. Nat. Gas Sci. Eng. https://doi.org/10.1016/j.jngse.2016.08.0171875-5100.

Yenugu, M., Han, D., 2013. Seismic Characterization of Kerogen Maturity: an Example from Bakken Shale. SEG Technical Program Expanded Abstracts. https://doi.org/10.1190/segam2013-0629.1.

Yenwongfai, H., Mondol, N.H., Lecomte, I., Faleide, J.I., Leutscher, J., 2019. Integrating facies-based Bayesion inversion and supervised machine learning for petro-facies characterization in the Snadd Formation Goliat Field, south-western Barents Sea. Geophys. Prospect. 67, 1020–1039. https://doi.org/10.1111/1365-2478.12654.

Yilmaz, O., 2001. Seismic Data Analysis: Processing, Inversion, and Interpretation of Seismic Data: SEG. https://doi.org/10.1190/1.9781560801580.

Zadeh, M.K., Mondol, N.H., Jahren, J., 2017. Velocity anisotropy of Upper Jurassic organic-rich shales. Norwegian Continental Shelf: Geophysics 82, 61–75. https://doi.org/10.1190/geo2016-0035.1.

Zargari, S., Prasad, M., Kenechukwu, C., Mattson, E.D., 2013. Organic maturity, elastic properties, and textural characteristics of self resourcing reservoirs. Geophysics 78, 223–235. https://doi.org/10.1190/geo2012-0431.1.

Zargari, S., Wilkinson, T.M., Packard, C.E., Prasad, M., 2016. Effect of thermal maturity on elastic properties of kerogen. Geophysics 81, 1942–2156. https://doi.org/10.1190/geo2015-0194.1.

Ziegler, P.A., 1992. North Sea rift system. Tectonophysics 208, 55–75. https://doi.org/10.1016/0040-1951(92)90336-5.

Zoback, M., 2007. Reservoir Geomechanics. Cambridge University Press. https://doi.org/10.1017/CBO9780511586477.

Paper 2

Multiscale synchrotron microtomography imaging of kerogen lenses in organic-rich shales from the Norwegian Continental Shelf

James R. Johnson
Maya Kobchenko
Nazmul H. Mondol
François Renard

II

International Journal of Coal Geology, 2022

International Journal of Coal Geology 253 (2022) 103954

Contents lists available at ScienceDirect

International Journal of Coal Geology

journal homepage: www.elsevier.com/locate/coal

Multiscale synchrotron microtomography imaging of kerogen lenses in organic-rich shales from the Norwegian Continental Shelf

James Ronald Johnson [a,*], Maya Kobchenko [a], Nazmul Haque Mondol [a,c], François Renard [a,b]

[a] Department of Geosciences, The Njord Centre, University of Oslo, P.O. Box 1047, Blindern, NO-0316 Oslo, Norway
[b] University Grenoble Alpes, University Savoie Mont Blanc, CNRS, IRD, ISTerre, 38000 Grenoble, France
[c] Norwegian Geotechnical Institute (NGI), P.O. Box 3930, Ullevaal Stadion, NO-0806 Oslo, Norway

ARTICLE INFO

Keywords:
Kerogen lenses
Organic-rich shale
Microfractures
Synchrotron microtomography
Norwegian continental shelf
Draupne Formation
Hekkingen Formation

ABSTRACT

Kerogen lens shape and size distribution control how organic-rich shales may behave as either source or seal rocks. Prior to thermal conversion, kerogen is a brittle, load-bearing constituent of the shale matrix. During thermal maturation, kerogen lenses become more ductile, and hydrocarbon expulsion may lead to the creation of microfractures, a process controlled not only by temperature and pressure but also by the size and shape of kerogen lenses and their total content in the rock. Here, we use high-resolution multiscale synchrotron microtomography imaging of centimeter-scale shale rock samples collected in two boreholes at different depths in the North Sea and the Barents Sea, respectively. From these three-dimensional microtomography data, we quantify the various shapes of kerogen lenses and discuss how each step of a kerogen lens's life-cycle (i.e. original biological structure, deposition, degradation, and diagenesis) impacted its shape before catagenesis. We quantify the relationship between kerogen volume and the number of kerogen lenses in a given rock volume. The relationship between total organic carbon (TOC) content and the average kerogen lens volume is also measured. For a given rock volume, results show that organic content increases with the number of kerogen lenses up to a point (~8–12 wt% TOC) above which TOC continues to increase, but the number of kerogen lenses decreases. These results combined with kerogen lens orientation may control microfracturing during kerogen maturation.

1. Introduction

Organic-rich shales are studied for their importance for many geo-engineering purposes. Understanding organic-rich shales as the source or seal rocks are critical to hydrocarbon exploration in both conventional and unconventional plays (Prasad et al., 2011; Bourg, 2015; Johnson, 2017; Hansen et al., 2020; Johnson et al., 2022). The presence of microfractures in mature or partially mature shales controls their quality as a seal, which is important for subsurface CO_2 storage as well as for the disposal of nuclear wastes (Bourg, 2015). Microfracturing occurring during kerogen maturation in organic-rich shales has been proposed to be driven predominantly by volume expansion of kerogen lenses due to hydrocarbon production (Hunt, 1996; Vernik, 1994; Lash and Engelder, 2005; Fan et al., 2010; Jin et al., 2010; Kobchenko et al., 2011; Panahi et al., 2019; Voltolini and Franklin, 2020). The coupling between kerogen maturation and microfracture growth has a critical impact on the geomechanical properties of shales and whether shales behave as a source or seal rocks (Vernik, 1994; Anders et al., 2014; Chauve et al., 2020; Voltolini and Franklin, 2020; Liu et al., 2021). Understanding shale as a seal for CO_2/water systems is inherently more complex due to reactivity of the mineralogy (Busch et al., 2016; Kalani, 2018; Skurtveit et al., 2018), miscibility of the fluids (Kalani, 2018; Skurtveit et al., 2018), and capillary sealing behavior (Kalani, 2018). Finally, understanding the presence and fabric of shales is critical to geotechnical investigations (Nichols et al., 1986; Nichols, 1992; Sabtan, 2005, Okewale and Grobler, 2020).

The distribution of organic matter present in shale and the degree of maturation that shale has undergone control the mechanical properties of this rock. When the shale is immature, the organic matter acts as a brittle, load-bearing constituent within the matrix (Prasad et al., 2009; Prasad et al., 2011; Brochard et al., 2013; Mondol, 2018; Johnson et al., 2022). The chemical composition of kerogen lenses, which depends on kerogen type, influences the dynamic modulus (Alstadt et al., 2016; Bousige et al., 2016; Shitrit et al., 2016). As maturation progresses, kerogen lenses become increasingly ductile, while both their surface area and volume increase (Kelemen et al., 2006; Craddock et al., 2018;

* Corresponding author.
E-mail address: j.r.johnson@geo.uio.no (J.R. Johnson).

https://doi.org/10.1016/j.coal.2022.103954
Received 17 December 2021; Received in revised form 16 February 2022; Accepted 17 February 2022
Available online 21 February 2022

Craddock et al., 2019) until hydrocarbon expulsion occurs, at which point the mineral grains become load-bearing (Prasad et al., 2009; Prasad et al., 2011; Johnson et al., 2022). During this process, it has been suggested that porosity internal to kerogen will be created, and that this will have an impact on the material properties of the shale (Alfred and Vernik, 2013; Pepper, 2017). However, at this point, a network of fractures may have also formed due to the conversion process (Fan et al., 2010; Jin et al., 2010; Fan et al., 2012; Chauve et al., 2020; Voltolini and Franklin, 2020). The lithostatic load can control the phase equilibrium between kerogen and the hydrocarbons expelled (Pepper and Corvi, 1995; Carcione and Avseth, 2015; Burnham, 2017; Pepper, 2017). Lithostatic load also influences the amount of porosity generated due to the microfracturing process (Pepper and Corvi, 1995; Carcione and Avseth, 2015; Burnham, 2017; Pepper, 2017). When considering the seal capacity of an immature shale, the volume percentage of organic material controls the geomechanical properties (e.g., Young's modulus, shear modulus, bulk modulus, Poisson's ratio). In contrast, when shale has undergone thermal maturation and microfractures were produced, the degree of microfracture healing and sealing controls the geomechanical properties (Voltolini and Franklin, 2020). This effect is related to the impact that porosity, both internal to kerogen lenses and created by microfractures, has on the material properties of shale (Eliyahu et al., 2015).

While organic-rich shale may behave as a seal rock, both before and after the hydrocarbon expulsion process, during hydrocarbon expulsion, shale becomes increasingly brittle with the growth of microfractures that nucleate at kerogen lenses. This process has been proposed and documented on a variety of scales (Pelet and Tissot, 1971; Vernik, 1994; Fan et al., 2010; Jin et al., 2010; Teixeira et al., 2017; Johnson et al., 2019; Chauve et al., 2020; Voltolini and Franklin, 2020). Numerical modeling studies have shown that the size of the kerogen lenses controls the rate of microfracture growth and ultimately, microfracture lengths (Fan et al., 2010; Fan et al., 2012). The size and spatial distribution of the kerogen lenses dictate the connectivity of the microfracture network that leads to hydrocarbon expulsion (Jin et al., 2010; Chauve et al., 2020; Liu et al., 2021). Finally, the shape of the kerogen lens can control microfracture growth direction during hydrocarbon expulsion (Li and Zhang, 2021; Chauve et al., 2020) and the geomechanical properties of the rock afterward (Dietrich, 2015).

The fabric of shales is influenced by both the organic and inorganic components (Eliyahu et al., 2015) as they are altered during depositional and diagenetic processes, and has been shown to influence mechanical properties, degree of anisotropy, and rate of maturation (Dewhurst and Siggins, 2006; Shitrit et al., 2016; Rahman et al., 2017). In order to characterize the microstructure of organic-rich shales (i.e.,> 2% organic content), it is important to separate out the organic and inorganic components. The primary focus of our study seeks to characterize the three-dimensional properties of the organic content (i.e., kerogen lenses) within shales that come from two main source rocks in the Norwegian Continental Shelf, the Draupne Formation in the North Sea and the Hekkingen Formation in the Barents Sea. We have obtained the shales samples from two boreholes drilled in these formations, and samples were collected at depths in the range 1360–2583 m. Dominantly Type II, Type II-S, and Type III kerogens were encountered. No internal kerogen porosity was identified, which falls in line with the maturation state of the samples collected. Using multiscale microscopy and synchrotron X-ray microtomography imaging, we determine the shape, size, and distribution of kerogen lenses in the shales and discuss how these parameters may influence the geomechanical properties of the rock. Note, the mechanical properties will determine yield stress and influence creep behavior. We explore how the kerogen lenses may control microfracture growth and coalescence as a part of the kerogen maturation process. The inorganic content of these two shales (i.e., mineralogy) is also quantified in order to provide a framework for understanding the shales as potential sources or seals. This includes an understanding of the shale fabric, which depends on the deposition environment (i.e., lacustrine, transitional, marine), and degree of diagenesis (Dewhurst and Siggins, 2006; Jiang et al., 2017; Rahman et al., 2017). We propose standard kerogen lens shapes tied to aspect ratios that are better representative of reality than what is currently being used for numerical modeling. Then, we develop a relationship between kerogen lens volume and the number of lenses of a given size. Furthermore, when a shale contains more than ~8–12 wt% total organic carbon content, the spatial density of kerogen lenses decreases, which is explained by the presence of larger kerogen lenses in the rock. We discuss how these results combined with kerogen lens orientation control the growth of microfractures during the maturation of organic-rich shales.

2. Geological setting and organic-rich shale samples

2.1. Upper Jurassic source rocks in the Norwegian Continental Shelf and Barents Sea

In the Norwegian Continental Shelf, both the Upper Jurassic Draupne and Hekkingen Formations contain organic-rich shales. They are major source rocks of their respective petroleum systems, typical of the Kimmeridge clay formations deposited from the Oxfordian to Ryazanian age (NPD, 2021). These shales are both described in the literature as being dark grey to black, usually non-calcareous, occasionally fissile claystones (Hansen et al., 2020; Rahman et al., 2020; NPD, 2021; Johnson et al., 2022). The Draupne Formation is a source rock distributed in the East Shetland Basin, the Viking Graben, and over the Horda Platform. While the Draupne and Hekkingen formations are considered equivalent shales, both with major source rock potential, key differences exist in their respective geological histories, resulting in significant distinctions between them (Hansen et al., 2020; Johnson et al., 2021; Johnson et al., 2022). Both formations also act as seals, with the Draupne Formation being critical to future CCUS projects in the North Sea (Johnson et al., 2021; Rahman et al., 2021; Johnson et al., 2022).

The deposition of the Draupne Formation was influenced by two major rifting events that occurred in the Norwegian North Sea (Ziegler, 1992; Faleide et al., 2008). The first event occurred in the Triassic, followed by post-rifting quiescence. This event was followed by a second larger rifting event that occurred in the Late Jurassic – Early Cretaceous forming significant structural relief within the region (Whipp et al., 2014). Coupled with eustatic sea-level rise, the subsequent anoxic, restricted environment was ideal for deep marine anaerobic conditions leading to the deposition of a source rock shale (Hansen et al., 2020; NPD, 2021). Thickness ranges from ~0 to 550 m, with the total depth range measured from wells in the Norwegian North Sea being from ~600 to 6500 m (Hansen et al., 2020; Johnson et al., 2021; NPD, 2021; Johnson et al., 2022). A typical range of total organic carbon (TOC) content for the Draupne Formation is 2–15 wt% with a mean value around 8.5 wt% (Hansen et al., 2020; Johnson et al., 2021). Kerogen type is predominantly Type II and Type II-S, with some Type III (Zadeh et al., 2017; Johnson et al., 2021; present study). Within the area studied, the mineralogy of the Draupne shales is relatively homogeneous with 40–70 wt% clay, 20–60 wt% quartz, and feldspar, and 0–20 wt% carbonate and pyrite (Hansen et al., 2020; Rahman et al., 2020; Johnson et al., 2021). Mineralogical compositions by weight percentage show a much larger proportion of soft minerals than hard minerals, with an average ratio of 2:1 (Rahman et al., 2020; Johnson et al., 2021; present study).

Like the Draupne Formation, the Hekkingen Formation underwent two rifting events, combined with eustatic sea level rise, resulting in a restricted marine ideal for the deposition of organic-rich shales environment (Dore et al., 1985; Hansen et al., 2020; NPD, 2021). Unlike the Draupne Formation in the North Sea, the Barents Sea experienced multiple uplift, and erosion episodes with estimates uplift around 1–1.2 km in the study area resulting in a diminished thickness for the Hekkingen Formation in the range ~ 0–100 m (NPD, 2021; Henriksen et al.,

2011; Baig et al., 2016). Furthermore, the erosion events in the Barents Sea coincide with significant exhumation that varies from 0.4 to 3.0 km, with an approximate 1.3 km of exhumation at well 7125/1–1 (Fig. 1b, Zadeh et al., 2017, Baig et al., 2019, Ohm et al., 2008; Henriksen et al., 2011; Baig et al., 2016). The large variation in the exhumation and subsequent erosion is correlated to localized salt remobilization (Muller et al., 2019). As a result, the present-day depth ranges for the Hekkingen Formation measured from wells in the Barents Sea is both narrower and shallower, from ~500 to 4300 m, than for the Draupne Formation (NPD, 2021). Despite the Hekkingen Formation being thinner, it is a prolific source rock with typical TOC content of 5–20 wt%, and a mean value of 12.2 wt% (Hansen et al., 2020). Kerogen type is predominantly Type II and Type II-S, with some Type III present (Abay, 2017; Johnson et al., 2019; Johnson et al., 2021). Mineralogical analyses within the area studied show that the Hekkingen Formation shales are composed of 60–70 wt% clay, 30–40 wt% quartz and feldspar, and 10–20 wt% carbonate and pyrite (Hansen et al., 2020; Johnson et al., 2021). Mineralogical compositions by weight percentage show a much higher proportion of soft minerals than hard minerals in the Hekkingen Formation, with the average ratio being 3:1 (Hansen et al., 2020; Johnson et al., 2021; present study).

Some broad similarities exist between the Draupne and Hekkingen Formations, including a shared depositional story. However, some clear and marked differences also exist. Notably, the Hekkingen Formation typically contains a higher clay percentage, while the Draupne Formation contains relatively more quartz and feldspar. Carbonate contents in both formations are roughly equal and considered low. Additionally, the Hekkingen Formation has a tendency to be a richer source rock with both a higher average and a greater range of TOC values than the Draupne Formation. The combination of these data indicate that the Hekkingen Formation was formed in a more restricted, more anaerobic environment than the Draupne Formation (Johnson et al., 2021). Subsequent diagenetic histories for the two formations are much different. While the Hekkingen Formation experienced significant erosion and exhumation in the Barents Sea as a result of salt remobilization, the Draupne Formation experienced comparatively little erosion in the Norwegian North Sea. Increased clay content and increased kerogen content have countermanding impacts on the geomechanical nature of the shale (Mondol et al., 2007; Brochard et al., 2013; Mondol, 2018; Johnson et al., 2021). Previous studies suggest that the samples for this study reached roughly equivalent depths (Baig et al., 2016; Zadeh et al., 2017; Baig et al., 2019); however, this depth does not necessarily correlate to equivalent maturation. Contrary to this, Johnson et al. (2021) showed that both geochemical and rock physics data support that

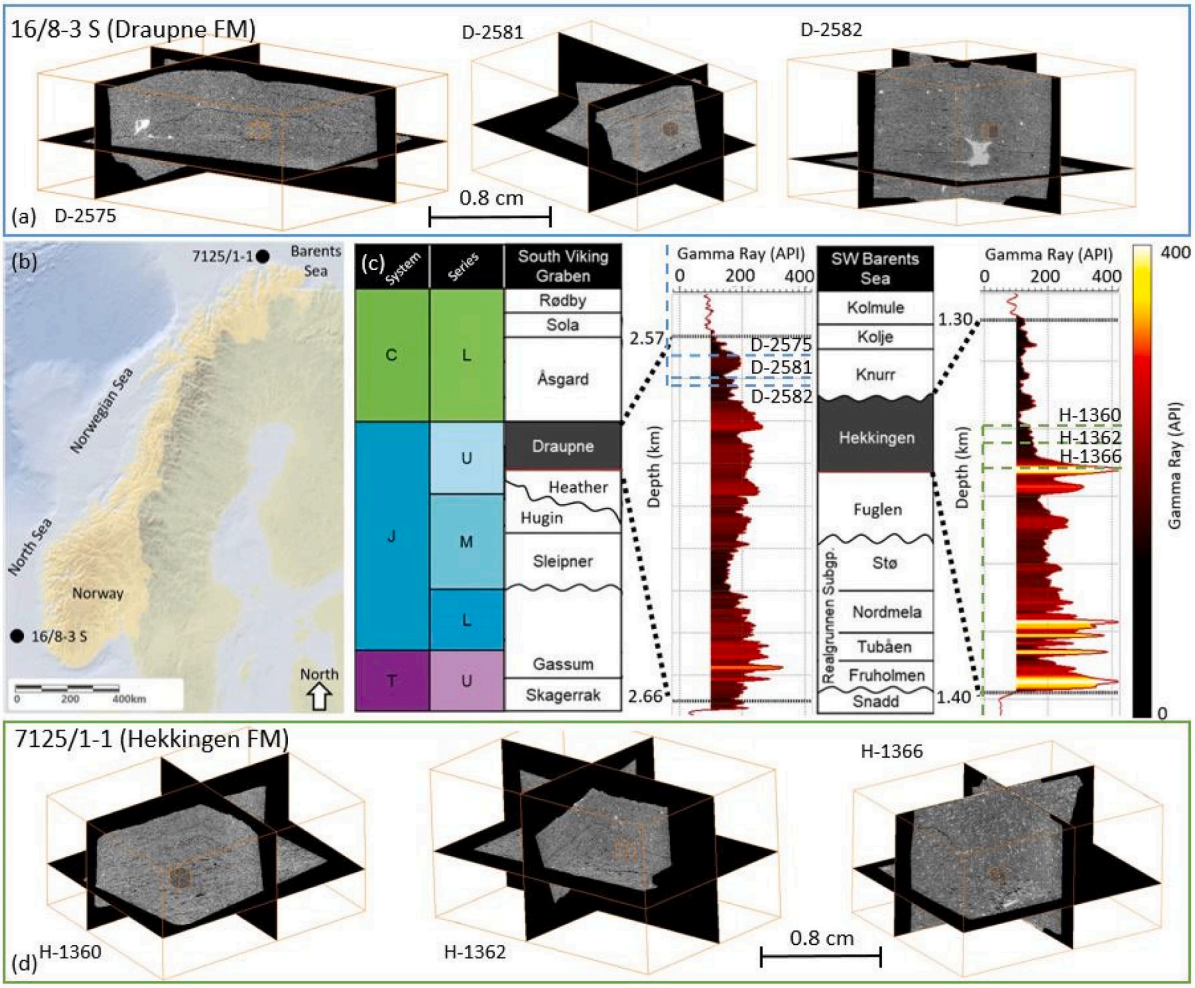

Fig. 1. (a) Synchrotron -ray microtomography images from three samples from the Draupne Formation with data collected at two spatial resolutions. The large cubes indicate the edges for the low-resolution scan (voxel size 6.63 μm), and the small cubes indicate the edges of the high-resolution scan (voxel size 0.7 μm). (b) Map showing the location of the two wells the samples were taken from. The Draupne Formation (well 16/8–3-5) samples are from the North Sea, and the Hekkingen Formation samples (well 7125/1–1) are from the Barents Sea. (c) The geological timeline given with Gamma Ray well logs for the two wells show that the Draupne and Hekkingen Formations are both organic-rich shales. The six samples, three from each formation, have depth labels and sample numbers indicated on the Gamma Ray log. (d) Synchrotron X-ray microtomography images from three samples from the Hekkingen Formation with the data collected at two resolutions.

the Draupne shale samples collected in well 16/8–3 S are immature and ductile in nature, while the Hekkingen shale samples collected in well 7125/1–1 are in the early oil generation window and are comparatively in the transition towards becoming more brittle as a result of kerogen maturation. Some limited oil and gas expulsion may have begun to occur for the Hekkingen shale samples, while this should not be the case for the Draupne shale samples.

2.2. Organic-rich shale samples

The six shale samples were collected at depth from borehole cores with three samples in the well 16/8–3 S drilled in the Draupne Formation and three samples in the well 7125/1–1 drilled in the Hekkingen Formation (Table 1, Fig. 1). Well logs were used to verify the sample's exact location and compare logging data with microstructural observations and geochemical measurements using the Rock-Eval technique. The depth range of the Draupne Formation in well 16/8–3 S is 2570–2660 m, with shale samples collected in the range 2575–2583 m and the depth range of the Hekkingen Formation in well 7125/1–1 is 1300–1400 m, with shale samples collected in the range 1360–1367 m (Fig. 1b).

3. Methods

3.1. Multiscale synchrotron microtomography imaging

For the six shale samples, a one centimeter core was drilled and imaged in three dimensions using synchrotron X-ray microtomography. Images were acquired on the beamline ID19 at the European Synchrotron Radiation Facility in Grenoble, France. X-ray adsorption data were collected at two different spatial resolutions. Each centimeter-scale core sample was scanned entirely with a spatial sampling of 6.63 μm/voxel and an energy of 110 keV. Then, a zoom located in the middle of the sample was acquired using a local microtomography technique with a spatial sampling of 0.7 μm/voxel and an energy of 115 keV (Fig. 1). X-ray adsorption data were reconstructed using a phase retrieval reconstruction algorithm (Mittone et al., 2017). The spatial resolution of the images was not measured, but a previous study indicated that it is between two and three times the voxel size (Mittone et al., 2017). The 16-bit images were saved in TIFF format and converted to 8-bit format for further processing. We verified that the conversion from 16-bit to 8-bit did not change the results shown below on all samples.

To process the data, we developed an image analysis workflow that includes a correction for the background variation, denoising, thresholding, and segmentation (Fig. 2). We used the image processing software AvizoFire (Avizo Reference Manual, 2021). The beam hardening artifact is corrected by identifying and removing the background from the original grayscale 3D image. To preserve the kerogen lens shape and denoise the image, a non-local means filter is used (Buades et al., 2011). This filter combines Gaussian smoothing and edge-preserving techniques to account for the kerogen boundaries. In order to separate the kerogen lenses, a unique threshold was determined for each shale sample. To enhance the results of the thresholding, a watershed algorithm is utilized to fill in local minima on the greyscale image that is a part of the kerogen lens without filling in the same pixels elsewhere in the 3D image. After thresholding, the image segmentation procedure allows separating the various kerogen lenses and microfractures from one another and labels them by different numbers and colors (Fig. 3). Few open microfractures have the same adsorption range as the kerogen lenses, and they were removed manually from the segmented image (Fig. 3).

After the images were segmented, we performed a series of quantitative analyses on the kerogen lenses such as volume fraction, size distribution, shape, smoothness, and dominant orientation. All calculations were carried out for the images of both 6.63 μm and 0.7 μm voxel sizes. The volume fraction of the kerogen lenses (v. %) was calculated by summing the volume of all lenses and dividing by the total volume of the 3D sample. To quantify the spatial distribution of the kerogen lenses inside the shale matrix, we calculated the position of the center of mass for each kerogen lense along each axis of the 3D image. These measurements were performed only on the images with 0.7 μm voxel size where the high-resolution allows separating each kerogen lens unambiguously.

To analyze kerogen lens shape and orientation in three dimensions, we calculated the 3D inertia matrix of each kerogen lense.

$$\mathbf{M_{3D}} = \begin{vmatrix} M_{xx} & M_{xy} & M_{xz} \\ M_{xy} & M_{yy} & M_{yz} \\ M_{xz} & M_{yz} & M_{zz} \end{vmatrix} \quad (1)$$

and then we calculated the three eigenvalues of the inertia matrix, $\lambda_1 > \lambda_2 > \lambda_3$ (Fig. 4). If the shape of a kerogen lens was a perfect ellipsoid, these three eigenvalues would correspond to the lengths of the three axes of the ellipsoid. For each kerogen lens, we also calculated three other parameters, the anisotropy, A_{3D}, the flatness, F_{3D}, and the elongation, E_{3D}, defined as:

$$A_{3D} = 1 - \frac{\lambda_3}{\lambda_1}; F_{3D} = \frac{\lambda_3}{\lambda_2}; E_{3D} = \frac{\lambda_2}{\lambda_1} \quad (2)$$

These three shape parameters have values in the range 0–1.

The dominant direction of a kerogen lens is defined by the orientation of the largest eigenvector of the inertia matrix. This direction is measured with two angles, θ and φ, which describe the orientation of the largest eigenvector relative to the x-axis and the z-axis of the 3D image, respectively (Fig. 4). Because the core samples were cored perpendicular to bedding, the z-direction is perpendicular to bedding and the XY plan is the bedding plane.

We also use the shape parameters α and β that describe the distribution of data in a range [0–1] (Rose and Smith, 2002). The probability density function of a given variable, x, is fitted with a function that contains two exponents, α and β:

$$f(x;\alpha,\beta) = \frac{x^{\alpha-1}(1-x)^{\beta-1}}{B(\alpha,\beta)} \quad (3)$$

Table 1
List of shale samples (D = Draupne, H = Hekkingen) used in the present study, with depth, temperature (from Bottom Hole Temperature, BHT), and mineralogical composition.

Sample	Depths (m)	Temperature (°C)	Mineralogy
D-2575	2575.30	86.2	Mixed clays (illite, kaolinite), quartz, pyrite, micas (muscovite), calcite, dolomite, siderite, apatite
D-2581	2581.65	86.4	Mixed clays (illite, kaolinite, smectite), quartz, pyrite, micas (muscovite), albite, calcite, dolomite, siderite, chlorite
D-2582	2582.15	86.4	Mixed clays (illite, kaolinite), quartz, pyrite, albite, calcite, dolomite, siderite, chlorite, rutile, sphalerite
H-1360	1360.85	48.2*	Mixed clays (illite, kaolinite), quartz, pyrite, micas (muscovite, biotite), potassium feldspar, calcite, dolomite
H-1362	1362.55	48.3*	Mixed clays (illite, kaolinite), quartz, pyrite, micas (muscovite), potassium feldspar, calcite, dolomite, apatite, rutile
H-1366	1366.40	48.4*	Mixed clays (illite, kaolinite), quartz, pyrite, micas (muscovite, biotite), potassium feldspar, calcite, sphalerite

* While the Draupne Formation shale (North Sea) is now situated at greater depth than the Hekkingen Formation shale (Barents Sea), the Barents Sea samples have been uplifted ~1300 m (Zadeh et al., 2017; Baig et al., 2019). Therefore, the Hekkingen Formation shale samples have undergone temperatures greater than 80 °C in the past (Zadeh et al., 2017).

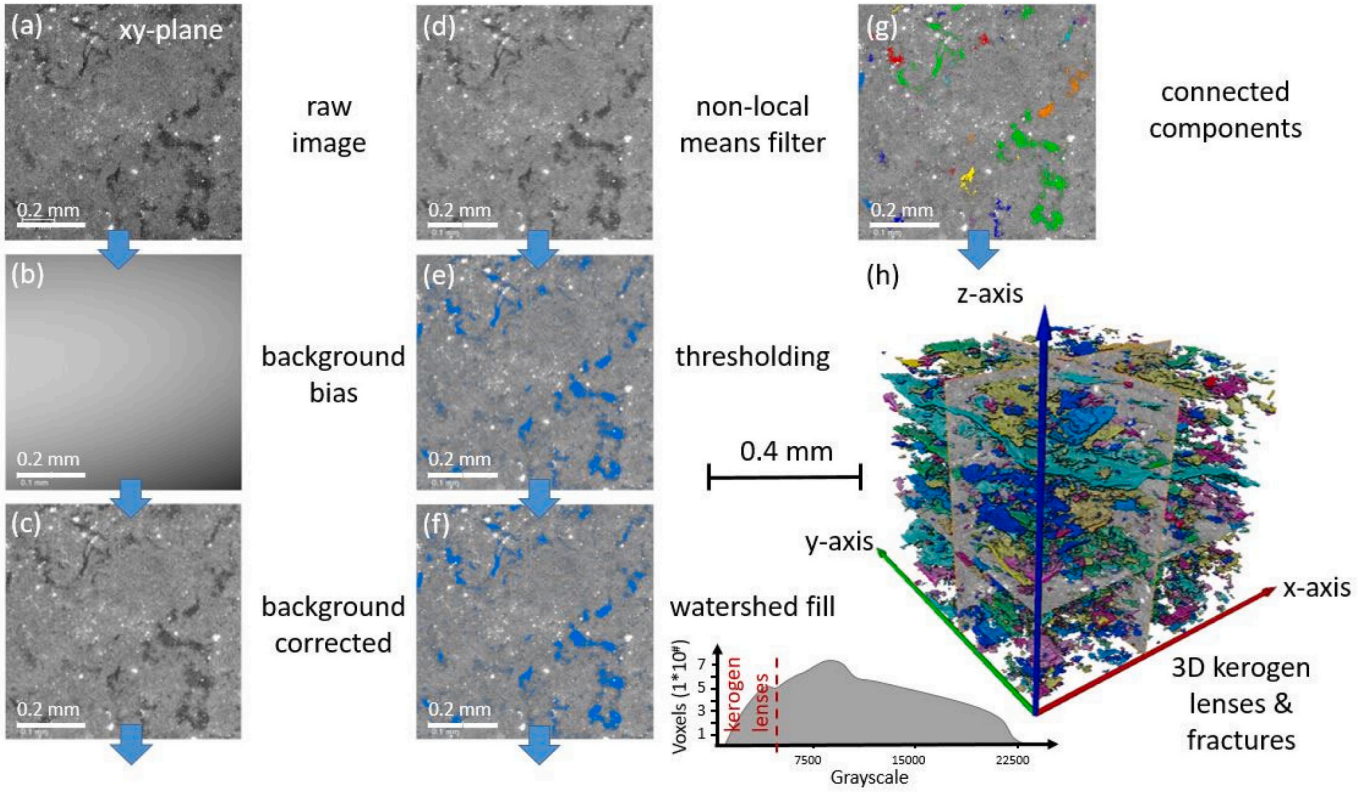

Fig. 2. Three-dimensional synchrotron X-ray microtomography imaging workflow (sample D-2575, 0.7 μm voxel size, 16 bits). (a) Raw initial X-ray phase-contrast image. (b) Background bias is identified and then (c) removed to obtain a background-corrected image. (d) Then, the image is denoised with a non-local means filter. (e) Simple thresholding is applied to separate kerogen lenses and fractures from the rock matrix. (f) Then, a watershed filling procedure is utilized to capture every kerogen lens and microfracture. (g) Image segmentation is followed by separating the data into kerogen lenses and fractures, respectively, by identifying components connected in three dimensions. (h) Volume rendering of the shale sample, the kerogen lenses, and the fractures. The grayscale histogram of the shale volume and the threshold used to segment the kerogen lenses and fractures is displayed.

where the variable x is one of the kerogen lens shape parameters (Eq. 2), B is a normalization constant in order to ensure that the total value of α and β sum to 1. The values of α and β quantify the similarity of curve shapes. If the curve shapes are similar, then the data distribution under those curves is also similar.

3.2. Scanning electron microscopy (SEM) imaging

We have prepared thin sections of the six shale samples in the directions parallel and perpendicular to the natural shale lamination (plane and section views, respectively). The thin sections were coated with carbon and imaged using a Hitachi SU5000 field emission scanning electron microscope, with Electron Dispersive Spectroscopy (EDS) detector, at an acceleration voltage of 15 kV, at the University of Oslo. The images collected cover a range of surface areas. The largest image has a surface area of 3.0×2.25 mm^2, while the smallest image has a surface area of ~0.01×0.007 mm^2 (Fig. 5).

To quantify the size, shape, and distribution of kerogen lenses on the SEM images, we performed image analysis using the image processing software AvizoFire. Because both epoxy glue and kerogen lenses appear black in SEM images, we separated kerogen from epoxy by chemical composition using EDS data.

The image analysis workflow consists of the following steps: denoising, thresholding, and segmentation (Fig. 6). A non-local means filter was applied to denoise the original grayscale SEM image (Buades et al., 2011). Then, we separated the organic content from the surrounding non-organic minerals. This was done by selecting a greyscale threshold that is unique to the phase of interest (Ketcham, 2005). After this segmentation step, we assigned to each kerogen lens a number (label), indicated by a set number of colors (Fig. 6d).

We quantitatively characterized the size distribution, shape, smoothness, and dominant direction of the kerogen lenses using the same techniques we applied for the microtomography data (Section 3.1). We calculated the two-dimensional inertia matrix of each kerogen lens. The dominant direction of the kerogen lens was defined by the direction of the largest eigenvector of the inertia matrix and is given by the angle θ relative to the x-axis of the 2D scanning electron microscopy image (Fig. 4b).

$$\mathbf{M_{2D}} = \begin{vmatrix} M_{xx} & M_{xy} \\ M_{xy} & M_{yy} \end{vmatrix} \tag{4}$$

In two-dimensions, the flatness parameter is not defined, and we calculated the 2D anisotropy and elongation parameters as follows:

$$A_{2D} = 1 - \frac{\lambda_3}{\lambda_1}; E_{2D} = \frac{\lambda_2}{\lambda_1} \tag{5}$$

We also quantified the roughness of the kerogen lenses by using the rugosity parameter, *Ru*, defined by Hamblin and Stachowiak (1995). This parameter quantifies the smoothness of a particle's edges based on the projected particles boundaries as triangles on many scales. Its values are between 0 for a circle and 1 for a highly 'spiky' shape (Hamblin and Stachowiak, 1995). The calculation of this parameter involves measuring the height and sharpness of all convex triangles. This step produces a multi-scale measure of particle spikiness utilized to describe the smoothness of kerogen lenses.

Finally, we used the segmented images (Fig. 6d) to calculate the areal percentage (a. %) of kerogen. We selected only images with surface areas in the range 0.6×0.45 to 3.0×2.25 mm^2 to ensure that a

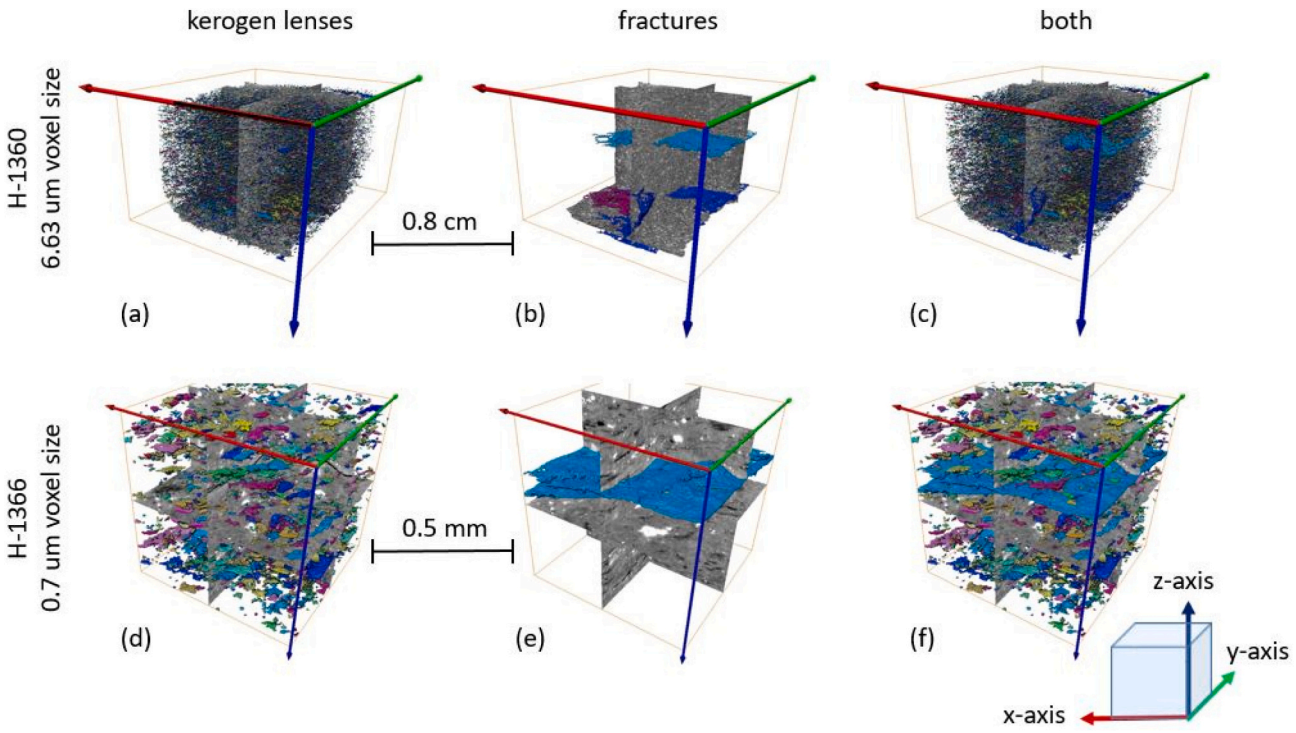

Fig. 3. Three-dimensional rendering views of two shale samples, H-1362, and H-1366. Sample H-1362 is shown at the 6.63 um voxel size, with H-1366 shown at the 0.7 um voxel size. Panels (a) and (d) display the kerogen lenses, panels (b) and (e) display the fractures, and panels (c) and (f) show both kerogen lenses and fractures. The axes are indicated, and the z-axis is perpendicular to sedimentary bedding. Most fractures are parallel to bedding, except one fracture in (b) that also contains a vertical plane (dark blue). (For interpretation of the references to colour in this figure legend, the reader is referred to the web version of this article.)

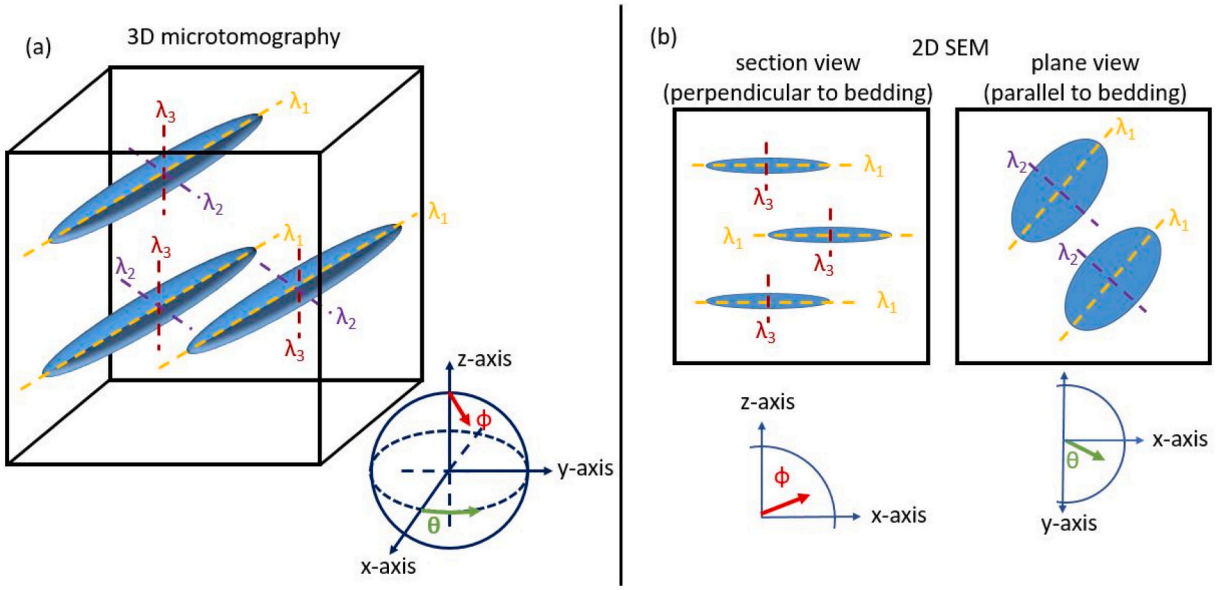

Fig. 4. Sketch showing the eigenvalues of kerogen lenses calculated from the inertia matrix ($\lambda_1 > \lambda_2 > \lambda_3$) and the orientation parameters (θ, φ) for (a) the 3D microtomography data and (b) the 2D scanning electron microscopy data. For the 2D SEM images, we call section view a thin section cut perpendicular to bedding and plane view a thin section cut parallel to bedding.

sufficiently large number of kerogen lenses is present on the image such that the areal percentage calculated is representative of the kerogen content in the shale.

3.3. Geochemical and mineralogical composition

The mineralogical composition of the Draupne and Hekkingen Formations has been characterized in previous studies (Skurtveit et al., 2015; Nooraiepour et al., 2017; Zadeh et al., 2017; Kalani, 2018; Hansen et al., 2020; Johnson et al., 2021), and is confirmed here. Mineralogy of the samples was measured using X-ray diffraction and confirmed on SEM images of the thin sections (Table 1). Density was calculated for every sample using the weight and volume of the core samples used for 3D microtomography imaging and compared to the well log data. Total

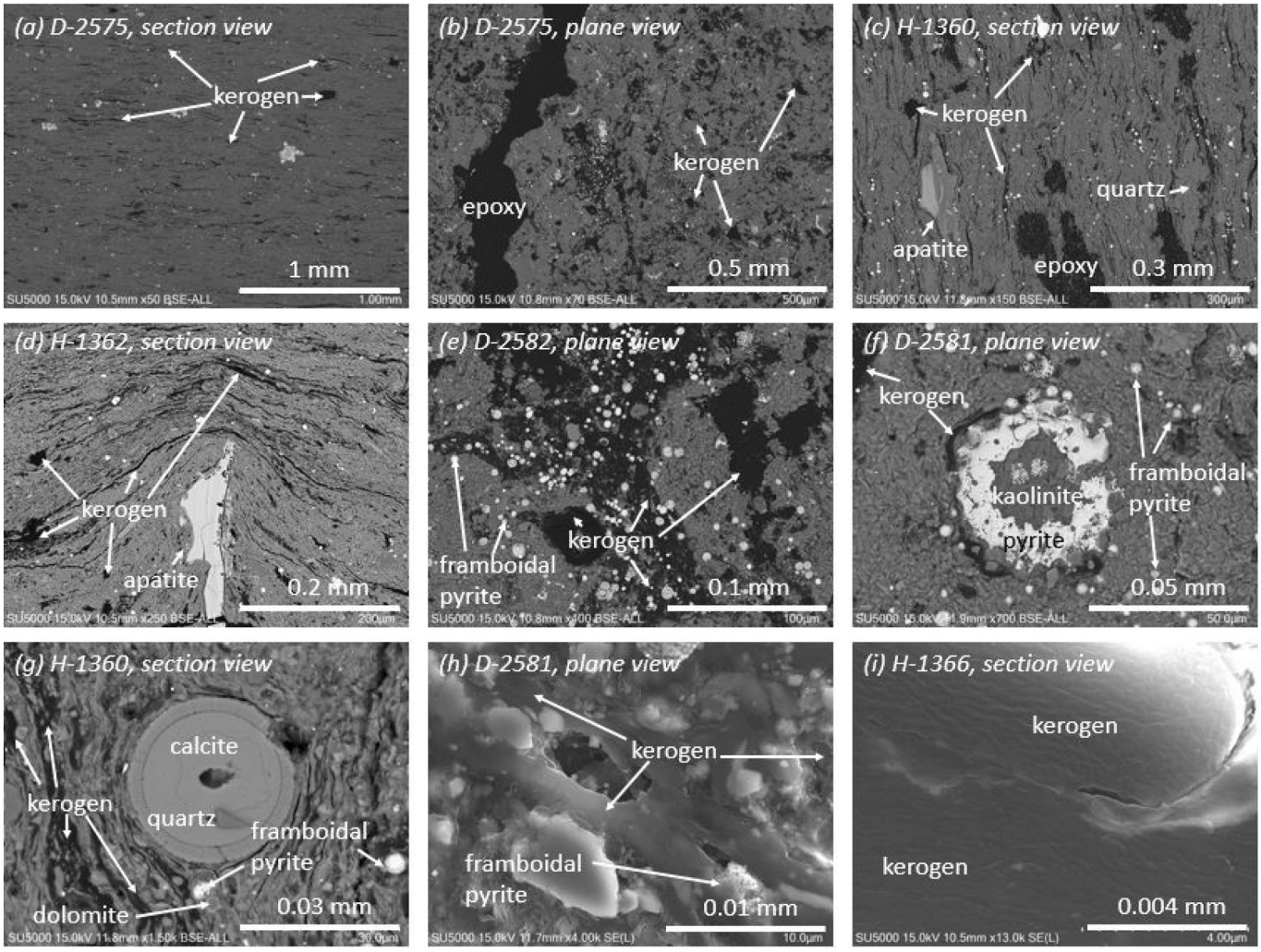

Fig. 5. Scanning electron microscopy images of the studied shale samples. (a) Sample D-2575 in section view (perpendicular to bedding). (b) Sample D-2575 in plane view (parallel to bedding). (c) Sample H-1360 in section view. (d) Sample H-1362 in section view. (e) Sample D-2582 in plane view. (f) Sample D-2581 in plane view. (g) Sample H-1360 in plane view. (h) Sample D-2581 in plane view. (i) Sample H-1366 in section view. See Fig. 4 for the definition of section and plane views.

organic content of the shale samples were taken from Rock-Eval data provided by the Norwegian Petroleum Directorate (NPD, 2021). The typical method of pyrolysis was used on cores/cuttings to determine total organic contents. Well log values of total organic content were calculated using the method of Schmoker and Hester (1983) due to the availability of well logs.

Using SEM data, the amount of organic content was derived by ascertaining the kerogen content within any given image and then accounting for how much of the total area it represented. Similarly, for the 3D microtomography data, the amount of organic content was determined by first identifying all the kerogen lenses and then accounting for how much of the total volume they represented. This calculation was performed at the two spatial sampling distances, 6.63 μm /voxel and 0.7 μm /voxel.

In order to make the comparison between the geochemical and petrophysical calculations of total organic content with total organic content derived from the SEM images and 3D microtomography data, the later total organic content measurement was converted from areal (a. %) or volume percentage (v. %) of the total to a weight percentage (wt%). The following conversion formulas were used:

$$W_{sample} = V_{sample} \times \rho_{sample} \tag{6}$$

where W_{sample} is the weight of the sample from laboratory measurements, V_{sample} is the volume of the sample used for 3D microtomography imaging, and ρ_{sample} can be derived from the previous two measurements. In addition,

$$W_{kerogen} = V_{kerogen} \times \rho_{kerogen} \tag{7}$$

where $W_{kerogen}$ is the weight of the kerogen calculated, $V_{kerogen}$ is the volume of the kerogen calculated from 3D microtomography, and $\rho_{kerogen}$ is 1.25 g/cm^3. Because it was not possible to obtain the density of each kerogen lens, we use here a kerogen density representative for an average of Type II and Type II-S kerogens from the region (Okiongbo et al., 2005), and

$$TOC_{sample} = \frac{W_{kerogen}}{W_{sample}} \tag{8}$$

where TOC_{sample} (wt%) is the total organic content derived from the ratio between W_{sample} and $W_{kerogen}$, as calculated in Eqs. 6 and 7.

4. Results

4.1. Fracture shape and size

The samples contain fractures that may have formed during decompaction after samples were recovered from depth. Here, we

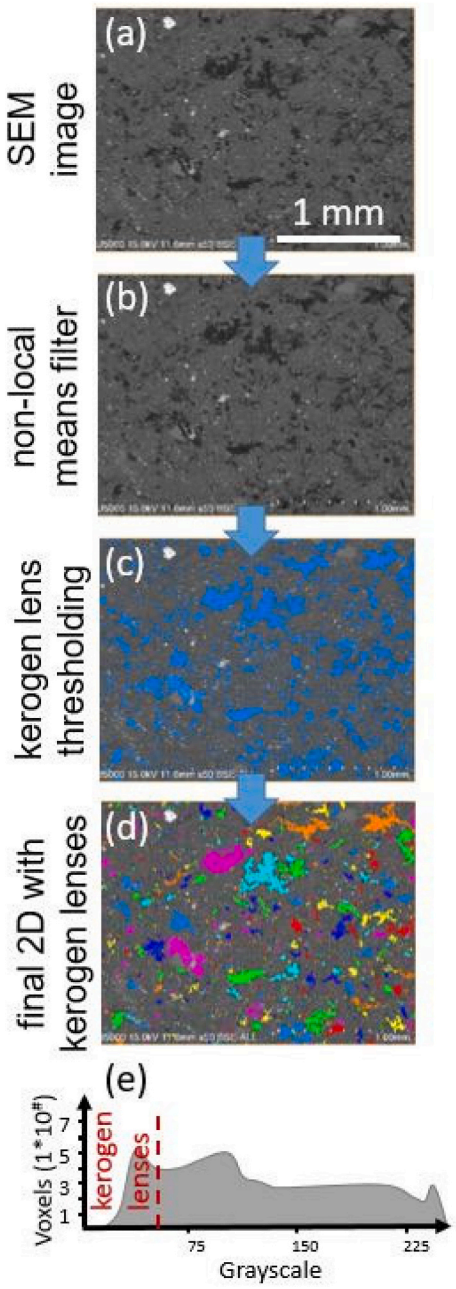

Fig. 6. Data segmentation of SEM images including the (a) original SEM image where we applied (b) a non-local means filter, (c) thresholding in order to select the kerogen lenses, and (d) image segmentation separating out each individual lens. (e) The grayscale histogram indicating the cutoff for separating the kerogen lenses from the rest of the image is indicated.

consider that a microfracture is a single entity of connected voxels, but it could have been formed by merging smaller microfractures with slightly different orientations. We characterize microfractures and their microstructural relationships with kerogen lenses. Fig. 3 shows a three-dimensional rendering of the kerogen lenses and fractures in two samples from the Hekkingen Formation (H-1360, H-1366). The number of fractures varied in each sample (3–13 fractures/sample), with three fractures present in sample H-1362 (Fig. 3b). All of the fractures are mainly horizontal except for one fracture in sample H-1362 (dark blue in Fig. 3b) that contains both horizontal and vertical planes. Most fractures are only found at the 6.63 μm /voxel sampling distance. However, two samples, D-2575 (Fig. 7) and H-1366 (Fig. 3e), contain fractures that can be seen in the 0.7 μm voxel size images.

The interactions between kerogen lenses and fractures can be seen in Fig. 7. A microfracture may intersect several kerogen lenses along its path. However, the total number of kerogen lenses that are in direct contact with fractures is relatively small. The kerogen lenses interact with both the top and bottom of the fracture with an angle of approximately 15 degrees, and in multiple instances, the fracture pathway changes orientation nearby a kerogen lens (Fig. 7). Since these kerogen lenses were connected to the fracture in the 3D tomography data, it was not possible to separate the two. However, the number of kerogen lenses removed in this process was very small (<0.01%), and we consider the impact of this effect on the kerogen statistics presented below very low.

In the six samples scanned at low resolution, we detected a total of 32 microfractures. Only two high-resolution scans contain fractures. The shape parameters of the fractures (Table 2) indicate that fracture length is significantly greater than aperture, with average values F = 0.997 and A = 0.003, respectively. Elongation provided a range of values distributed between 0 and 1, with 17 of the 32 fractures in the range 0.4–0.6 (Table 2). This result indicates that the microfractures have a more or less isotropic shape in their main plane. Together, these data show that microfractures have a penny shape, with an aperture around two orders of magnitude smaller than their length. All fracture planes, except one, are oriented within 25 degrees of bedding. Inside of this category, 17 microfractures were within 10 degrees, and 29 were within 20 degrees. This result indicates that microfracture orientations do not deviate significantly from bedding within our samples.

4.2. Kerogen lens shape and orientation

Fig. 8 shows a three-dimensional rendering of three representative kerogen lenses. The kerogen lenses often do not conform to a typical 'penny-shape' used in numerical models (e.g. Jin et al., 2010; Chauve et al., 2020). Instead, the kerogen lenses occur with a wide variety of shapes and forms. This range in shapes is most apparent in plane-view (XY-plane), where there is a smaller difference in axis size, leading to a larger variety in possible aspect ratios affecting their final form (Fig. 8a). The lens ID #974 from sample H-1360 has a typical penny-shape (Fig. 8). However, in contrast to the typical penny-shape, lens ID# 5292 in sample D-2582 has a tear drop shape, while lens ID # 2697 in sample D-2575 is almost lenticular (Fig. 8). While most kerogen lenses can clearly be described by a compact volume, some lenses appear to be a patchwork of many connected lenses. Another feature of the individual kerogen lenses is the presence of holes that penetrate a certain portion of them (Fig. 8a and c, sample H-1360, lens ID#974).

The shape of all kerogen lenses were also quantitatively analyzed in both plane and section views (Table 3, Fig. 9). In section view, the anisotropy and flatness can be calculated in this reference frame, while the elongation applies to plane-view. In samples scanned at 6.63 um/voxel we identified around 10^4 lenses per sample. In samples scanned at 0.7 um/voxel, we identified around 10^3 lenses per sample. Anisotropy and flatness parameters for all samples are asymmetrically skewed towards higher levels of anisotropy between axis lengths (Table 3, Fig. 9). The skewness is the largest for the anisotropy parameter, with almost all data for the high-resolution scans with values around 0.7, and almost all data for the low resolution scans with values above 0.85 (Table 3, Fig. 9). The flatness parameter shows a broad distribution with almost all data between 0 and 0.8 for the high-resolution scans and almost all data between 0 and 0.4 for the low-resolution scans (Table 3). As the elongation parameter explores plane view, both the total distribution is larger, and the position of the peak is more centered. For elongation, the range of values are within 0.21–0.28 (Table 3). As the dataset size increases, the peak position shifts towards ~0.2 from ~0.3 (Table 3, Fig. 9). The relatively low peak position value indicates that kerogen lenses have a tendency towards an asymmetrical shape (Table 3, Fig. 9). Although, the broad distribution also shows that lenses approaching symmetry are also relatively commonplace.

In our dataset, all of the α and β values across different image

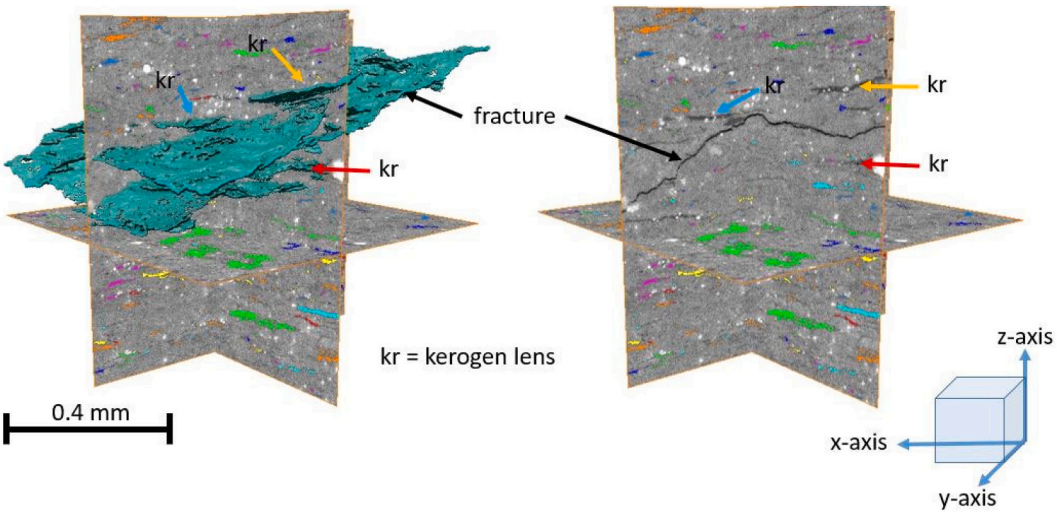

Fig. 7. a) View of sample D-2575 at 0.7 um voxel size showing the presence of kerogen lenses (kr) attached to a fracture. b) Same as panel a) without the 3D rendering of the fracture.

Table 2
Mean values of anisotropy, flatness, elongation, and orientation, φ, for the 32 fractures identified in the six samples. For the anisotropy, flatness, and elongation, the value is in the range 0–1, and the relative proportion in each class (i.e quartile) is given.

Parameters	Average mean	Class (0.00–0.25)	Class (0.25–0.50)	Class (0.50–0.75)	Class (0.75–1.00)
Anisotropy, A	0.003	100%	0%	0%	0%
Flatness, F	0.997	0%	0%	0%	100%
Elongation, E	0.47	21.9%	37.5%	25.0%	15.6%
Orientation, φ	10.6°	–	–	–	–

resolutions are very close (Table 3). The fact that α and β values are similar to one another quantitatively shows that the statistical comparisons between 3D and 2D data hold and are valid.

We utilize the orientation parameters φ and θ to investigate whether kerogen lenses have a dominant alignment direction with their longest principle axis (λ_1). Qualitatively, the high-resolution tomography data from sample H-1366 (Fig. 3d and f) indicate that kerogen lenses have a similar alignment to one another along the y-axis.

The kerogen lenses orientation is represented in Fig. 10 for both microtomography and SEM data. The longest axis of the lenses is oriented close to 90° from the vertical direction, indicating that the main plane of kerogen lenses is oriented parallel to bedding (Fig. 10 a, b). The largest deviation for φ for both the high and low resolutions data is 30 degrees from the bedding plane. Thus, the data at both resolutions show an alignment between the main plane of kerogen lenses and bedding plane, with a rapidly diminishing number of lenses that deviate from bedding (Fig. 10 a, b).

In the bedding plane (plane view in Fig. 10 c, d), the lenses for different samples are oriented along with various directions. This result comes from the sampling because core samples were not oriented when extracted from the boreholes. The total range of angles θ varies between samples. For example, a trend of kerogen lenses directions is measured within the range 165–330 degrees for sample H-1366 (Fig. 10c). However, the same trend can also be relatively confined in a smaller angular range; for example, samples D-2575 and D-2582 both show a 45 degrees dominant trend. Similarly, for the 0.7 μm /voxel data, the dominant directional trends range from 45 to 60 degrees for all samples (Fig. 10).

To summarize, these data show that the kerogen lenses are flat objects whose longest axes are oriented along the bedding plane and that in this plane, the orientation of these lenses has weak directionality.

4.3. Kerogen lens size distribution from synchrotron microtomography data

The segmented tomography images were used to quantify the distribution of sizes of kerogen lenses. Using the spatial coordinates of the center of mass of each kerogen lens in high-resolution images, Fig. 11 displays the distribution of the centers of mass of all of the kerogen lenses in the X-Z and Y-Z planes (perpendicular to bedding) along the X- and Y-axis, and in the XY plane (parallel to bedding) along the *Z*-axis. The two components perpendicular to bedding show similar curve trends and standard deviations (Fig. 11b, c). This observation suggests a fairly uniform and random distribution of kerogen lenses along the bedding laminations. Along the Z-axis (Fig. 11a), fluctuations in the positions of the centers of mass are larger, suggesting the distribution of kerogen lenses in the direction perpendicular to the lamination is more heterogeneous than along bedding.

One can also differentiate two groups of shales based on total organic carbon (TOC wt%) content and the centre of mass results. The two Hekkingen samples contain above 12 wt% total organic content according to Rock-Eval data, and the remaining four samples contain between 6 and 8 wt% total organic content (Table 4, Fig. 11). Higher values of total organic content correlate with lower total counts of separate kerogen lenses. This inverse relationship suggests that the volume of kerogen lenses in the samples with higher TOC (i.e., H-1362 and H-1366) are greater than for samples with the lower TOC.

Fig. 12a shows the distribution of kerogen lens volumes in relation to the total count in a normalized probability distribution function on a logarithmic scale. Kerogen lenses with volumes between 1×10^{-16} and 5×10^{-13} m^3 are taken from the high-resolution tomography images with 0.7 μm /voxel. Kerogen lenses with volumes between 2×10^{-13} to 7×10^{-10} m^3 are taken from the low-resolution images with 6.63 μm /voxel. The kerogen lens volumes of these two datasets overlap in the range 9×10^{-14} to 1×10^{-12} m^3, as shown by the bounding orange dashed

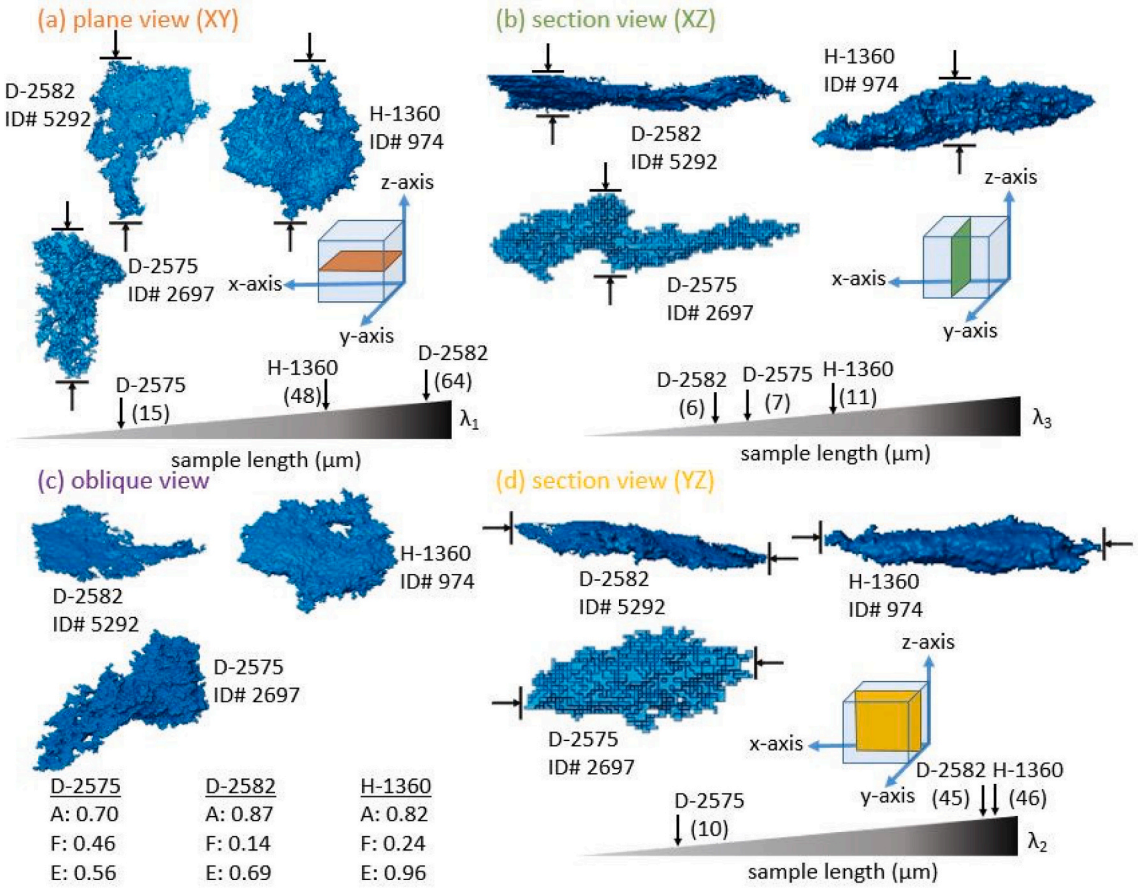

Fig. 8. Three-dimensional rendering of three representative kerogen lenses in samples D-2582 (lens ID# 5292), H-1360 (lens ID# 974), and D-2575 (lens ID# 2697) in (a) plane view, XY-plane (b) section view, XZ-plane (c) oblique view, askew of the XY-plane and (d) section view, YZ-plane. Sample lengths for λ_1, λ_2, and λ_3 are given on scale bars where units are given in micrometers. The anisotropy (A), flatness (F), and elongation (E) values for each kerogen lens are given (bottom left corner), and the eigenvalues of each lens are displayed.

Table 3
Peak position and areas under the asymmetrical curves described by curve shape parameters α and β (Fig. 9) for the anisotropy, flatness, and elongation in both 2D and 3D. Bold numbers indicate the quartile with the greatest percentage of kerogen lenses (% Values).

Data & parameter	Position of the peak	α	β	% Values (0.00–0.25)	% Values (0.25–0.50)	% Values (0.50–0.75)	% Values (0.75–1.00)
0.7 μm / voxel, anisotropy (A_{3D})	0.97	11.83	1.33	0.0	0.5	6.3	**93.3**
6.63 μm / voxel, anisotropy (A_{3D})	0.99	12.28	0.49	0.1	0.3	1.1	**98.5**
0.7 μm / voxel, flatness (F_{3D})	0.15	1.36	3.45	**54.2**	31.5	11.6	2.6
6.63 μm / voxel, flatness (F_{3D})	0.10	0.84	4.22	**78.8**	14.5	5.3	1.4
SEM anisotropy (A_{2D})	0.88	3.31	1.74	4.3	17.5	38.3	**39.9**
0.7 μm / voxel, elongation (E_{3D})	0.21	2.02	3.14	29.3	**43.4**	22.0	5.3
6.63 μm / voxel, elongation (E_{3D})	0.26	2.58	3.14	35.8	**40.0**	18.9	5.3
SEM, elongation (E_{2D})	0.29	2.29	2.98	27.2	**43.3**	21.4	8.2

lines in Fig. 12a. Kerogen lenses can be separated into three distinct groups within the dataset, depending on volume. Between 1×10^{-16} and 2×10^{-13} m^3 (Fig. 12a), one power-law relationship with a slope of 0.7 describes the correlations of the volume distribution of kerogen lenses. At a transition scale, corresponding to kerogen lens volumes of around 2×10^{-13} m^3 (Fig. 12a), the slope of the power-law that describes the number of kerogen lenses and their volume changes to a value of 1.1. The break in the slope occurs at 2×10^{-13} m^3 (Fig. 12a) inside the overlap zone between the low- and high-resolution datasets. Therefore, we consider that the two power laws observed here do not result from the two different resolutions of the images but represent a physical effect.

Finally, a few large kerogen lenses do not appear to be described by either of these power laws (blue dashed square box in Fig. 12a). Note that these three groups of kerogen lenses exist for all samples regardless of whether they come from the Draupne or Hekkingen Formations.

A relationship is shown between total organic content (wt%) and total kerogen volume in the high-resolution microtomography images (Fig. 12b). The trend for low-resolution data shows a similar result (Fig. S1). In Fig. 12b, two groups of data can be separated. The first group contains shales with a lower total organic content, ranging from ~6 to 8 wt%, and a higher kerogen lens spatial density within a given rock volume (Fig. 12b, green box). The second group contains shales with a higher total organic content, ranging upwards of 12 wt%, and a lower kerogen lens spatial density (Fig. 12b, red box). Fewer kerogen lenses correlating with a higher total organic content is also supported by Fig. 11, where the samples with higher total organic content contain a smaller number of kerogen lenses per volume unit.

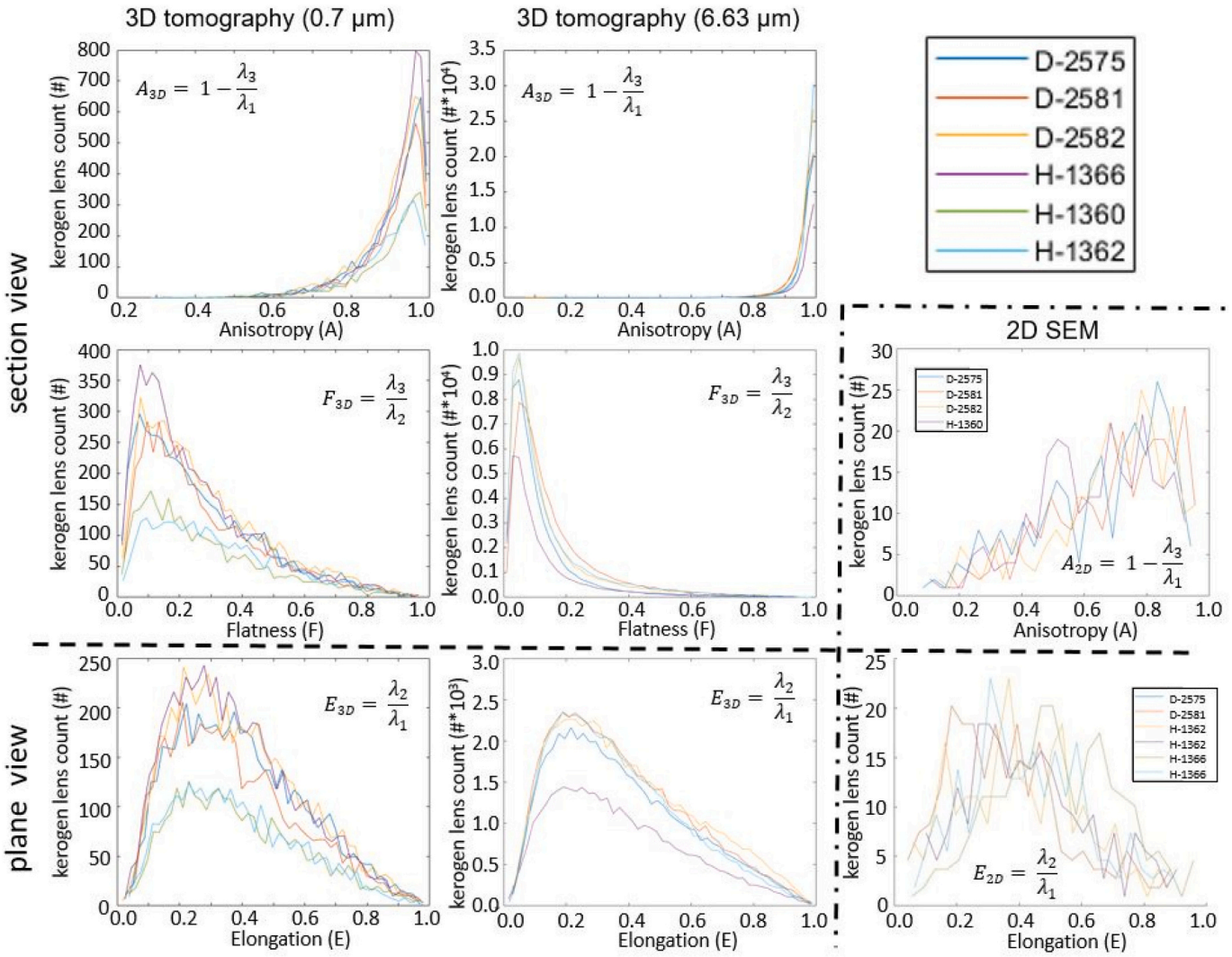

Fig. 9. Probability distribution function both 2D and 3D parameters of anisotropy, flatness, and elongation for synchrotron microtomography data at both high and low resolution, as well as for 0.5–1.0 mm size SEM images. Data are separated into plane and section views, corresponding to parallel and perpendicular orientations to bedding.

Fig. 12c shows the average length of the longest axis of kerogen lenses (λ_1) for both high- and low-resolution microtomography data. A trend can be estimated between the longest axis (λ_1) and total organic content, with an R^2 value of 0.72.

Importantly, the samples with a greater amount of organic matter content also have a longer λ_1 axis. Together, data shown in Figs. 10, 11b, and c suggest that for shales with total organic content in the range 8–12 wt%, organic matter is organized in a smaller number of kerogen lenses that have a longer extension when compared with shales with organic content in the range 5–10%.

4.4. Kerogen lens shape, size, and distribution from SEM data

On SEM images at the 0.5–1 mm scale, the kerogen lenses are often nearly imperceptible in section view (perpendicular to bedding), blending in with the fabric of the shale as a whole, except for a few larger lenses. In plane view (parallel to bedding), the orientation of the lenses allows one to see them more clearly (Figs. 5a, b). In SEM images at higher resolution, kerogen lenses in both the organic-rich Draupne and Hekkingen Formations can be seen in abundance. Fig. 5c and d show soft-sediment deformation around harder fossil clasts and how kerogen lenses follow the fabric of the shale. Fig. 5e, f, and g taken at 0.03–0.1 mm scale show how kerogen lenses interact with the minerals around them. The kerogen lenses are frequently associated with pyrite, most often framboidal. In this case, pyrite clusters preferentially accumulated in and near the organic matter (Fig. 5e). Coccoliths are abundant in both the Draupne and Hekkingen, and kerogen lenses can be seen conforming to their circular shape (Fig. 5f-g). Using SEM images at higher resolutions, the structure of the kerogen itself at scales less than 0.03 mm is displayed in Fig. 5h and i. Fig. 5h shows a web of kerogen interacting with minerals of the shale matrix. At this scale, some mineral replacement within a kerogen lens can be observed. This mineral replacement may account for the holes seen in some kerogen lenses in the 3D tomography data (Fig. 8, sample H-1360, kerogen lens ID#974). Fig. 5i shows the internal structure of a kerogen lens. The lens has an undular fabric with a dominant direction.

The shape of kerogen lenses is quantified using the aspect ratios of the main axes in 2D (Eqs. 5). The peak position value for the anisotropy parameter of the SEM data is 0.88, which is closer to 3D flatness (F_{3D}) values than 3D anisotropy (A_{3D}) values (Table 3, Fig. 9).

We report the angles φ and θ to investigate whether kerogen lenses have a dominant alignment direction on the longest axis, λ_1. Figs. 2 and 9 show that alignment between kerogen lenses is more apparent in section view than it is in plane view. The angle φ shows a large range of variability, with deviations of +/− 90° (i.e., perpendicular) to the bedding plane (Fig. 10e). However, the majority of deviations occur

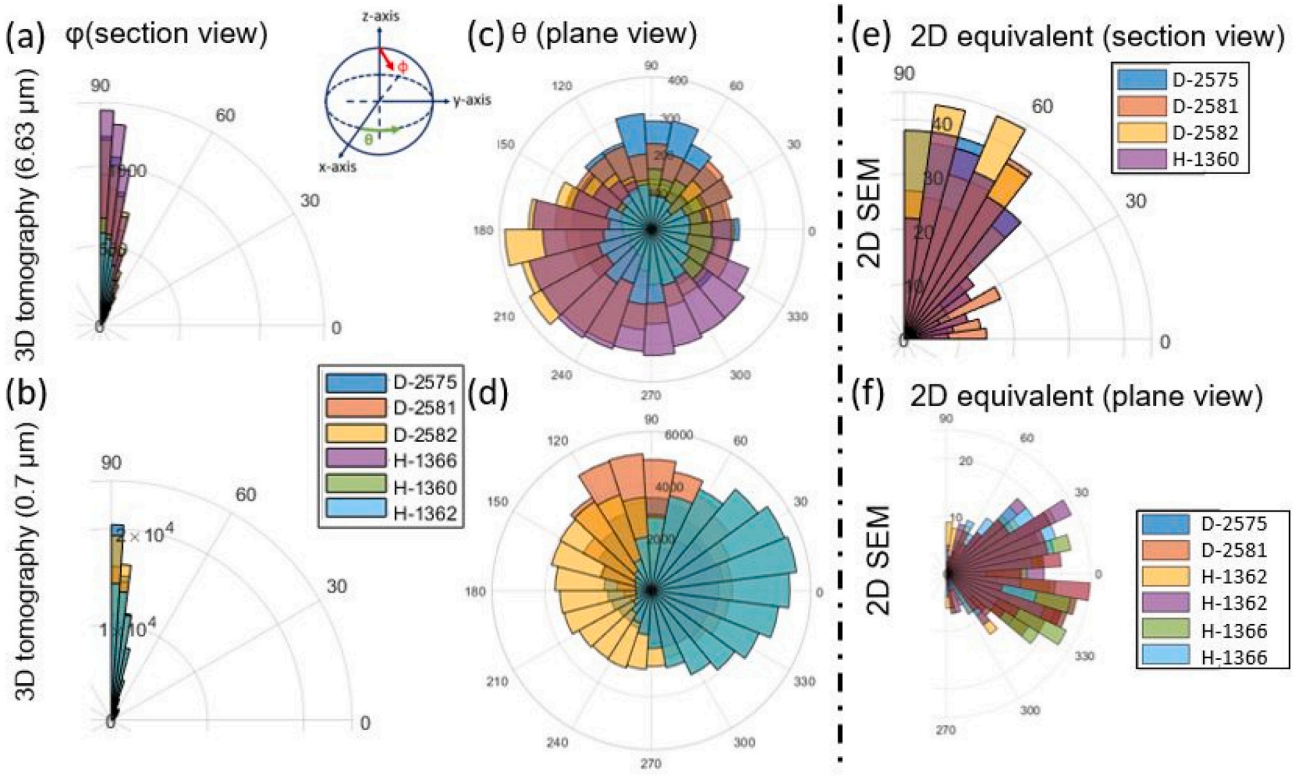

Fig. 10. Rose diagrams showing the orientation angles φ (a, b) and θ (c, d) of kerogen lenses for both high- and low- resolution microtomography data. Rose diagrams show the directions of kerogen lenses for SEM data in both plane and section view (e, f). See inset and Fig. 4 for the definitions of the angles. (For interpretation of the references to colour in this figure legend, the reader is referred to the web version of this article.)

within +/− 30° of the bedding plane (Fig. 10e). Furthermore, a visual inspection of the section view SEM images reveals that a significant amount of the deviation from the bedding plane is the result of soft-sediment deformation (Fig. 5d and g) around fossils and hard minerals. The angle θ shows that individual samples have kerogen lens orientation within ~15 degrees of one another, while the total data ranges +/− 30 degrees for all samples (Fig. 10f). These results suggest a weak directionality of kerogen lenses when they are imaged perpendicular to bedding.

Image analysis from the SEM images of the six samples was used to calculate rugosity, a parameter quantifying the shape of the kerogen lenses. Fig. 13 compares the rugosity of kerogen lenses from SEM images taken at 0.5–1.0 mm scale in both plane (parallel to bedding) and section (perpendicular to bedding) views. The peak value of the rugosity curves is similar for all images, with an average of 0.59 and a standard deviation of 0.1 (Fig. 13). The kerogen lenses have a higher rugosity and therefore are more 'spikey', than reference values for rounded and unrounded quartz grains (Fig. 13).

4.5. Geochemistry and mineralogy

Rock density values calculated from both well data and from the borehole samples are shown in Table 4. The mean rock density from well log analysis is 2.25 g/cm^3 with a standard deviation of 0.08. The mean density from laboratory measurements, calculated from the sample weight and volume from the microtomography data, is 2.28 g/cm^3 with a standard deviation of 0.20. TOC content was estimated using four independent measurements: Rock Eval analysis (pyrolysis), well log analysis (petrophysical analysis), SEM areal analysis, and 3D tomographical volumetric analysis (Table 4). Total organic content values above 2 wt% are considered to be a potential source rock (Kuuskraa et al., 2013; Cooke, 2014). Rock-Eval data show that all six samples have TOC above 6 wt% (Table 4), with Hekkingen samples H-1362 and H-1366 having TOC above 12 wt%.

Comparisons utilizing all methods show a reasonable agreement between Rock-Eval, well log, and to a lesser degree SEM areal analysis.

The TOC values calculated using 3D tomography data are significantly lower than the values collected from Rock-Eval, well log, and SEM. The TOC (wt%) detected for the samples scanned using 3D microtomography at higher resolution was greater than for the same samples scanned at lower resolution. These results indicate that only the largest kerogen lenses were observed at the spatial resolution of the microtomography images. The samples also contain a large number of kerogen lenses with volumes too small to be detected in the 3D images.

Organic-rich shales are complex assemblages of both organic and inorganic components. The inorganic components have a significant impact on the structural integrity of the shale. XRD analyses are used to determine the composition of inorganic components, while SEM is used to the interaction between the organic and inorganic elements. The inorganic material can be classified into three components – stiff quartz and feldspar grains, comparatively soft clay grains, and finally carbonate and pyrite (Fig. 5, Tables 1 and 5). Carbonate and pyrite fractions within the samples are relatively low, with an average of ~10% (Table 5, Fig. S2). Stiffer minerals, quartz, and feldspars, show a significantly greater range for the Draupne and Hekkingen Formations, ranging from 15 to 45% and 20–32%, respectively (Table 5, Fig. S2). Softer clay minerals represent a significant amount in both formations ranging from 40 to 71% for the Draupne Formation, and 58–72% for the Hekkingen Formation (Table 5, Fig. S2). XRD analyses of our samples agree with previous studies within and near our study area (Zadeh et al., 2017; Hansen et al., 2020; Rahman et al., 2020; Johnson et al., 2021).

Clay composition can be classified into four categories: chlorite (< 1% for all samples), kaolinite, smectite, and illite (Fig. 5, Tables 1 and 5, Fig. S2). For both the Draupne and Hekkingen Formations, kaolinite is the dominant clay mineral, with an average of 62.1% and 47%, respectively (Table 5, Fig. S2). The range of kaolinite content is larger

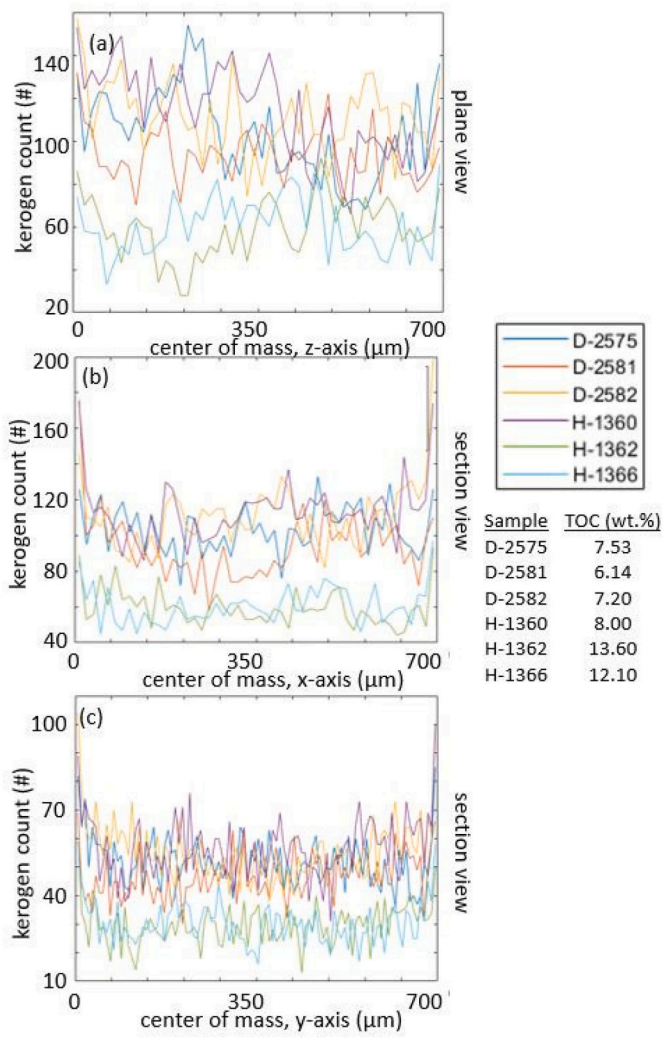

Fig. 11. (a) Number of kerogen lenses versus the centre of mass along the z-axis (plane view, perpendicular to bedding). (b-c) The number of kerogen lenses versus the centre of mass along the x-axis and y-axis (section views, parallel to bedding). For the same rock volume, the two samples with higher total organic content (H-1362, H-1366) contain fewer kerogen lenses.

for the Hekkingen Formation, 46–78%, than for the Draupne Formation, 57–72% (Table 5, Fig. S2). Illite also shows a larger fraction range for the Hekkingen Formation, 14–33%, than for the Draupne Formation, 19–31% (Table 5, Fig. S2). Smectite represents the smallest percentages for both formations. The smectite content in the Hekkingen Formation is in the range 2–22% and is slightly larger than in the Draupne Formation, where the range is 9–17% (Table 5, Fig. S2).

5. Discussion

Kerogen lenses have a direct impact on the microfracturing process during burial and primary migration of hydrocarbon from source rock shales (Kobchenko et al., 2011; Jin et al., 2010; Anders et al., 2014; Chauve et al., 2020). The conversion of kerogen lenses drives microfracturing within shales under appropriate pressure-temperature regimes. The degree of hydrocarbon expulsion and microfractruring (i.e., porosity creation) is influenced by the lithostatic load and modifies the mechanical properties of the rock. While internal kerogen porosity has been documented in some studies (Alfred and Vernik, 2013; Pepper, 2017), our samples do not present any at the resolution of our microscopy images. The present study focuses first on the relationship between the organic and inorganic constituents of organic-rich shale. We quantify the shape, size, and distribution of kerogen lenses based on synchrotron microtomography imaging of six samples collected at different depths in two different organic-rich shale formations in the North Sea and the Barents Sea (dominantly Type II, Type II-S, and Type III kerogen).

5.1. Comparison of techniques – advantages and shortcomings

Investigating the shape of kerogen lenses and TOC in 2D SEM images and 3D microtomography volumes shows significant differences. The two methods are complementary in that SEM imaging can be used to identify mineralogy (Harding, 2002), while 3D microtomography does not yet have this capability unless it is coupled to 3D X-ray diffraction, a technique that was not available on beamline ID19 at ESRF when the samples were imaged. Further to this, certain geological characteristics (i.e., mineral replacement, soft-sediment deformation, etc.) are easier to observe in SEM images than in microtomography volumes. However, 3D microtomography data offer a complete understanding of the organic component of the rock and how it impacts the organic-rich shale as a whole (i.e., fracture-kerogen lens relationship, kerogen lens sizes, and kerogen lens distribution).

Interestingly, SEM areal analyses provide reasonable estimates of TOC compared to other conventional TOC analysis techniques (i.e. Rock-Eval pyrolysis, well log-based TOC estimation). A larger study would be required to confirm repeatability. Conversely, 3D tomography TOC results show that an increase in the spatial resolution correlates to more representative data in terms of TOC because a greater percentage of the total kerogen lenses can be imaged when increasing resolution. The 6.63 μm /voxel data can image on average 5.4% of the organic matter present when utilizing Rock-Eval as a benchmark (Table 4). The 0.7 μm /voxel data can image on average 19.1% of the organic matter present, again compared to Rock-Eval (Table 4). It is likely that the

Table 4
List of samples with density and total organic content (TOC) calculated using different techniques.

Sample	Density well logs (g/cm^3)	Density borehole sample (g/cm^3)	TOC Rock Eval (wt%)	TOC Well (wt%)	TOC SEM (a. %)	TOC SEM (wt%)	TOC 3D Tomo High Res (v. %)	TOC 3D Tomo Low Res (v. %)	TOC 3D Tomo High Res (wt %)	TOC 3D Tomo Low Res (wt%)
D-2575	2.32	2.39	7.53	6.42	16.4	8.57	2.67	1.00	1.40	0.52
D-2581	2.29	2.12	6.14	5.74	13.3	7.84	2.05	1.15	1.21	0.68
D-2582	2.28	2.23	7.20	5.73	19.0	10.62	2.66	0.48	1.49	0.27
H-1360	2.14	2.21	8.00	7.32	14.5	8.89	2.55	0.89	1.20	0.42
H-1362	2.30	2.66	13.60	12.15	21.3	12.07	4.74	0.67	2.91	0.41
H-1366	2.14	2.04	12.10	11.42	24.6	11.55	4.11	0.49	2.33	0.28

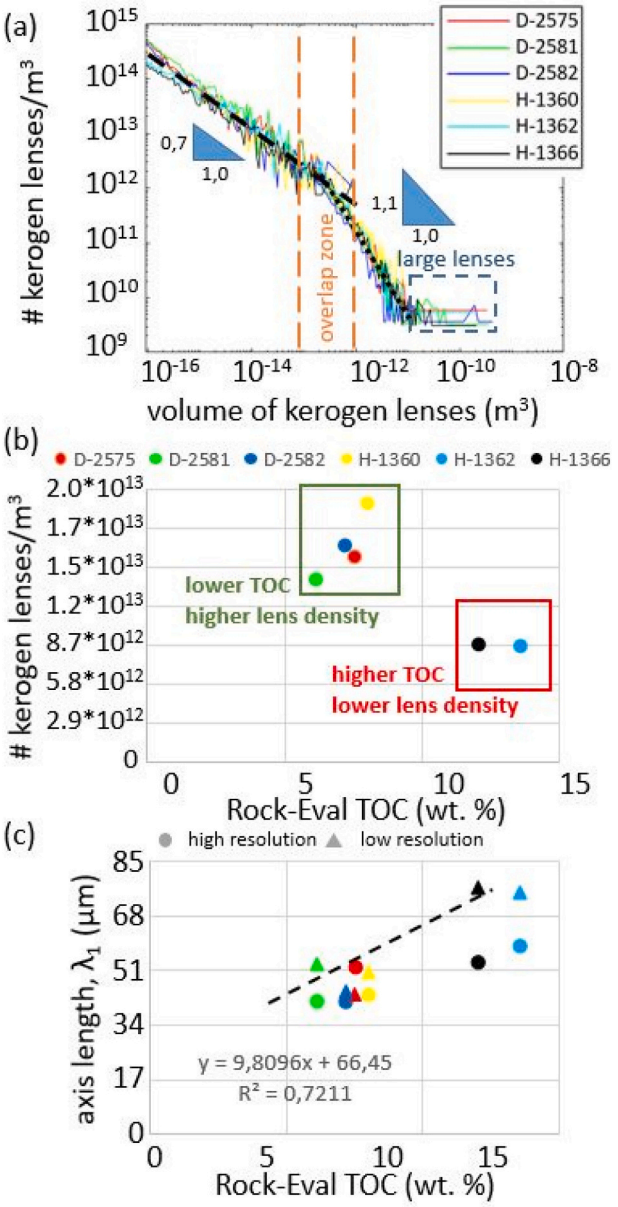

Fig. 12. (a) The probability density function of the volume of kerogen lenses normalized by the sample volume (m^3) shows two distinct power-law relationships with slopes 0.7 and 1.1. A group of large kerogen lenses without a clear trend is indicated with a dashed blue box. (b) Number of kerogen lenses per rock volume in high-resolution 3D images (0.7 um/voxel) versus total organic content (wt%). The two boxes separate two class of shale samples. (c) Average longest axis (λ_1) of kerogen lenses versus total organic content (wt%) for high-resolution (circles) and low-resolution (triangles) microtomography data. (For interpretation of the references to colour in this figure legend, the reader is referred to the web version of this article.)

remaining 80.9% would require higher resolution imaging techniques.

5.2. Impact of kerogen lens size, distribution, and shape on primary migration

Kerogen size, distribution, and shape impact the source-rock potential of organic-rich shales. Our study shows a relationship between the spatial distribution and the kerogen lens size (Figs. 12b, c, and 13). Organic-rich shales with TOC of ~12% wt% have larger but ~50% fewer kerogen lenses than shales with TOC between 6 and 8% wt%. The shape of kerogen lenses is classified by aspect ratios given by A_{3D}, F_{3D},

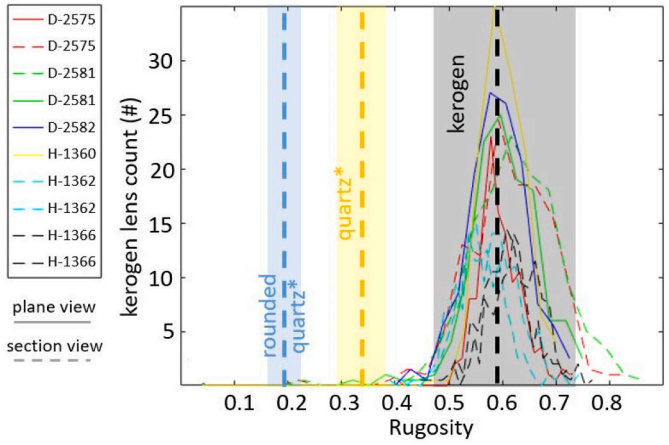

Fig. 13. Shape rugosity of kerogen lenses in 2D calculated from scanning electron microscopy images. Here, rugosity defines the 'spikiness' or roughness of a shape, where a greater value is correlated to a rougher surface. Kerogen lenses are shown to have a rougher surface on average than standard values for quartz and rounded quartz grains (Hamblin and Stachowiak, 1995). Additionally, kerogen lenses show a greater range of roughness values than these minerals. Higher TOC samples show a lower kerogen count (samples H-1362 and H-1366). The mean values of shape roughness are nearly identical for plane views (solid line) and section views (dashed line).

and E_{3D}.

The size and distribution of kerogen lenses play a critical role in microfracture nucleation and growth during hydrocarbon conversion and expulsion. The spatial density of kerogen increases with TOC up to a certain point between 8 and 12% TOC (wt%), above which the kerogen content continues to rise; however, the spatial density of kerogen lenses decreases (Figs. 11, 12, and 13). This effect could be the result of kerogen lenses increasingly combining to form larger kerogen lenses resulting in fewer overall and the production of patchwork lenses (Fig. 14). The 0.7 µm /voxel data captures on average 19.1% of the kerogen lenses present.

To a first-order, linear fracture mechanics indicate that the fluid overpressure required to propagate a fracture, P_p, is inversely proportional to the size of an initial crack (a kerogen lense in our case):

$$P_p \propto \frac{K_c}{\sqrt{\pi^* l}} \tag{9}$$

where K_c is the fracture toughness, and l is the length of the crack. Therefore, larger kerogen lenses may propagate as microfractures under lower fluid pressure. Numerical modeling performed by Fan et al. (2010) showed that kerogen lenses with twice the volume of smaller lenses will propagate faster and farther. Jin et al. (2010) proposed that the development of collinear, subhorizontal cracks connecting kerogen lenses along a given plane plays a role in the pace at which kerogen is converted. Oil pressure decreases exponentially as crack length grows, wherein the full transformation of kerogen to hydrocarbon occurs at the same time that the cracks cease to propagate (Jin et al., 2010; Liu et al., 2021). This effect may control the vertical migration of hydrocarbons, as shales with a complex distribution of kerogen and/or larger kerogen lenses may be more prone to form macroscopic cracks that may connect with pre-existing vertical cracks. Furthermore, the largest kerogen lenses with volume greater than 10^{-11} m^3 (Fig. 12a) present in all samples may control the formation of the first and largest microfractures and could have a significant impact on fracture connectivity. Kerogen lens shape and orientation also have an impact on microfracture growth.

The factors that control the shape of kerogen lenses are not fully understood. The final shape is the result of the original biological structure undergoing deposition, degradation, and diagenesis (Farrimond et al., 1998; Farrimond et al., 2002; Vandenbroucke and Largeau,

Table 5
Average bulk and clay mineralogies for the Draupne and Hekkingen from XRD for the study area (Johnson et al., 2021).

Formation	Mineralogy from XRD data					Clay mineralogy			
	Quartz	Feldspar	Pyrite	Carbonate	Total clay	Kaolinite	Smectite	Chlorite	Illite
Draupne shale	22.4	17.8	7.7	1.9	50.7	62.1	18	0.7	19.3
Hekkingen shale	24.2	4.6	5.6	4.5	61	47	20.8	–	32

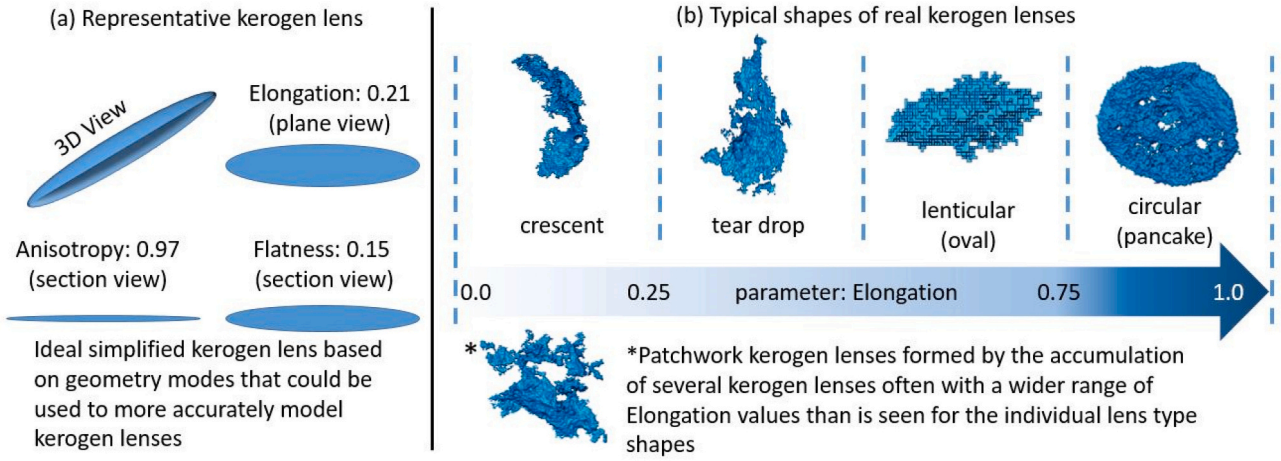

Fig. 14. Shape of kerogen lenses in organic-rich shales. (a) a representative kerogen lens in 3D and cross-section views could be used for better modeling of microfracture nucleation during primary migration. (b) Typical real kerogen lens shapes are classified into five categories. Four of the shapes show aspect ratios based on the elongation parameter: crescent (0.0–0.25), tear drop (0.25–0.5), lenticular (0.5–0.75), and circular (0.75–1.0). Patchwork is another commonly encountered shape that likely resulted from the accumulation of several kerogen lenses.

2007). In our sample, the same basic shapes and forms are present in all samples despite these samples having two distinct well locations with variable geological history. The kerogen here is predominantly Type II and II-S (Johnson et al., 2019; Hansen et al., 2019; Johnson et al., 2021), which supports that shape is influenced by the original biological structures. The erosion due to transport has an impact on the final shape of the organic matter and depends on its pathway to deposition. It is conceivable that Type III kerogen transiting from a terrestrial source will undergo significantly more erosion than Type II kerogen transiting from a marine source. However, the degree to which this process has an impact on the final shape of kerogen lenses remains to be quantified (Huc, 1988; Vandenbroucke and Largeau, 2007). When considering kerogen degradation, studies often refer to changes in the chemical composition of the organic matter, but not how these changes may affect the shape of kerogen lenses (Farrimond et al., 1998; Farrimond et al., 2002; Vandenbroucke and Largeau, 2007). During diagenesis, the interaction between organic and inorganic components may significantly impact kerogen lens shape (Zeszotarski et al., 2004; Prasad et al., 2011; Allan et al., 2014; Zargari et al., 2016). This includes the creation of internal porosity to kerogen lenses (Alfred and Vernik, 2013; Pepper, 2017), followed by the extrusion of bitumen into the created pore space (i.e., microfractures), controlled by lithostatic load.

The consensus is that immature kerogen is a brittle constituent (Brochard et al., 2013; Mondol, 2018; Johnson et al., 2022) that is matrix supporting (Prasad et al., 2011; Allan et al., 2014), and that the dynamic moduli of the lens being dependent on its chemical composition (Alstadt et al., 2016; Bousige et al., 2016). Furthermore, prior to conversion during catagensis, as a result of maturation, kerogen is at its most brittle stage (Zargari et al., 2016). This, in combination with the difference in diagenetic histories between the Draupne and Hekkingen Formations, indicates that if diagenesis plays a significant role in final kerogen shape, it does it during early diagenesis.

Kerogen lenses modelled in the literature (Vernik, 1994; Lash and Engelder, 2005; Fan et al., 2010; Jin et al., 2010; Fan et al., 2012; Chauve et al., 2020; Liu et al., 2021) are lenticular when viewed in section view and circular (penny-shaped) when viewed in plane view. From our data, a representative kerogen lens, based on peak values for anisotropy, flatness, and elongation, is displayed in Fig. 14a.

However, our study also shows that if the dominant shape is lenticular, some variations exist (Fig. 14b). The values of anisotropy and flatness parameterize the variance in aspect ratios that occurs for kerogen lenses in section view (Fig. 9 and Table 3). In plane view, a significant range of kerogen lens shapes exist. Here, we propose to classify the kerogen shapes into five main categories. Four categories are based on the elongation parameter, and the fifth one contains kerogen lenses with patchwork geometry that likely resulted from the coalescence of several smaller lenses (Fig. 14b).

Modeling of fracture propagation within organic-rich shales has been used to propose that the initial direction of the microfracture is guided by the dominant axis alignment of kerogen lenses (Fan et al., 2012; Jia et al., 2018; Chauve et al., 2020). The direction of kerogen lenses is often not perfectly parallel to bedding (Fig. 10), which may have an impact on the early stages of microfracture propagation. As the dominant direction of the lens can vary up to 30° from the bedding plane, it is possible that microfractures initially propagate across bedding, increasing the three-dimensional connectivity of the microfracture network. Further to this, analogue modeling of fracture propagation within shales has shown that fracture can propagate away from areas where stress relief is occurring and continue to propagate in the initial direction of propagation (Kobchenko et al., 2013; Kobchenko et al., 2014; Vega and Kovscek, 2019). This effect could control the growth of some fractures that interact across a wide range of bedding planes, as seen in Fig. 7.

5.3. Impact of mineralogy and total organic content on the sealing properties of shales

The ratio of soft to hard minerals dictates the geomechanical behavior of organic-rich shales under burial temperatures and pressures and, by extension, the sealing behavior of these rocks (Bourg, 2015; Hansen et al., 2020; Rahman et al., 2020; Johnson et al., 2022). Clay

content above 33% within shales dramatically increases sealing capacity (Bourg, 2015), suggesting the Draupne and Hekkingen Formations would have a good sealing property for both hydrocarbons and for geological CO_2 sequestration. As proposed by Eliyahu et al. (2015), the shale fabric is influenced by both its organic and inorganic components. Local studies of both the Draupne and Hekkingen shales have indicated that both formations may act as a seal for hydrocarbons (Hansen et al., 2019) and potentially could for CO_2 (Rahman et al., 2020). However, because of chemical interactions between CO_2/water and clay minerals, it has been proposed that understanding CO_2 seals is more complex (Kalani, 2018; Skurtveit et al., 2018). A limited amount of carbonaceous minerals reduces the likelihood of reactivity with CO_2 (Busch et al., 2016; Kalani, 2018; Skurtveit et al., 2018), enhancing the potential sealing properties of the Draupne and Hekkingen Formations. However, the amount of smectite present could lead to swell due to CO_2 sorption resulting in a stress regime change and ultimately seal failure (Busch et al., 2016).

Comparing the Draupne and Hekkingen Formations, the higher values of smectite and illite with lower average kaolinite content for the Hekkingen Formation (Table 5) suggest it is potentially a better seal (Mondol et al., 2007; Kalani, 2018). However, the Draupne Formation would also objectively be a good seal based on both the overall mineralogy and clay mineralogy, which is supported by other studies within and around the study area (Mondol et al., 2007; Kalani, 2018; Hansen et al., 2020; Rahman et al., 2020; Johnson et al., 2022). Previous studies have shown that higher quantities of organic matter are associated with smectite and illite more than with kaolinite (Ransom et al., 1998; Vandenbroucke and Largeau, 2007). This observation agrees with our results that the Hekkingen Formation has, on average, higher TOC content. One interpretation could be that organic matter has a tendency to adhere around clay particle edges, wherein smectite and illite particles are rougher than kaolinite (Mayer et al., 2004).

Prior to hydrocarbon expulsion, this study confirms the absence of porosity between kerogen lenses and the surrounding minerals at the resolution of our images (Fig. 2). Eliyahu et al. (2015) suggest that porosity would be visible at the nanometer scale in immature kerogen. The large values of kerogen lenses rugosity, or 'spikiness', seen in the 2D SEM images indicate that potential pore-space may have been filled in. Organic-rich shales have the ability to act as a seal after hydrocarbon expulsion, as well as before. Voltolini and Franklin (2020) pointed out that once a fracture network is created, it might not remain open. The ability for organic-rich shales to reseal depends on the ratio of stiff minerals to soft minerals (i.e., clays) (Bourg, 2015; Bourg and Franklin, 2017; Rahman et al., 2020). Soft minerals, such as compressible kaolinite and illite clays, assist the process of shale resealing the most (Bourg and Franklin, 2017). While the Draupne and Hekkingen Formations contain enough kaolinite and illite to assist in resealing, other shales may not. In these cases, kerogen lens shape will also have an impact on sealing capacity after hydrocarbon expulsion. Dietrich (2015) proposed that the pore space left behind from a converted kerogen lens will have an impact on the material properties of the shale. While softer, ductile clay minerals will essentially fill this void space (Voltolini and Franklin, 2020), the stiffer, more brittle minerals will help create porous space within the shale post maturation.

6. Conclusions

Kerogen lens size, distribution, and shape play an important role in determining the properties of organic-rich shales to be the source and seal rocks. We have used multiscale microscopy 2D and 3D imaging techniques to quantify the range of kerogen lens sizes and their frequency of occurrence on six samples collected at depth in boreholes in two locations within the Norwegian North Sea and the Barents Sea. Our study establishes a relationship between the size of kerogen lenses and TOC content wherein an increased TOC content above 12% TOC (wt%) is correlated with an increase in the kerogen lens size and a decrease in the total number of kerogen lenses per rock volume, for kerogen lenses with a volume larger than the resolution of the images. As a consequence, organic-rich shale with TOC above ~12% contains larger kerogen lenses, whereas organic-rich shales with lower TOC values will contain many more smaller kerogen lenses. Kerogen lenses may provide nucleation sites for microfracture formation during kerogen conversion. Kerogen lenses with a longer extension (TOC > 12%) will fracture under lower fluid pressure than shales with smaller lenses (TOC < 8%). However, shales with a lower TOC may contain many more kerogen lenses and therefore, more nucleation sites to initiate microfractures. There is likely an optimum combination of kerogen lens sizes and spatial density that maximizes damage to the host rock during kerogen maturation.

Our study also provides a range of kerogen lens shapes (Fig. 14) that could be used to model the nucleation and growth of microfractures during primary migration, beyond the simplified penny-shape used in previous numerical studies (Vernik, 1994, Lash and Engelder, 2005; Fan et al., 2010; Jin et al., 2010; Fan et al., 2012; Chauve et al., 2020; Liu et al., 2021). These studies also assume that the tips of kerogen lenses are aligned with the bedding plane, which is not always the case. This assumption also depends on how laminar the rock is, which can be influenced by both deposition (i.e. lacustrine, transition, marine) and diagenesis. The variety of kerogen lens geometries may have an impact on microfracture growth and how microfractures may connect in three dimensions. This microfracture network controls primary migration or the sealing capacities of shales for CO_2 or nuclear waste storage in cases where a significant degree of uplift has occurred, as it is the case in the Barents Sea.

Declaration of Competing Interest

The authors declare that they have no known competing financial interests or personal relationships that could have appeared to influence the work reported in this paper.

Acknowledgements

The Research Council of Norway funded this study (project Prometheus, no. 267775). We thank Equinor and the license partners for obtaining the cores and the permission to use them. We acknowledge the European Synchrotron Radiation Facility for provision of synchrotron radiation facilities, and we thank Elodie Boller and Benoît Cordonnier for assistance in using beamline ID19.

Appendix A. Supplementary data

Supplementary data to this article can be found online at https://doi.org/10.1016/j.coal.2022.103954.

References

Abay, B.T., 2017. Diversity of Petroleum in Terms of Source Rock Properties and Secondary Alteration Processes. PhD Thesis. University of Oslo.
Alfred, D., Vernik, L., 2013. A new petrophysical model for organic shales. Petrophysics 54 (3), 240–247.
Allan, A.M., Vanorio, T., Dahl, J.E.P., 2014. Pyrolysis-induced P-wave velocity anisotropy in organic-rich shales. Geophysics 79, 41–53. https://doi.org/10.1190/geo2015-0514.1.
Alstadt, K.N., Katti, K.S., Katti, D.R., 2016. Nanoscale morgphology of kerogen and in situ nanomechanical properties of Green River oil shale. J. Nanomech. Micromech. 6, 1. https://doi.org/10.1061/(ASCE)NM.2153-5477.0000103.
Anders, M.H., Laubach, S.E., Scholz, C.H., 2014. Microfractures: a review. J. Struct. Geol. 69, 377–394. https://doi.org/10.1016/j.jsg.2014.05.011.
Avizo Reference Manual, 2021. https://assets.thermofisher.com/TFS-Assets/MSD/Product-Guides/users-guide-avizo-software-2019.pdf.
Baig, I., Faleide, J.I., Jahren, J., Mondol, N.H., 2016. Cenozoic exhumation on the southwestern Barents Shelf: estimates and uncertainties constrained from compaction and thermal maturity analyses. Mar. Pet. Geol. 73, 105–130. https://doi.org/10.1016/j.marpetgeo.2016.02.024.

Baig, I., Faleide, J.I., Mondol, N.H., Jahren, J., 2019. Burial and exhumation history control on shale compaction and thermal maturity along the Norwegian North Sea basin margin areas. Mar. Pet. Geol. 104, 61–85. https://doi.org/10.1016/j.marpetgeo.2019.03.010.

Bourg, I.C., 2015. Sealing Shales versus Brittle Shales: a sharp threshold in the material properties and energy technology uses of fine-grained sedimentary rocks. Environ. Sci. Technol. Lett. 2, 255–259. https://doi.org/10.1021/acs.estlett.5b00233.

Bourg, I.C., Franklin, J.B.A., 2017. Clay, water, and salt: controls on the permeability of fine-grained sedimentary rocks. Acc. Chem. Res. 50, 2067–2074. https://doi.org/10.1021/acs.accounts.7b00261.

Bousige, C., Ghimbeu, C.M., Guterl, C.V., Pomerantz, A.E., Suleimenova, A., Vaughan, G., Garbarino, G., Feygenson, M., Wildgruber, C., Ulm, F.J., Pellenq, R.J.M., Coasne, B., 2016. Realistic molecular model of kerogen's nanostructure. Nat. Mater. 15 https://doi.org/10.1038/NMAT4541.

Brochard, L., Hantal, G., Laubie, H., Ulm, F.J., Pellenq, R.J.M., 2013. Fracture mechanisms in organic-rich shales: role of kerogen. Poromechanics V 2471–2480. https://doi.org/10.1061/9780784412992.288.

Buades, A., Coll, B., Morel, J.M., 2011. Non-local means denoising. Image Process. On Line 1, 208–212. https://doi.org/10.5201/ipol.2011.bcm_nlm.

Burnham, A.K., 2017. Porosity and permeability of Green River oil shale and their changes during retorting. Fuel 2017 (203), 208–213. https://doi.org/10.1016/j.fuel.2017.04.119.

Busch, A., Bertier, P., Gensterblum, Y., Rother, G., Spiers, C.J., Zhang, M., Wentinck, H. M., 2016. On sorption and swelling of CO2 in clays. Geomech. Geophys. Geo-Energy Geo-Resour. 2, 111–130. https://doi.org/10.1007/s40948-016-0024-4.

Carcione, J.M., Avseth, P., 2015. Rock-physics templates for clay-rich source rocks. Geophysics 80 (5), D481–D500. https://doi.org/10.1190/GEO2014-0510.1.

Chauve, T., Scholtès, L., Donzé, F., Mondol, N.H., Renard, F., 2020. Layering in shales controls microfracturing at the onset of primary migration in source rocks. J. Geophys. Res. 125, e2020JB019444 https://doi.org/10.1029/2020JB019444.

Cooke, I.L., 2014. User Guide Total Organic Carbon (TOC) Dataset: British Geological Survey (BGS). Internal Report.

Craddock, P.R., Bake, K.D., Pomerantz, A.E., 2018. Chemical, molecular, and microstructural evolution of kerogen during thermal maturation: case study from the Woodford Shale of Oklahoma. Energy Fuel 32, 4859–4872. https://doi.org/10.1021/acs.energyfuels.8b00189.

Craddock, P.R., Mosse, L., Bernhardt, C., Ortiz, A.C., Tomassini, F.G., Saldungaray, P., Pomerantz, A.E., 2019. Characterization and range of kerogen properties in the Vaca Muerta Formation Neuquen Basin, Argentina. Org. Geochem. 129, 42–44.

Dewhurst, D.N., Siggins, A.F., 2006. Impact of fabric, microcracks and stress field on shale anisotropy. Geophys. J. Int. 165, 135–148. https://doi.org/10.1111/j.1365-246X.2006.02834.x.

Dietrich, A.B., 2015. The Impact of Organic Matter on Geomechanical Properties and Elastic Anisotropy in the Vaca Muerta Shale. M.Sc. Thesis. Colorado School of Mines.

Dore, A.G., Vollset, J., Hamar, G.P., 1985. Correlation of the offshore sequences referred to the Kimmeridge Clay Formation – relevance to the Norwegian sector. Petrol. Geochem. Explor. Norwegian Shelf 1, 27–37. https://doi.org/10.1007/978-94-009-4199-1_2.

Eliyahu, M., Emmanuel, S., Day-Stirrat, R., Macaulay, C.I., 2015. Mechanical properties of organic matter in shales mapped at the nanometer scale. Mar. Pet. Geol. 59, 294–304. https://doi.org/10.1016/j.marpetgeo.2014.09.007.

Faleide, J.I., Tsikalas, F., Breivik, A.J., Mjelde, R., Ritzmann, O., Engen, O., Wilson, J., Eldholm, O., 2008. Structure and evolution of the continental margin off Norway and the Barents Sea. Episodes 31, 82–91. https://doi.org/10.18814/epiiugs/2008/v31i1/012.

Fan, Z.Q., Jin, Z.H., Johnson, S.E., 2010. Subcritical propagation of an oi-filled penny-shaped crack during kerogen-oil conversion. Geophys. J. Int. 182, 1141–1147. https://doi.org/10.1111/j.1365-246X.2010.04689.x.

Fan, Z.Q., Jin, Z.H., Johnson, S.E., 2012. Gas-driven subcritical crack propagation during conversion of oil to gas. Pet. Geosci. 18, 191–199. https://doi.org/10.1144/1354-079311-030.

Farrimond, P., Taylor, A., Telnaes, N., 1998. Biomarker maturity parameters: the role of generation and thermal degradation. Org. Geochem. 29, 1181–1197. https://doi.org/10.1016/S0146-6380(98)00079-5.

Farrimond, P., Griffiths, T., Evdokiadis, E., 2002. Hopanoic acids in Mesozoic sedimentary rocks: their origin and relationship with hopanes. Org. Geochem. 33, 965–977. https://doi.org/10.1016/S0146-6380(02)00059-1.

Hamblin, M.G., Stachowiak, G.W., 1995. A multi-scale measure of particle abrasivity, and its relation to two-body abrasive wear. Wear 190, 190–196. https://doi.org/10.1016/0043-1648(95)06624-1.

Hansen, J.A., Mondol, N.H., Fawad, M., 2019. Organic content and maturation effects on elastic properties of source rock shales in the Central North Sea. Interpretation 7, 477–497. https://doi.org/10.1190/INT-2018-0105.1.

Hansen, J.A., Mondol, N.H., Tsikalas, F., Faleide, J.I., 2020. Caprock characterization of Upper Jurassic organic-rich shales using acoustic properties, Norwegian continental shelf. Mar. Pet. Geol. 121, 104603 https://doi.org/10.1016/j.marpetgeo.2020.104603.

Harding, D.P., 2002. Mineral identification using a scanning electron microscope: Mining. Metall. Explor. 19, 215–219. https://doi.org/10.1007/BF03403272Kal.

Henriksen, E., Bjornseth, H.M., Hals, T.K., Heide, T., Kiryukhina, T., Klovjan, O.S., Larssen, G.B., Ryseth, A.E., Ronning, K., Sollid, K., Stoupakova, A., 2011. Uplift and erosion of the greater Barents Sea: impact on prospectivity and petroleum systems. Geol. Soc. Mem. 35, 1–271. https://doi.org/10.1144/M35.17.

Huc, A.Y., 1988. Aspects of depositional processes of organic matter in sedimentary basins. Org. Geochem. 13, 263–272.

Hunt, J.M., 1996. Petroleum Geochemistry and Geology. Freeman, New York.

Jia, Y., Lu, Y., Tang, J., Fang, Y., Xia, B., Ge, Z., 2018. Mechanical-chemical-mineralogical controls on permeability evolution of shale fractures. Geofluid. https://doi.org/10.1155/2018/7801843.

Jiang, S., Tang, X., Cai, D., Xue, G., He, Z., Long, S., Peng, Y., Gao, B., Xu, Z., Dahdah, N., 2017. Comparison of marine, transitional, and lacustrine shales: a case study from the Sichuan Basin in China. J. Pet. Sci. Eng. 150, 334–347. https://doi.org/10.1016/j.petrol.2016.12.014.

Jin, Z.H., Johnson, S.E., Fan, Z.Q., 2010. Subcritical propagation and coalescence of oil-filled cracks: getting the oil out of low-permeability source rocks. Geophys. Res. Lett. 37, L01305. https://doi.org/10.1029/2009GL041576.

Johnson, J.R., 2017. Applications of Geostatistical Seismic Inversion to the Vaca Muerta, Neuquen Basin, Argentina. M.S. thesis. Colorado School of Mines.

Johnson, J.R., Hansen, J., Renard, F., Mondol, N.H., 2019. Modeling maturation, elastic, and geomechanical properties of the Draupne Formation, offshore Norway. In: 2019 SEG Annual Meeting. SEG.

Johnson, J.R., Renard, F., Mondol, N., 2021. Salt remobilization timing and its impact on two Norwegian Contentinental Shelf organic-rich shale formations. Geoconvention 2021. https://geoconvention.com/wp-content/uploads/abstracts/2021/67503-salt-removilization-timing-and-its-impact-on-two.n.pdf.

Johnson, J.R., Hansen, J.A., Rahman, J., Renard, F., Mondol, N.H., 2022. Mapping the maturity of organic-rich shale with combined geochemical and geophysical data, Draupne Formation, Norwegian Continental Shelf. Mar. Pet. Geol. 138, 105525 https://doi.org/10.1016/j.marpetgeo.2022.105525.

Kalani, M., 2018. Implications from Clay Sedimentology, Well Log Interpretation and Seismic Analyses. PhD Thesis. University of Oslo.

Kelemen, S.R., Walters, C.C., Ertas, D., Kwiatek, L.M., Curry, D.J., 2006. Petroleum expulsion part 2. Organic matter type and maturity effects on Kerogen swelling by solvents and thermodynamic parameters for Kerogen from regular solution theory. Energy Fuel 20, 301–308. https://doi.org/10.1021/ef0580220.

Ketcham, R.A., 2005. Three-dimensional grain fabric measurements using high-resolution X-ray computed tomography. J. Struct. Geol. 27, 1217–1228. https://doi.org/10.1016/j.jsg.2005.02.006.

Kobchenko, M., Panahi, H., Renard, F., Dysthe, D.K., Malthe-Sorenssen, A., Mazzini, A., Scheibert, J., Jamtveit, B., Meakin, P., 2011. 4D imaging of fracturing in organic-rich shales during heating. J. Geophys. Res. 116, B12201. https://doi.org/10.1029/2011JB008565.

Kobchenko, M., Hafver, A., Jettestuen, E., Galland, O., Renard, F., Meakin, P., Jamtveit, B., Dysthe, D., 2013. Drainage fracture networks in elastic solids with internal fluid generation. Lett. J. Explor. Front. Phys. 102, 66002. https://doi.org/10.1209/0295-5075/102/66002.

Kobchenko, M., Hafver, A., Jettestuen, E., Renard, F., Galland, O., Jamtveit, B., Meakin, P., Dysthe, D.K., 2014. Evolution of a fracture network in an elastic medium with internal fluid generation and expulsion. Phys. Rev. 90, 052801 https://doi.org/10.1103/PhysRevE.90.052801.

Kuuskraa, V.A., Stevens, S.H., Moodhe, K., 2013. Technically Recoverable Shale Oil and Shale Gas Resources: An Assessment of 137 Shale Formations in 41 Countries outside the United States. U.S. Energy Information Administration. https://www.eia.gov/analysis/studies/worldshalegas/pdf/overview.pdf?zscb=79906188.

Lash, G.G., Engelder, T., 2005. An analysis of horizontal microcracking during catagenesis: example from the Catskill delta complex. AAPG Bull. 89, 1322–1449. https://doi.org/10.1306/05250504141.

Li, S., Zhang, D., 2021. Development of 3-D curved fracture swarms in shale rock driven by rapid fluid pressure buildup: Insights from numerical modeling. Geophys. Res. Lett. 4, 1–12. https://doi.org/10.1029/2021GL0926338.

Liu, G., Chen, Y., Du, X., Xiao, P., Liao, S., Azzam, R., 2021. Investigation of microcrack propagation and energy evolution in brittle rocks based on the voronoi model. Materials 14, 1–24. https://doi.org/10.3990/ma14092108.

Mayer, L.M., Schick, L.L., Hardy, K.R., Wagal, R., McCarthy, J., 2004. Organic matter in small mesospores in sediments and soil. Geochim. Cosmochim. Acta 68, 3863–3872.

Mittone, A., Manakov, I., Broche, L., Jarnias, C., Coan, P., Bravin, A., 2017. Characterization of a sCMOS-based high-resolution imaging system. J. Synchrotron Radiat. 24 (6), 1226–1236.

Mondol, N.H., 2018. Seal quality prediction using E-Poisson's ratio rock physics template – a case study from the Norwegian Barents Sea. Geoconvention 2018. https://geoconvention.com/uploads/2018abstracts/241_GC2018_Seal_quality_prediction_using_E-v_rock_physics_templet.pdf.

Mondol, N.H., Bjorlykke, K., Jahren, J., Hoeg, K., 2007. Experimental mechanical compaction of clay mineral aggregates – changes in physical properties of mudstones during burial. Mar. Pet. Geol. 24, 289–311. https://doi.org/10.1016/j.marpetgeo.2007.03.006.

Muller, R., Klausen, T.G., Faleide, J.I., Olaussen, S., Eide, C.H., Suslova, A., 2019. Linking regional unconformities in the Barents Sea to compression-induced forebulge uplift at the Triassic-Jurassic transition. Tectonophysics 765, 35–51. https://doi.org/10.1016/j.tecto.2019.04.006.

Nichols, T.C., 1992. Rebound in the Pierre Shale of South Dakota and Colorado – field and laboratory evidence of physical conditions related to processes of shale rebound. In: USGS Report Open-File, pp. 92–440.

Nichols, T., Collins, D.S., Davidson, R.R., 1986. In situ and laboratory tests of the Pierre Shale near Hayes, South Dakota – a characterization of engineering behavior. Can. Geotech. J. 23, 181–194. https://doi.org/10.1139/t86-028.

Nooraiepour, M., Mondol, N.H., Hellevang, H., Bjorlykke, K., 2017. Experimental mechanical compaction of reconstituted shale and mudstone aggregates: Investigation of petrophysical and acoustic properties of SW Barents Sea cap rock sequences. Mar. Pet. Geol. 80, 265–292. https://doi.org/10.1016/j.marpetgeo.2016.12.003.

NPD, 2021. Norwegian Petroleum Directorate FactPages. http://factpages.npd.no/ accessed March 27, 2021.
Ohm, S.E., Karlsen, D.A., Austin, T.J.F., 2008. Geochemically driven exploration models in uplifted areas: examples from the Norwegian Barents Sea. AAPG Bull. 92, 1191–1223. https://doi.org/10.1306/0618080808028.
Okewale, I.A., Grobler, H., 2020. Mechanics of compression behaviour in shale. In: 2020 World Congress on Advances in Civil, Environmental, & Materials Research, Seoul, Korea. http://www.i-asem.org/publication_conf/acem20/2.GE/3.General/GE1161_6330F1.pdf.
Okiongbo, K., Aplin, A., Larter, S., 2005. Changes in type II Kerogen density as a function of maturity: evidence from the Kimmeridge clay formation. Energy Fuel 19, 2495–2499.
Panahi, H., Kobchenko, M., Meakin, P., Dysthe, D.K., 2019. Fluid expulsion and microfracturing during the pyrolysis of an organic rich shale. Fuel 235, 1–16. https://doi.org/10.1016/j.fuel.2018.07.069.
Pelet, R., Tissot, B., 1971. Nouvelles Données sur les Mécanismes de Genèse et de Migration du Pétrole Simulation Mathématique et Application à la Prospection. In: 8th World Petroleum Congress, 13–18 June, Moscow, USSR, 12 pgs.
Pepper, A., 2017. Definition, modes of occurrence and pitfalls in understanding the term 'bitumen' in conventional and unconventional petroleum systems. In: 2017 AAPG Convention & Exhibition. https://www.searchanddiscovery.com/documents/2017/42111pepper/ndx_pepper.pdf.
Pepper, A.S., Corvi, P.J., 1995. Simple kinetic models of petroleum formation. Part III: modelling an open system. Mar. Pet. Geol. 12 (4), 417–452. https://doi.org/10.1016/0264-8172(95)96904-5.
Prasad, M., Pal-Bathija, A., Johnston, M., Rydzy, M., Batzle, M., 2009. Rock physics of the unconventional. Lead. Edge 28, 34–38. https://www.mines.edu/crusher/wp-content/uploads/sites/126/2018/03/Publication_Prasad_UnconvRockPhysics_TLE2009.pdf.
Prasad, M., Kenechukwu, C., McEvoy, T.E., Batzle, M., 2011. Maturiy and impedance anlaysis of organic-rich shales. SPE Reserv. Eval. Eng. 14, 533–543. https://doi.org/10.2118/123531-PA.
Rahman, H.M., Kennedy, M., Lohr, S., Dewhurst, D.N., Sherwood, N., Yang, S., Horsfield, B., 2017. The influence of shale depositional fabric on the kinetics of hydrocarbon generation trhough control of mineral surface contact area on clay catalysis. Geochem. Cosmochim. Acta 220, 429–448. https://doi.org/10.1016/j.gca.2017.10.012.
Rahman, M.J., Fawad, M., Mondol, N.H., 2020. Organic-rich shale caprock properties of potential CO2 storage sites in the northern North Sea, offshore Norway. Mar. Pet. Geol. 122, 104665 https://doi.org/10.1016/j.marpetgeo.2020.104665.
Rahman, M.J., Lebedev, M., Mondol, N.H., 2021. Nanoscale mechanical properties of organic-rich Draupne shale caprock, offshore Norway. In: 2021 SEG Annual Meeting. SEG. https://doi.org/10.1190/segam2021-3581994.1.
Ransom, B., Kim, D., Kastner, M., Wainwright, S., 1998. Organic matter preservation on continental slopes: importance of mineralogy and surface area. Geochim. Cosmochim. Acta 62, 1329–1345. https://doi.org/10.1016/S–16-7037(98)00050–7.
Rose, C., Smith, M.D., 2002. Mathematical Statistics with Mathematica. Springer Texts in Statistcs.
Sabtan, A.A., 2005. Geotechnical properties of expansive clay shale in Tabuk, Saudi Arabia. J. Asian Earth Sci. 25, 747–757. https://doi.org/10.1016/j.j.seaes.2004.07.003.
Schmoker, J.W., Hester, T.C., 1983. Organic carbon in Bakken Formation, United States portion of Williston Basin. AAPG Bull. 67, 2165–2174.
Shitrit, O., Hatzor, Y.H., Feinstein, S., Palchik, V., Vinegar, H.J., 2016. Effect of kerogen on rock physics of immature organic-rich chalks. Mar. Pet. Geol. 73, 392–404. https://doi.org/10.1016/j.marpetgeo.2016.03.023.
Skurtveit, E., Grande, L., Ogebule, O.Y., Gabrielsen, R.H., Faleide, J.I., Mondol, N.H., Maurer, R., Horsrud, P., 2015. Mechanical testing and sealing capacity of the Upper Draupne Formation, North Sea. In: 49th US Rock Mechanics/Geomechanics Symposium, ARMA-2015-331. American Rock Mechanics Association. In: https://onepetro.org/ARMAUSRMS/proceedings-abstract/ARMA15/All-ARMA15/ARMA-2015-331/65734.
Skurtveit, E., Miri, R., Hellevang, H., 2018. Geological Carbon Storage: Subsurface Seals and Caprock Integrity. American Geophysical Union. https://doi.org/10.1002/9781119118657.
Teixeira, M.G., Donzé, F., Renard, F., Panahi, H., Papachristos, E., Scholtes, L., 2017. Microfracturing during primary migration in shales. Tectonophysics 694, 268–279. https://doi.org/10.1016/tecto.2016.11.010.
Vandenbroucke, M., Largeau, C., 2007. Kerogen origin, evolution, and structure. Org. Geochem. 38, 719–833. https://doi.org/10.1016/j.orggeochem.2007.01.001.
Vega, B., Kovscek, A.R., 2019. A systematic study of internal gas generation in shale source rocks using analogy experiments. J. Pet. Sci. Eng. 173, 209–221. https://doi.org/10.1016/j.petrol.2018.10.006.
Vernik, L., 1994. Hydrocarbon-generation-induced microcracking of source rocks. Geophysics 59, 555–563. https://doi.org/10.1190/1.1443616.
Voltolini, M., Franklin, J.G.A., 2020. The sealing mechanisms of a fracture in Opalinus clay as revealed by in situ synchrotron X-Ray Micro-tomography. Front. Earth Sci. 8, 1–13. https://doi.org/10.3389/feart/2020.00207.
Whipp, P.S., Jackson, C.A.-L., Gawthorpe, R.L., Dreyer, T., Quinn, D., 2014. Normal fault array evolution above a reactivated rift fabric; a subsurface example from the northern Horda Platform, Norwegian North Sea. Basin Res. 26, 523–549. https://doi.org/10.1111/bre.12050.
Zadeh, M.K., Mondol, N.H., Jahren, J., 2017. Velocity anisotropy of Upper Jurassic organic-rich shales, Norwegian Continental Shelf. Geophysics 82, 61–75. https://doi.org/10.1190/GEO2016-0035.1.
Zargari, S., Wilkinson, T.M., Packard, C.E., Prasad, M., 2016. Effect of thermal maturity on elastic properties of kerogen. Geophysics 81, M1–M6. https://doi.org/10.1190/GEO2015-0194.1.
Zeszotarski, J.C., Chromik, R.R., Vinci, R.P., Messmer, M.C., Michels, R., Larsen, J.W., 2004. Imaging and mechanical property measurements of kerogen via nanoindentation. Geochem. Cosmochm. Acta 20, 4113–4119. https://doi.org/10.1016/j.gca.2003.11.031.
Ziegler, P.A., 1992. North Sea rift system. Tectonophysics 208, 55–75. https://doi.org/10.1016/0040-1951(92)90336-5.

Paper 3

Experimental modeling of primary migration in a layered, brittle analogue system

James R. Johnson
Maya Kobchenko
Andrew C. Johnson
Nazmul H. Mondol
François Renard

Tectonophysics, 2022

III

Tectonophysics 840 (2022) 229575

Contents lists available at ScienceDirect

Tectonophysics

journal homepage: www.elsevier.com/locate/tecto

Experimental modelling of primary migration in a layered, brittle analogue system

James Ronald Johnson [a,*], Maya Kobchenko [a], Andrew Charles Johnson [b], Nazmul Haque Mondol [a,c], François Renard [a,d]

[a] Department of Geosciences, The Njord Centre, University of Oslo, P.O. Box 1048, Blindern, NO-0316 Oslo, Norway
[b] Subsurface Characterization and Reservoir Engineering Unit, SM Energy, 1775 Sherman St., CO 80203, USA
[c] Norwegian Geotechnical Institute (NGI), P.O. Box 3930, Ullevaal Stadion, NO-0806 Oslo, Norway
[d] ISTerre, Univ. Grenoble Alpes, Grenoble INP, Univ. Savoie Mont Blanc, CNRS, IRD, Univ. Gustave Eiffel, 38000 Grenoble, France

ARTICLE INFO

Keywords:
Primary migration
Microfractures
Fluid expulsion
Organic-rich shale
Rock analogue

ABSTRACT

A 2D Hele-Shaw cell was built to study microfracture nucleation, growth, and network formation during internal fluid production. Fluid is slowly produced into a low permeability solid, which leads to a local fluid pressure increase that controls the nucleation of microfractures that grow and then connect to create flow pathways. This process occurs during the primary migration of hydrocarbons in source rocks, which is the main topic of our study. It may also occur in other geological systems, such as the expulsion of water during dehydration of clay-rich sediments in sedimentary basins or serpentinite rocks in subduction zones and the transport of magmatic melts. Our system consists of a transparent, brittle gelatin material mixed with yeast and sugar. The consumption of sugar by yeast leads to CO_2 formation, resulting in microfracture nucleation and growth. We varied three parameters, (1) anisotropy (i.e., number of layers), (2) lateral sealing, and (3) rate of fluid production. We tracked fluid movement through the opening and closing of microfractures within the system. Microfracture nucleation density is similar in a layered system to previous studies (0.45 microfracture per cm^2). However, we observed that lateral confinement (0.31 microfracture per cm^2) and rate of expulsion (0.99 microfracture per cm^2) affect nucleation density and the geometrical characteristics of the microfracture network. The size, extent, and geometry of the microfracture network are dependent on all three parameters investigated, where lateral confinement and a higher rate of expulsion result in greater microfracture network connectivity. Layers control the angle of intersection between microfractures. Furthermore, layering and sealing have an impact on fracture topology. Results also show that the microfracture pattern significantly influences the fluid expulsion rate. Our results have direct applications to understanding how fluid migration occurs in low-permeability rocks through the development of a connected microfracture network produced by internal fluid generation.

1. Introduction

Natural hydraulic fracturing can form within a rock matrix due to internal fluid generation and the resulting pore pressure build-up. Initially, the internally produced fluid will diffuse through the rock matrix. However, if the rate of fluid expulsion is too high, tensile microfractures may nucleate within the rock (e.g., Anders et al., 2014; Kobchenko et al., 2014). This process occurs in the subsurface in systems that involve partial magma melt processes coupled with compaction of the solid (McKenzie, 1985; Zhu et al., 2011), the transition of hydrous to anhydrous minerals (e.g., gypsum to bassanite) (Davies, 1999; Fusseis et al., 2012), and in the maturation and expulsion of hydrocarbons within organic-rich shale during primary migration (Tissot et al., 1974; Ozkaya, 1988; Kobchenko et al., 2011; Craddock et al., 2015).

Rock anisotropy and lateral sealing, resulting from variable porosity and permeability gradients, can exist in these geological systems. Anisotropy is prevalent in migmatites (Bons et al., 2009; Saukko et al., 2020) and is known to influence fracturing within them (Petruzalek et al., 2019). In the case of both the conversion of hydrous to anhydrous minerals and the expulsion of hydrocarbons from shales, the inherent rock structure contains two kinds of anisotropy because of i) sedimentary layering (e.g., Fusseis et al., 2012; Kobchenko et al., 2011; Anders

* Corresponding author.
E-mail address: j.r.johnson@geo.uio.no (J.R. Johnson).

https://doi.org/10.1016/j.tecto.2022.229575
Received 16 April 2022; Received in revised form 30 August 2022; Accepted 2 September 2022
Available online 10 September 2022

et al., 2014; Backeberg et al., 2017) and ii) the composite microstructure of the shale rocks that contain planar clay particles. Lateral sealing may occur due to the lateral variations of permeability and porosity of the mantle in partial melting processes (McKenzie, 1984; Takada, 1989; Zhu et al., 2011). Lithological changes and structural elements can create lateral sealing in environments where shale and gypsum are present (Demaison and Huizinga, 1991).

Layering anisotropy in organic-rich shales has been investigated utilizing wireline logs and seismic (e.g., Vernik and Liu, 1997; Sayers, 1999), image analysis (Kuila et al., 2011; Cardenes et al., 2021; Johnson et al., 2022b), and modelling – both computational (Chauve et al., 2020; Rabbel et al., 2020) and experimental (Johnson et al., 2021). Similarly, fluid generation rates have been studied using wireline logs and seismic (e.g., Li et al., 2003; Takei, 2017), image analysis (Sorbadere et al., 2018), and modelling – both computational (Hirschmann et al., 1999; Bourdon et al., 2003) and experimental (Kobchenko et al., 2014). The studies of anisotropy and fluid expulsion within organic-rich shales reviewed here occur at a number of different scales, from the regional scale (e.g., seismic) to the microscale. For organic-rich shales within the context of primary migration, the present study is best applied at a finer scale (i.e., mm-cm), wherein microfractures form and connect with one another. While lateral sealing often exists in the subsurface, it is also frequently used to control fluid expulsion in laboratory experiments. For example, lateral seals were used by Fusseis et al. (2012) for the thermal dehydration of gypsum, resulting in internal fluid generation and microfracturing. Experimental studies that induced artificial maturation of organic-rich shale have also utilized a lateral seal both in-situ and ex-situ (e.g., Craddock et al., 2015; Romero-Sarmiento et al., 2016; Panahi et al., 2019).

In geological systems, the rate of fluid migration depends on the rate of microfracture formation and growth, as well as pore fluid pressure diffusion through the medium (Bons and van Milligen, 2001; Kobchenko et al., 2014). The rate of creation of drainage pathways is critical to converting hydrous to anhydrous minerals (Fusseis et al., 2012). Variations in kerogen content and heating source can drive different rates of microfracture nucleation and growth in organic-rich shales (Kobchenko et al., 2014; Ougier-Simonin et al., 2016; Rabbel et al., 2020; Johnson et al., 2022a; Johnson et al., 2022b).

Here, we have developed a simple analogue model to explore the behavior of an elastic medium with internal fluid production, based on previous experimental setups utilizing sugar, yeast, and gelatin (Kobchenko et al., 2013; Kobchenko et al., 2014; Vega and Kovscek, 2019). Prior to these studies, gelatin has been used to model other subsurface processes, including the segregation and ascent of magma and hydrofracturing (Dahm, 2000; Bons et al., 2001; Rivalta et al., 2005). We explore three parameters that can interact with one another during reaction-induced fracturing. First, we studied the effect of structural anisotropy (i.e., rock layering). Second, we investigated the effect of lateral sealing or compartmentalization of the system. Third, we varied the rate of internal fluid production. Each parameter was tested alone against a base case where the solid contains only one layer, is not laterally sealed, and shows a fixed rate of fracturing. Then, we subsequently tested combinations of the three parameters. While each parameter has an impact on the microfracturing kinetics, they can interact with another with a positive or a negative feedback loop.

2. Methods

2.1. Experimental protocol

The experimental setup consists of a Hele-Shaw cell, 40 × 40 cm, with open boundaries, creating a quasi-2D environment. A 3 mm thick gelatin layer is emplaced within the cell, simulating a low permeability elastic and brittle material. CO_2 gas is internally produced utilizing a combination of sugar (sucrose) and yeast mixed together in the gelatin in order to induce fermentation (Fig. 1).

The Hele-Shaw is made up of two 10 mm thick glass plates separated by a 3 mm gap filled with the gelatin, yeast, and sugar mixture. The plates are clamped together. A white LED light source of 60 × 60 cm backlights the experiment. A Nikon D5300 camera records the ongoing fracturing process in the Hele-Shaw cell (Fig. 1a). A temperature sensor is located near the Hele-Shaw cell in order to track the laboratory ambient conditions (Fig. 1a). The temperature for all experiments was 16.7 ± 0.3 °C. It is critical that the gelatin stays within the temperature range of 16 ± 2.0 °C to ensure it remains mechanically brittle (Parker and Povey, 2010; Kobchenko et al., 2013; Kavanagh et al., 2018). Above this temperature range, the gelatin would behave viscously.

A volumeter is utilized to measure the production of CO_2. A volume of the same gelatin utilized for the Hele-Shaw experiment is placed into a bottle with a tube that feeds into a water-locked graduated cylinder. Production of CO_2 is then tracked with a second Nikon D5300 camera through the displacement of water by CO_2 from the graduated cylinder into the surrounding volumetric beaker (Fig. 1b). CO_2 production rate is dependent on the reaction rate of sugar and yeast. This study confirms that the use of sugar and yeast results in a consistent production rate, as established in previous studies (Kobchenko et al., 2013; Kobchenko et al., 2014; Vega and Kovscek, 2019).

Several studies have shown that, in such systems, ethanol is produced (Bai et al., 2008; Hendersen et al., 2013; Matthew et al., 2015; Beigbeder et al., 2021). However, under both the relatively low temperature of our experiments (16 °C) and low sugar concentrations used, these studies showed that very little ethanol could be produced. Therefore, we neglected the possible effect of ethanol production in our experiments.

The same Hele-Shaw cell was used for all experiments (Fig. 2). It was carefully cleaned between each experiment. This was done first by rinsing it with water and detergent, followed by distilled water, and finally ethanol. This procedure ensures good adhesion of the gelatin to

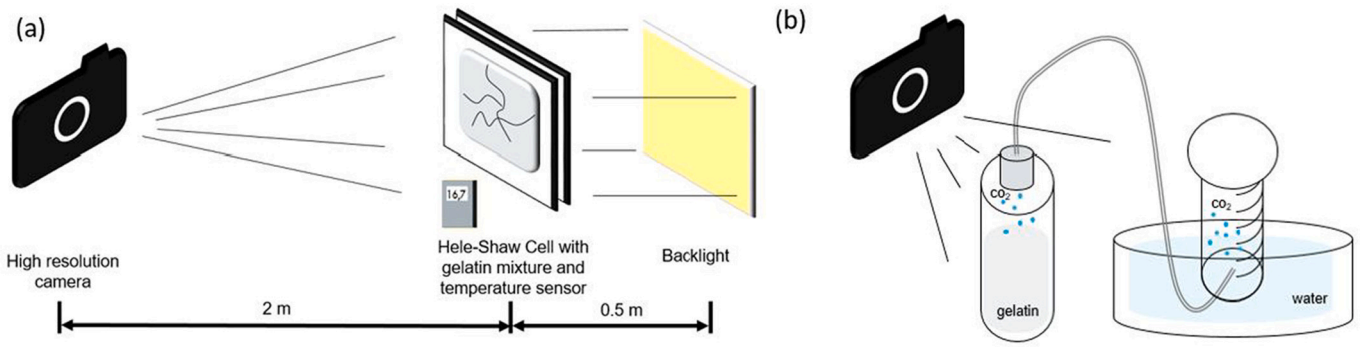

Fig. 1. The experimental setup (a) includes a high-resolution camera, Hele-Shaw Cell with gelatin matrix, temperature sensor, and backlighting. (b) A volumetric setup is used to measure the rate of CO_2 production in each experiment, with a camera used to ensure a consistent rate of gas production.

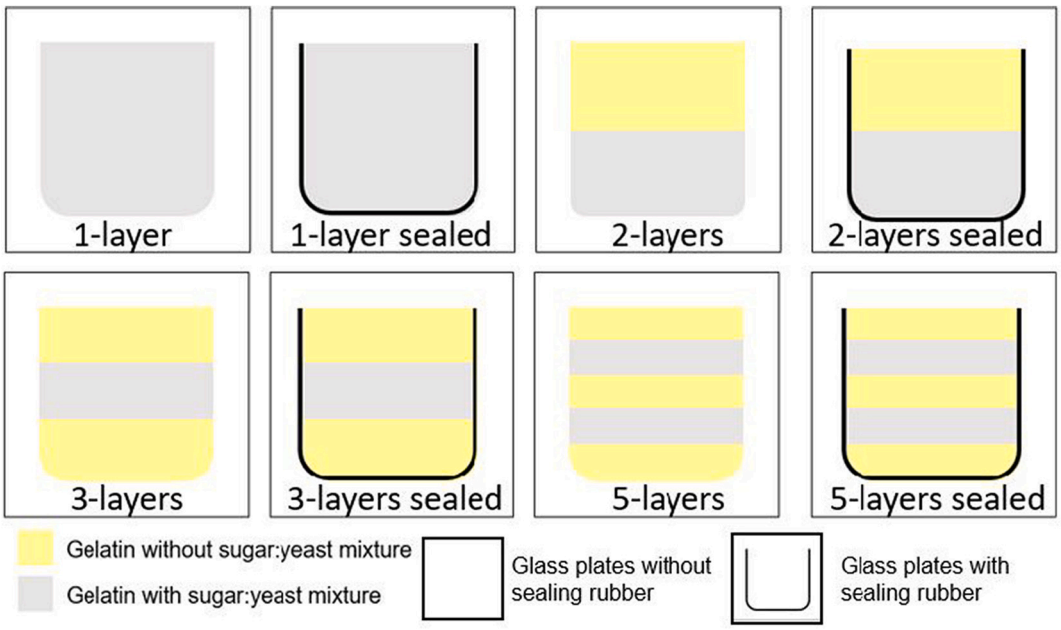

Fig. 2. Sketches of the different experiment types, including 1-layer, 2-layers, 3-layers, and 5-layers setups. Some experiments were partially sealed on three edges by a rubber o-ring, the other ones were performed under open conditions. The concentration of the sugar:yeast mixture also varied between 0.5×, 1.0×, and 1.5× for every setup variation shown here (Table 1). The Hele-shaw cell (i.e., glass plates) has dimensions of 40 × 40 cm and an opening of 3 mm between the two plates.

the glass, which prevents the accumulation of a CO_2 layer along with the interfaces between the gelatin and the glass plates. This is important as an accumulation of gas at the interfaces between the plates, and the gelatin reduces the production of microfractures in the gelatin.

To prepare the gelatin mixtures, a set number of gelatin plates (24 g of Gelita gelatin) are placed first in cold water for five minutes to soften the gelatin and then placed in 300 ml boiling distilled water to dissolve. Then, this water-gelatin mixture was left to cool down to 25 °C before the mixture of sugar and yeast was added. If the yeast is added to the water at a temperature higher than 25 °C, it may die. For the reference case, we added 3 g of sugar and 1 g of yeast per liter of water, which corresponds to the reference case 1.0× in Table 1. We also used 0.5× and 1.5× concentrations of yeast and sugar. Then, a rubber strip was placed along three edges between the glass plates for sealing purposes before the liquid was poured into the Hele-Shaw cell. We then placed the cell vertically into a refrigerator set to 4 °C such that the gelatin could solidify while the yeast remained effectively dormant. After one hour of curing, the cell was rotated 90° and placed horizontally in the fridge in order to ensure good adhesion between the gelatin and the glass plates. The total curing time was 24 h. Once cured, the sealing rubber was either removed for experiments not laterally sealed or left in place for experiments that were partially sealed (Fig. 2).

Table 1
List of experiments, number of experiments performed, and parameters.

Experiment	Ref. case (1.0× yeast + sugar)	Sealed (rubber)	Low ratio (0.5× yeast + sugar)	High ratio (1.5× yeast + sugar)	High ratio, sealed (1.5× yeast + sugar)	Total
1-layer	1	1	0	1	1*	3 + 1*
2-layers	1	1	0	1	1*	3 + 1*
3-layers	3	1	1	1	1*	6 + 1*
5-layers	3	1	0	1*	1*	4 + 2*
Sum	8	4	1	3 + 1*	4*	16 + 5*

Note – The five experiments marked with '*' experienced overpressure resulting in gas accumulation at the interface between the gelatin layer and the glass plates. This bias made it impossible to perform quantitative image analysis. Therefore, these experiments are used for discussion purposes only. The remaining sixteen experiments were used for quantitative image analysis.

In total, 21 experiments were performed under varying three parameters: 1) the number of layers within the Hele-Shaw cell, 2) the concentration of sugar and yeast inside certain gelatin layers, and 3) whether or not the experiment is sealed on three edges (Table 1). For some conditions, several experiments are performed to verify the reproducibility of the results. Sixteen experiments were quantitatively analyzed for 2D microfracture patterns and fluid migration, and the remaining five experiments were qualitatively analyzed. For one of these five experiments, the CO_2 diffused outside of the cell, and no microfracture formed because of the too low concentration of sugar and yeast (0.5×). The remaining four experiments contained a microfracture pattern; however, overpressure resulted in a loss of adhesion between the gelatin and the glass plates of the Hele-Shaw cell and an accumulation of gas along with the interfaces.

The first parameter varied is the number of gelatin layers. Experiments were tested with one layer, two layers, three layers, and five layers (Fig. 2 and Table 1). For the 2-layers, 3-layers, and 5-layers experiments, layers that contain a mixture of sugar and yeast alternate with layers that do not. Efforts were made to ensure proper welding between the layers, including introducing the newest layer at a temperature several degrees warmer than the layer already emplaced (Kavanagh et al., 2017). Very slight differences in elastic properties have possibly been introduced due to variable composition between the layers (Brizzi et al., 2016; Sili et al., 2019), and we neglected this effect. For the 2-layers experiment, the bottom layer contains a mixture of sugar and yeast. The 3-layers experiment contains a mixture of sugar and yeast in the middle layer. The 5-layers experiment contains sugar and yeast mixture in layers 2 and 4 (Fig. 2). In addition to varying the number of layers, two other parameters were varied for some of the experimental setups. Experiments were either partially sealed, with a rubber o-ring, on three edges or not. Finally, the ratio of sugar and yeast was varied in the range of 0.5×, 1.0×, and 1.5× the standard mixture of

sugar and yeast per setup (Table 1).

The dimensions of the layers (thickness of 3 mm and height) were the same between experiments with the same number of layers by prescribing a defined amount of gelatin for every layer. The height of all layers was then measured afterward to ensure consistency. In the 5-layers 1.5× sugar:yeast mixture experiment, fluid overpressure occurred, leading to a detachment between the glass and the gelatin in the Hele-Shaw cell. The sealing of three of the four edges of the Hele-Shaw cell was done utilizing the same rubber strip used during the gelatin curing process.

2.2. Image analysis and microfracture characterization

A Nikon D5300 camera was used to collect 16-bits RGB images of the Hele-Shaw cell every 15 s for a minimum of 36 h. Every experiment produced a set of time-lapse images that displayed the nucleation and growth of microfractures with time as the result of the production of CO_2 gas from the reaction between the yeast and sugar. Images were first preprocessed, including image cropping, masking, artifact removal, and thresholding. We then quantitatively analyzed the microfracture networks.

The following workflow was used for the preprocessing of all images. First, all images were reviewed to provide a visual reference for cropping and converting the RGB images into a single-channel grayscale image. We corrected the images from backlight intensity variations and any other subtle changes in light settings. The baseline light settings are set to the initial image at time $t = 0$. Each subsequent image is normalized to this initial image so that only the development of microfracture nucleation sites and the resulting microfracture network is captured. A mask is created using the final image, with the complete microfracture network, in order to isolate the salient information from the rest of the image. Gray scale thresholding is applied to extract the microfractures and microfracture network through time for the entirety of each experiment. The connectivity of the microfractures was analyzed by labeling with a different color every connected set of microfractures and by identifying each microfracture extremity.

Our data contain the microfracture nucleation sites and the subsequent growth and interactions of microfractures with each other. Microfracture interactions with the interfaces between layers with different gelatin mixtures are also followed. Upon the initial development of microfractures, every nucleation site is assigned an ID# that follows every new microfracture. Microfracture nodes are defined as any location(s) where microfractures that have a unique nucleation point meet (Fig. 3). Angles δ (Fig. 3a) when microfractures coalesce are measured for all microfracture nodes. In addition, the microfracture network is described by the parameter ω, defined as:

$$\omega = \frac{n_d - n_j}{n_d + n_j} \tag{1}$$

where n_d is the number of microfractures terminated by dead ends, n_j is the total number of microfracture junctions (Fig. 3a). The parameter ω quantifies the microfracture network in terms of two endmembers. If the network is fully connected and contains only microfractures that are connected to other microfractures or to the system boundaries (n_j=n_d), then $\omega = 0$. If the network contains isolated microfractures (n_j=0), then $\omega = 1$. A fracture network branching event occurs when none or one of the two growing microfracture tips connects with another given microfracture. A fracture network fragmenting event occurs when both of the growing microfracture tips interact with other given microfractures or the system boundaries.

A microfracture-layer node is defined as a location where a microfracture tip interacts with the interface between two gelatin layers. The angle of deflection, θ (Fig. 3b), is also measured for all microfracture-layer nodes.

Utilizing ω, calculated from dead-end and junction nodes (Fig. 3a), the influence of structural changes to the system (i.e., introducing anisotropy) can be understood. In addition to this, the XYI classification of microfracture nodes can be utilized to characterize the rate of fluid flow a system can maintain (Sanderson and Nixon, 2015; Alvarez et al., 2021; Silva et al., 2021). With the framework of XYI-nodes (Fig. 3c), the number of branches, N_B, can be calculated:

$$N_B = \frac{1}{2}(N_I + 3N_Y + 4N_X) \tag{2}$$

from the number of I-nodes (NI), Y-nodes (NY), and X-nodes (NX) within a microfracture network from a given gelatin experiment. It has been hypothesized and later empirically shown that I-nodes are the least permeable (i.e., poorly connected) pathways and that Y-nodes are the

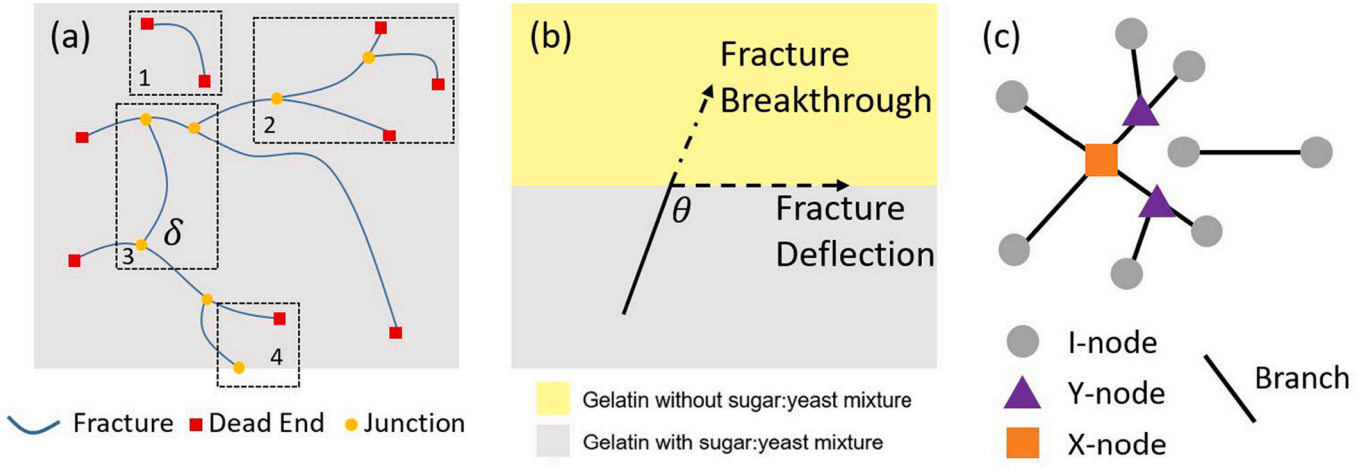

Fig. 3. (a) Four scenarios have been highlighted to show how individual microfracture nodes are characterized by the number of dead ends (red squares), n_d, and the number of junctions (orange circles), n_j, results in a more fragmented or branching network. (1) A microfracture that does not interact with another microfracture at both ends represents an isolated branch in the fracture network. (2) A dendritic (i.e., river-like) pattern will result in a greater number of dead-ends points than junctions. (3) Cross-cutting microfractures will result in a fragmentation event in the network. The angle between two microfractures is δ. (4) A node at the matrix boundary is considered as a junction, while a node within the boundary is considered as a dead-end. (b) Microfracture propagation will either deflect at the layer interface with an angle θ or will continue to propagate into the layer above (i.e., breakthrough event). (c) An alternative method of identifying nodes depends on the relationship that node has with the branches it's connected to. A node connected to one branch is an I-node, with three branches is a Y-node, and with four branches is an X-node. (For interpretation of the references to color in this figure legend, the reader is referred to the web version of this article.)

most permeable (i.e., well connected) pathways (Sanderson and Nixon, 2015; Silva et al., 2021). The parameter ε, calculated from the ratio of nodes, can be used as a proxy to quantify the ability of a fluid to flow through a given fracture network:

$$\varepsilon = \frac{N_I + 3N_Y + 4N_X}{N_I + N_Y} \tag{3}$$

The opening and closing of fractures can also be used to track fluid flow within the experiments. The procedure of image analysis applied to the entire image sequence captures the total surface area of the aperture of open microfractures at a given moment in time, A(t). The Fourier transform of the time series A(t) is used to capture the dynamics of fluid movement within the Hele-Shaw cell. The low-frequency trend is subtracted from the time series, and the discrete Fourier transform (|Y(f)|) is calculated. The power spectrum ((|Y(f)|)^2) of the Fourier transform for each experiment shows a well-pronounced peak that indicates the dominant frequency of closing-opening dynamics of the microfractures and fluid expulsion process.

3. Background theory

3.1. Principles of linear elastic microfracture mechanics

Fluid-driven tensile microfracture propagation within organic-rich shales, similar to magmatic intrusion during dyke propagation, can be described, to a first order, using linear elastic microfracture mechanics (Lister and Kerr, 1991; Clemens and Mawer, 1992; Rivalta et al., 2015). In both situations, a fluid moves throughout a brittle solid matrix, driven by fluid pressure gradients (Nur and Byerlee, 1971; Secor and Pollard, 1975; Bear, 1975). Once a critical fluid pressure gradient threshold is reached, the release of pressure is achieved (Coulomb, 1776) through the formation of tensile microfractures in the solid (e.g., Anders et al., 2014). The balance of pressure necessary for a tensile microfracture to propagate under the effect of an internal increase of fluid pressure is described in the literature (e.g., Griffith, 1921; Secor, 1965; Lister and Kerr, 1991; Clemens and Mawer, 1992; Kavanagh et al., 2006; Kobchenko et al., 2014; Vega and Kovscek, 2019). For a microfracture to propagate, the fluid pressure in the microfracture, P_p, must be larger than the fluid pressure, P_e, that maintains a microfracture open and in equilibrium.

$$P_e = \frac{E}{2(1-\upsilon^2)} * \frac{w}{y} \tag{4}$$

where E and υ are Young's modulus and Poisson's ratio of the gelatin, w is half the aperture of the microfracture, and y is half the second smallest dimension of the microfracture. Microfracture propagation occurs when the dissipation of strain at the tip of the microfracture overcomes the microfracture toughness, K_c:

$$K_c = \sqrt{2\gamma_s * E} \tag{5}$$

where γ_s is the surface energy necessary to break the gelatin. The fluid pressure at the onset of microfracture propagation, P_p, is then expressed:

$$P_p = \frac{K_c}{\sqrt{\pi * l}} \tag{6}$$

where l is the length of the crack. For a system in equilibrium, $P_p \leq P_e$, whereas a microfracture propagates when $P_p > P_e$. The Poisson's ratio for gelatin is close to 0.5 (Kavanagh et al., 2013; Van Otterloo and Cruden, 2016; Vega and Kovscek, 2019). The values of Young's modulus (E) are reported in the range ~ $1.5{\cdot}10^5$–$8.35{\cdot}10^5$ Pa (Kavanagh et al., 2013; Van Otterloo and Cruden, 2016; Vega and Kovscek, 2019). Kavanagh et al. (2013) and Vega and Kovscek (2019) report surface energy for gelatin equal to 1 J m^{-2}. We used these values to calculate the parameters in eqs. 4–6.

3.2. Microfracture formation and fluid migration

The consumption of sugar by the yeast produces CO_2, which subsequently diffuses through the gelatin matrix (Kobchenko et al., 2013; Kobchenko et al., 2014). In order for a microfracture to nucleate, a critical supersaturation is needed. This is calculated as follows:

$$p_c = \frac{c_c}{k_H} \tag{7}$$

where c_c is the concentration of the dissolved CO_2 required for the nucleation of a gas bubble, p_c is the pressure required to nucleate a microfracture using the ideal gas approximation, and k_H (mL·atm/mol) is Henry's coefficient that relates the diffusion kinetics to the partial pressure of the gas. Kobchenko et al. (2013) determined that diffusion of the CO_2 from the gelatin matrix to the fractures controls the growth of microfractures, which is described by:

$$\delta_c = \sqrt{\frac{2D}{\gamma}\frac{p_c - p}{k_H}} \propto \gamma^{-\frac{1}{2}} \tag{8}$$

where, δ_c (m) describes the critical distance between microfractures, γ is the gas production rate (mL/h), D is the diffusion coefficient of CO_2 in the gelatin and is equal to $1.85{\cdot}10^{-9}$ m^2 s^{-1}, and p is the gas pressure determined from the concentration of the dissolved CO_2 (atm).

Once a microfracture has nucleated, the rate of microfracture growth follows:

$$l = l_0 exp\left(\frac{2\varphi RTt}{p_c a}\right) \tag{9}$$

where l is the microfracture length, l_0 is an integration constant that characterizes the critical length above which a gas bubble evolves into a microfracture, φ is the flux of CO_2 (mol·m^{-2}·h^{-1}), R is the ideal gas constant, T is temperature, t is time, and a is microfracture aperture. Microfracture aperture is limited to $a = 3$ mm due to the adhesion of the gel to the walls of the Hele-Shaw cell (Kobchenko et al., 2013).

When a microfracture reaches an open outside edge of the Hele-Shaw cell, the CO_2 flows out of the experimental setup. Gas expulsion out of the system is controlled by the intermittent opening and closing of microfractures. The drainage network is influenced by the microfracture topology and connectivity.

4. Results

Gas production as the reaction between sugar and yeast was measured by the CO_2 production tracker (Fig. 1). The start times for CO_2 production range from 10 min to three hours after the experiment has begun (Fig. 4a). In this stage, the diffusion of gas is impossible to vizualize in the Hele Shaw cell but can be detected by the CO_2 production tracker. The timing of the initial microfracture nucleation depended on the concentration of the sugar:yeast mixture, with experiments that had 1.5× sugar:yeast ranged in start times from ~5:45–7:15 h. Experiments with the normal (1.0×) concentration started in the range ~ 12:30–17:30 h (Fig. 4b).

During the initial stages of microfracture propagation, the microfractures nucleate in a penny-shape and then may propagate from one or both ends until they reach the edge or coalesce with another microfracture (Fig. 4c). Microfracture creation continued for ~35 h until the final microfracture pattern is obtained (Fig. 4d). The number of layers or the presence of sealing appears to have no apparent impact on the amount of time to CO_2 production, initial microfracture nucleation, and total experiment duration. However, layers introduce the possibility for microfractures to either penetrate or be deflected by the interface (Fig. 4d). Further to this, sealing three edges fundamentally changes the way microfractures interact with one another, as discussed below.

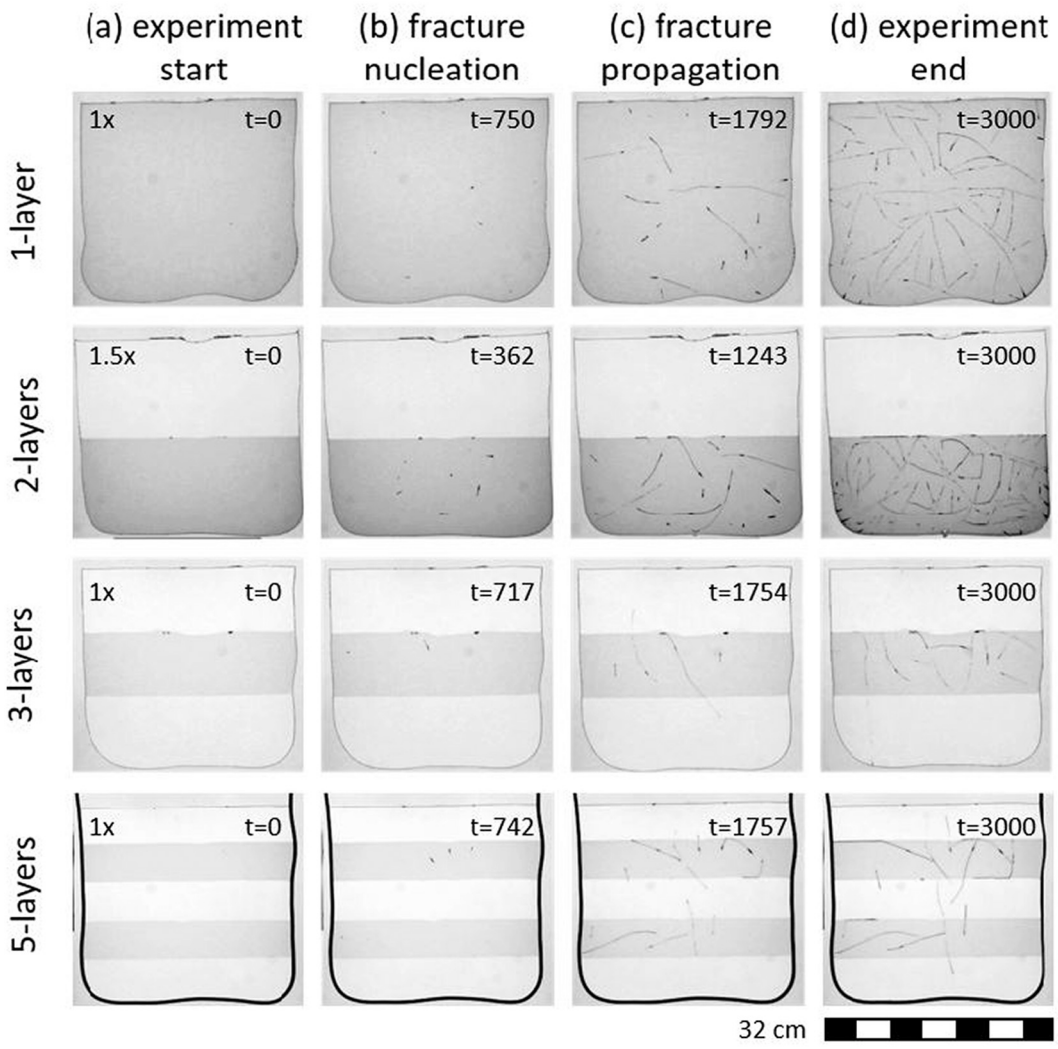

Fig. 4. Time series showing the evolution from (a) start of the experiment, (b) initial microfracture nucleation, (c) microfracture development and interaction, and (d) final microfracture network pattern for 1-layer sugar:yeast concentration 1.0×, 2-layers sugar:yeast concentration 1.5×, 3-layers sugar:yeast concentration 1.0×, and 5-layer sealed and sugar:yeast concentration 1.0× experiments. These raw images are processed to extract the microfractures over time. Time is given in minutes. Gelatin layers with a darker gray shade contain the sugar:yeast mixture.

4.1. Microfracture nucleation and growth

The nucleation site of every microfracture is identified in both space and time for all experiments (Fig. 5). Every nucleation site is given an identification number (ID#) so that the continued growth of the microfracture network is tracked.

The distribution of nucleation sites appears to be dependent, or at least influenced by all parameters that were varied: the number of layers, the composition of the mixture of sugar and yeast, and whether or not the gelatin is sealed on three edges. This influence is more pronounced with some variables than it is for others (e.g., the introduction of layers without sugar and yeast prevents nucleation in certain areas). For the simplest case (i.e., one layer, open, 1.0× sugar:yeast), there is a spatially random distribution of 53 nucleation sites, with a density of 0.58/cm^2 (Fig. 5, left column). The density of nucleation sites, when normalized by the surface area of the gelatin layers that contain the mixture of yeast and sugar, is 0.48/cm^2 (28 nucleation sites), 0.40/cm^2 (12 nucleation sites), and 0.44/cm^2 (14 nucleation sites) for two layers, three layers, and five layers respectively (Fig. 5). Therefore, the density of the nucleation site is comparable when varying the number of layers. However, the nucleation sites form across a greater range of time for layered experiments (Figs. 5, S1).

An increase in sugar and yeast concentrations results in a greater density of nucleation sites (Fig. 5). The average nucleation density for 1.5× sugar:yeast experiments is 0.99 ± 0.20/cm^2. This value corresponds to an increase of 0.44/cm^2, ~2× increase in density due to a 1.5× increase in sugar:yeast concentration. Nucleation site density for 1-layer, 2-layers and 3-layers experiments are 1.27/cm^2 (118 nucleation sites), 0.91/cm^2 (49 nucleation sites), and 0.80/cm^2 (25 nucleation sites). Values for 5-layers experiments are not available due to the overpressure in the Hele-Shaw cell. A larger number of nucleation sites through time is observed for the 1.5× sugar:yeast concentration experiments (Figs. 5, Fig. S1).

Sealing on three sides, utilizing a rubber o-ring, also causes a change in the number of nucleation sites (Fig. 5). The average nucleation density for the partially sealed experiments is 0.31 ± 0.13/cm^2, representing a decrease of ~36% compared to open experiments. Nucleation site density for 1-layer, 2-layers, 3-layers, and 5-layers experiments are 0.31/cm^2 (28 nucleation sites), 0.14/cm^2 (8 nucleation sites), 0.50/cm^2 (16 nucleation sites), and 0.30/cm^2 (12 nucleation sites). Like open experiments, an increase in the number of layers results in nucleation sites having a greater distribution through time (Fig. 5, S1).

Microfracture growth over time occurs with similar kinetics for all experiments. After an initial period of quiescence due to diffusion of CO_2

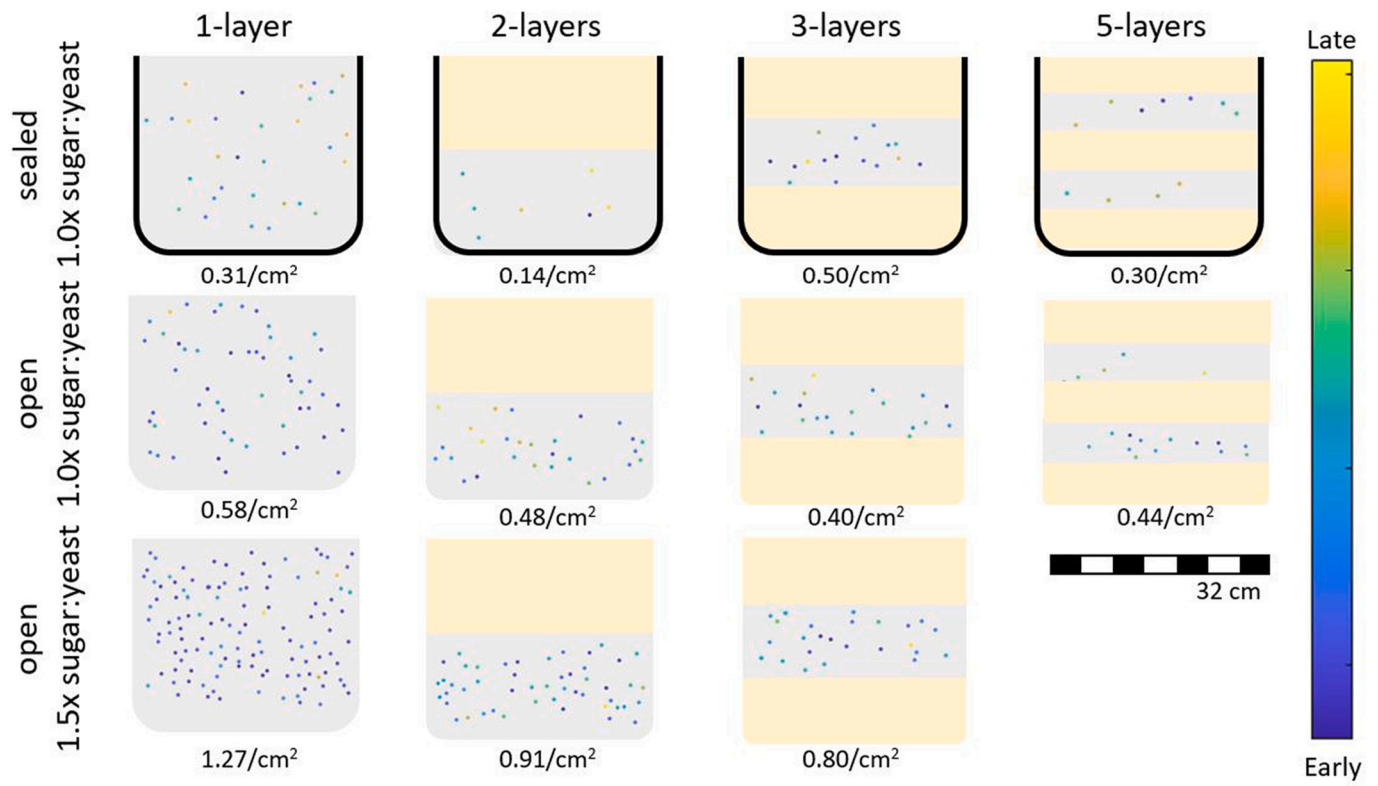

Fig. 5. Microfracture nucleation points and density for all experimental types. The color scale indicates the time.

throughout the matrix (Phase I, Fig. 6), a period of microfracture rapid growth occurs as microfractures first nucleate and then propagate (Phase II, Fig. 6). The transition point between Phase I and II is based on reaching a threshold at ~20% of the total fracture length calculated from an average of all the experiments. There is an acceptable standard deviation across all experiments of +/− 4%, with slight variations among the different experiment types. A greater number of initial nucleation points (e.g., 1.5× sugar:yeast experiments) results in a slightly higher threshold.

Conversely, a lower number of initial nucleation points (e.g., 1.0× sugar:yeast sealed experiments) results in a slightly lower threshold (Fig. 6). Finally, microfracture growth plateaus as a fully developed microfracture network are able to drain the gas produced, and the sugar becomes totally consumed by the yeast (Phase III, Fig. 6). Comparisons between experiments with the same number of layers reveal how experiment type influences the cumulative microfracture length. Experiments with a higher sugar:yeast concentration have the highest cumulative microfracture length. Experiments with the 1.0× sugar:yeast concentration have the next most microfracture length, and sealed experiments have the least (Fig. 6). The total microfracture length for the 1.5× concentration of sugar and yeast is ~500 cm, while it is ~300 cm for the 1.0× concentration of sugar and yeast. Sealed experiments had a smaller total microfracture length up to ~250 cm, indicating that alterations in the concentration of sugar and yeast had a larger impact on the total microfracture network length, whether the experiment was open or partially sealed (Fig. 6).

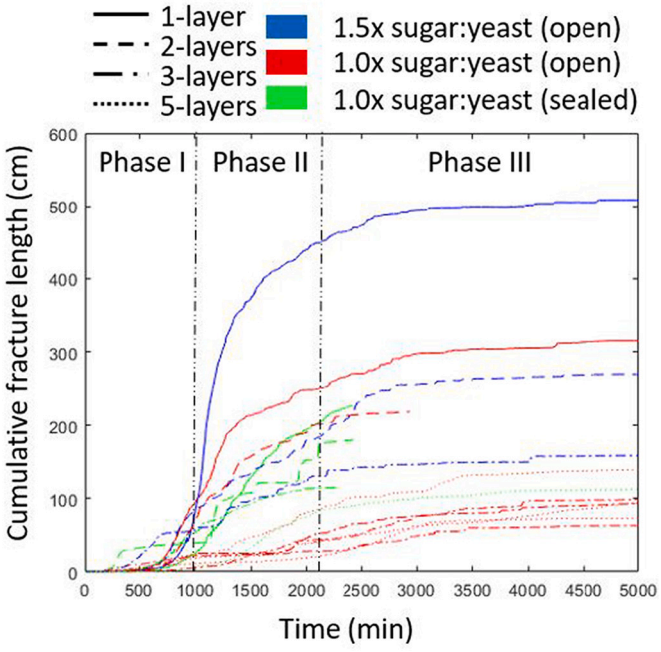

Fig. 6. Cumulative microfracture length shows a sigmoidal evolution with time for all experiments. Black vertical lines separate approximately the three phases of fracture network growth discussed in the text.

Microfracture growth over time is characterized by a sigmoidal growth curve for all experiments. However, 1-layer experiments show a nearly perfect sigmoidal shape (Fig. 6). For the 2-layers and 3-layers experiments, this shape is disrupted whenever slower microfracture growth occurs as a result of microfractures penetrating the non-active gelatin layers (Figs. 4 and 6). Microfracture growth accelerates again whenever microfractures connect. This intermittent growth pattern is perhaps most visible in the sealed experiments (Fig. 6), which also had the greatest distribution of microfracture nucleation sites over time (Fig. 5). This typical sigmoidal growth shape is further influenced in 5-layers experiments, wherein fracture nucleation does not always begin simultaneously in the two different active layers (Figs. 4 and 6).

The 3-layers and 5-layers experiments contain a nearly identical amount of active and inactive gelatin and are therefore ideal to compare

the effect of layering on the total microfracture length. For the 3-layers and 5-layers open experiments, which were all reproduced several times (Table 1), values range from ~50–130 cm for total fracture length, and the variation is due to experimental variability.

The connectivity of microfracture patterns is labeled with colors in Fig. 7, where each color represents a fully connected set of microfractures. Microfracture density is greatest for the 1.5× concentration of sugar and yeast and lowest for sealed experiments (Fig. 7), which is in line with higher nucleation site densities (Fig. 5). Likewise, microfracture density generally decreases with an increasing number of layers; however, there is some similarity between 3-layers and 5-layers experiments (Fig. 7). Connectivity of the microfracture network is higher for both the sealed and high sugar:yeast concentration experiments than for the open 1.0× sugar:yeast concentration experiments (Fig. 7). Connectivity in the microfracture network is the result of two different processes. In the case of the high sugar:yeast concentration experiments, higher nucleation density results in a greater number of microfractures, that become ultimately better connected. In the case of partial sealing utilizing a rubber o-ring on three sides, connectivity is required for the created CO_2 to exit the apparatus, despite fewer nucleation sites.

4.2. Microfracture-microfracture interactions

Microfracture growth results in individual microfractures interacting with each other, as shown by the final microfracture pattern (Fig. 7). Angles of coalescence between two microfractures, δ (Fig. 3), are measured (Fig. 8).

These angles are usually in the range of 55–90° (Fig. 8, Table S1). While the dominant coalescence angle does not change significantly until 5-layers experiments, we measured an increase in the proportion of coalescence angles between 0-54° as the number of layers increases (Table S1). Average coalescence angles based on the experiments from the present study and image analysis on experiments from Kobchenko et al. (2014) reveals one trend. The increase in sugar:yeast concentration impacts the distribution of coalescence angles. The starting point for coalescence angle is ~10° higher for 1.5× sugar:yeast concentration compared to 1.0× concentration. However, the decrease of coalescence angle with the number of layers is similar regardless of sugar:yeast concentration (Fig. 9b). There is also a general decrease in the starting angle; however, the current error for each angle (Fig. 8) is too large compared to the decrease in starting angle to show a robust trend.

There is no apparent relationship between the concentration of the sugar:yeast mixture and ω. Note, 1.5× sugar-yeast mixture experiments show a higher than average value of ω in the 1-layer and 2-layers experiments and a lower than average value of ω in the 3-layers experiments. There is also no apparent relationship due to partial sealing, although these experiments consistently show a value of ω close to the mean value of all experiments.

The 1-layer experiments have the highest average value of ω (Eq. 1) and, therefore, the most fragmented networks, with a value $\omega = 0.38 \pm 0.07$ (Fig. 9). For 2-layers and 3-layers experiments, the average values are $\omega = 0.25 \pm 0.05$ and $\omega = 0.23 \pm 0.09$, respectively (Fig. 9). In the 5-layers experiments, the value of $\omega = 0.08 \pm 0.05$ is the lowest, corresponding to the networks with more branches (Fig. 9). A linear relationship between the number of layers and the parameter ω can be defined as:

$$\omega = -0.07l + 0.43 \quad (10)$$

wherein ω correlates negatively with an increase in the number of layers (l). Therefore, increasing the number of layers results in a shift from a fragmented microfracture network to an almost entirely branched microfracture network.

4.3. Microfracture-layer interface interactions

Microfractures interact not only with one another but also with the interface between layers that contain the mixture of sugar and yeast (i.e., active layers), and layers that do not contain the mixture (i.e., inactive layers). Certain microfractures within multi-layer experiments propagate until interacting with the active and non-active layers interfaces. When a microfracture reaches an interface, it will either breakthrough into the non-active layer or it will be deflected by the interface to propagate along with it. The angle of intersection between the microfracture and interface layer plays a critical role in whether a microfracture penetrates into the next layer or is deflected along with the interface (Figs. 3, 10). Microfracture propagation behavior changes for angles $\theta > 50°$, with significantly more deflection below this value and more breakthrough above it. The average percentage of microfractures that breakthrough for angles above 50° is 70%, and below 50°, it is 15% (Fig. 10).

The number of microfracture-layer interface interactions increases as

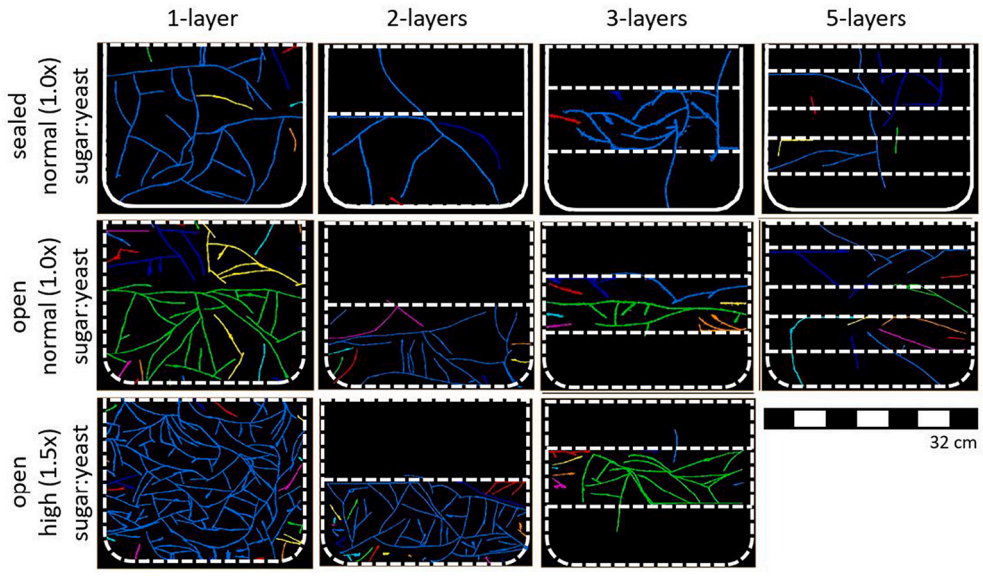

Fig. 7. Final microfracture patterns for representative experiments. Each color is indicative of a connected network of microfractures. Dashed white lines underline the edges and the boundary between layers. A solid white line underlines the sealed portion of some experiments.

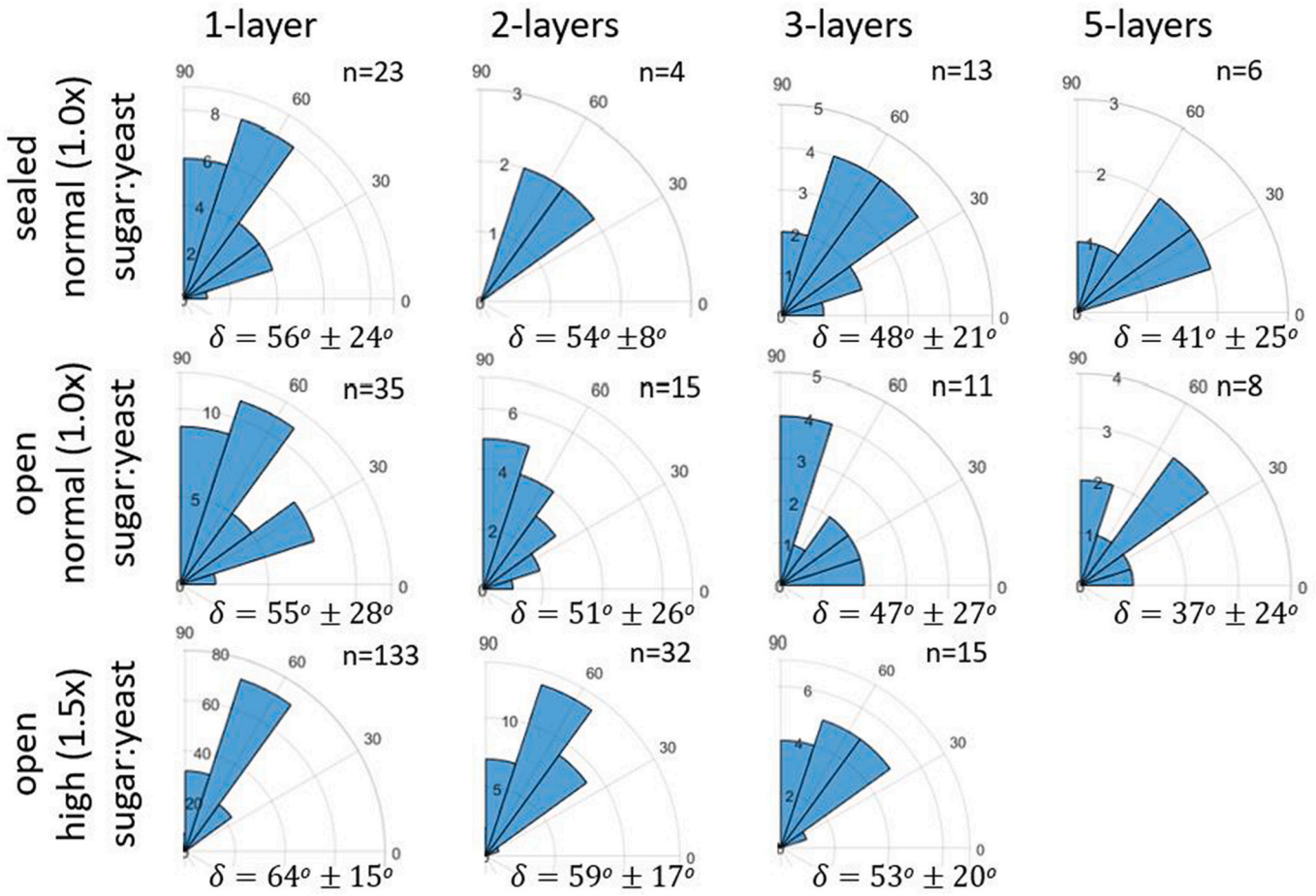

Fig. 8. Distributions of coalescence angle δ (Fig. 3) between any two microfractures for every experiment type. The mean angle and standard deviation are indicated on each plot.

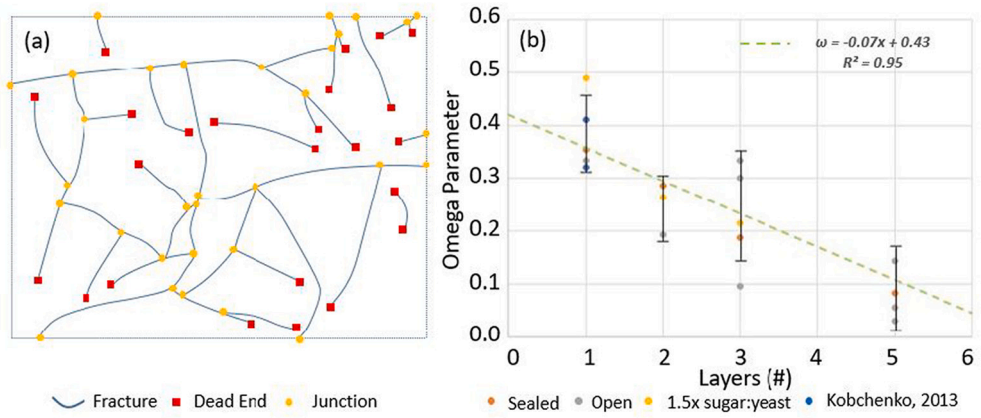

Fig. 9. a) Identification of dead-end nodes and junction nodes in the 1.0× sugar:yeast concentration 1-layer experiment. b) Relationship between the parameter ω (Eq. 1) and the number of layers.

the number of layers increases. Therefore, more data is available for experiments with more layers. Additionally, the increase in the sugar:yeast concentration from 1.0× to 1.5× implies a greater number of microfractures resulting in a greater number of microfracture-interface interactions. However, the data available indicates that the concentration of the sugar:yeast mixture has no effect on the direction of microfracture propagation. Sealing, utilizing a rubber o-ring on three sides, has a clear effect on the angle of interaction between microfractures and layers. The impact of sealing is most noticeable in the 5-layers experiments, where the dominant microfracture angles to the interface are in the range of 70 – 90° (Fig. 10). From the data available in open experiments, increasing the number of layers results in a greater number of interactions that are more oblique (i.e., <50°) to the interface (Figs. 8 and 10).

4.4. *Microfracture network connectivity and fluid flow*

Once the microfracture network as a whole, or an individual

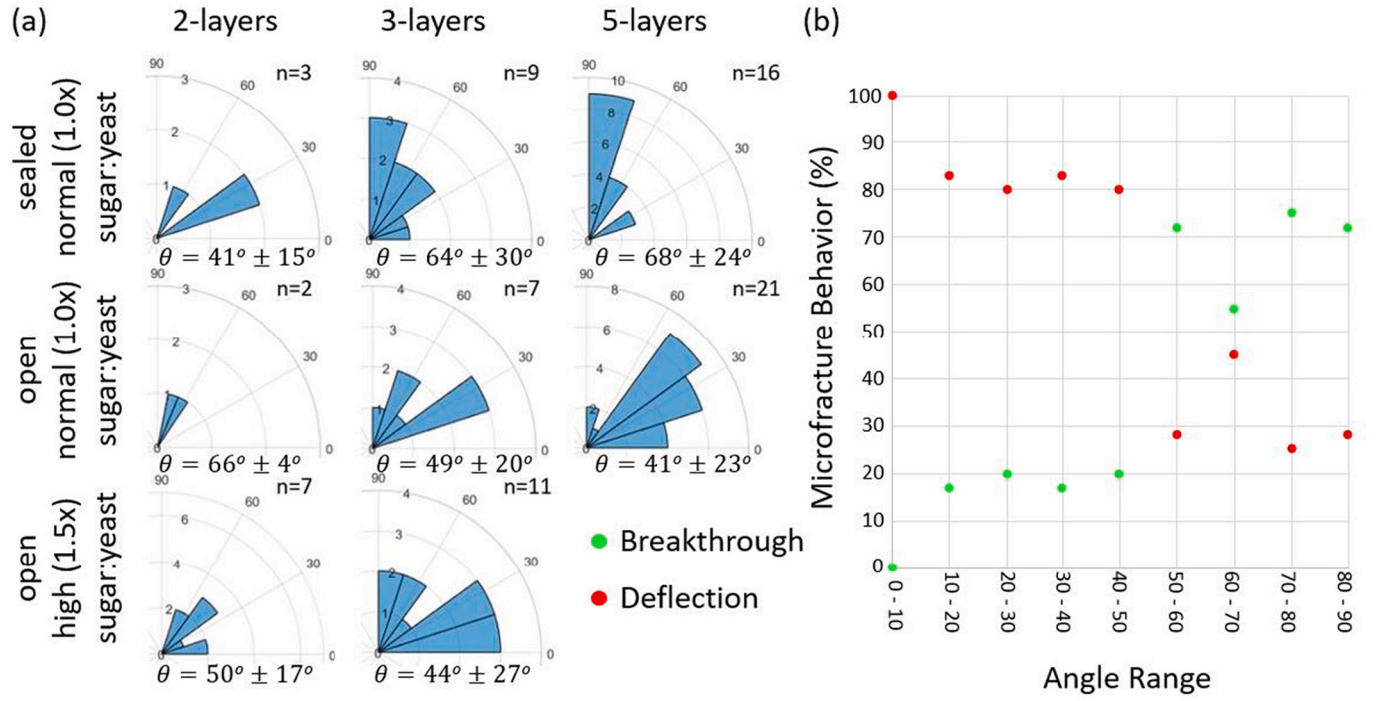

Fig. 10. Angles θ between microfractures and gelatin layer interfaces: 0° is parallel to the interface, while 90° is perpendicular. (a) The angle of intersection between a microfracture and the layer interface for all multi-layer experiments. Mean angle for each experiment, θ, is given with the standard deviation. (b) Microfracture behavior is described as either breakthrough or deflection along with the interface depending on the angle θ between the microfracture and the layer interface (see also Fig. 3b).

microfracture, is connected to an outside edge, a pathway allows the migration of the CO_2 to either other microfractures or outside of the apparatus. At this point, the fluid filling microfractures can be expelled from the gelatin resulting in the closing of microfractures. As CO_2 continues to flow from the host matrix into the microfractures, they will reopen again intermittently. This behavior can be seen when plotting the total surface area of the open microfractures as a function of time, A(t), for all fifteen quantifiable experiments (Fig. 11). An initial period of microfracture nucleation and growth correlates with Phases I and II, defined in Fig. 6. After some time, the total microfracture length plateaus and the increase and decrease in microfracture aperture surface area relate to the opening and closing of the microfracture network, corresponding to Phase III (Fig. 11). The amplitude of variation for the microfracture area is the largest in sealed experiments and smallest for open experiments with a 1.0× sugar:yeast concentration (Fig. 11).

Partially sealed experiments that utilized a rubber o-ring on three sides show a greater amount of build-up time compared to other experiment types before fluid expulsion from the microfracture network occurs (Fig. 11). The greater time required for expulsion may be an indicator that the partial seal altered the ability of the system to transfer stress within its stress field (i.e., greater fluid pressure is required locally to expel fluids). This interpretation is supported by the lower nucleation density in partially sealed experiments compared to open experiments.

A Fourier transform was applied to the signal, A(t), in order to characterize its intermittency (Fig. 12a). The signal contains both a periodic component, identified by the main peak of the signal and a decay towards higher frequencies (Fig. 12a).

The data are plotted on a logarithmic scale (Fig. 12b) in order to compare the peak frequencies for all of the experiments. The amplitude of the peak generally correlates to the number of layers, with 1-layer experiments having the largest amplitude and 5-layers the smallest one (Fig. 12b). All experiments had a tight grouping of peak values within their experiment class. Peak frequencies for open experiments with 1.0× concentration of sugar:yeast varied in the range of $10^{-2.91}$ to $10^{-2.85}$ Hz, corresponding to time scales in the range of 700–800 s

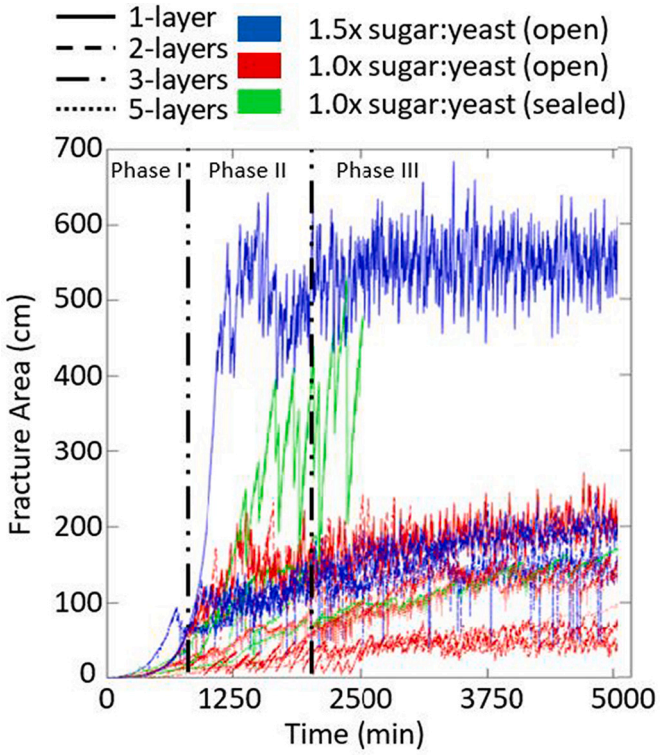

Fig. 11. Total surface area of microfracture aperture as a function of time. The intermittent expansion and contraction of the surface area in Phase III correlate to the opening and closing of microfractures as CO_2 is expelled from a fully developed network. Black vertical dash-dot-dot lines separate out approximately three phases discussed in the text: I (nucleation), II (microfracture growth), and III (intermittent closing and opening of the microfractures). See also Fig. 6.

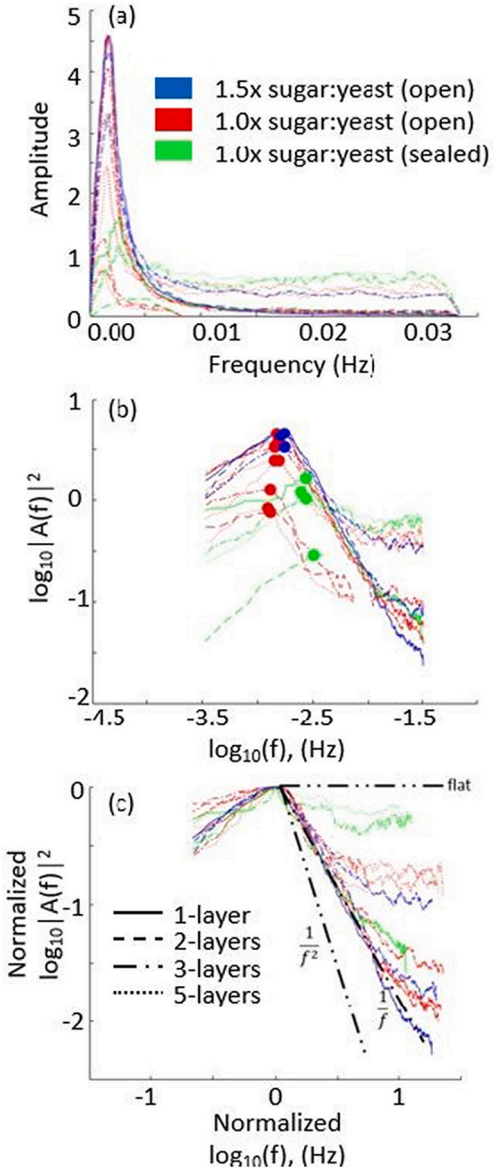

Fig. 12. Fourier transform of the total surface area of microfracture aperture, (A(t), as a function of time and the characterization of intermittent fluid flow within the microfracture network for each experiment. a) Fourier transform showing the peak frequency of A(t). b) Same as a) on a double logarithmic scale to isolate the peak frequencies and their amplitudes. c) Fourier transform normalized by the peak frequency of each experiment in order to investigate the degree of microfracture interactions in each experiment type. Black dash-dot-dot lines indicate $1/f^2$, 1/f, and a flat slope.

(Fig. 12b). Open experiments with a higher concentration of sugar:yeast (1.5×) consistently had slightly greater peak frequency values, ranging from $10^{\text{ to } 2.79}$ to $10^{-2.77}$ Hz, corresponding to time scales in the range of 590–620 s (Fig. 12b). Finally, sealed experiments had even greater peak frequency values, ranging from $10^{\text{ to } 2.65}$ to $10^{-2.52}$ Hz, corresponding to time scales in the range of 330–450 s (Fig. 12b).

To obtain Fig. 12c, the curves in Fig. 12b were collapsed by normalizing the FFT by the position and amplitude of the peak. The nonlinear dynamics of microfracture opening and closing are described by the slope of linear trends in the log-log plot, which correspond to power laws. Based on the work of Bons and van Milligen (2001), Kobchenko et al. (2014) established that $1/f^2$ describes the frequency evolution of a single fracture, while 1/f describes the frequency evolution of a well-connected fracture network that pulsates as a whole system due to the existence of long-range elastic interactions. Conversely, the frequency independent correlation ($1/f^0$) indicates a poorly interconnected network, resulting in pulsations that are comparatively random. The power-law exponents vary between −1.74 and − 0.28 (Fig. 12c). Experiments with 1-layer were closest to the reference line 1/f within their experiment class. Increasing the number of layers and introducing lateral sealing resulted in smaller power-law exponents (i.e., poorer connectivity).

Fluid flow relationships are tied to fracture topology that is effectively established by the end of Phase II (Figs. 9, 13). XYI-nodes are particularly helpful in understanding the relationship between the fracture network and ease of fluid flow. Fig. 13 shows the distribution of XYI-nodes on a ternary diagram. Utilizing Eq. 3, the parameter ε quantifies how well the fracture pattern may accommodate the fluid flow. Analysis of the distribution of XYI-nodes (Fig. 13) in relationship to ε reveals that a more interconnected network with a greater number of X- and Y-nodes results in higher permeability for the 1.5× sugar:yeast concentration experiments. Sealed experiments are the next most permeable, with open 1.0× sugar:yeast experiments being the least (Fig. 13).

The open experiments with 1.0× sugar and yeast concentration plot below the line ε = 2. Sealed experiments plot on either side of the line ε = 2, indicating that the experiments generally are better connected, facilitating flow. Similarly, the 1.5× sugar and yeast concentration experiments have significantly more X-nodes and plot below the line ε = 3. It is also worth noting that the 1-layer experiments always have the best potential flow rate (i.e., permeability) within an experiment class. Increasing the number of layers generally correlates to a decrease in potential flow rate within each experiment class.

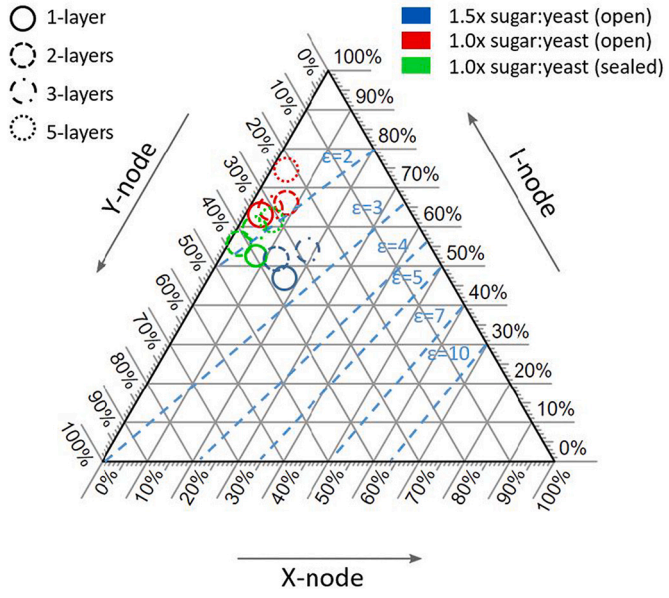

Fig. 13. Ternary diagram representing the distribution (%) of XYI-nodes (Fig. 3c). The dashed blue lines correlate to hypothesized and later empirically established degrees of connectivity that influence the permeability of a given microfracture network, where ε = 2 is poorly connected, and ε =10 is considered well connected (Sanderson and Nixon, 2015; Silva et al., 2021). Note, for natural systems, values of ε are dominantly in the range 2–4 (Sanderson and Nixon, 2015; Alvarez et al., 2021; Silva et al., 2021). (For interpretation of the references to color in this figure legend, the reader is referred to the web version of this article.)

5. Discussion

5.1. Comparison to previous experimental studies

The work presented here follows previous experimental studies completed by Kobchenko et al. (2013, 2014) and Vega and Kovscek (2019), who also studied organic-rich shale microfracturing by incorporating additional complexity found in natural systems. Similar to the goals of previous experiments (Kobchenko et al., 2013; Kobchenko et al., 2014; Vega and Kovscek, 2019), the focus was placed on small deformations due to elastic interactions related to the opening and closing of microfractures. This precludes the more elasto-plastic rheology of shale at a macro-scale. The 1-layer experiments are best representative of the isotropic plane within transversely isotropic rocks, including organic-rich shales at a finer scale (mm-cm) (Kobchenko et al., 2013; Kobchenko et al., 2014; Vega and Kovscek, 2019; Johnson et al., 2022b). Our experiments used a 1-layer model, including varying the concentration of sugar:yeast, to reproduce the results of these previous studies. Our results extend the data available on microfracture nucleation sites. We calculated the nucleation densities for the experimental data reported in Kobchenko et al. (2013) and found values of 0.41/cm^2 and 0.55/cm^2 compared to our value of 0.58/cm^2. Vega and Kovscek (2019) utilized the 1.5× sugar:yeast concentration for their experiments. They measured nucleation densities of 0.76/cm^2, 1.16/cm^2, 1.19/cm^2, and 1.28/cm^2 compared to 1.27/cm^2 for our 1.5× sugar:yeast 1-layer experiment. Therefore, the results in the present study show comparable values to previous experiments.

Kobchenko et al. (2014) and Vega and Kovscek (2019) observed that microfracture growth occurs in three stages, as is the case for the present study. During the initial stage, penny-shaped microfractures nucleate as CO_2 diffusion through the matrix fails to expel the gas quickly enough from the apparatus. This stage is followed by a period of rapid microfracture growth and further nucleation, wherein microfractures propagate from initial nucleation points. During this stage, in 1-layer experiments, the microfractures coalesce, ultimately creating a dominant connected microfracture network (Fig. 7), that may be assisted in draining the CO_2 by a series of smaller microfracture networks (Kobchenko et al., 2013; Kobchenko et al., 2014; Vega and Kovscek, 2019). Our experiments confirm this pattern for both the 1.0× and 1.5× sugar:yeast concentrations in the 1-layer experiments (Fig. 6). Furthermore, the final microfracture patterns appear similar to Kobchenko et al. (2013, 2014), which is also quantified by similar values of the parameter ω (Fig. 9). The average value of ω in the present study is 0.38, compared to 0.37 for Kobchenko et al. (2013). The microfracture patterns observed by Vega and Kovscek (2019) were more curvilinear. However, the values of the angle of coalescence between microfractures (Fig. 8) confirm the results previously established in all comparable studies (Kobchenko et al., 2013; Kobchenko et al., 2014).

In the final stage (i.e., Phase III), little to no microfracture growth occurs. However, the microfractures continue to open and close intermittently as the CO_2 is drained (Fig. 12, Phase III), as observed in previous studies (Kobchenko et al., 2014; Vega and Kovscek, 2019). This is represented by the periodic opening and closing of fractures (Fig. 11). Stronger periodicity is indicative of diffusion, while more irregular behavior as seen in Fig. 11 indicates a combination of fracture dominated flow alongside diffusion (de Reise et al., 2020). Kobchenko et al. (2014) noted that the drainage is defined by a characteristic frequency and non-linear behavior characterized by power laws. The peak frequency of microfractures opening and closing, which characterizes the fluid movement of the system within microfractures, varies depending on the concentration of sugar:yeast in the system (Fig. 12b). The power spectrum slope of 1/f for 1-layer experiments is confirmed with a value of −1.74 from Kobchenko et al. (2014) and a value of −1.69 for the present study. Kobchenko et al. (2014) noted that, while the dynamics of a single microfracture will have a slope of 1/f^2, a slope of 1/f is representative of a connected microfracture system with good intermicrofracture communication. The results of both Kobchenko et al. (2014) and the present study also show self-organized criticality (Bons and van Milligen, 2001).

Li et al. (2020) conducted a series of experiments using gelatin in 3D, where they investigated the behavior of an elastic medium during the microfracturing process. However, instead of internal fluid generation, red ink was injected in order to create a singular extensive microfracture to investigate hydraulic fracturing. Similar to other studies with gelatin (Kobchenko et al., 2013; Kobchenko et al., 2014; Vega and Kovscek, 2019; Li et al., 2020), the relationship between mechanical properties of gelatin (i.e., Young's modulus, Poisson's ratio) and temperature is highlighted. Orientation of microfracture propagation (i.e., horizontal or vertical) was controlled by applying a vertical force to encourage the growth of vertical microfractures. This is in line with what is known about how stress-regimes impact microfracture growth (Zoback, 2007). Therefore, for microfracture growth to occur, the pressure applied would need to be greater than the inherent strength of gelatin, in addition to the force applied. However, with the absence of anisotropy and the presence of only one microfracture front modelled utilizing Perkins-Kern-Nordgren (PKN) and Kristonouch-Geertsma-Daneshy (KGD) microfracture propagation models (Smith and Montgomery, 2015; Li et al., 2020), it represents a single-porosity homogenous system (Heinemann and Mittermeir, 2012; Uzun et al., 2017; Johnson, 2018). The present study does not introduce a stress regime, and the base case has a complex microfracture network where all orientations are equally likely, as observed in previous studies (Kobchenko et al., 2013; Kobchenko et al., 2014; Vega and Kovscek, 2019). Nonetheless, all these studies are complementary to understanding hydraulic fracturing behavior. The introduction of anisotropy and a complex microfracture network is representative of dual-porosity systems commonly encountered during hydraulic fracturing in oil and gas reservoirs of all lithologies (Heinemann and Mittermeir, 2012; Smith and Montgomery, 2015; Uzun et al., 2017; Johnson, 2018). Li et al. (2020) highlight the importance of a stress regime to artificial fracturing, while the present study reveals the importance of rock fabric as it impacts the propagation of microfractures. Furthermore, the present study could help evaluate how fracture topology will influence hydrocarbon extraction (Fig. 13).

5.2. Gas diffusion and nucleation of microfractures (phase I) in the context of primary migration

Gas diffusion is the dominant form of fluid expulsion prior to the onset of microfracturing (Kobchenko et al., 2013, 2014). This is confirmed by the 0.5× sugar:yeast experiment (Table 1) that had CO_2 production without fracture nucleation. When diffusion is not sufficiently fast enough in expelling fluids compared to the CO_2 production rate, microfractures nucleate (Eq. 6). Increasing the sugar and yeast concentration increases the density of nucleation sites for microfractures. In the context of organic-rich shales during primary migration, this result indicates that increases in total organic carbon (TOC) content will have a comparatively greater impact on the number of nucleation points (i.e., kerogen lenses) that are activated. Modelling of organic-rich shales during kerogen conversion supports this supposition for shale with TOC between 0 and 8 wt% (Jin et al., 2010; Fan et al., 2010; Chauve et al., 2020). However, it has been established that, for Jurassic source rocks in the North Sea and the Barents Sea, TOC above ~8% does not result in a greater number of kerogen lenses (i.e., nucleation points) since the kerogen lenses begin to combine, resulting in a net decrease of the number of kerogen lenses per rock unit volume (Johnson et al., 2022b). The present study establishes that layering does not impact the number of nucleation points. This would suggest that all other factors being equal (i.e., kerogen type, chemical composition of lenses), a highly anisotropic shale (e.g., Hekkingen Formation, Vaca Muerta Formation, Wolfcamp Formation) with 2 wt% TOC would have just as many nucleation points as a shale with comparatively lower anisotropy (e.g., Bakken Formation, Green River Formation, Montney Formation) and

containing 2 wt% TOC.

Sealing the environment resulted in a ~ 36% drop in microfracture nucleation point density (Fig. 5) from an average of 0.45/cm^2 for the open experiments to 0.31/cm^2 for the partially sealed experiments. We suggest that the decrease in nucleation point density may correlate to a change in the ability for long range stress to be transferred within the system due to the presence of the partial seal (Eq. 4). Therefore, factors that influence the shale stress field (i.e., mineralogy, fluid) and loading stress may also impact the density of microfractures that nucleate during primary migration. The inhibition of new fractures in the vicinity of pre-existing microfractures may also influence the number and distribution of microfracture nucleation sites (Kobchenko et al., 2013).

5.3. Fracture growth and network interconnection (phase II) in the context of primary migration

In 1-layer (isotropic) open experiments, the angle of coalescence between two microfractures is usually high (i.e., >50^o) by the end of Phase II (Fig. 6), similar to previous studies (Kobchenko et al., 2013; Kobchenko et al., 2014; Vega and Kovscek, 2019). In an isotropic environment, a microfracture tip deflection can occur when the maximum component of the stress tensor around a microfracture tip changes orientation such that the microfracture tip will bend towards a pre-existing microfracture (Takada, 1994; Watanabe et al., 2002). The introduction of anisotropy in the system, through varying the number of layers, has an effect on the angle of coalescence between two microfractures (Fig. 8; Table S1). This growth of microfractures parallel to layer boundaries can be seen in Fig. 7 more consistently for the 3-layers and 5-layers experiments than for the 1-layer and 2-layers experiments. Similar patterns have been observed in organic-rich shales during and after kerogen maturation (Kobchenko et al., 2011; Kalani et al., 2015; Ougier-Simonin et al., 2016; Johnson et al., 2022b). It is also worth noting that few microfractures propagate perpendicularly (i.e., vertically) between the layers (Fig. 7), connecting the largely parallel horizontal microfracture swarms in 3-layers and 5-layers experiments. This process has also been observed in nature and artificial maturation of organic-rich shales, wherein few vertical microfractures connect swarms of roughly horizontal (bedding parallel) microfractures (Kalani et al., 2015; Ougier-Simonin et al., 2016; Panahi et al., 2019; Johnson et al., 2022b).

The parameter ω has been used to characterize the topology of networks in isotropic and anisotropic media. For example, this parameter was used to study the statistical topology of river networks for more than 70 years (Horton, 1945; Wang et al., 2020). Rocks in the subsurface can contain well-developed anisotropic structures (e.g., shale, slates, gypsum, phyllites, schists, gneisses). Additionally, anisotropic rocks are generally isotropic in one direction and anisotropic in the other two directions (Kuila et al., 2011; Agliardi et al., 2014; Johnson et al., 2022b). Our experiments suggest that the microfracture network topology in isotropic rocks, or the isotropic direction of an anisotropic rock, is intermediate between a network that contains only isolated branches and an entirely fragmented network. Furthermore, the experiments indicate that a minimal number of layers (i.e., ~5) is required to shift microfracture interaction behavior to an almost entirely branching network (Fig. 9), as described by Eq. 10. This result would suggest that the way microfracture networks grow and interact with themselves is at least partially controlled by the fabric of the medium. The described pattern can be seen in organic-rich shales (Kobchenko et al., 2011; Ougier-Simonin et al., 2016; Johnson et al., 2022b).

Our experiments highlight that the likelihood of a microfracture breaking through a layer is dependent on the angle of intersection with that layer (Fig. 10). For an angle equal to or larger than 50°, a microfracture has a ~ 70% probability of breakthrough, while this probability drops to ~15% on average if the angle is below 50° (Fig. 9). When a microfracture fails to break through a layer, it may deflect along with the interface between the two layers (Figs. 3 and 10). Ghani et al. (2015) developed numerical models to show that stronger seals will result in fracture deflection, while weaker seals will initially build up horizontal fractures that ultimately allow the progression of 'evenly' spaced vertical seals. While there are not enough fractures in our experiments to provide even spacing, the analogue model confirms a collection of horizontal fractures linked by a few vertical fractures (Fig. 7). Analysis of natural systems also show this observation (Vass et al., 2014; Koehn et al., 2020). In the laboratory, vertical microfracture breakthrough for angles larger than 50° has been shown to occur during the artificial maturation of organic-rich shales that were laterally sealed (Ougier-Simonin et al., 2016; Panahi et al., 2019). However, the introduction of sealing in our experiments favored microfracture growth that had a tendency to interact at an angle greater than 50^o in the layered experiments (Fig. 10). Therefore, the development of microfractures that propagate perpendicular to layering may be the result of laboratory conditions in our experiments.

However, if all naturally occurring microfractures due to maturation within organic-rich shale were at a low angle (<30^o) with respect to layering, the amount of interactions that typically occur would result in a certain number of microfractures penetrating each subsequent layer allowing for fluid migration across sedimentary layers. Johnson et al. (2022b) suggested that the initial angle of microfracture propagation will depend on the internal orientation of the kerogen lens, which can deviate ±30^o from bedding, on average. Therefore, depending on the number of kerogen lenses present (Johnson et al., 2022b) and the degree of maturation (Zhao et al., 2016; Johnson et al., 2022a), high angle (i.e.,>50^o) fracturing should not be required for hydrocarbon migration to occur.

5.4. Fluid migration (Phase III) in the context of primary migration

The relationship between fractures and fluid flow is well established (e.g., Heinemann and Mittermeir, 2012; Nolte and Nolte, 2015; Sanderson and Nixon, 2015; Uzun et al., 2017). XYI-node classification has been proposed as one possible tool to help understand this relationship (Sanderson and Nixon, 2015). Silva et al. (2021) established that media dominated by X- or Y- nodes are ~1000× more permeable than those dominated by I-nodes, while those with an equal distribution of all three are ~400× more permeable than those with solely I-nodes. Increasing layering (i.e., anisotropy) results in a less permeable fracture network (Figs. 7, 12, 13). Triaxial tests performed on shale and classified according to XYI-nodes confirm this result. As the stress regimes applied become more anisotropic, an increase in the number of I-nodes results in decreased permeability (He et al., 2021). The impact of fluid viscosity was also studied in the triaxial tests, suggesting that increasing fluid viscosity results in increased permeability (He et al., 2021). The present study did not introduce different viscosities for the fluid produced, but this is a variable present in primary migration (Jones, 1987; Vandenbroucke and Largeau, 2007). It was found that lower viscosity fluids resulted in greater network fracturing, interconnection, and higher permeability (He et al., 2021). Therefore, as viscosity increases with hydrocarbon chain complexity, all other variables being equal, shales with Type I kerogen (e.g., Barremian Bucomazi Formation, Vaca Muerta Formation) should form less permeable microfracture networks than those dominated by Type II kerogen (e.g., Bakken Formation, Kimmeridge Formation, Montney Formation, Wolfcamp Formation). Similarly, fracture networks in shale with Type III kerogen (e.g., Kimmeridge Formation, Wolfcamp Formation) will be more complex than that dominated by either Type I or Type II.

Beyond fracture topology, our experiments have established that higher TOC content will result in both faster and greater hydrocarbon production (Figs. 11, 12). Numerous studies confirm this result (Fan et al., 2010; Jin et al., 2010; Kobchenko et al., 2014; Kalani et al., 2015; Johnson, 2017; Teixeira et al., 2017; Chauve et al., 2020; Rabbel et al., 2020; Johnson et al., 2022b). Our study also shows that changes in the stress field that occurs due to the placement of the rubber o-ring result in

faster gas production (Fig. 12b), which has also been previously established (Heinemann and Mittermeir, 2012; Nolte and Nolte, 2015; Uzun et al., 2017). The experiments with a higher stress field also had greater periodicity, potentially suggesting diffusion is a greater factor for fluid flow within these systems (de Reise et al., 2020). It is, however, interesting to note that the experiments indicate that systems with a lower stress field have a poorer ability to transmit stress, and increased layering (i.e., anisotropy) will result in poorer fluid flow connection (Fig. 12c).

5.5. Applications to other subsurface systems

Organic-rich shales exhibit layering at the millimeter to centimeter scale, wherein some layers are organic-rich and others are organic-poor (Hoosen, 1747; Blatt and Tracy, 1996; Merrimen et al., 2003; Chauve et al., 2020; Johnson et al., 2022b). Numerical simulations and 3D microtomography imaging have revealed that microfractures will grow within and interact between these layers (Fan et al., 2010; Rabbel et al., 2020; Chauve et al., 2020; Johnson et al., 2022b). The focus of the present study is placed on such organic-rich shales in the context of primary migration at a fine scale (mm-cm), wherein the emphasis can be placed on brittle deformations that occur prior to larger plastic deformations often observed in shales and other rocks. However, the results of our experiments may find some relevance for a number of other subsurface systems, including the conversion of hydrous to anhydrous minerals (e.g., gypsum to basanite, smectite to illite), interlayered limestone, and mudstone at a larger scale (m-km), dehydration of serpentine rocks in subduction zones, fracture growth within layered rocks (e.g., slates, gypsum, phyllites, schists, gneisses), and within partial melts.

During Phase I, the experiments are representative of the conversion of hydrous to anhydrous minerals (e.g., smectite to illite). Specifically, the reduction of three to zero water layers in the transition of smectite to illite results in a substantial decrease in volume resulting in fluid expulsion (Vidal and Dubacq, 2009). This transition occurs in a similar PT regime to the conversion of kerogen lenses (Tissot et al., 1974; Vidal and Dubacq, 2009). The orientation of the long-axis of clay minerals, similar to that of kerogen lenses, is generally parallel to the layering (i.e., anisotropy) of the shale fabric (Vandenbroucke and Largeau, 2007; Johnson et al., 2022b). It has been proposed that fracturing will occur in line with the long-axis (Fan et al., 2010; Voltolini and Franklin, 2020; Johnson et al., 2022b) or pre-existing anisotropy, as seen in the present study (Fig. 7). Another form of anisotropy that has a similar impact on nucleation and initial fracture growth direction is the presence of a preferential stress direction (Fusseis et al., 2012; Rummel et al., 2020). During the conversion of gypsum to basanite, fracture growth will propagate parallel to the pre-existing anisotropy direction (Fusseis et al., 2012). Similarly, Rummel et al. (2020) have shown that alterations in stress direction have a significant impact on the direction of fracture growth.

Once microfractures begin to coalesce during Phase II, the fabric of the medium or layering (i.e., anisotropy) influences how microfracture networks grow and release fluids. Comparisons of relatively isotropic rocks or orientations of those rocks with anisotropic rocks or orientations reveal that fabric influences the angles of coalescence between fractures. Furthermore, the fabric influences the fracture topology of the networks. It has been noted that this is observable in organic-rich shales (Kobchenko et al., 2011; Ougier-Simonin et al., 2016; Johnson et al., 2022b), gypsum/basanite systems (Fusseis et al., 2012), and metamorphic schists and gneisses (Agliardi et al., 2014). Occasional microfractures that break through across layering have also been recorded in these same systems. The material properties of the fabric also influence microfracturing, wherein a layer of comparably higher strength will result in a greater number of microfractures deflecting while a layer of lower strength will result in comparatively few vertical fractures interconnected by many horizontal fractures (Ghani et al., 2015; Koehn et al., 2020). This material property element, within anisotropy, was not directly investigated. However, it sits at the axis between anisotropy and sealing.

The influence of layering (i.e., anisotropy) and sealing has a significant impact on fracture topology and, by extension, fluid flow within layered rocks other than shale (e.g., slates, gneisses, schists). Our experiments indicate that higher levels of layering will result in poorer communication (Fig. 13). This is further complicated by variations in layer thickness (Rijken and Cooke, 2001) which can vary by a significant percentage in metamorphic rocks (Williams, 1990). Fractures transecting layers have greater success when they are thinner. This is well represented by the number of fractures that transect the inactive host of the 5-layer experiments as opposed to the 2-layer experiments (Fig. 7).

Crustal partial melt systems are usually anisotropic (e.g., stromatic migmatites), although it has not been fully established what structure partial melts may take in the mantle (Vigneresse and Clemens, 2000; Marchildon and Brown, 2003; Bons et al., 2009). Within the model of fractured networks, emplacement occurs through a fractured network system (Clemens and Droop, 1998), wherein the percolation rate is dependent on the drain rate (Vigneresse and Clemens, 2000; Bons et al., 2009). This mechanism of magma-emplacement may explain how the smallest fractures can feed larger dykes and, finally, plutons (Brown and Solar, 2009). Bons et al. (2009) suggested that the mechanism of magma emplacement would stop because of sealing, preventing stable connectivity as seen in the experiments (Fig. 7). Instead, melt accumulation would occur in a stepwise manner (Bons et al., 2009; Saukko et al., 2020). Other studies proposed a stable connection between melt accumulations (Brown and Solar, 1998; Sawyer, 2001; Vanderhaeghe, 2009). Xiong et al. (2019) modeled melt transport within a connected system that would be an apt comparison to the analogue models of the present study. Most models of melt transport exhibit some degree of self organization (Vanderhaeghe, 2009; Bons et al., 2009; Saukko et al., 2020), as displayed in Fig. 12. Should lateral sealing be present within these systems (Chakraborty, 2017; Rummel et al., 2020), it would have an impact on network communication, as seen within our experiments (Figs. 11–13). Critically the degree of connectivity, as modeled, may impact the rate of magma drainage.

6. Conclusions

Our analogue experiment explores the formation of microfractures in low permeability and layered brittle solids during internal fluid production. The presence of yeast and sugar that leads to the production of gaseous carbon dioxide controls fluid production in the solid. Three phases are observed within all experiments, starting with (1) an initial production of CO_2 resulting in the nucleation of penny-shaped microfractures, (2) followed by the growth of a microfracture network, and (3) finally, fluid expulsion resulting in intermittent microfractures opening and closing. This analogue system exhibits a rich dynamical behavior that provides a proxy for several natural processes in the Earth's crust in which fluid expulsion is controlled by both internal fluid production and elastic interactions.

The presence of layering (i.e., anisotropy) in the system has no influence on the nucleation density of microfractures. Furthermore, layering impedes and influences microfracture growth. Specifically, an increase in the number of microfractures parallel to the anisotropy direction results in more oblique angle intersections between microfractures. Increased layering also results in a more disconnected microfracture network resulting in poorer fluid communication.

The introduction of sealing potentially alters the ability for stress to be transmitted within the host matrix and reduces the nucleation density of microfractures. Despite fewer nucleation sites, the microfractures created showed a better connectivity even when anisotropy is introduced. This results in a greater number of microfractures intersecting layers at high angles ($>50^{o}$), thereby ensuring greater breakthrough success. However, this change in the stress field also appears to have

impacted the rate of fluid production. Interestingly, the combination of layering with a poorer ability to transmit stress resulted in poorer fluid flow connection while maintaining a higher total rate of fluid production.

Applications of the study are particularly relevant when trying to understand organic-rich shales in the context of primary migration. Important parameters, including the impact of layering and changes in stress transmissibility (e.g., changes in mineralogy), are common and complex problems that apply to primary migration within organic-rich shales. The results of the experiments are also applicable to other natural processes (i.e., partial melts, conversion of hydrous minerals to anhydrous, fracturing in layered media).

Supplementary data to this article can be found online at https://doi.org/10.1016/j.tecto.2022.229575.

Declaration of Competing Interest

The authors declare that they have no known competing financial interests or personal relationships that could have appeared to influence the work reported in this paper.

Data availability

Data will be made available on request.

Acknowledgements

The Research Council of Norway funded this work (grant no. 267775).

References

Agliardi, F., Zanchetta, S., Crosta, G.B., 2014. Fabric controls on the brittle failure of folded gneiss and schist. Tectonophysics 637, 150–162. https://doi.org/10.1016/j.tecto.2014.10.006.

Alvarez, L.L., Guimaraes, L.J.N., Gomes, I.F., Beserra, L., Pereira, L.C., Miranda, T.S., Maciel, B., Barbosa, J.A., 2021. Impact of fracture topology on the fluid flow behavior of naturally fractured reservoirs. Energies. 14, 5488. https://doi.org/10.3390/en14175488.

Anders, M.H., Laubach, S.E., Scholz, C.H., 2014. Microfractures: a review. J. Struct. Geol. 69, 377–394. https://doi.org/10.1016/j.jsg.2014.05.011.

Backeberg, N.R., Iavoviello, F., Rittner, M., Mitchell, T.M., Jones, A.P., Day, R., Wheeler, J., Shearing, P.R., Vermeesch, P., Striolo, A., 2017. Quantifying the anisotropy and tortuosity of permeable pathways in clay-rich mudstones using models based on X-ray tomography. Sci. Rep. 7, 14838. https://doi.org/10.1038/s41598-017-14810-1.

Bai, F.W., Anderson, W.A., Moo-Young, M., 2008. Ethanol fermentation technologies from sugar and starch feedstocks. Biotechnol. Adv. 26, 89–105. https://doi.org/10.1016/j.biotechadv.2007.09.002.

Bear, J., 1975. Dynamics of fluids in porous media. Soil Sci. 120 (2), 162–163. https://doi.org/10.1097/00010694-197508000-00022.

Beigbeder, J.B., Dantas, J.M.M., Lavoie, J.M., 2021. Optimization of yeast, sugar and nutrient concentrations for high ethanol production rate using industrial sugar beet molasses and response surface methodology. Fermentation 7, 86. https://doi.org/10.3390/fermentation7020086.

Blatt, H., Tracy, R.J., 1996. Petrology: Igneous, Sedimentary, and Metamorphic, 2nd ed.

Bons, P.D., van Milligen, B.P., 2001. New experiment to model self-organized critical transport and accumulation of melt and hydrocarbons from their source rocks. Geology 29 (10), 919–922. https://doi.org/10.1130/0091-7613(2001)029<0919:NETMSO>2.0.CO;2.

Bons, P.D., Dougherty-Page, J., Elburg, M.A., 2001. Stepwise accumulation and ascent of magmas. J. Metamorph. Geol. 19, 627–633. https://doi.org/10.1046/j.0263-4929.2001.00334.x.

Bons, P.D., Becker, J.K., Elburg, M.A., Urtson, K., 2009. Granite formation: stepwise accumulation of melt or connected networks? R. Soc. Edinburgh Trans. Earth Environ. Sci. 100, 105–115. https://doi.org/10.1017/S175569100901603X.

Bourdon, B., Turner, S., Dosseto, A., 2003. Dehydration and partial melting in subduction zones: Constraints from U-series disequilibria. J. Geophys. Res. 108 (B6), 2291. https://doi.org/10.1029/2002JB001839.

Brizzi, S., Funiciello, F., Corbi, F., Giuseppe, E.D., Mojoli, G., 2016. Salt matters: how salt affects the rheological and physical properties of gelatine for analogue modelling. Tectonophysics. 679, 88–101. https://doi.org/10.1016/j.tecto.2016.04.021.

Brown, M., Solar, G., 1998. Shear-zone systems and melts: feedback relations and self-organization in orogenic belts. J. Struct. Geol. 20 (2–3) https://doi.org/10.1016/s0191-8141(97)00068-0.

Brown, M., Solar, G.S., 2009. Shear-zone systems and melts: feedback relations and self-organization in orogenic belts. J. Struct. Geol. 20 (2–3), 211–227. https://doi.org/10.1016/S0191-8141(97)00068-0.

Cardenes, V., Lopez-Sanchez, M.A., Barou, F., Olona, J., Llana-Funez, S., 2021. Crystallographic preferred orientation, seismic velocity and anisotropy in roofing slates. Tectonophysics. 808, 228815 https://doi.org/10.1016/j.tecto.2021.228815.

Chakraborty, S., 2017. A new mechanism for upper crustal fluid flow driven by solitary porosity waves in rigid reactive media? Geophys. Res. Lett. 44, 10324–10327. https://doi.org/10.1002/2017GL075798.

Chauve, T., Scholtès, L., Donzé, F., Mondol, N.H., Renard, F., 2020. Layering in shales controls microfracturing at the onset of primary migration in source rocks. J. Geophys. Res. Solid Earth 125. https://doi.org/10.1029/2020JB019444 e2020JB019444.

Clemens, J.D., Droop, G.T.R., 1998. Fluids, P–T paths and the fates of anatectic melts in the Earth's crust. Lithos 44 (1–2), 21–36. https://doi.org/10.1016/S0024-4937(98)00020-6.

Clemens, J.D., Mawer, C.K., 1992. Granitic magma transport by fracture propagation. Tectonophysics. 204 (3–4), 339–360. https://doi.org/10.1016/0040-1951(92)90316-X.

Coulomb, C.A., 1776. Essai sur une application des regles des maximis et minimis a quelquels problemesde statique relatifs, a la architecture. Mem. Acad. Div. Sav. 7, 343–387.

Craddock, P.R., Doan, T.V.L., Bake, K., Polyakov, M., Charsky, A.M., Pomerantz, A.E., 2015. Evolution of kerogen and bitumen during thermal maturation via semi-open pyrolysis investigated by infrared spectroscopy. Energy Fuel 29, 2197–2210. https://doi.org/10.1021/ef5027532.

Dahm, T., 2000. On the shape and velocity of fluid-filled fractures in the Earth. Geophys. J. 142 (1), 181–192. https://doi.org/10.1046/j.1365-246x.2000.00148.x.

Davies, J.H., 1999. The role of hydraulic fractures and intermediate-depth earthquakes in generating subduction-zone magmatism. Nature 398 (11), 142–145. https://www.nature.com/articles/18202.

de Reise, T., Bons, P.D., Gomez-Rivas, E., Sachau, T., 2020. Interaction between crustal-scale darcy and hydrofracture fluid transport: a numerical study. Geofluids. 8891801 https://doi.org/10.1155/2020/8891801.

Demaison, G., Huizinga, B.J., 1991. Genetic classification of petroleum systems. AAPG Bull. 75 (10), 1626–1643. https://doi.org/10.1306/0C9B29BB-1710-11D7-8645000102C1865D.

Fan, Z.Q., Jin, Z.H., Johnson, S.E., 2010. Subcritical propagation of an oi-filled penny-shaped crack during kerogen-oil conversion. Geophys. J. Int. 182, 1141–1147. https://doi.org/10.1111/j.1365-246X.2010.04689.x.

Fusseis, F., Schrank, C., Liu, J., Karrech, A., Llana-Funez, S., Xiao, X., Regenauer-Lieb, K., 2012. Pore formation during dehydration of a polycrystalline gypsum sample observed and quantified in a time-series synchrotron X-ray micro-tomography experiment. Solid Earth. 3, 71–86. https://doi.org/10.5194/se-3-71-2012.

Ghani, I., Koehn, D., Toussaint, R., Passchier, C.W., 2015. Dynamics of hydrofracturing and permeability evolution in layered reservoirs. Front. Phys. 3, 67. https://doi.org/10.3389/fphy.2015.00067.

Griffith, A.A., 1921. The phenomena of rupture and flow in solids. Philos. Trans. R. Soc. Lond. Ser. A Contain. Pap. Math. Phys. Character 221, 163–198. https://doi.org/10.1098/rsta.1921.0006.

He, Q., He, B., Li, F., Shi, A., Chen, J., Xie, L., Ning, W., 2021. Fractal characterization of complex hydraulic fractures in oil shales via topology. Energies. 14, 1123. https://doi.org/10.3390/en14041123.

Heinemann, Z.E., Mittermeir, G.M., 2012. Derivation of the Kazemi-Gilman-Elsharkawy generalized dual porosity shape factor. Transp. Porous Media 91, 123–132. https://doi.org/10.1007/s11242-011-9836-4.

Hendersen, C.M., Zeno, W.F., Lerno, L.A., Longo, M.L., Block, D.E., 2013. Fermentation temperature modulus phosphatidylethanolamine and phosphatidylinositol levels in the cell membrane of saccharomyces cerevisiae. Appl. Environ. Microbiol. 79 (17), 5345–5356. https://doi.org/10.1128/AEM.01144-13.

Hirschmann, M.M., Asimow, P.D., Ghiorso, M.S., Stolper, E.M., 1999. Calculation of peridotite partial melting from thermodynamic models of minerals and melts. III. Controls on isobaric melt production and the effect of water on melt production. J. Petrol. 40 (5), 831–851. https://doi.org/10.1093/petroj/40.5.831.

Hoosen, W., 1747. The Miner's Dictionary. Wrexham.

Horton, 1945. Erosional development of streams and their drainage basins; hydrophysical approach to quantitative morphology. GSA Bull. 56, 275–370. https://doi.org/10.1130/0016-7606(1945)56[275:EDOSAT]2.0.CO;2.

Jin, Z.H., Johnson, S.E., Fan, Z.Q., 2010. Subcritical propagation and coalescence of oil-filled cracks: getting the oil out of low-permeability source rocks. Geophys. Res. Lett. 37, L01305. https://doi.org/10.1029/2009GL041576.

Johnson, J.R., 2017. Applications of Geostatistical Seismic Inversion to the Vaca Muerta, Neuquen Basin, Argentina. Colorado School of Mines. M.Sc. Thesis. https://mountainscholar.org/bitstream/handle/11124/170976/Johnson_mines_0052N_11230.pdf?sequence=1.

Johnson, A.C., 2018. Constructing a Niobrara Reservoir Model Using Outcrop and Downhole Data. Colorado School of Mines. M.Sc. Thesis. https://mountainscholar.org/bitstream/handle/11124/172518/Johnson_mines_0052N_11579.pdf?sequence=1.

Johnson, J.R., Kobchenko Mondol, N.H., Renard, F., 2021. Analogue modelling of primary migration in shales using organic-rich and organic-poor layered gel. NGF Winter Conf. 34. https://geologi.no/images/NGWM20/Abstractvolume_NGWM20.pdf.

Johnson, J.R., Hansen, J.A., Rahman, J., Renard, F., Mondol, N.H., 2022a. Mapping the maturity of organic-rich shale with combined geochemical and geophysical data,

Draupne Formation, Norwegian Continental Shelf. Mar. Pet. Geol. 138, 105525 https://doi.org/10.1016/j.marpetgeo.2022.105525.
Johnson, J.R., Kobchenko, M., Mondol, N.H., Renard, F., 2022b. Multiscale synchrotron microtomography imaging of kerogen lenses in organic-rich shales from the Norwegian Continental Shelf. Int. J. Coal Geol. 103954 https://doi.org/10.1016/j.coal.2022.103954.
Jones, R.W., 1987. Organic Facies, advances in Petroleum Geochemistry, Brooks, J., Welte, D. Academic Press, London 2, 1–90.
Kalani, M., Jahren, J., Mondol, N.H., Faleide, J.I., 2015. Petrophysical implications of source rock microfracturing. Int. J. Coal Geol. 143, 43–67. https://doi.org/10.1016/j.coal.2015.03.009.
Kavanagh, J.L., Menand, T., Sparks, S.J., 2006. An experimental investigation of sill formation and propagation in layered elastic media. Earth Planet. Sci. Lett. 245, 799–813. https://doi.org/10.1016/j.epsl.2006.03.025.
Kavanagh, J.L., Menand, T., Daniels, K.A., 2013. Gelatine as a crustal analogue: determining elastic properties for modelling magmatic intrusions. Tectonophysics 582, 101–111. https://doi.org/10.1016/j.tecto.2012.09.032.
Kavanagh, J.L., Rogers, B.D., Boutelier, D., Cruden, A.R., 2017. Controls on sill and dyke-sill hybrid geometry and propagation in the crust: the role of fracture toughness. Tectonophysics. 698, 109–120. https://doi.org/10.1016/j.tecto.2016.12.027.
Kavanagh, J.L., Burns, A.J., Hazim, S.H., Wood, E.P., Martin, S.A., Hignett, S., 2018. Challenging dyke ascent models using novel laboratory experiments: implications for reinterpreting evidence of magma ascent and volcanism. J. Volcanol. Geotherm. Res. 354, 87–101. https://doi.org/10.1016/j.jvolgeores.2018.01.002.
Kobchenko, M., Panahi, H., Renard, F., Dysthe, D.K., Malthe-Sørenssen, A., Mazzini, A., Scheibert, J., Jamtveit, B., Meakin, P., 2011. 4D imaging of fracturing in organic-rich shaled during heating. J. Geophys. Res. 116, B12201. https://doi.org/10.1029/2011JB08565.
Kobchenko, M., Hafver, A., Jettestuen, E., Galland, O., Renard, F., Meakin, P., Jamtveit, B., Dysthe, D.K., 2013. Drainage fracture networks in elastic solids with internal fluid generation. Europhys. Lett. 102, 66002. https://doi.org/10.1209/0295-5075/102/66002.
Kobchenko, M., Hafver, A., Jettestuen, E., Renard, F., Galland, O., Jamtveit, B., Meakin, P., Dysthe, D.K., 2014. Evolution of a fracture network in an elastic medium with internal fluid generation and expulsion. Phys. Rev. 50, 052801 https://doi.org/10.1103/PhysRevE.90.052801.
Koehn, D., Piazolo, S., Sachau, T., Toussaint, R., 2020. Fracturing and porosity channeling in fluid overpressure zones in the shallow Earth's crust. Geofluids 7621759. https://doi.org/10.1155/2020/7621759.
Kuila, U., Dewhurst, D.N., Siggins, A.F., Raven, M.D., 2011. Stress anisotropy and velocity anisotropy in low porosity shale. Tectonophysics 503, 34–44. https://doi.org/10.1016/j.tecto.2010.09.023.
Li, S., Unsworth, M.J., Booker, J.R., Wei, W., Tan, H., Jones, A.G., 2003. Partial melt or aqueous fluid in the mid-crust of Southern Tibet? Constraints from INDEPTH magnetotelluric data. Geophys. J. Int. 153 (2), 289–304. https://doi.org/10.1046/j.1365-246X.2003.01850.x.
Li, Z., Wang, J., Gates, I.D., 2020. Fracturing gels as analogs to understand fracture behavior in shale gas reservoirs. Rock Mech. Rock. Eng. 53, 4345–4355. https://doi.org/10.1007/s00603-020-02153-9.
Lister, J.R., Kerr, R.C., 1991. Fluid-mechanical models of crack propagation and their application to magma transport in dykes. J. Geophys. Res. Solid Earth 96 (B6), 10049–10077. https://doi.org/10.1029/91JB00600.
Marchildon, N., Brown, M., 2003. Spatial distribution of melt-bearing structures in anatectic rocks from Southerm Brittany, France: implications for melt transfer at grain- to orogeny-scale. Tectonophysics. 364 (3–4), 215–235. https://doi.org/10.1016/S0040-1951(03)00061-1.
Matthew, A.S., Wang, J., Luo, J., Yau, S.T., 2015. Enhanced ethanol production via electrostatically accelerated fermentation of glucose using saccharomyces cerevisiae. Sci. Rep. 5, 15713. https://doi.org/10.1038/srep15713.
McKenzie, D., 1984. The generation and compaction of partially molten rock. J. Petrol. 25 (3), 713–765. https://doi.org/10.1093/petrology/25.3.713.
McKenzie, D., 1985. The extraction of magma from the crust and mantle. Earth Planet. Sci. Lett. 74 (1), 81–91. https://doi.org/10.1016/0012-821X(85)90168-2.
Merrimen, R.J., Highley, D.E., Cameron, D.G., 2003. Definiton and characteristics of very-fine grained sedimentary rocks: clay, mudstone, shale and slate. British Geological Surv. 3 (281N), 1–14. https://nora.nerc.ac.uk/id/eprint/527458/1/CR03281N.pdf.
Nolte, L.J.P., Nolte, D.D., 2015. Approaching a universal scaling relationship between fracture stiffness and fluid flow. Nat. Commun. 7, 10663. https://doi.org/10.1038/ncomms10663.
Nur, A., Byerlee, J.D., 1971. An exact effective stress law for elastic deformation of rock with fluids. J. Geophys. Res. 76 (26), 6414–6419. https://doi.org/10.1029/JB076i026p06414.
Ougier-Simonin, A., Renard, F., Boehm, C., Vidal-Gilbert, S., 2016. Microfracturing and microporosity in shales. Earth Sci. Rev. 162, 198–226. https://doi.org/10.1016/j.earscirev.2016.09.006.
Ozkaya, I., 1988. A simple analysis of oil-induced fracturing in sedimentary rocks. Mar. Pet. Geol. 5 (3), 293–297. https://doi.org/10.1016/0264-8172(88)90008-6.
Panahi, H., Kobchenko, M., Meakin, P., Dysthe, D.K., Renard, F., 2019. Fluid expulsion and microfracturing during the pyrolysis of an organic rich shale. Fuel. 235, 1–16. https://doi.org/10.1016/j.fuel.2018.07.069.
Parker, N.G., Povey, M.J.W., 2010. Ultrasonic study of the gelation of gelatin: phase diagram hysteresis and kinetics. Food Hydrocoll. 26 (1), 99–107. https://doi.org/10.1016/j.foodhyd.2011.04.016.
Petruzalek, M., Lokajicek, T., Svitek, T., 2019. Fracturing of migmatite: Influence of anisotropy. In: Rock Mechanics for Natural Resources and Infrastructure Development, 1st ed. CRC Press.
Rabbel, O., Mair, K., Galland, O., Gruhser, C., Meier, T., 2020. Numerical modeling of fracture network evolution in organic-rich shale with rapid internal fluid generation. J. Geophys. Res. Solid Earth 125. https://doi.org/10.1029/2020JB019445 e2020JB019445.
Rijken, P., Cooke, M.L., 2001. Role of shale thickness on vertical connectivity of fractures: application of crack-bridging theory to the Austin Chalk, Texas. Tectonophysics 337, 117–133. https://doi.org/10.1016/S0040-1951(01)00107-X.
Rivalta, E., Bottinger, M., Dahm, T., 2005. Buoyancy-driven fracture ascent: experiments in layered gelatine. J. Volcanol. Geotherm. Res. 144 (1–4), 273–285. https://doi.org/10.1016/j.jvolgeores.2004.11.030.
Rivalta, E., Taisne, B., Bunger, A.P., Katz, R.F., 2015. A review of mechanical models of dike propagation: schools of thought, results and future directions. Tectonophysics 638, 1–42. https://doi.org/10.1016/j.tecto.2014.10.003.
Romero-Sarmiento, M.F., Euzen, T., Rohais, S., Jiang, C., Littke, R., 2016. Artificial thermal maturation of source rocks at different thermal maturity levels: Application to the Triassic Montney and Doig Formations in the Western Canada Sedimentary Basin. Org. Geochem. 97 (2016), 148–162. https://doi.org/10.1016/j.orggeochem.2016.05.002.
Rummel, L., Kaus, B.J.P., Baumann, T.S., White, R.W., Riel, N., 2020. Insights into the compositional evolution of crustal magmatic systems from coupled petrological-geodynamical models, 61(2), p. egaa029. https://doi.org/10.1093/petrology/egaa02961.
Sanderson, D.J., Nixon, C.W., 2015. The use of topology in fracture network characterization. J. Struct. Geol. 72 (2015), 55–56. https://doi.org/10.1016/j.jsg.2015.01.005.
Saukko, A., Ahlang, C., Nikkila, K., Soesoo, A., Eklund, O., 2020. Double power-law leucosome width distribution: implications for recognizing melt movement in migmatites. Front. Earth Sci. 8, 591871 https://doi.org/10.3389/feart.2020.591871.
Sawyer, E.W., 2001. Melt segregation in the continental crust: distribution and movement of melt in anatectic rocks. J. Metamorph. Geol. 19 (3), 291–309. https://doi.org/10.1046/j.0263-4929.2000.00312.x.
Sayers, C., 1999. Stress-dependent seismic anisotropy of shales. Geophysics. 64 (1), 93–98. https://doi.org/10.1190/1.1444535.
Secor, D.T., 1965. Role of fluid pressure in jointing. Am. J. Sci. 263, 633–646. https://doi.org/10.2475/ajs.263.8.633.
Secor, D.T., Pollard, D.D., 1975. On the stability of open hydraulic fractures in the Earth's crust. Geophys. Res. Lett. 2 (11), 510–513. https://doi.org/10.1029/GL002i011p00510.
Sili, G., Urbani, S., Acocella, V., 2019. What controls sill formation: an overview from analogue models. J. Geophys. Res. Solid Earth 124, 8205–8222. https://doi.org/10.1029/2018JB017005.
Silva, J.P., Gomes, I.F., Santos, R.F.V.C., Mirand, T.S., Guedes, R.P., Barbosa, J.A., Guimaraes, E.X., Beserra, L.B., Guimaraes, L.J.N., 2021. Topological analysis of fracture networks integrated with flow simulation models for equivalent fracture permeability estimation. J. Struct. Geol. 147, 104338 https://doi.org/10.1016/j.jsg.2021.104338.
Smith, M.B., Montgomoery, C., 2015. Hydraulic Fracturing. CRC Press. https://doi.org/10.1201/b16287.
Sorbadere, F., Laurenz, V., Frost, D.J., Wenz, M., Rosenthal, A., McCammon, C., Rivard, C., 2018. The behaviour of ferric iron during martial melting of peridotite. Geochemica et Cosmochimica Acta. 239 (2018), 235–254. https://doi.org/10.1016/j.gca.2018.07.019.
Takada, A., 1989. Magma transport and reservoir formation by a system of propagating cracks. Bull. Volcanol. 52, 118–126. https://doi.org/10.1007/BF00301551.
Takada, A., 1994. Accumulation of magma in space and time by crack interaction. International Geophysics. 57 (1994), 241–257. https://doi.org/10.1016/S0074-6142(09)60099-1.
Takei, Y., 2017. Effects of partial melting on seismic velocity and attenuation: a new insight from experiments. Annu. Rev. Earth Planet. Sci. 45, 447–470. https://doi.org/10.1146/annurev-earth-063016-015820.
Teixeira, M.G., Donze, F., Renard, F., Panahi, H., Papachristos, E., Scholtes, L., 2017. Microfracturing during primary migration in shales. Tectonophysics 694, 268–279. https://doi.org/10.1016/j.tecto.2016.11.010.
Tissot, B., Durand, B., Espitalie, J., Combaz, A., 1974. Influence of nature and diagenesis of organic matter in formation of petroleum. AAPG Bull. 58 (3), 499–506.
Uzun, I., Eker, E., Cho, Y., Kazemi, H., Rudledge, J.M., 2017. Assessment of rate transient analysis techniques for multiphase flow in unconventional reservoirs: applications to the Eagleford formation. In: SPE Western Regional Meeting. SPE-185737-MS. https://doi.org/10.2118/185737-MS.
Van Otterloo, J., Cruden, A.R., 2016. Rheology of pig skin gelatine: defining the elastic domain and its thermal and mechanical properties for geological analogue experiment applications. Tectonophysics 638, 86–97. https://doi.org/10.1016/j.tecto.2016.06.019.
Vandenbroucke, M., Largeau, C., 2007. Kerogen origin, evolution, and structure. Org. Geochem. 38, 719–833. https://doi.org/10.1016/j.orggeochem.2007.01.001.
Vanderhaeghe, O., 2009. Migmatites, granites and orogeny: flow modes of partially-molten rocks and magmas associated with melt/solid segregation in orogenic belts. Tectonophysics. 477 (3–4), 119–134. https://doi.org/10.1016/j.tecto.2009.06.021.
Vass, A., Koehn, D., Ghani, I., Piazolo, S., Toussaint, R., 2014. The importance of fracture-healing on the deformation of fluid-filled layered systems. J. Struct. Geol. 67, 94–106. https://doi.org/10.1016/j.jsg.2014.07.007.

Vega, B., Kovscek, A.R., 2019. A systematic study of internal gas generation in shale source rocks using analog experiments. J. Pet. Sci. Eng. 173, 2019–2221. https://doi.org/10.1016/j.petrol.2018.10.006.

Vernik, L., Liu, X., 1997. Velocity anisotropy in shales: a petrophysical study. Geophysics. 62 (2), 521–532. https://doi.org/10.1190/1.1444162.

Vidal, O., Dubacq, B., 2009. Thermodynamic modelling of clay dehydration, stability and compositional evolution with temperature, pressure and H2O activity. Geochim. Cosmochim. Acta 73, 6544–6564. https://doi.org/10.1016/j.gca.2009.07.035.

Vigneresse, J.L., Clemens, J.D., 2000. Granitic magma ascent and emplacement: neither diapirism nor neutral buoyancy. Geol. Soc. Lond. Spec. Publ. 174 (1), 1. https://doi.org/10.1144/GSL.SP.1999.174.01.01.

Voltolini, M., Franklin, J.G.A., 2020. The sealing mechanisms of a fracture in Opalinus clay as revealed by in situ synchrotron X-Ray Micro-tomography. Front. Earth Sci. 8, 1–13. https://doi.org/10.3389/feart/2020.00207.

Wang, K., Yan, D., Qin, T., Weng, B., Wang, H., Bi, W., Li, X., Dorjsuren, B., 2020. A new topological and hierarchicical river coding method based on the hydroglogy structure. J. Hydrol. 580, 124243 https://doi.org/10.1016/j.jhydrol.2019.124243.

Watanabe, T., Masuyama, T., Nagaoka, K., Tahara, T., 2002. Analog experiments on magma-filled cracks: competition between external stresses and internal pressure. Earth, Planets, and Space. 54, 1247–1261. https://doi.org/10.1186/BF03352453.

Williams, P.F., 1990. Differentiate layering in metamorphic rocks. Earth Sci. Rev. 29 (1–4), 267–281. https://doi.org/10.1016/0012-8252(0)90042-T.

Xiong, Y., Zuo, R., Clarke, K.C., 2019. A fractal model of granitic intrusion and variability based on cellular automata. Comput. Geosci. 129, 40–48. https://doi.org/10.1016/j.cageo.2019.05.002.

Zhao, L., Qin, X., Han, D.H., Geng, J., Yang, Z., Cao, H., 2016. Rock-physics modeling for the elastic properties of organic shale at different maturity stages. Geophysics 81 (5), 527–541. https://doi.org/10.1190/GEO2015-0713.1.

Zhu, W., Gaetini, G.A., Fusseis, F., Montesi, L.G.J., Carlo, F.D., 2011. Microtomography of partially molten rocks: three-dimensional melt distribution in mantle peridotite. Science 232 (6025), 88–91. https://doi.org/10.1126/science.1202221.

Zoback, M., 2007. Reservoir Geomechanics. Cambridge University Press. https://doi.org/10.1017/CBO9780511586477.

Section 3 (Appendix-1)

(Extended Abstracts)

EA-1

Geomechanical analysis of maturation for the Draupne Shale, Offshore Norway

James R. Johnson
Jørgen A. Hansen
François Renard
Nazmul H. Mondol

Sixth EAGE Shale Workshop

28 April – May 1 2019

Mo P05

Geomechanical Analysis of Maturation for the Draupne Shale, Offshore Norway

J. Johnson[1]*, J. Hansen[1], F. Renard[1], N. Mondol[1,2]

[1]University of Oslo; [2]Norwegian Geotechnical Institute (NGI)

Summary

Understanding maturation of source rock is increasingly of interest in both conventional and unconventional plays. Shale diagenesis and hydrocarbon generation in shales has a direct relationship with the evolution of the mechanics of maturation. The Draupne Formation, a world class source rock, which stretches over a broad range of depths and maturity, provides the ideal candidate to study the interplay between maturation and geomechanical parameters. Wireline logs and Rock-Eval data from eight wells were used to analyse how seismic waves and rock strength interplays with the source rock shales. Results reveal that the Draupne shale behaves typically in terms of maturation, however the relationship between maturation and geomechanics counters the common trend for shale. There are a wide variety of factors that could impact the geomechanical trends, including but not limited to, lithology, mineralogy, pressure, temperature, fluid content, diagenesis, compaction, fracture density, and organic content. This paper identifies key relationships between geomechanical parameters and a number of these factors, while identifying further work that could be carried out in other areas. This further highlights the importance of in-depth play fairway analysis and presents questions that require answers for successful exploration and exploitation of hydrocarbon.

Introduction

Understanding the maturation mechanics of shale is critical to discerning the key parameters concerning the sourcing of hydrocarbons in both conventional and unconventional plays. A full understanding of the proximity and nature of source rocks has been shown to drive success both within exploration and development. Research of the Upper Jurassic Draupne shale in the North Sea, a world class organic-rich source rock, provides the ideal opportunity to study maturation processes. The Draupne shale is oil-prone, ranging from immature to overmature with a maximum reported TOC of 20 wt. %.

A critical component of the maturation process is the cracking of kerogen to form hydrocarbons. Kerogen maturation in shale drives horizontal and vertical fracturing which in turn drives migration pathways (Texeira et al., 2017). Fracturing has been shown to influence a number of parameters including seismic velocity, rock strength, and permeability (Anders et al., 2014), which provides the opportunity to analyse the mechanics of maturation indirectly as wireline logs provide insight into two of three of these parameters (Herron, 1991).

Despite the importance of understanding source rock shales and their maturation mechanics, play fairway assessment of these parameters often consist of a small number of wells as calibration points (Badics et al., 2015). Therefore, maximizing the potential of the data available when building an understanding of regional maturation mechanics is important. Further to this, analysis of the interplay between geomechanical parameters and maturation provides insight into how the cracking of kerogen impacts shale.

Method

Eight exploration wells were taken from a wide range of depths and maturity in the Norwegian North Sea (Figure 1) in order to provide a broad baseline for the maturation processes of the Draupne Shale Formation within the basin. The data transects the Ling Depression, moves through the Utsira High, and into the Gudrun Terrace. Eight wells are shown with the average depths of the Draupne Formation in cross-section below the map of Figure 1. All eight wells have a basic petrophysical log suite, only two of which (16/8-3 S and 15/3-8) have S-wave velocity data. Additionally all the wells have basic Rock-Eval pyrolysis data, with five of those wells also containing vitrinite reflectance (R_0).

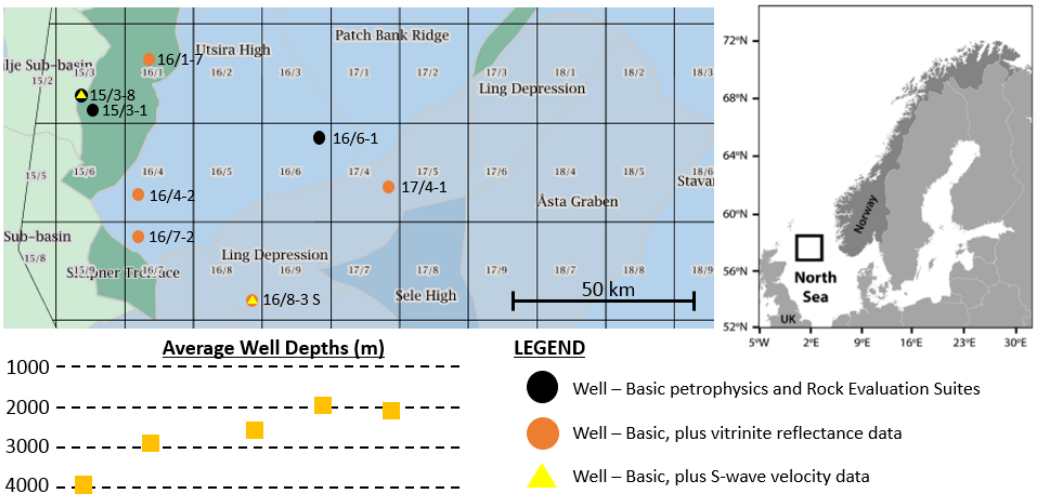

Figure 1 *Study area location outlining the number of wells and availability of various data pertaining. Maps show the study area and structural elements.*

The major benefits of wireline logs include continuous vertical sampling, better depth control, and a greater vertical resolution (Herron, 1991) than would be available through either seismic or core data alone. Basic petrophysical well log and Rock-Eval data provides the tools necessary to outline

parameters of the Draupne Formation including total organic carbon (TOC), porosity, T_{max}, and Hydrogen Index (HI). With the addition of S-wave (Vs), in combination with P-wave (Vp) and density (ρ), calculating a variety of geomechanical properties can be derived, including Poisson's ratio (ν) and Young's modulus (E). The addition of vitrinite reflectance data allows a metric by which the degree of maturation can be determined (Isaksen and Ledje, 2001).

Results and Discussion

Organic-rich shales underwent a series of changes throughout the maturation process. Around 70 – 80 ºC a thermodynamically driven process result in shales releasing water and in some cases precipitating micro-quartz as a cement (Thyberg and Jahren, 2011). Near 90 – 100 ºC maturation of solid kerogen results in the generation of hydrocarbons. The combination of these processes have mechanical effects (Vernik, 1994). Understanding the maturation of the shale first, and then the effects allow one to frame the results within a mechanical view of source rock shale maturation.

Hydrogen Index (HI) plotted against both Oxygen Index (OI) and T_{max} show that the Draupne Formation is predominantly Type II kerogen (Figure 2c). A clear relationship can be shown between depth and vitrinite reflectance with R^2 of 0.72 (Figure 2a). Comparisons with the same relationship derived by Isaksen and Ledje (2001) in the Draupne Formation show a similar trend. The available data shows the Draupne maturation ranges from immature to oil producing, while also showing the depths required to exit the oil window.

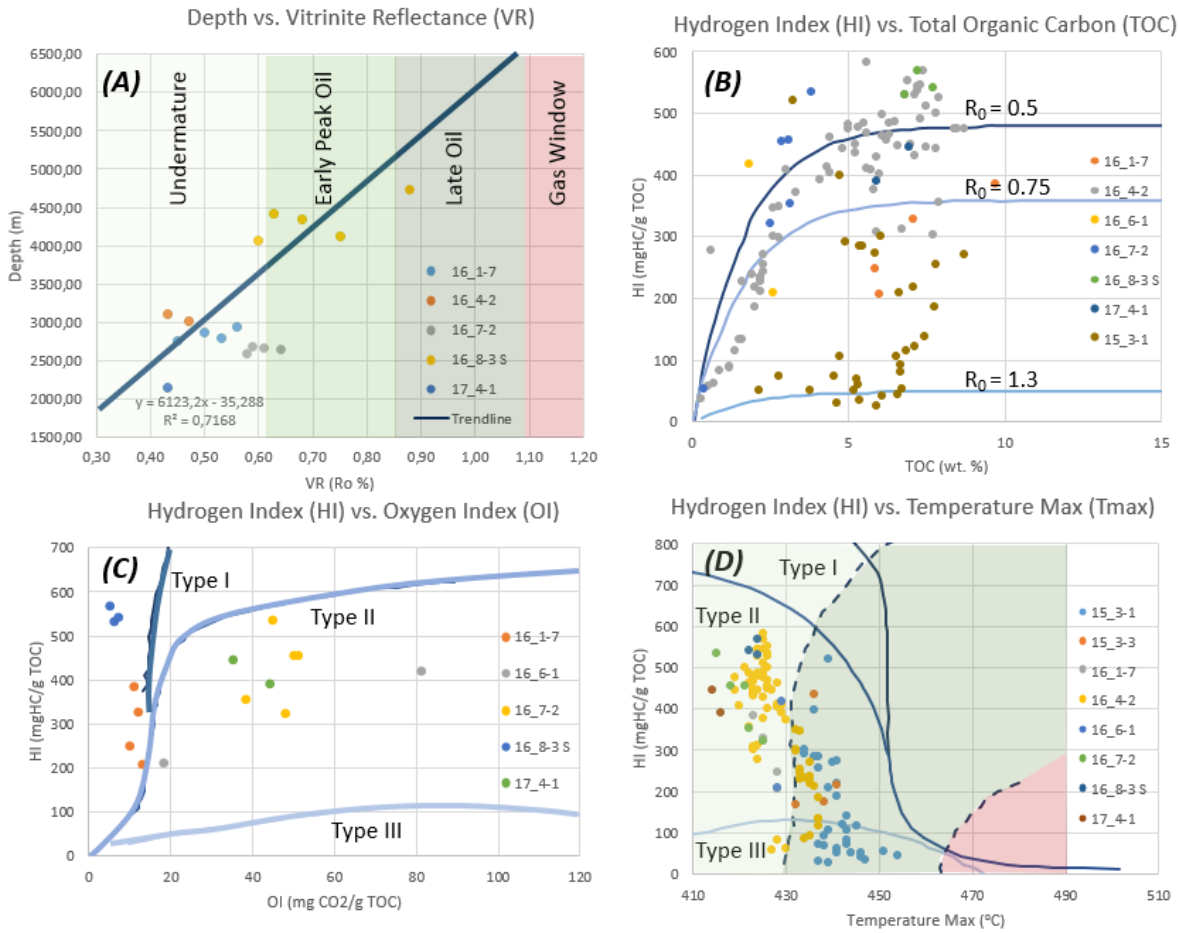

Figure 2 *Analysis utilizing Rock Eval data in order to determine kerogen type and maturation window: (A) Depth vs. Vitrinite Reflectance (B) Hydrogen Index vs. Total Organic Carbon (C) Hydrogen Index vs. Oxygen Index and (D) Hydrogen Index vs. T_{max}.*

Analysis was conducted using HI and T_{max} (Fig. 3d), utilizing trends determined by Espitalie et al., (1985) confirming the Draupne ranges from immature to oil generating within the maturation

window. Modelling of vitrinite reflectance (R_0) using HI and TOC, from Vernik and Landis (1996), for Type II kerogen reveal that the deepest data where VR data is unavailable may have reached the gas window (Figure 2b). Therefore, geomechanical and elastic wave velovcity analysis will focus on Type II kerogen over a wide range of depths and states of maturation.

Utilizing wireline logs, by plotting depth and temperature with P-wave velocity (Vp) and rock density (ρ) the relationship between maturity and elastic wave properties can be determined (Figure 3). Relationships from Sheriff and Geldart (1995) can be used to break the data out into two lithologies that show two distinct trends that mirror one another. Depth has been shown to have a clear relationship with temperature. Higher values of P-wave velocity and density are associated with deeper wells that experience higher temperatures, and the source rocks are more mature. Porosity has been shown to decrease with depth and temperature, likely a result of compaction.

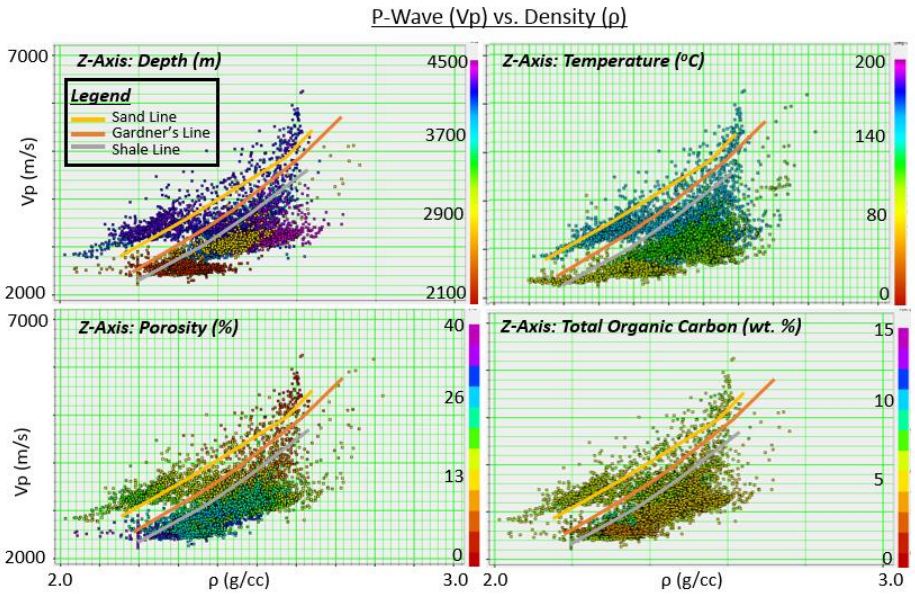

Figure 3 *Analysis utilizing petrophysical suites in order to establish the relationship between maturation and key parameters. The z-axes represents Depth (top left), TOC temperature (top right), porosity (bottom left), and TOC (bottom right).*

Total organic carbon (TOC) is more distributed, however higher values of TOC tend to be correlated with higher P-wave velocity and rock density. A more detailed inspection of TOC values, measured and calculated, within individual wells shows a strong correlation with geomechanical parameters, as can be seen in well 15/3-8 (Figure 4). In wells where it is possible to calculate Poisson's ratio and Young's modulus higher values of TOC appear to correlate with more brittle behaviour, with background trends defined by Mondol (2018). While in many shales it has been shown that higher values of TOC typically correlate to more ductile behaviour (Wilson et al., 2017), the trend appears to be reversed here. This could be correlated to a number of factors, including increased quartz content in the cement, however it merits further investigation. However, modelling by Mondol (2018) shows kerogen is brittle and could pull trends in that direction.

Conclusions

A full exploration of the maturation processes in source rocks is critical to exploration and development success. The relation between maturation and geomechanical parameters has shown interesting results. While typical maturation trends and values of the Draupne Formation have been shown, an analysis of elastic wave and rock strength parameters have shown trends currently disputed for typical shales values. Additionally, these same parameters provide the possibility for indirect measurements of fracturing critical to understanding many elements of the petroleum system. A variety of factors not limited to variations in lithology, rock strength, texture, stress, temperature, fluid

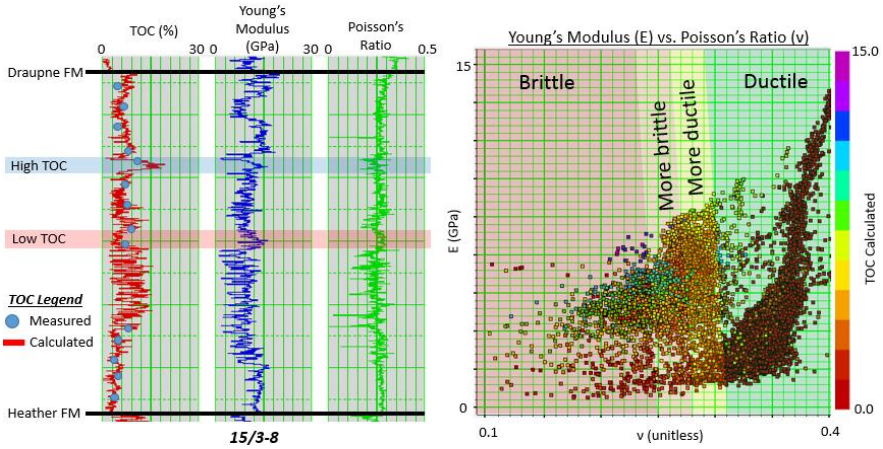

Figure 4 *Comparison of TOC (measured using Rock Eval technique and calculated from wireline data) for the Draupne formation of well 15/3-8 (left), and Young's modulus vs. Poisson's ratio with TOC on the z-axis for 15/3-8 and 16/8-3 S (right).*

content, diagenesis, compaction, fracture density, and organic content. Further investigation is required to understand the nature of the relationship between maturation, TOC, and geomechanical parameters.

References

Anders, M.H., Laubach, S.E. and Scholz, C.H. [2014] Microfractures: A review. Journal of Structural Geology, **69**, 377 – 394.

Badics, B., Avu, A. and Mackie, S. [2015] Assessing source rock distribution in Heather and Draupne Formations of the Norwegian North Sea: A workflow using organic geochemical petrophysical, and seismic character. Interpretation, **3**, 45 – 68.

Espitalie, J, Deroo, G., and Marquis F., [1985] La pyrolyse Rock-Eval et ses applications. Revue de l'Institut Francais du Petrole, **32**, 23 – 42.

Teixeira, M. G., Donzé, F., Renard, F., Panahi, H., Papachristos, E., & Scholtès, L. (2017). Microfracturing during primary migration in shales. Tectonophysics, **694**, 268 – 279.

Herron, S., [1991] In situ evaluation of potential source rocks by wireline logs. In R.K. Merill, (ed.), Source and migration processes and evaluation techniques: Treatise of petroleum geology: AAPG 127 – 139.

Isaksen and Ledje, [2001] Source rock quality and hydrocarbon migration pathways within the greater Utsira High area, Viking Graben, Norwegian North Sea. AAPG Bulletin, **85**, 861 – 883.

Mondol, N.H. [2018] Seal quality prediction using E-Poisson's ratio rock physics templet- A case study from the Norwegian Barents Sea. GeoConvention

Sheriff, R.E., and Geldart, L.P. [1995] Exploration Seismology. Cambridge University Press, Cambridge.

Thyberg, B. and J. Jahren [2011] Quartz cementation in mudstones: sheet-like quartz cement from clay mineral reactions during burial. Petroleum Geoscience, **17**, 55-63.

Vernik, L. [1994] Hydrocarbon-generation-induced microcracking of source rocks. GEOPHYSICS, **59**, 555-563.

Vernik, L. and C. Landis [1996] Elastic anisotropy of source rocks-implications for hydrocarbon generation and primary migration. AAPG Bulletin, **80**, 531-544.

Wilson, T., Kavousi, P., Carr, T., Carney, B. and Uschner, N. [2017] Relationships of λσ, μσ, brittleness index, Young's modulus, Poisson's ratio and high TOC for the Marcellus Shale, Morgantown, West Virginia. SEG International Exposition and 87th Annual Meeting

EA-2

Cap rock evaluation of central North Sea shales, through log-derived Poisson's ratio and Young's modulus

Jørgen A Hansen
James R. Johnson
François Renard
Nazmul H. Mondol

Sixth EAGE Shale Workshop

28 April – May 1 2019

Mo P02

Cap Rock Evaluation of Central North Sea Shales, Through Log-Derived Poisson's Ratio and Young's Modulus

J.A. Hansen[1]*, J.R. Johnson[1], N.H. Mondol[1,2]

[1]University of Oslo; [2]Norwegian Geotechnical Institute (NGI)

Summary

We present an evaluation of shale dominated cap rocks relevant for Middle Jurassic sandstone reservoirs in the Central North Sea, based on well log data from the Norwegian Continental Shelf. Previously established indicators for brittleness and seal quality, E (Young's modulus) and ν (Poisson's ratio), are utilized in the analysis. Similar ductile to fairly ductile behaviour is found in different formations for five analysed wells, of which two are oil discoveries, one contains only oil shows, and two are dry. Cap rocks in the discovery wells are comparatively most brittle, compared to a published E–ν template. Uplift of ~500 m in one of the discovery wells is not found to have compromised the sealing capability. We also investigate how organic content influence an organic-rich shale interval in terms of cap rock properties by using kerogen substitution and comparing to the other more organic-lean shales, which does not support a direct correlation between TOC and ductility. Finally, we consider how observed properties of different shales relate to different mineralogical composition.

Introduction

Middle Jurassic sandstone-dominated formations are main target reservoirs for hydrocarbon in the Central North Sea on the Norwegian Continental Shelf. Potential cap rocks for these reservoirs are primarily the Egersund, Heather and Draupne shale-dominated formations, or in some cases shaly intervals within the Sandnes or Bryne sand-dominated Formations. Due to limited amounts of hydrocarbon generation in the area, related to source rock maturity status and upliftment, seal quality must be good enough to retain oil and gas accumulations that are likely not being replenished. This study therefore aims to evaluate proven and potential cap rocks from the aforementioned formations in wells from the Central North Sea area. The database is summarized in Table 1. Young's modulus (E) and Poisson's ratio (ν) are properties that have been used to indicate brittleness and serve as cap rock quality indicators in previous studies (e.g., Grieser and Bray 2007; Perez and Marfurt 2014; Mondol 2018). We consequently utilize crossplots of these properties to perform our analysis.

Table 1 *Summary of wells and cap rock shales in this study.*

Well (prospect)	Cap rock depth (maximum burial) m BSF	Cap rock formation	Content
17/12-4 (Vette)	2568-2573	L. Sandnes – U. Bryne silty shale	Oil
16/8-3 S (Lupin)	2687-2708	Draupne organic rich shale	Dry
17/6-1 (Svanegle)	2875-2888	Egersund silty shale	Shows
15/12-21 (Grevling)	2888-2903	Heather silty shale	Oil
9/2-11 (Aubrey)	2989-3001	Egersund shale	Dry

Theory and methods

Seal quality is highly influenced by brittleness and consequent fracture potential, which can be particularly important in uplifted regions like the Central North Sea. The brittleness of a rock is dependent on lithology, rock strength, texture, stress, temperature, fluid content, diagenesis (compaction) and organic content (Walles 2004; Perez and Marfurt 2014). Uplift magnitude and corrected maximum burial depth was predicted by comparing shale velocity-depth data to experimental compaction trends (Hansen et al. 2017). Increasing TOC (soft matter) is typically described to have an inverse influence on shale brittleness (Walles 2004). Conversely, depending on the distribution of kerogen in relation to matrix grains, Perez and Marfurt (2014) find that kerogen does not directly relate to higher ductility when the source rock quartz content is significant. In their findings from the Barnett Shale, grains around intergranular kerogen support the stress, meaning that the high-TOC source rock is brittle stratigraphically.

Wireline log recordings of V_p, V_s and bulk density can be used to calculate dynamic elastic parameters such as E, ν, $\lambda\rho$ and $\mu\rho$. We also calculate a TOC log from bulk density as (Vernik and Landis, 1996; Carcione, 2000):

$$\text{TOC (wt. \%)} = a\,[\rho_k(\rho_m - \rho_b)] / [\rho_b(\rho_m - \rho_k)] \quad (1)$$

Here, ρ_k is kerogen density which has a range of 1.1–1.6 g/cm^3, and is dependent on maturity (Vernik and Landis 1996; Dang et al. 2016). ρ_m is matrix density, which in reality varies according to mineralogy and diagenesis, i.e., clay mineral transformation (Carcione and Avseth 2015). ρ_b is the bulk density log measurement, and a is a constant related to the fraction of carbon in organic matter and can vary according to maturation level. Additionally, a method referred to as kerogen substitution proposed by Vernik (2016) has been applied to the Draupne Formation in the Lupin well (16/8-3 S), to predict elastic properties of the same rock at different organic content. Input parameters for this modelling are determined from core plug measurements of TOC, porosity, maturity, grain- and bulk density.

Examples

Figure 1 shows data from the five cap rock intervals in our database in crossplots of E versus ν. Considering that these cap rocks have fairly similar maximum burial (max. difference ~450 m), oil reservoir cap rocks have comparatively lower ν and lower E than the Svaneøgle cap rock which has signs of leaking (oil shows only). $\mu\rho$, another parameter that can be indicative of stiffness and brittleness, display slightly higher values in the Svaneøgle and Aubrey wells, but is overall similar to the Grevling oil discovery well (Table 1). The thin cap rock interval in the Vette well (oil) has slightly lower values of E and $\mu\rho$. An important difference is however that Aubrey, Svaneøgle and Vette locations all have experienced uplift in the order of ~500 m, whereas the area of Lupin and Grevling is predicted to have minor to no uplift history (Hansen et al. 2017). Uplift-induced stress release can lead to fracturing, which in turn would decrease compressional and shear stiffness of the rock (Bjørlykke 2015). Contrarily, if fractures are already present in situ, the velocity- and density log-derived elastic properties could lead to bias, giving the impression of a more ductile behaviour (i.e., *less* prone to fracturing). In either case, the uplift has apparently not affected the seal integrity in the Vette well which retains oil (intra Sandnes–Bryne Formation). There is also a thin coal layer within this particular shaly interval which could aid sealing capacity.

TOC is comparatively low in four of the seal intervals (predominantly < 3 wt. %), whereas the Draupne Formation (Lupin) contains fairly uniformly ~5–8 wt. % TOC (Figure 1). The Draupne Formation has both source- and cap rock potential in the North Sea. Lower E, $\mu\rho$ and higher ν are observed for this organic-rich shale. Skurtveit et al. (2015) find that the Draupne Formation in the Lupin well has very good sealing properties based on core measurements, with vertical permeability around $1.2–1.4 \times 10^{-7}$ mD. The fact that the fluid in this particular reservoir is brine is most likely due to a lack of mature source rock to charge it rather than cap rock integrity.

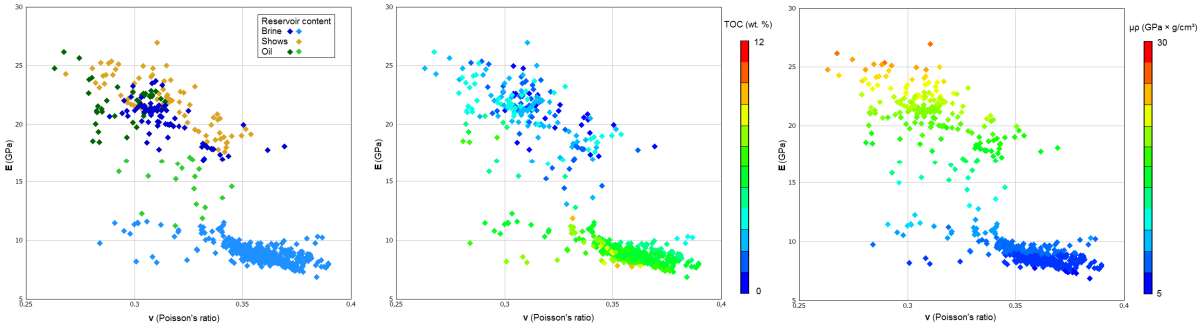

Figure 1 *E–ν crossplot showing five shale dominated rocks serving as seals above reservoirs containing brine, oil shows, and oil. Color coded after well/reservoir content (left), cap rock TOC (middle), and μρ (right).*

E– ν relationships between cap rocks that retain oil, leak (Svaneøgle), or cap brine reservoirs do not display any direct correlation with brittleness interpretations based on mineralogy proposed by Perez and Marfurt (2014). All are classified as ductile to fairly ductile, as the "brittle region" in this template is outside the left side of the plot axis (Figure 2). Predicted E and ν after applying kerogen substitution indicate that variable organic content mainly relates to changing Young's modulus, and does in fact not lead to an interpretation of increased brittleness (Figure 2). Kerogen-substituted properties fall onto a fairly narrow trend of other cap rock data. If instead observing the trend of mineral properties (clay to quartz – ductile to brittle) in this domain, data in the upper left region of the plot is indicated as more brittle. This indicates relatively more favourable properties in Vette and Lupin wells, but the proven functional Grevling well cap rock also plot towards the upper left. The range of values observed in our data is nevertheless small compared to quartz mineral properties (E = 95, ν = 0.074).

Some mineralogical data are available for the Egersund Formation, which is time equivalent to the Heather Formation, from other wells in the Egersund Basin (Kalani et al. 2015). Furthermore, five core samples are available from the Draupne Formation in the Lupin well (Ling Depression). The core

analysis is courtesy of the CO2SEAL project (financed by the RCN, Gassnova and Equinor). Based on averages, the Draupne Formation is richer in quartz and K-feldspar, whereas mixed-layer illite/smectite is more abundant in the Egersund Formation (Figure 3). Total clay is on average 46% and 66%, respectively. However, the Draupne Formation still displays the most ductile properties along the mineral property trend. Data from the Egersund and Heather Formations plot around theoretical mineral properties of clay (Mondol, 2018). Calcite and dolomite content is negligible in terms of determining the brittleness of both these formations. A thin section image under UV light indicates scattered organic matter rather than continuous accumulations (Figure 3).

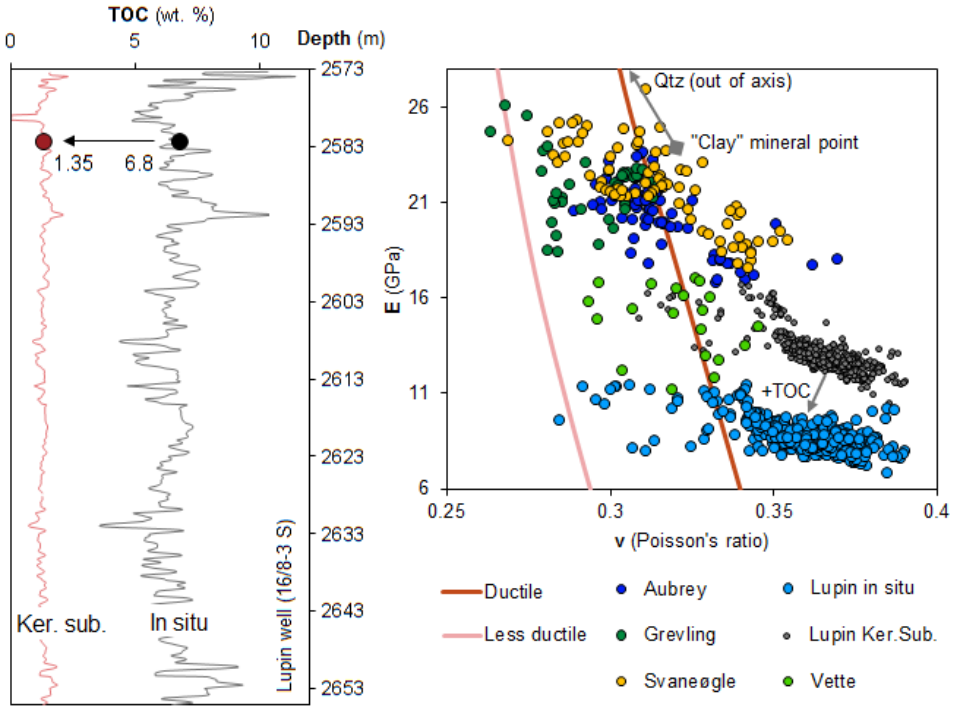

Figure 2 *TOC signature of the Draupne Formation in the Lupin well (left) with one calibration sample, before and after applying kerogen substitution to predict the v-E response (right) with reduced TOC influence. Ductile-less ductile cutoffs are adapted from Perez and Marfurt (2014).*

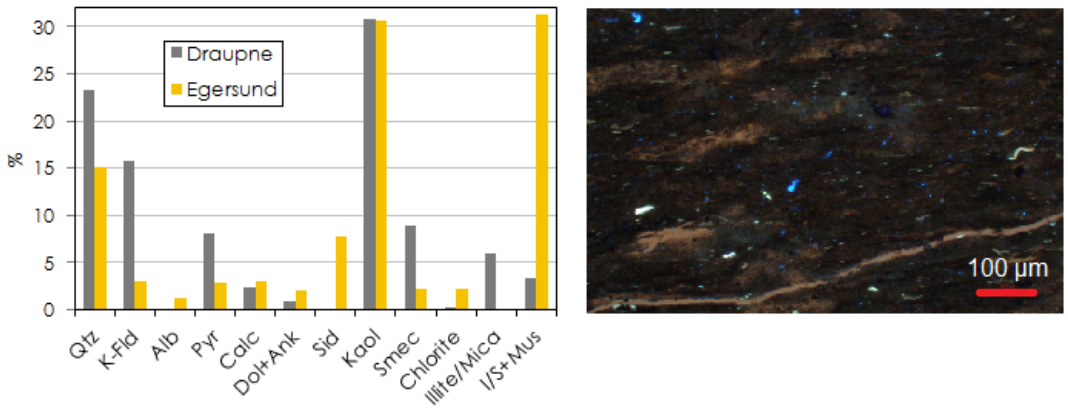

Figure 3 *Average mineralogy of Egersund and Draupne Formations (left), and thin section image from a Draupne Formation sample in Lupin well (right). Blue fluorescence indicates organic matter.*

Conclusions

According to the relationship between Young's modulus and Poisson's ratio, seal quality of the studied formations is not separated by differences in brittleness or ductility. All five wells are characterized as fairly ductile based on a proposed classification template, and if anything, the cap

rocks in oil discovery wells are shifted slightly towards the brittle side compared to wells encountering oil shows or brine. Relating brittleness to the trend of mineral-points in the *E*–*v* domain infers a higher brittleness towards increasing *E* and decreasing *v*. This type of classification still does not differentiate hydrocarbon-sealing and brine-sealing cap rocks. Uplift can potentially influence both the measured properties and the actual sealing capacity, but has not caused seal failure in an uplifted, thin, intra-reservoir shale interval (well 17/12-4, Vette discovery). Kerogen substitution predicts a minor increase in *v* (+0.05) and around ~3 GPa increase in *E* by decreasing TOC from 5–8 to 1–2 wt. %, fairly consistent with data from shales with lower organic content. Consequently, this modelling does not reflect a more brittle behaviour from increasing the amount of brittle minerals. This is counterintuitive in terms of individual mineral properties, but not necessarily erroneous on larger scales, as earlier studies display the importance of rock texture and kerogen distribution on brittle/ductile behaviour.

Acknowledgements

This study was carried out under the ReSource project, an R&D collaboration between the University of Oslo and Eni Norge. We extend our sincere thanks to Eni Norge for funding the project. Data used in this study was provided by DISKOS (Norwegian Petroleum Directorate). Academic software licences were provided by Lloyd's Register for Interactive Petrophysics and Ikon Science for RokDoc.

References

Bjørlykke K. [2015] Petroleum Geoscience: From Sedimentary Environments to Rock Physics – Second Edition. Springer-Verlag Berlin Heidelberg.

Carcione, J.M. [2000] A model for seismic velocity and attenuation in petroleum source rocks. GEOPHYSICS, **65**, 1080-1092.

Carcione, J.M. and Avseth, P. [2015] Rock-physics templates for clay-rich source rocks: GEOPHYSICS, **80**, D481-D500.

Dang, S. T., C. H. Sondergeld and C. S. Rai [2016] A New Approach to Measuring Organic Density. Petrophysics, **57**, 112-120.

Grieser, B. and Bray, J. [2007] Identification of production potential in unconventional reservoirs: SPE Production and Operations Symposium. SPE #106623.

Hansen, J.A., Yenwongfai, H.D., Fawad, M. and Mondol, N. H. [2017] Estimating exhumation using experimental compaction trends and rock physics relations, with continuation into analysis of source and reservoir rocks: Central North Sea, offshore Norway: SEG, Expanded Abstracts, 3971-3975.

Kalani, M., J. Jahren, N.H. Mondol and J. I. Faleide [2015] Petrophysical implications of source rock microfracturing. Internation Journal of Coal Geology, **143**, 43-67.

Mondol, N.H. [2018] Seal quality prediction using E-Poisson's ratio rock physics templet- A case study from the Norwegian Barents Sea. GeoConvention

Perez, R.A. and Marfurt, K.J. [2015] Identification of brittle/ductile areas in unconventional reservoirs using seismic and microseismic data: Application to the Barnett Shale. Interpretation, **2**, T255-T271.

Skurtveit, E., Grande, L., Ogebule, O.Y., Gabrielsen, R.H., Faleide, J.I., Mondol, N.H., Maurer, R. and Horsrud, P. [2015] Mechanical testing and sealing capacity of the Upper Jurassic Draupne Formation, North Sea. 49th US Rock Mechanics/Geomechanics Symposium, ARMA, Expanded Abstracts.

Vernik, L. [2016] Seismic petrophysics in Quantitative Interpretation. Society of Exploration Geophysicists.

Vernik, L. and Landis, C. [1996] Elastic anisotropy of source rocks-implications for hydrocarbon generation and primary migration. AAPG Bulletin, **80**, 531-544.

Walles, F. [2004] A new method to help identify unconventional targets for exploration and development through integrative analysis of clastic rock properties. Houston Geological Society Bulletin, **47**, 35–49.

EA-4

Salt remobilization timing and its impact on two Norwegian Continental Shelf organic-rich shale formations

James R. Johnson
François Renard
Nazmul H. Mondol

Geoconvention 2021

13-15 September 2021

geoconvention
Virtual Event
September 13 - 15
2021

Salt remobilization timing and its impact on two Norwegian Continental Shelf organic-rich shale formations

James R Johnson[1], François Renard[1], and Nazmul Mondol[1,2]
Njord Centre, Department of Geosciences, University of Oslo, Norway[1]
Norwegian Geotechnical Institute[2]

Summary

Two world-class source rocks from the Norwegian North Sea and the Barents Sea, the Draupne Formation and the Hekkingen Formation, respectively, are compared through a variety of techniques to understand the impact that the timing of salt mobilization has had on the maturation and geomechanical characteristics of these formations. The more recent salt diapirism has had a relatively limited impact on the Draupne Formation for well 16/8-3 S when compared to the historical regional salt diapirism at play within the Barents Sea Hekkingen Formation around well 7125/1-1. Despite the similar depositional history, this marked difference in diagenetic history has played a significant role in the variation of both maturation and, subsequently, geomechanical parameters between these two areas. This has a critical impact on the behavior of these shales in terms of both sealing and source capacity.

Introduction

Within the oil and gas industry, the presence of salt can mark some of the most productive or prospective oil and gas provinces. Primarily found in rift basins and along passive margins, most salt basins are formed during the early post-rift phase (e.g., Smith, 2008). However, some are older than the main rifting phase. Within the North and Barents Seas studied here, the Permian salt is older than the subsequent Triassic and Jurassic rifting events. Salt can play a significant role in many parts of petroleum systems. Warren (2017) highlights that it is a potential seal, although it does sometimes leak. As salt geometries are altered, they can play a major role in the migration of hydrocarbons (Hindle, 1997). Finally, due to salt's thermal capacity, it can significantly alter the thermal gradient (Daniilidis and Herber, 2017). This alteration may result in hydrocarbon maturation occurring faster than it would have otherwise within organic-rich shale, a potential source rock. However, this effect may also have an impact on a shale's geomechanical properties influencing its quality as a potential seal (Johnson et al., 2019).

Due to salt's complex and pervasive relationship within the basins they inhabit, understanding the impact of salt mobilization timing is also critical to the energy transition. Specifically, 'grey hydrogen' is turned to 'blue hydrogen' when it is coupled with carbon capture and storage (CCS) (Rystad Energy, 2021). Understanding the thermal relationship that salt has with the maturation of shales, and subsequent alteration of geomechanical parameters is critical to understanding the role these shales may play for CCS systems. The present study demonstrates how two organic-rich shales share a similar depositional history but do not share a similar diagenetic evolution due to salt remobilization (Figure 1).

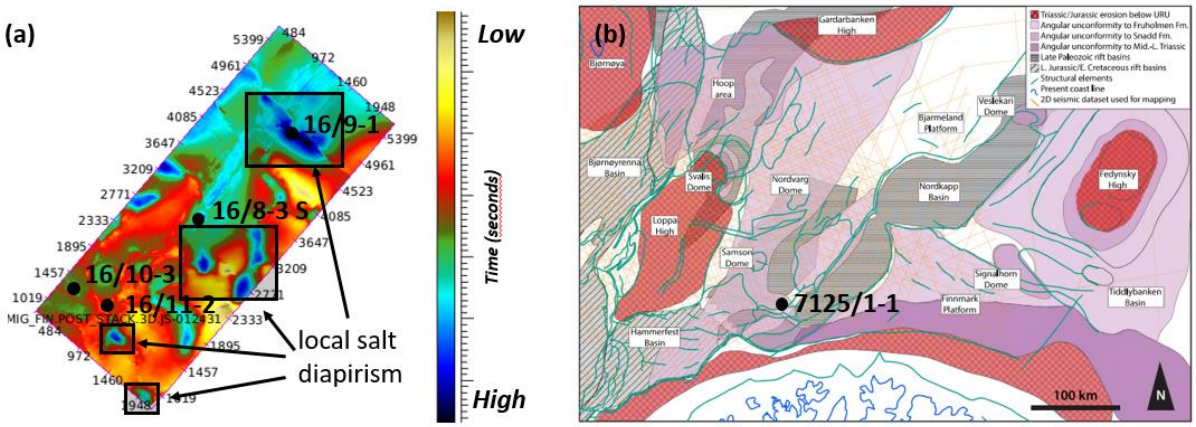

Figure 1 – (a) Recent local salt diapirism within the vicinity of well 16/8-3 S and other wells in the study area (modified from Johnson et al., 2019) and (b) Regional highs and lows resulting from historical salt diapirism with well location 7125/1-1 (modified from Muller et al., 2019).

Geological Background

Major salt deposition occurred in the Permian formations of the Norwegian Continental Shelf (NCS) for both the Norwegian North Sea and the Barents Sea (Gerard and Buhrig, 1990; Rossland et al., 2013). Subsequently, two major rifting events occurred during the Triassic and Jurassic in both regions (Dore et al., 1985; Faleide et al., 2008; Hansen et al., 2020). The coupling of the two rifting events, with a eustatic sea-level rise and the subsequent deep marine, anaerobic conditions, provided the requirements for the depositions of two organic-rich shale formations with predominantly Type II and II-S kerogen, the Draupne and Hekkingen Formations.

Comparing the mineralogy of the two rocks from a variety of sources, including this study, one can see that they are not vastly different in composition. For mineralogical content, both formations have clay content between 30 – 70%, quartz and feldspar content between 30 – 50%, and carbonate and pyrite content between 5 – 20 % (Figure 2). They also share similar contents in terms of clay minerals, with kaolinite representing 45 – 75%, smectite representing 5 – 25%, and Mica/Illite representing 15 – 35%. Chlorite is found in trace amounts (>1%) within the Draupne Formation and not within the Hekkingen Formation (Figure 2). Kerogen content is considered very high for both formations. Average kerogen values for the samples used in the present study, combined with those from earlier studies (Kalani et al., 2015; Skurtveit et al., 2015; Nooraiepour et al., 2017; Zadeh et al., 2017; Johnson et al., 2019; Hansen et al., 2020) within the local area are 8.5 wt. % for the Draupne and 12.2 wt.% for the Hekkingen. Interaction between the kerogen with the fabric of the non-organic component is seen for both formations in the SEM analysis at a range of scales (present study). These data further support a similar depositional history.

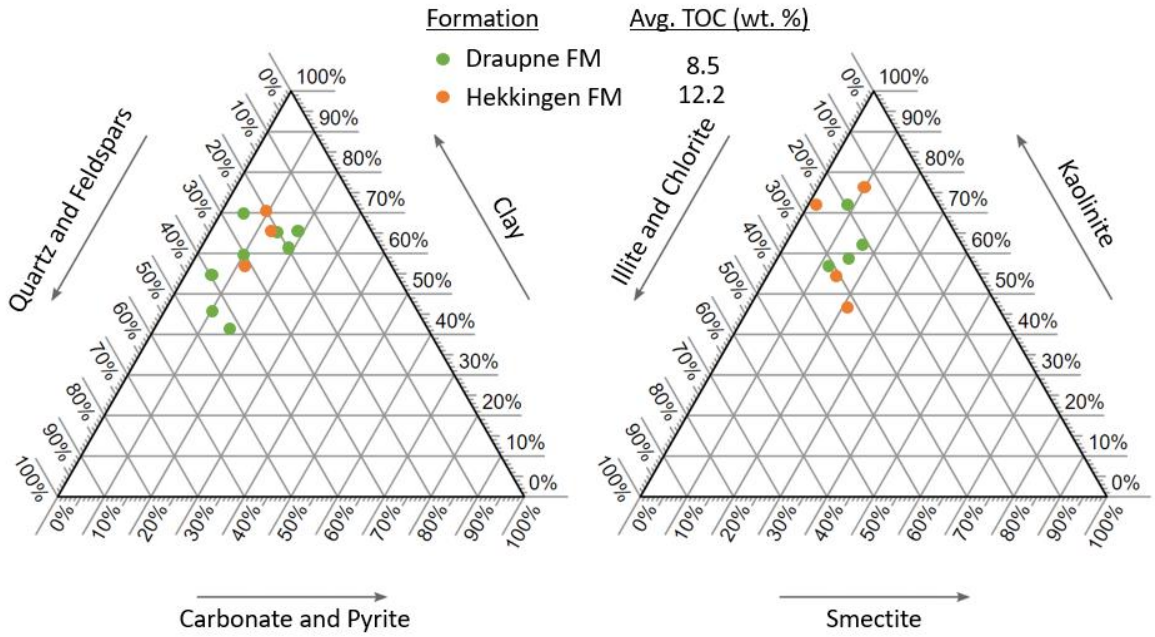

Figure 2 – Ternary diagrams are showing compiled bulk mineralogy and clay compositions for wells within the study area (Kalani et al., 2015; Skurtveit et al., 2015; Nooraiepour et al., 2017; Zadeh et al., 2017; Hansen et al., 2020; present study).

While both organic-rich shales were buried experiencing diagenesis, the Hekkingen Formation experienced significant subsequent uplift as the result of salt remobilization (Baig et al., 2016; Muller et al., 2019). Exhumation of the Hekkingen Formation in the Barents Sea is estimated to be between 0.4 – 3.0 km, coinciding with major erosional events (Henriksen et al., 2011; Baig et al., 2016). This did not occur in the same way for the Draupne Formation in the North Sea, with exhumation ranging from 0.0 – 0.7 km (Hansen et al., 2017; Baig et al., 2019). While the impact of salt diapirism on organic-rich shales can be seen in both the North Sea (Johnson et al., 2019) and the Barents Sea (present study), the difference in the geomechanical properties of the shales is profound.

Method

This study focuses on a 120 km area around two wells, 16/8-3S in the Norwegian North Sea and 7125/1-1 in the Barents Sea who penetrated the Draupne and Hekkingen Formations, respectively (red dots in Figure 3, left). These two formations are considered geologically equivalent in time (Figure 3, right). Nine wells penetrate the Draupne Formation, and five wells penetrate the Hekkingen Formation (red, yellow, and purple dots in Figure 3, left). These wells are used to establish broad geochemical and rock physics trends for their respective areas. The disparity between the numbers of wells used for the North Sea compared to the Barents Sea is explained by the presence of greater well data availability in the North Sea study area (NPD, 2021), as seen in Figure 3.

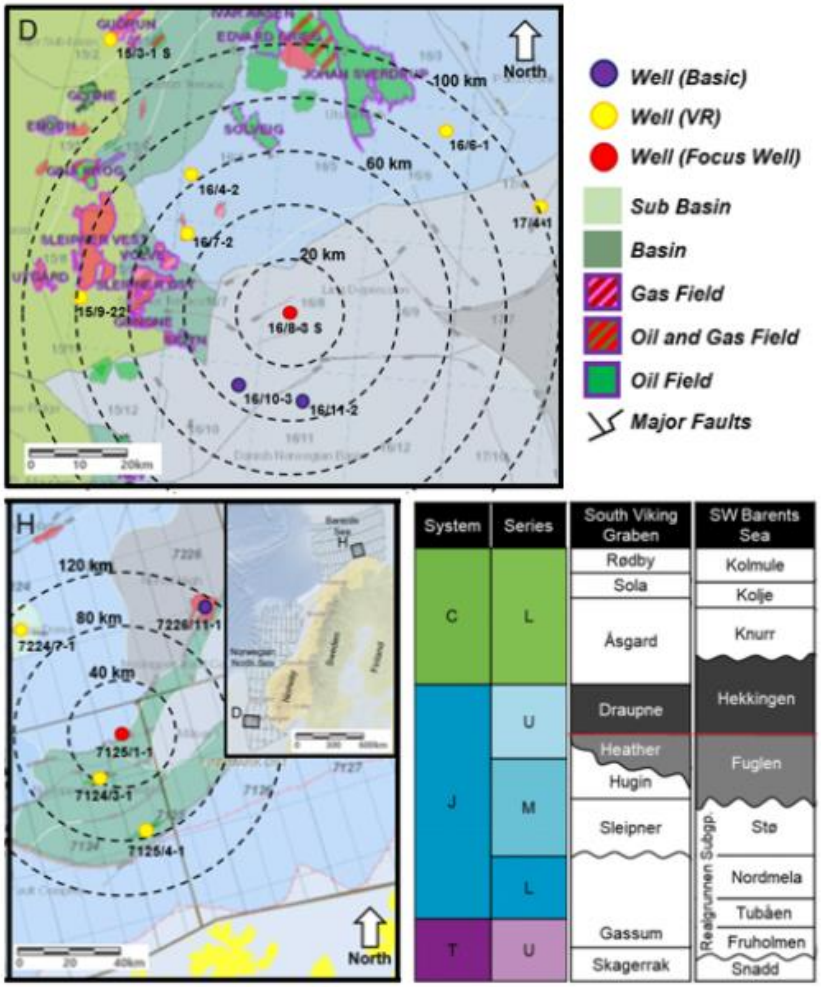

Figure 3 – Well locations (red, purple, and yellow dots) and data availability (D) with geological timing of the two organic-rich formations studied, Draupne (South Viking Grabben) and Hekkingen (SW Barents Sea) (H). The inset shows a map of Scandinavia with the locations of the two maps shown on the left side of the figure. Modified from NPD (2021). Geological timing of the Draupne and Hekkingen Formations (bottom right)

Geochemical data are available through Rock-Eval measurements from thirteen of these wells, including Hydrogen Index (HI), Oxygen Index (OI), total organic carbon (TOC), S2, T_{max}, and vitrinite reflectance (R_o). The vitrinite reflectance (Ro) data provides the best proxy for maturation (Tissot and Welte, 1984) where available. However, there are notoriously fewer data points for R_o, many of which are unreliable for other geochemical types (NPD, 2021). Therefore, other crossplots quantify shale maturation, such as HI versus TOC (modified from Vernik and Landis, 1996). Kerogen type and its likely origin are ascertained using S2 versus TOC plot, while HI versus T_{max} (modified from Isaksen and Ledje, 2001) is used to confirm understanding of both kerogen type and maturation trends. This study also uses SEM and XRD analysis to compare the mineralogical makeup of the two formations. Furthermore, the relationship between the organic matter and the non-organic components of the formations is obtained utilizing SEM analysis.

Rock physics analysis carried out focuses on understanding the geomechanical parameters of the two formations. Perez and Marfurt (2014) proposed a rock physics template that explores the geomechanical parameters in terms of Young's Modulus (E) and Poisson's ratio (**υ**). These two parameters are calculated:

$$\upsilon = \frac{V_p^2 - 2V_s^2}{2V_p^2 - 2V_s^2} \quad (1)$$

$$\mathrm{E} = \rho V_s^2 \frac{3V_p^2 - 4V_s^2}{V_p^2 - V_s^2} \quad (2)$$

where, V_P is P-wave velocity, V_s is S-wave velocity, and ρ is bulk density obtained from well logs. This model was updated by Mondol (2018), who highlighted the critical nature the detailed composition of the shale has on these parameters utilizing compositional end-members (i.e., quartz, kerogen, clay, and carbonate). Johnson et al. (2019) further appended this model, highlighting a clear relationship between TOC content and the degree of maturation in terms of geomechanical parameters. This work Johnson et al. (2019) is extended to include wells from the Barents Sea, Hekkingen Formation in the present study.

Results

The Draupne and the Hekkingen Formations centered around wells 16/8-3 S and 7125/1-1 are compared utilizing a broad swathe of techniques. The study uses two wells that reached historically equivalent maximum depths and temperature regimes (Baig et al., 2016; Zadeh et al., 2017; Baig et al., 2019). In these two wells, results show that different levels of maturation produced various geomechanical parameters.

Analysis utilizing XRD and SEM have revealed that while there are differences, the Draupne and Hekkingen Formations are broadly similar in terms of organic and non-organic composition. Those differences include a typically slightly higher organic matter (OM) content for the Hekkingen Formation, confirmed by both geochemical and well log analysis (Figure 2). Additionally, the Draupne Formation shows a larger variation in mineralogical content for the categories clay, as well as quartz and feldspar (Figure 2). This seems to be due to the presence of feldspars more than quartz. Kaolinite content also appears to be typically higher in the Draupne Formation, with more Illite/Mica than in the Hekkingen Formation. These differences are also apparent looking at the SEM data. Furthermore, the interaction between organic matter and inorganic matter is readily visible. Clear soft-sediment deformation can be seen at multiple scales, while the association between frambroidal pyrite and kerogen lenses is abundant on some of the closer zooms in the SEM analysis.

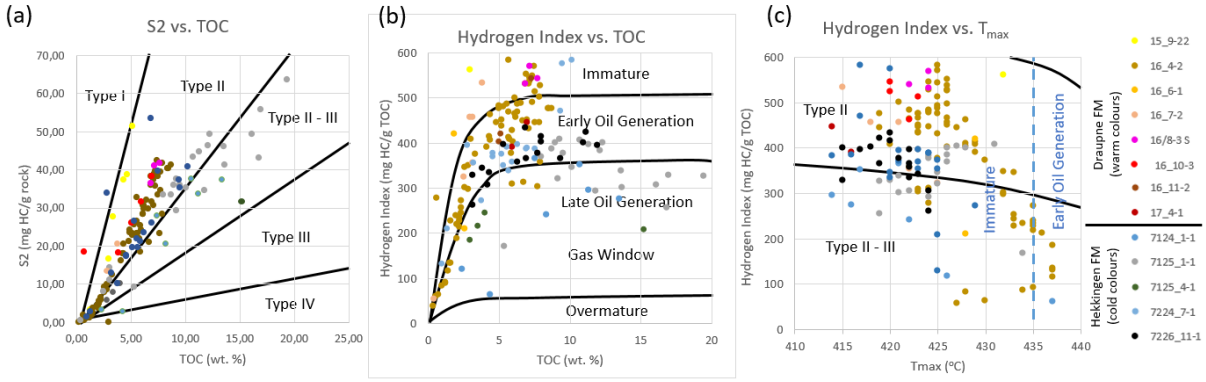

Figure 4 – Crossplots of geochemical data of the Draupne and Hekkingen formations. (a) S2 vs. TOC crossplot is used for discerning kerogen type. (b) Hydrogen Index (HI) vs. TOC is used for determining maturation. (c) Hydrogen Index vs. T_{max} is used for discerning both kerogen type and maturation. Dots are colored according to the well data it comes from.

Maturation levels of the two areas and kerogen type are obtained from the geochemical analysis. Crossplots of S2 versus TOC and HI versus T_{max} show that the predominant kerogen types are Type II and Type II-III (Figure 4a and 4c). Although the vitrinite reflectance (R_o) data was both limited and poor, the trends in the available data show a reasonable correlation with an R^2 value of 0.72 as defined by Equation 3:

$$R_o = \frac{d-1259.6}{6985} \quad (3)$$

where, R_o is vitrinite reflectance, and d is depth in meters. However, comparing the wells in the area shows that Hekkingen Formation appears to be typically more mature. This separation in maturation is visible in Figure 4b showing the crossplot of HI versus. TOC. Note the relative position of well 16/8-3 S in the immature window, while well 7125/1-1 has the majority of its data points in the early oil generation window. The difference in maturation is not as clear utilizing the crossplot of HI versus T_{max}. However, this seems broadly related to the data from well 16/4-2, with the other data generally agreeing with this trend. Again, note the relative position of the data from well 16/8-3 S compared to well 7125/1-1 (Figure 4c).

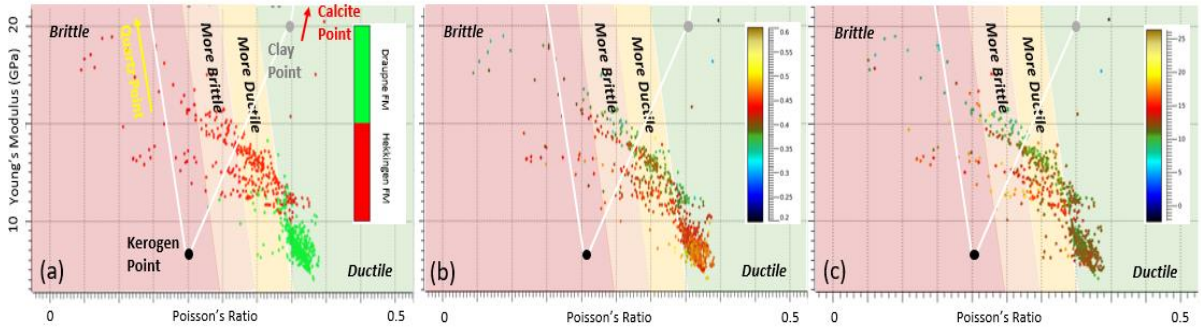

Figure 5 – Geomechanical analysis (modified from Perez and Marfurt, 2014) with salient end-member mineralogical points (modified from Mondol, 2018) of the (a) Draupne and Hekkingen Formations geomechanical parameters within the study areas compared with (b) porosity (%) and (c) TOC (wt. %).

Comparing the geomechanical parameters of the two areas utilizing all of the available wells, or just the two wells highlighted in this study, show the same trends. For simplicity, the template defined here focuses on the differences between wells 16/8-3 S and 7125/1-1. Utilizing a geomechanical rock physics template from Perez and Marfurt (2014), Young's modulus is displayed on the y-axis, and Poisson's ratio is displayed on the x-axis (Figure 5). The z-axis (color) in the three different panels displays the Draupne and Hekkingen Formation points (Figure 5a) in the two wells used in the present study (red points, Figure 3), porosity (Figure 5b), and TOC (Figure 5c). Porosity seems generally higher for the Hekkingen Formation than for the Draupne Formation. TOC values vary significantly for both formations, but one can see that the Hekkingen Formation shows general higher values than the Draupne Formation. Finally, one can see that the Draupne Formation plots predominantly in the ductile regime while the Hekkingen Formation plots predominantly in the transitionary regimes of more ductile and more brittle.

Discussion

The maturation of organic-rich shales is complex with a multitude of factors influencing it. Further to this, the sealing capacity of shales depends on more than just maturation, with temperature-pressure regime, mineralogy, shale fabric, TOC content, and more all playing a role (Johnson et. al., 2019; Rahman et al., 2020). However, the difference in both maturation and geomechanical parameters exhibited by the Draupne and Hekkingen Formations is significant given similar depositional history. The two main wells in this study, 16/8-3 S and 7125/1-1 have similar maximum depths and burial temperatures (Baig et al., 2016; Zadeh et al., 2017; Baig et al., 2019; present study). Slightly higher levels of TOC within the Hekkingen Formation may have assisted maturation, and specifically the changes in geomechanical parameters (Johnson et al., 2019). Vandenbroucke and Largeau (2007) suggest higher levels of TOC are associated with greater proportions of smectite and illite, which is seen in this study for the Hekkingen. Greater proportions of smectite and illite are also considered to make for a better seal (Mondol, 2007) which may revoke some of the maturation effects on the quality of the seal. So, while the proportion of hard to soft minerals and variations in clay mineralogy itself may have some influence on the different geomechanical responses, it is more likely that the subsequent diagenetic history played a larger role in the variation seen today.

The diagenetic history varied significantly between the two basins (Baig et al., 2016; Baig et al., 2019; Muller et al., 2019; Hansen et al., 2020). Proximity to the increased thermal capacity provided by salt mobilization would account for the maturation difference seen between the Draupne and Hekkingen Formations within the study areas. Indeed, Daniilidis and Herber (2017) highlight that the temperature gradient can be significantly altered by the presence of salt. The impact of the increased local temperature gradient can have an effect on the degree of maturation and the geomechanical parameters of the shales. Johnson et al. (2019) show this effect of salt locally within the Draupne Formation. However, the combination of both earlier, and potentially comparably prolonged exposure to increased thermal activity in the Hekkingen Formation (Muller et al., 2019) best accounts for the variation in geomechanical parameters.

Conclusion

Salt has a critical role in altering the geomechanical parameters of all rock it is exposed to. In the case of organic-rich shale, the maturation of kerogen lenses and fluid expulsion from them may

cause the initial growth of microfractures. The subsequent fracturing as the microfractures expand and connect have a large influence on the shale's strength. Mineralogy and clay composition, in addition to TOC content, will have a role on how well the shale mechanical properties evolve with geological history in terms of being a potential seal. The comparison between the Draupne and Hekkingen formations shows how organic-rich shales with a similar depositional history may reach different levels of maturation and geomechanical states as the result of a varied diagenetic history.Variation in diagenetic history has an influence on the quality that the two formations have in terms of being considered as a potential source rock, or potential seal. In terms of CCS, the long-term influence of mineralogy, clay composition, and TOC content must be considered as the present geological state is bound to change.

Acknowledgements

We thank the Norwegian Research Council for providing funding through the Prometheus project Prometheus (RCN #267775). Further, thanks for the helpful conversations that are extended to Maya Kobchenko and Manzar Fawad. Data is made available through the public databases DISKOS (https://portal.diskos.cgg.com/whereoil-data/) and NPD (https://factpages.npd.no/en/wellbore). Academic software licenses have been provided by Lloyd's Register for Interactive Petrophysics, CGG for both Jason and Hampson-Russell, and Schlumberger for Petrel.

References

Baig, I., Faleide, J.I., Jahren, J., and Mondol, N.H., 2016, Cenozoic exhumation on the southwestern Barents Shelf: Estimates and uncertainties constrained from compaction and thermal maturity analyses, Marine and Petroleum Geology, vol. 73, pgs. 105 - 130

Baig, I., Faleide, J.I., Mondol, N.H., and Jahren, J., 2019, Burial and exhumation history controls on shale compaction and thermal maturity along the Norwegian North Sea basin margin areas, Marine and Petroleum Geology, vol. 104, pgs. 61 - 85

Daniilidis and Heber, 2017, Salt intrusions providing new geothermal exploration target for higher energy recovery at shallower depths, Energy, vol. 118, 658 – 670

Dore, A.G., Vollset, J. and Hamar, G.P., 1985, Correlation of the offshore sequences referred to the Kimmeridge Clay Formation – relevance to the Norwegian Sector, Petroleum Geochemistry in Exploration of the Norwegian Shelf, vol. 1, pgs. 27 - 37

Faleide, J.I., Tsikalas, F., Breivik, A.J., Mjede, R., Ritzmann, O., and Engen, O., 2008, Structure and evolution of the continental margin off Norway and the Barents Sea, vol. 31, pgs. 82 - 91

Gerard and Buhrig, 1990, Seismic facies of the Permian section of the Barents Shelf: analysis and interpretation, Marine and Petroleum Geology, vol. 7, pgs. 234 - 252

Hansen, J.A., Yenwongfai, H.D., Fawad, D., and Mondol, N.H., 2017, Estimating exhumation using experimental compaction trends and rock physics relations, with continuation into analysis of source and reservoir rocks: central North Sea, offshore Norway. SEG, vol. 2017, pgs. 3971 - 3975

Hansen, J.A., Mondol, N.H., Tsikalas, F., and Faleide, J.I., 2020, Caprock characterization of Upper Jurassic organic-rich shales using acoustic properties, Norwegian Continental Shelf, Marine and Petroleum Geology, vol. 121

Henriksen, E., Bjornseth, H.M., Hals, T.K., Heide, T., Kiryukhina,T., and Klovjan, O.S., 2011, Uplift and erosion of the greater Barents Sea: impact on prospectivity and petroleum systems, Arctic Petroleum Geology, vol. 25, pgs. 271 - 281

Hindle, A., 1997, Petroleum migration pathways and charge concentration: a three-dimensional model, AAPG Bulletin, vol. 81, pgs. 1451 - 1481

Isaksen, G.H., and Ledje, H.I., 2001, Source rock quality and hydrocarbon migration pathways within the greater Utsira High area, Viking Graben, Norwegian North Sea: AAPG Bulletin, vol. 85, pgs. 861 - 883

Johnson, J.R., Hansen, J.A., Renard, F., and Mondol, N.H., 2019, Modeling maturation, elastic, and geomechanical properties of the Draupne Formation, offshore Norway, SEG, vol. 2019, pgs. 3251 - 3401

Kalani, M., Jahren, J., Mondol, N.H., and Faleide, J.I., 2015, Petrophysical implications of source rock microfracturing, International Journal of Coal Geology, vol. 143, pgs. 43–67

Mondol, N.H., Bjorlykke, K., Jahren, J., and Hoeg, K., 2007, Experimental mechanical compaction of clay mineral aggregates – Changes in physical properties of mudstones during burial, Marine and Petroleum Geology, vol. 24, pgs. 289 - 311

Mondol, N.H., 2018, Seal quality prediction using E-Poisson's ratio rock physics template – A case study from the Norwegian Barents Sea: Geoconvention 2018

Muller, R., Klausen, T.G., Faleide, J.I., Olaussen, S., Eide, C.H., and Suslova, A., Linking regional unconformities in the Barents Sea to compression-induced forebulge uplift at the Triassic-Jurassic transition, Tectonophysics, vol. 765, pgs. 35 - 51

Nooraiepour, M., Mondol, N.H., Hellevang, H., and Bjørlykke, K., 2017, Experimental mechanical compaction of reconstituted shale and mudstone aggregates: investigation of petrophysical and acoustic properties of SW Barents Sea cap rock sequences. Marine Petroleum Geology, vol. 80, pgs. 265–292

NPD, 2021, Norwegian Petroleum Directorate Fact Pages, http://factpages.npd.no/factpages/

Perez, R., and Marfurt, K., 2014, Mineralogy-based brittleness prediction from surface seismic data: Application to the Barnett Shale: Interpretation, vol. 2, pgs. 1 – 17

Rahman, M.D.J., Fawad, M., and Mondol, N.H., 2020, Organic-rich shale caprock properties of potential CO2 storage sites in the northern North Sea, offshore Norway, Marine and Petroleum Geology, vol. 122

Rossland, A., Escalona, A., and Rolfsen, R., 2013, Permian-Holocene tectonostratigraphic evolution of the Mandal High, Central Graben, North Sea, AAPG Bulletin, vol. 97, pgs. 923 – 957

Rystad Energy, 2021, Energy Transition Webinar: Hydrogen – all hype, or a huge opportunity? March 4, 2021

Skurtveit, E., Grande, L., Ogebule, O.Y., Gabrielsen, R.H., Faleide, J.I., and Mondol, N.H., 2015, Mechanical testing and sealing capacity of the Upper Jurassic Draupne formation, North Sea, 49th US Rock Mechanics/Geomechanics Symposium Expanded Abstracts ARMA-2015-331. American Rock Mechanics Association, San Francisco, California

Vandenbroucke and Largeau, 2007, Kerogen origin, evolution, and structure, Organic Geochemistry, vol. 38, pgs. 719 - 833

Vernik, L., and Landis, C., 1996, Elastic anisotropy of source rocks – implications for hydrocarbon generation and primary migration: AAPG Bulletin, vol. 80, pgs. 531 – 544.

Warren, J.K., 2017, Salt usually seals, but sometimes leaks: Implications for mine and cavern stabilities in the short and long term, Earth-Science Reviews, vol. 165, pgs. 302 - 341

Zadeh, M.K., Mondol, N.H., and Jahren, J., 2017, Velocity anisotropy of Upper Jurassic organic-rich shales, Norwegian Continental Shelf: Geophysics, vol. 82, pgs. 61 – 75.

EA-5

A potential alternative to Rock-Eval or wireline log calculations of TOC? – A case study from the Norwegian Continental Shelf

James R. Johnson
Maya Kobchenko
Nazmul H. Mondol
François Renard

83rd EAGE Annual Conference and Exhibition

6-9 June 2022

2022 EAGE ANNUAL
83RD CONFERENCE & EXHIBITION
MADRID I SPAIN

POTENTIAL ALTERNATIVE TO ROCK-EVAL OR WIRELINE CALCULATIONS OF TOC? CASE STUDY FROM THE NORWEGIAN CONTINENTAL SHELF

J. Johnson[1], M. Kobchenko[1], N. Mondol[1,2], F. Renard[1]

[1] University of Oslo; [2] Norwegian Geotechnical Institue

Summary

A potential alternative approach to the Rock-Eval or wireline log calculations of TOC is presented. Rock-Eval analysis was first carried out on 11 samples from 4 wells along the Norwegian Continental Shelf (3 North Sea, 1 Barents Sea). The source rock of interest is the Kimmeridge Formation (local names: Draupne Formation, Formation, Hekkingen Formation). An image analysis technique was then developed and carried out, utilizing SEM on the rock of the same depth for each sample. The data were compared to one another to confirm the accuracy of the technique. Afterward, the technique's accuracy was compared to the original TOC estimation results for Passey et al. (1990) and Schmoker and Hester (1983). Additionally, the data was compared to estimations of TOC utilizing these techniques from well logs available for these wells. Results from the current, and other studies, indicate that this alternative avoids potential limitations of the techniques it is compared to (i.e., Rock-Eval). With the dawn of machine learning and increased interest in image analysis, this technique offers a way to characterize the TOC (wt. %) content of organic-rich shales.

A potential alternative to Rock-Eval or wireline log calculations of TOC? – A case study from the Norwegian Continental Shelf

Introduction

Rock-Eval was invented in the mid-1970s (Baudin et al., 2015), and has continued to be improved upon since then (Espitalie et al., 1977; Camp, 1987; Baudin et al., 2015; Labus and Matyasik, 2018). However, the apparatus's principles, and basic operating conditions have remained relatively unchanged from the description set forth by Espitalie et al. (1977). Since that time, Rock-Eval pyrolysis analysis has become the standard for total organic carbon (TOC) content characterization.

Here, we present an alternative approach to classifying TOC content for organic-rich shales. The methodology proposed depends on image analysis. Here, we explore how the proposed workflow has been applied to 2D SEM images from organic-rich shales for the Norwegian Continental Shelf, specifically the Upper Jurassic Draupne and Hekkingen Formations (Kimmeridge equivalent). However, as microtomographic techniques improve, this workflow could be applied successfully to 3D images as well. Note, while it is currently possible to image shales using microtomography, the highest resolution now available only captures ~20% of the organic matter present based on comparisons with Rock-Eval analysis.

The advantages and disadvantages of each approach are discussed, including some of the potential pitfalls. Image analysis, utilized for TOC content, is a novel approach that requires further testing for validation. In its current form, it is important to verify the results with Rock-Eval pyrolysis. Note, Rock-Eval pyrolysis depends on the decomposition of organic matter by applying heat, absent oxygen (AAPG, 2021). A potential flaw with this approach, especially in clay-rich shales, is the dehydration and alteration of clay minerals that could affect the TOC (wt. %) reading.

Geological Background and Database

Before introducing the technique, it is important to understand in what geological context this case study is being carried out. The database is composed of 4 wells penetrating the Late Jurassic/Early Cretaceous Kimmeridge shale equivalent Draupne and Hekkingen Formations. Three of the wells (16/8-3 S, 17/4-1, and 34/4-3) sample the Draupne Formation within the North Sea and one well (7125/1-1) samples the Hekkingen Formation within the Barents Sea. The mineralogy for wells 16/8-3 S and 7125/1-1 (Johnson et al., 2022) are given in Figure 1 compared to averages for both the Kimmeridge (in grayscale), as well as other shales worldwide.

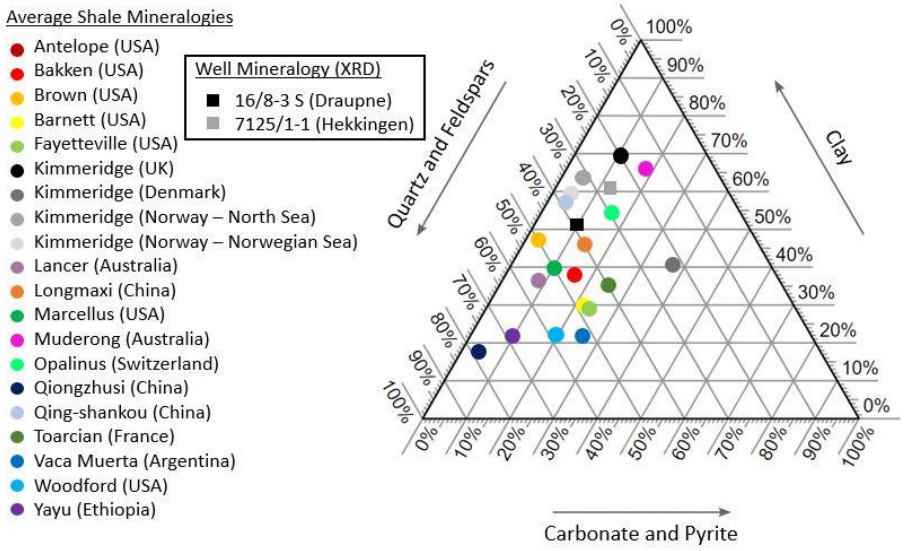

Figure 1 *Ternary diagram with average mineralogies from shales worldwide (circles) based on Ougier-Simonin et al. (2016). Kimmeridge Formation (in grayscale) with specific wellbore mineralogies from the study area (square) based on Johnson et al., 2022*

Compared to shale samples worldwide, the Draupne and Hekkingen Formations generally are more clay-rich (Figure 1). It has been established by Johnson et al. (2022) that the clay mineralogy for the study area is kaolinite-rich (~60%), with significant amounts of illite (~25%) and smectite (~15%). Chlorite is extremely sparse (<1%). The smectite to illite transformation begins to occur at ~60ºC (Thyberg and Jahren, 2010), with the dehydration of both smectite and kaolinite occurring between 250 – 600ºC (Bhargava et al., 2005; Vidonish et al., 2018).

Theory and Method

In Rock-Eval pyrolysis, a sample is placed in a vessel and is progressively heated to a minimum of 550ºC (AAPG, 2021) and often exceeding that (Camp, 1987; Lafargue et al., 1998; Bhargava et al., 2004; Labus and Matyasik, 2018). In theory, as the temperature increases, matter in various states is volatized, representing recorded peaks S1, S2, and S3 (Espitalie, 1977; AAPG, 2021), and residual carbon representing peak S4 (Figure 2a). Then, TOC is calculated as proposed by AAPG (2021):

$$TOC = \frac{(0.82(S1+S2)+S4)}{10} \quad (1)$$

Where TOC (wt. %) is derived from Rock-Eval analysis and the four recorded peak values (i.e., S1, S2, S3, and S4) as shown in Figure 2a.

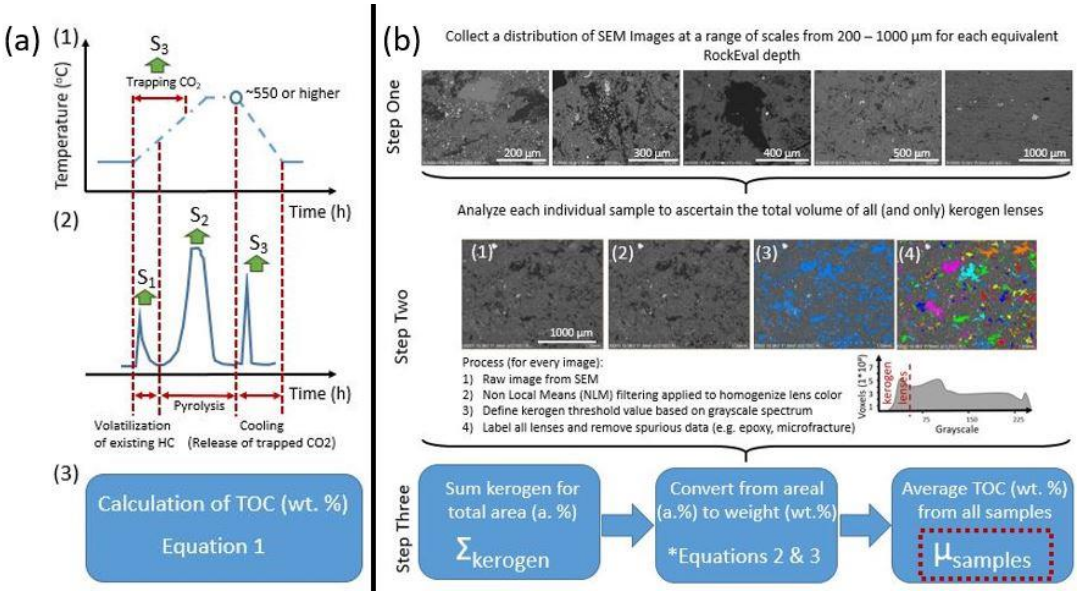

Figure 2 *Compares (a) Rock-Eval TOC estimation technique with (b) SEM image analysis technique*

The proposed imaging technique has three essential steps (Figure 2b). The first step is capturing SEM images of a given organic-rich shale from a slide. Note, in order for the best comparison to Rock-Eval pyrolysis data, the prepared sample should be taken from the core of the same depth. In this study, ~20 images were taken from each prepared slide varying in scale from 200 – 1000 µm. The second step is to clean the SEM images and isolate all kerogen lenses. The sum of the area of all kerogen lenses over the area of the total SEM image size will give an areal percent (a. %) for TOC. In order to convert to TOC (wt. %), optimally, the density of each kerogen lens would be assessed. However, in this case, a density of 1.25 g/cm3 was assumed for the kerogen (Okiongbo et al., 2005) based on a study of kerogen from the Norwegian Continental Shelf (NCS). With this information, the weight of kerogen can be calculated:

$$W_{kerogen} = V_{kerogen} \times \rho_{kerogen} \quad (2)$$

Where $W_{kerogen}$ is the weight of kerogen, $V_{kerogen}$ is the volume of the kerogen, and $\rho_{kerogen}$ is the assumed density of kerogen. Combine this with the weight of the sample (i.e. W_{sample}) derived from laboratory measurements, one can calculate the TOC of the sample (wt. %) as follows:

$$TOC_{sample} = \frac{W_{kerogen}}{W_{sample}} \quad (3)$$

The third step is to average the TOC (wt. %) values for all 20 images for each given sample being analyzed and compare the averages for each sample against the Rock-Eval data for the equivalent depth. Finally, a comparison between TOC (wt. %) obtained from Rock-Eval and the novel image analysis technique is carried out in order to provide statistical validity.

Results and Discussion

A comparison between TOC (wt. %) obtained from Rock-Eval pyrolysis and SEM image analysis shows a reasonable correlation of 0.79 for R^2 (Figure 3). While the number of data points is still limited; the match is currently better than what is available when TOC is calculated from wireline logs. Indeed, currently, the correlation from this technique is better than the original work by by Schmoker and Hester (1983) or Passey et al. (1990) on correlations of wireline log TOC estimates with measured values. They both presented R^2 values of 0.65 based on their original work, compared to 0.79. Furthermore, the number of outliers that existed beyond 20% deviation was 23 out of 37 [i.e., ~62%] for the Passey et al. (1990) dataset and 11 out of 59 [i.e., ~19%] for the Schmoker and Hester (1983) dataset. Currently, only 1 out of 11 [i.e., ~9%] datapoints is beyond 20% deviation utilizing estimates from SEM images (Figure 3).

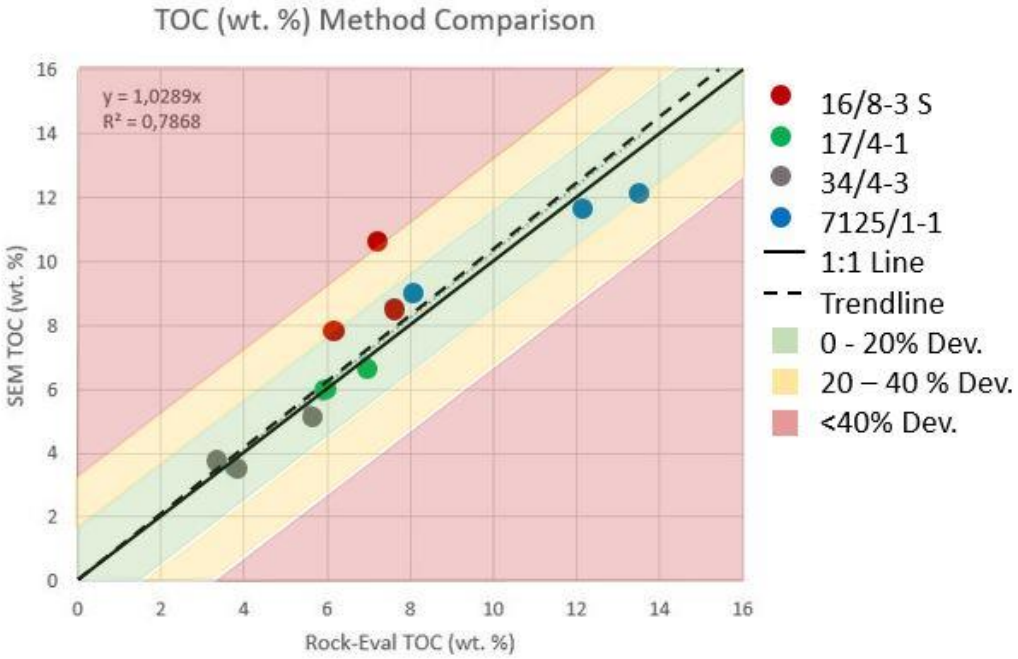

Figure 3 *Comparison of TOC (wt. %) from Rock-Eval with TOC (wt. %) from SEM image analysis (process outlined in Figure 2) from 4 wells (3 wells from the North Sea and 1 well from the Barents Sea). Most data points sit within a 20% deviation from the 1:1 line, with an average deviation of ~13%.*

Zhao et al. (2016) investigated the impact of kerogen on maturation, looking at SEM images prior to and after maturation to Ro ~2.0 (i.e., ~450 ºC). It is noted that there is a significant impact on both the organic and inorganic material in terms of distribution and size after maturation. Given the approximate temperatures required for the alteration and dehydration of clays (Bhargava et al., 2005; Ijiri et al., 2018; Vidonish et al., 2018), it is not surprising that this would have some impact on recorded TOC (wt. %) from the Rock-Eval technique. However, it may only have a material effect on the most clay-rich shales (Figure 1). This includes the Draupne and Hekkingen Formations, but also the Opalinus (Switzerland), Muderong (Australia), and the Qing-Shankou (China) shales.

Conclusions

While further work is required to confirm the validity, the study presents a novel way to derive TOC from image analysis utilizing 2D SEM images. With the dawn of machine learning and an increased interest in image analysis worldwide, this technique represents an alternative way to characterize

organic-rich shales' TOC (wt. %) content cheaply and efficiently. A significant advantage that image analysis has over Rock-Eval long term is the ability to physically see and analyze the entire distribution of organic matter, especially utilizing 3D microtomography. However, the 2D SEM imaging technique provides presently provides enough data to warrant a proper investigation – comparing data gleaned here to both Rock-Eval and wireline log estimates.

References

AAPG, [2021]. Rock-Eval pyrolysis. Tulsa, OK, USA. *accessed December 27th* https://wiki.aapg.org/rock-eval_pyrolysis

Baudin, F., Disnar, J., Aboussou, A., and Savignac, F. [2015]. Guidelines for Rock-Eval analysis of recent marine sediments. Organic Geochemisty. **86**(2015), 71-80

Bhargava, S., Awaja, F., and Subasinghe, N. [2005]. Characteriation of some Australian oil shale using thermal X-ray and IR techniques. Fuel, **84**(2005), 707-715

Camp, D. [1987]. Oil shale heat-capacity relations and heats of pyrolysis and dehydration. *20th Oil Shale Symposium.*

Espitalie, J, Deroo, G., and Marquis F., [1985] La pyrolyse Rock-Eval et ses applications. Revue de l'Institut Francais du Petrole, **32**, 23 – 42.

Johnson, J., Hansen, J., Rahman, J., Renard, F., and Mondol, N. [2022]. Mapping the maturity of organic-rich shale with combined geochemical and geophysical data, Draupne Formation, Norwegian Continental Shelf. Marine and Petroleum Geology, 138 (2022), 105525

Labus, M., and Matyasik, I. [2018]. Application of different thermal analysis techniques for the evaluation of petroleum source rocks. Journal of Thermal Analysis and Calorimetry, **136**, 1185-1194.

Lafargue, E., Marquis, F., and Pillot, D. [1998]. Rock-Eval Applications in hydrocarbon exploration, production, and soil contamination studies. Institut Francais du Petrole, **53** (4), 421 – 437.

Okiongbo, K., Aplin, A., Larter, S. [2005]. Changes in type II kerogen density as a function of maturity: evidence from the Kimmeridge Clay Formation. Energy & Fuels, 19(6), 2495-2499.

Ougier-Simonine, A., Renard, F., Boehm, C., and Vidal-Gilbert, S. [2016] Microfracturing and microporosity in shales. Earth-Science Reviews, **162** (2016), 198-226.

Passey, Q., Creaney, S., Kulla, J., Moretti, F., and Stroud, J. [1990]. A practical model for organic richness from porosity and resistivity logs. AAPG Bulletin, **74** (12), 1777-1794.

Schmoker, J., and Hester, T. [1983]. Organic carbon in Bakken Formation, United States portion of Williston Basin. AAPG Bulletin, **67**(12), 2165-2174.

Thyberg, B., Jahren J., Winje. T., Bjørlykke, K., Faleide, J., and Marcussen, Ø. [2010]. Quartz cementation in Late Cretaceous mudstones, northern North Sea: Changes in rock properties due to dissolution of smectite and precipitation of microquartz crystals. Marine and Petroleum Geology, **27**, 1752–1764.

Vidonish, J., Alvarez, P., and Zygourakis, K. [2018]. Pyrolytic remediation of oil-contaminated soils: reaction mechanisms, soil changes, and implication for treated soil fertility. Industrial & Engineering Chemistry Research, **57**, 3489-3500.

Zhao, L., Qin, X., Han, D., Geng, J., Yang, Z., and Cao., H. [2016]. Rock-physics modeling for the elastic properties of organic shale at different maturity stages. Geophysics, **81**(5), 527 -541.

EA-6

Using microscopy image analysis to calculate the Mineral Brittleness Index in organic-rich shale

James R. Johnson
Austin Bailey
Nazmul H. Mondol
François Renard

Sixth International Conference on Faults and Top Seals

26-28 September 2022

FAULT&TOPSEALS VIENNA•2022

EAGE

Using microscopy image analysis to calculate the Mineral Brittleness Index in organic-rich shale

J. Johnson[1], A. Bailey[2], N.H. Mondol[1,3], F. Renard[1]
[1] University of Oslo; [2] Coterra Energy; [3] NGI

Summary

The study investigates the factors that influence the mechanical and acoustic properties of shale as a potential top seal for CO2 sequestration, nuclear waste disposal, and oil and gas traps. Using scanning electron microscopy (SEM) and X-ray diffraction (XRD) techniques on borehole samples from the Norwegian Continental Shelf, we separate shale bulk mineralogy into three major components: hard minerals (quartz, feldspar, pyrite), soft minerals (clays), and kerogen content. These outputs are used for calculating the Mineralogical Brittleness Index (MBI). The separation process utilizes a novel image analysis technique, and then the results are compared with the X-ray diffraction data. From the results, estimates of the mechanical and acoustic properties of the organic-rich Draupne and Hekkingen formation shales as a potential seal are proposed. After validation of the proposed image analysis technique, correlations with Elastic Brittleness Index (EBI) are highlighted as they apply to the acoustic properties of the shale. By separating shale out into three phases, defined by the transition of kerogen into hydrocarbons and the nearly simultaneous smectite-illite transformation, the effect of organic and inorganic components on top seal integrity is investigated during each stage relate to both mechanical and acoustic properties.

Introduction

The study investigates factors that influence the mechanical and acoustic behaviors of shale as a potential top seal for CO_2 sequestration, nuclear waste disposal, and hydrocarbon traps. Organic-rich shales are described in three phases defined by the transition of kerogen into hydrocarbons and the nearly simultaneous smectite-illite transformation. Image analysis of scanning electron microscopy data is presented as a possible alternative to X-ray diffraction data of bulk mineralogy to identify the three phases. As big data and statistical analysis thereof becomes more relevant, separating MBI utilizing the suggested method could become both more cost and time effective.

Geological Background and Database

The database is composed of two wells penetrating the Upper Jurassic/Early Cretaceous Kimmeridge shale of the Draupne and Hekkingen formations, Norwegian Continental Shelf. Well 16/8-3 S penetrates the Draupne formation in the North Sea and well 7125/1-1 penetrates the Hekkingen formation in the Barents Sea. Bulk mineralogy analyses indicate that the samples are clay-rich, ranging from ~51-61%, contain a reasonable amount of quartz/feldspar, sranging from ~29-40%, and are carbonate/pyrite poor around ~10% (Johnson et al., 2022b). In terms of clay mineralogy, the samples here contain ~47 – 62% kaolinite and contain virtually no chlorite (<1%). The samples are at a depth and PT regime that places them in the smectite-illite transition. This is reflected by values of smectite ~20% and illite values ranging from ~19-32%. TOC values for the Draupne shale samples are ~7 wt. %, while the values for the Hekkingen shale range from ~8-14 wt. %.

Theory and Method

Mineralogy has a fundamental impact on the material properties of shales (Ougier-Simonin et al., 2016; Johnson et al., 2022b). Proponents that relate mineralogy and brittleness would suggest that the ratio of hard (i.e., stiff) minerals to soft minerals is critical to understanding how brittle or ductile the shale will behave (Jarvie et al., 2007; Jin et al., 2014; Alzahabi et al., 2015, Johnson et al., 2022a). These studies use an equation, also presented by Johnson et al., (2022a), to calculate a Mineralogy Brittleness Index (MBI)

$$MBI = \frac{\mathrm{Qtz+Carb+Fsp+Py}}{Qtz+Carb+Fsp+Py+Cly+TOC} \quad (1)$$

where, Qtz is quartz (wt. %), Carb is carbonate (wt. %), Fsp is feldspar (wt. %), Py is pyrite (wt. %), Cly is total clay (wt. %), and TOC (wt. %) is total organic carbon. MBI ranges between 0, which is ductile, and 1, which is brittle.

Processing of scanning electron microscopy images, of organic-rich shale samples from the Draupne and Hekkingen formations is carried out. Each image is segmented into three components (Figure 1):

- Inorganic component A: hard minerals (i.e., quartz, feldspar, pyrite, etc.)
- Inorganic component B: soft minerals (i.e., clay)
- Organic component: kerogen

In this study, ~20 images were taken from each prepared shale thin section, varying in width from 50-500 µm. Every thin section correlates to a given depth of core from two wells studied here. Samples with megacrysts are discounted as they disproportionality represent stiff minerals. Similarly, images with dimension greater than ~500 µm were not used as they disproportionately represent clay minerals as a result of the decimation of stiff mineral pixels. For the inorganic component, an average is taken from all the samples and the results are compared to bulk mineralogy estimates from X-ray diffraction data (XRD). For the organic component, similarly an average is taken from all samples and compared to Rock-Eval analysis.

In addition to the ratio of hard minerals to soft minerals, the individual clay minerals show a variety of attributes that impact the material properties of shales. Table 1 displays the four clay mineral groups (i.e. kaolinite, smectite, illite, and chlorite), and their attributes as they relate to shale behaviour. Comparisons of the physical geometry of clay minerals reveal that the diameter-thickness ratio, D/t, is typically greater for illite (D/t ~2000), and smaller for both kaolinite (D/t in the range 141-1408) and chlorite (D/t in the range 213-1418). Smectite's D/t ratio roughly spans between the upper limit for kaolinite and that of illite. D/t correlates with stronger material properties (Lee et al., 2001).

Furthermore, geometrical anisotropy relates to particle alignment at the microscale, and will have a macroscale impact on material properties (Ougier-Simonin et al., 2016).

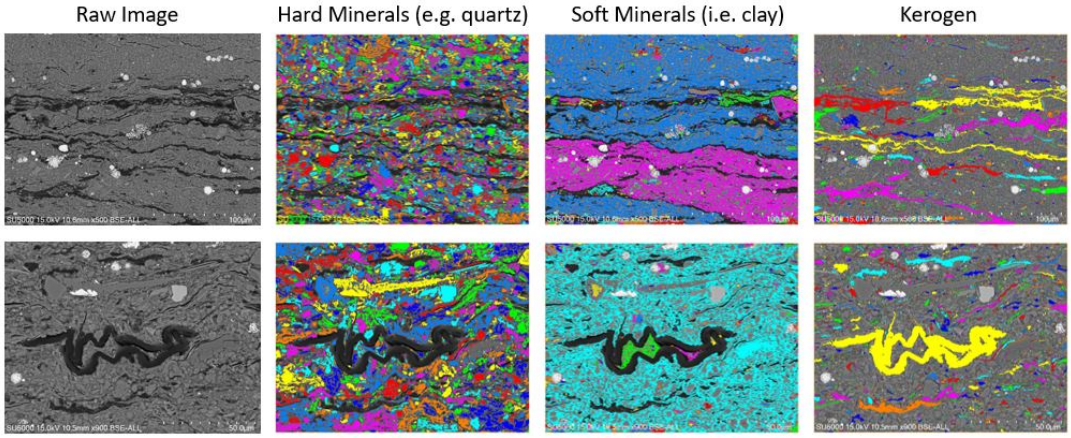

Figure 1 *From left to right, the initial raw SEM image, segmentation of hard minerals (i.e. quartz, feldspar, pyrite, etc.), segmentation of soft minerals, (i.e. clay), and segmentation of kerogen. Top row is larger scale (100 µm) and bottom row is smaller scale (50 µm). The colors indicate connected surfaces areas of the same mineral or kerogen lens.*

Table 1: Clay mineral groups with attributes displaying the degree of geometrical and material (i.e. moduli) anisotropy (Wang et al., 2001; Mondol et al., 2008; Ougier-Simonin et al., 2016; Zhao et al., 2016; Sayers and Boer, 2018). '*' indicates a swelling clay, while '**' indicates a non-swelling clay.

Clay Group	Thickness (Å)	Diameter (µm)	Density (g/cm3)	Bulk Modulus (GPa)	Shear Modulus (GPa)
Kaolinite**	7.1	0.1 – 1.0	2.65	44.0	21.0
Smectite*	9.6 – 14.8	~2.0	2.15	9.3	6.9
Illite**	10.0	~2.0	2.75	60.1	25.3
Chlorite**	14.1	0.3 – 2.0	2.80	81.0	27.0

The ratio between the bulk modulus and the shear modulus, K/µ, compares how anisotropic materials behave mechanically, where the order of anisotropy is chlorite (K/µ~3.0), illite (K/µ~2.4), kaolinite (K/µ~2.1), and smectite (K/µ~1.3). Density is also much lower for smectite (Table 1). Mechanical anisotropy has been shown to influence the minimum horizontal stress impacting the rate of fracture formation and degree of fracture tortuosity (Khan et al., 2012). while density is known to have a strong influence on the acoustic properties (Berndt et al., 2004; Prasad et al., 2009; Sayers and Boer, 2018).

Results

Average bulk mineralogy values were calculated from the scanning electron images of shales collected at various depths in the two wells and compared to XRD data. Since the technique is geared towards separating out hard and soft minerals from each other, it is ideal for calculating MBI (Equation 1). The aspect ratio of the hard minerals reveals that their behaviour is comparatively isotropic. Apparent orientation is comparatively random for the stiff minerals, while nearly bedding parallel for kerogen lenses. It was not possible to get either an aspect ratio or a direct orientation of clay minerals due to their connectivity. In fact, soft minerals (i.e. clays) are shown to dominate the compositional matrix while hard minerals (i.e. quartz, feldspar, pyrite, etc.) are distributed throughout said compositional matrix. Kerogen is both a good indicator of soft mineral orientation and is shown to create breaks in the continuity of the soft mineral matrix (Figure 1). Utilizing kerogen as a proxy, soft minerals have an orientation of +/-30°, more or less parallel to bedding (Table 2). Note, there appears to be a relationship between the geometrical and mechanical behaviour of minerals, and how they are expected to influence material properties.

Table 2: Comparison of MBI calculations from XRD and SEM data. Additionally, the hard mineral (HM) and kerogen lens (KL) aspect ratio range and average orientations (degrees) are compared to one another.

Sample (well)	XRD (hard:soft)	SEM (hard:soft)	MBI (XRD/SEM)	HM aspect ratio range	KL aspect ratio range	HM orientation	KL orientation
D1 (16/8-3 S)	46:54	43:57	0.46/0.43	~0.5	~0.9	random	~ bedding parallel
D2 (16/8-3 S)	42:58	45:55	0.42/0.45				
H1 (7125/1-1)	36:64	38:62	0.36/0.38				
H2 (7125/1-1)	33:67	37:63	0.33/0.37				

Discussion

The mechanical and acoustic properties of shale is significantly impacted by two chemical conversions that take place with increased burial. The first is the conversion of kerogen to hydrocarbons, and the second is the smectite-illite transformation. These two processes take place within a very similar depth window (Figure 2). Utilizing Figure 2, we can separate the state of shale into three phases – before conversion (Phase I), during conversion (Phase II), and after conversion (Phase III).

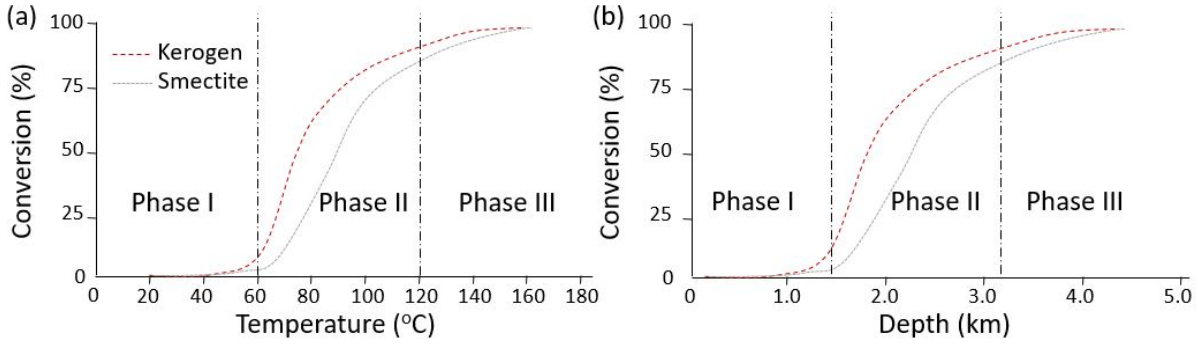

Figure 2 *The conversion of kerogen to hydrocarbon (red) as a percentage composition (Tissot and Welte, 1984) compared to the conversion of smectite to illite (grey) as a percentage composition (Carcione and Avseth, 2015), separated into three phases: Phase I (prior to conversion), Phase II (conversion), and Phase III (after conversion) as a function of temperature (a) and depth (b). Temperature to depth conversion is based on a relationship from the Norwegian Continental Shelf (Johnson et al., 2022a).*

Prior to conversion, in Phase I, the material properties of the shale are primarily controlled by composition, as derived using Equation 1. However, the composition of clay mineralogy has a secondary impact. This is expressed by variations in the clay mineralogy composition. A tertiary impact is provided by the presence of kerogen lenses that act as a brittle, load-bearing constituent of the matrix (Prasad et al., 2009). During the conversion, in Phase II, bulk mineralogy interacts with both kerogen content and shale mineralogy and may control the formation of microfractures (Anders et al., 2014; Ougier-Simonin et al., 2016). During this process, the relationship between bulk mineralogy and organic content becomes the primary factor influencing the material property (Zhao et al., 2016). The smectite-illite transition becomes a secondary factor, however the proximity of transition times between the two does have a measurable impact on acoustic properties (Berndt et al., 2004; Alfred and Vernik, 2013; Sayers and Boer, 2018). It has been shown that MBI can be correlated to elastic brittleness index (EBI), which is quantified using acoustic properties (Johnson et al., 2022a). The processes have competing influences on acoustic properties, where:

- An increase in porosity (i.e. microfracturing), due to both processes results in a decrease in density and thereby an increase of acoustic waves transit times. Likewise, the fracture network will be largely transversely isotropic resulting in greater transit times (Sayers and Boer, 2018).
- Contrary to this, the smectite-illite conversion greatly increases density, which in turn will decrease transit times (Berndt et al., 2004).

After conversion, in Phase III, the microfractures created in combination with larger structural elements allow for hydrocarbon migration (Johnson et al., 2022b). While, bulk mineralogy continues to be the primary factor influencing material properties there is a reversion to shale mineralogy playing a secondary role (Voltolini and Franklin, 2020). Again, this is influenced by the composition of clay mineralogy, their geometry, and mechanical behavior thereof (Table 1).

Conclusion

Understanding the phase of conversion for both kerogen and smectite-illite informs which parameters have the greatest influence on material properties. Being able to separate out shale into three components: hard minerals, soft minerals, and organic matter allows one to understand what the material properties are likely to be. Furthermore, estimation of MBI utilizing image analysis of SEM data is becoming faster and increasingly time effective due to advances in data analytics. By combining this information, one can utilize the information provided at the microscale to estimate material properties at the macroscale for shale in a variety of states (i.e. metagenesis, diagenesis, catagenesis). All of this is critical to understanding top seals and their potential weaknesses in the context of oil and gas exploration, nuclear waste repository sites, and CO_2 sequestration.

References

Alfred, D. and Vernik, L. [2013]. A new petrophysical model for organic shales. Petrophysics. **54**(3), 240-247

Alzahabi, A., AlQahtani, G., Soliman, M.Y., Bateman, R.M., Asquith, G., Vadapalli, R., [2015]. Fracturability index is a mineralogical index: a new approach for fracturing decision. *SPE Saudi Arabia Technical Symposium 2015*

Ander, M.H., Laubach, S.E., and Scholz, C.H. [2014]. Microfractures: a review. Journal of Structural Geology. **69**(B). 377-394.

Berndt, C., Bunz, S., Clayton, T., Mienert, J., Saunders, M., [2004]. Seismic character of bottom simulating reflectors: examples from the mid-Norwegian marign. Marine and Petroleum Geology. **21**(2004), 723-733

Carcione, J.M., and Avseth, P., [2015]. Rock-physics templates for clay-rich source rocks. Geophysics. **80**(5), 481-500.

Jarvie, D.M., Hill, R.J., Ruble, T.E., Pollastro, R.M., [2007]. Unconventional shale-gas systems: the Mississippian Barnett Shale of north-central Texas as one model for thermogenic shale-gas assessment. AAPG Bulletin. **91**, 475-499.

Jin, X., Shah, S.N., Roegiers, J.C., Zhang, B., [2014]. Fracability evaluation in shale reservoirs-an integrated petrophysics and geomechanics approach. *SPE Hydraulic Fracturing Technology Conference 2014*

Johnson, J.R., Hansen, J.A., Rahman, J., Renard, F., Mondol, N.H., [2022a]. Mapping the maturity of organic-rich shale with combined geochemical and geophysical data, Draupne Formation, Norwegian Continental Shelf. Marine and Petroleum Geology. **138**(2002), 105525

Johnson, J.R., Kobchenko, M., Mondol, N.H., Renard, F., [2022b]. Multiscale synchrotron microtomography imaging of kerogen lenses in organic-rich shales from the Norwegian Continental Shelf. International Journal of Coal Geology. **253**(2022), 103954

Lee, K., Pan, W., Kuo, J., [2001]. The influence of the diameter-to-thickness ratio on the stability of circular tubes under cyclic bending. International Journal of Solids and Structures. **38**(14), 2401-2413

Mondol, N.H., Jahren, J., Bjorlykke, K., [2008]. Elastic properties of clay minerals. Leading Edge. **27**(6), 758-770

Ougier-Simonin, A., Renard, F. Boehm, C., and Vidal-Gilbert, S., [2014]. Microfracturing and microporosity in shales. Earth-Science Reviews. **162**(2016), 198-226

Prasad, M., Pal-Bathija, A., Johnston, M., Rydzy, M., Batzle, M., [2009]. Rock physics of the unconventional. Leading Edge. **28**, 34-38.

Sayers, C.M., and Boer, L.D., [2018]. The elastic properties of clay in shales. Journal of Geophysical Research: Solid Earth. **123**, 5965-5974

Tissot, B.P., and Welte, D.H. [1984]. Petroleum formation and occurrence. *Springer-Verlag Berlin Heidelberg GmBH*

Voltolini, M., and Franklin, J.G.A., [2020]. The sealing mechanisms of a fracture in clay as revealed by in situ synchrotron X-Ray micro-tomography. Frontiers of Earth Science. **8**, 1-13.

Wang, Z., Wang, H., and Cates, M.E., [2001]. Effective elastic properties of solid clays. Geophysics. **66**(2), 428-440

Zhao, L., Qin, X., Han, D., Geng, J., Yang, Z., and Cao, H., [2016]. Rock-physics modeling for the elastic properties of organic shale at different maturity stages. Geophysics. **81**(5). 527-541